

Advances in Civil Engineering

Fluid-Solid Coupling Problems in Coal Mine Gas Drainage

Lead Guest Editor: Quanle Zou

Guest Editors: Ting Liu, Xin Wang, Zhiheng Cheng, and Peng Liu





Fluid-Solid Coupling Problems in Coal Mine Gas Drainage

Advances in Civil Engineering

Fluid-Solid Coupling Problems in Coal Mine Gas Drainage

Lead Guest Editor: Quanle Zou

Guest Editors: Ting Liu, Xin Wang, Zhiheng Cheng,
and Peng Liu



Copyright © 2022 Hindawi Limited. All rights reserved.

This is a special issue published in "Advances in Civil Engineering." All articles are open access articles distributed under the Creative Commons Attribution License, which permits unrestricted use, distribution, and reproduction in any medium, provided the original work is properly cited.


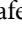
Chief Editor

Cumaraswamy Vipulanandan, USA










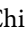



Associate Editors

Chiara Bedon , Italy
Constantin Chalioris , Greece
Ghassan Chehab , Lebanon
Ottavia Corbi, Italy
Mohamed ElGawady , USA
Husnain Haider , Saudi Arabia
Jian Ji , China
Jiang Jin , China
Shazim A. Memon , Kazakhstan
Hossein Moayedi , Vietnam
Sanjay Nimbalkar, Australia
Giuseppe Oliveto , Italy
Alessandro Palmeri , United Kingdom
Arnaud Perrot , France
Hugo Rodrigues , Portugal
Victor Yepes , Spain
Xianbo Zhao , Australia

Academic Editors

José A.F.O. Correia, Portugal
Glenda Abate, Italy
Khalid Abdel-Rahman , Germany
Ali Mardani Aghabaglou, Turkey
José Aguiar , Portugal
Afaq Ahmad , Pakistan
Muhammad Riaz Ahmad , Hong Kong
Hashim M.N. Al-Madani , Bahrain
Luigi Aldieri , Italy
Angelo Aloisio , Italy
Maria Cruz Alonso, Spain
Filipe Amarante dos Santos , Portugal
Serji N. Amirkhanean, USA
Eleftherios K. Anastasiou , Greece
Panagiotis Ch. Anastasopoulos , USA
Mohamed Moafak Arbili , Iraq
Farhad Aslani , Australia
Siva Avudaiappan , Chile
Ozgur BASKAN , Turkey
Adewumi Babafemi, Nigeria
Morteza Bagherpour, Turkey
Qingsheng Bai , Germany
Nicola Baldo , Italy
Daniele Baraldi , Italy

Eva Barreira , Portugal
Emilio Bastidas-Arteaga , France
Rita Bento, Portugal
Rafael Bergillos , Spain
Han-bing Bian , China
Xia Bian , China
Huseyin Bilgin , Albania
Giovanni Biondi , Italy
Hugo C. Biscaia , Portugal
Rahul Biswas , India
Edén Bojórquez , Mexico
Giosuè Boscato , Italy
Melina Bosco , Italy
Jorge Branco , Portugal
Bruno Briseghella , China
Brian M. Broderick, Ireland
Emanuele Brunesi , Italy
Quoc-Bao Bui , Vietnam
Tan-Trung Bui , France
Nicola Buratti, Italy
Gaochuang Cai, France
Gladis Camarini , Brazil
Alberto Campisano , Italy
Qi Cao, China
Qixin Cao, China
Iacopo Carnacina , Italy
Alessio Cascardi, Italy
Paolo Castaldo , Italy
Nicola Cavalagli , Italy
Liborio Cavaleri , Italy
Anush Chandrappa , United Kingdom
Wen-Shao Chang , United Kingdom
Muhammad Tariq Amin Chaudhary, Kuwait
Po-Han Chen , Taiwan
Qian Chen , China
Wei Tong Chen , Taiwan
Qixiu Cheng, Hong Kong
Zhanbo Cheng, United Kingdom
Nicholas Chileshe, Australia
Prinya Chindaprasirt , Thailand
Corrado Chisari , United Kingdom
Se Jin Choi , Republic of Korea
Heap-Yih Chong , Australia
S.H. Chu , USA
Ting-Xiang Chu , China

Zhaofei Chu , China
Wonseok Chung , Republic of Korea
Donato Ciampa , Italy
Gian Paolo Cimellaro, Italy
Francesco Colangelo, Italy
Romulus Costache , Romania
Liviu-Adrian Cotfas , Romania
Antonio Maria D'Altri, Italy
Bruno Dal Lago , Italy
Amos Darko , Hong Kong
Arka Jyoti Das , India
Dario De Domenico , Italy
Gianmarco De Felice , Italy
Stefano De Miranda , Italy
Maria T. De Risi , Italy
Tayfun Dede, Turkey
Sadik O. Degertekin , Turkey
Camelia Delcea , Romania
Cristoforo Demartino, China
Giuseppe Di Filippo , Italy
Luigi Di Sarno, Italy
Fabio Di Trapani , Italy
Aboelkasim Diab , Egypt
Thi My Dung Do, Vietnam
Giulio Dondi , Italy
Jiangfeng Dong , China
Chao Dou , China
Mario D'Aniello , Italy
Jingtao Du , China
Ahmed Elghazouli, United Kingdom
Francesco Fabbrocino , Italy
Flora Faleschini , Italy
Dingqiang Fan, Hong Kong
Xueping Fan, China
Qian Fang , China
Salar Farahmand-Tabar , Iran
Ilenia Farina, Italy
Roberto Fedele, Italy
Guang-Liang Feng , China
Luigi Fenu , Italy
Tiago Ferreira , Portugal
Marco Filippo Ferrotto, Italy
Antonio Formisano , Italy
Guoyang Fu, Australia
Stefano Galassi , Italy

Junfeng Gao , China
Meng Gao , China
Giovanni Garcea , Italy
Enrique García-Macías, Spain
Emilio García-Taengua , United Kingdom
DongDong Ge , USA
Khaled Ghaedi, Malaysia
Khaled Ghaedi , Malaysia
Gian Felice Giaccu, Italy
Agathoklis Giaralis , United Kingdom
Ravindran Gobinath, India
Rodrigo Gonçalves, Portugal
Peilin Gong , China
Belén González-Fonteboa , Spain
Salvatore Grasso , Italy
Fan Gu, USA
Erhan Güneyisi , Turkey
Esra Mete Güneyisi, Turkey
Pingye Guo , China
Ankit Gupta , India
Federico Gusella , Italy
Kemal Hacıfendioglu, Turkey
Jianyong Han , China
Song Han , China
Asad Hanif , Macau
Hadi Hasanzadehshooiili , Canada
Mostafa Fahmi Hassanein, Egypt
Amir Ahmad Hedayat , Iran
Khandaker Hossain , Canada
Zahid Hossain , USA
Chao Hou, China
Biao Hu, China
Jiang Hu , China
Xiaodong Hu, China
Lei Huang , China
Cun Hui , China
Bon-Gang Hwang, Singapore
Jijo James , India
Abbas Fadhil Jasim , Iraq
Ahad Javanmardi , China
Krishnan Prabhakan Jaya, India
Dong-Sheng Jeng , Australia
Han-Yong Jeon, Republic of Korea
Pengjiao Jia, China
Shaohua Jiang , China

MOUSTAFA KASSEM , Malaysia
Mosbeh Kaloop , Egypt
Shankar Karuppanan , Ethiopia
John Kechagias , Greece
Mohammad Khajehzadeh , Iran
Afzal Husain Khan , Saudi Arabia
Mehran Khan , Hong Kong
Manoj Khandelwal, Australia
Jin Kook Kim , Republic of Korea
Woosuk Kim , Republic of Korea
Vaclav Koci , Czech Republic
Loke Kok Foong, Vietnam
Hailing Kong , China
Leonidas Alexandros Kouris , Greece
Kyriakos Kourousis , Ireland
Moacir Kripka , Brazil
Anupam Kumar, The Netherlands
Emma La Malfa Ribolla, Czech Republic
Ali Lakirouhani , Iran
Angus C. C. Lam, China
Thanh Quang Khai Lam , Vietnam
Luciano Lamberti, Italy
Andreas Lampropoulos , United Kingdom
Raffaele Landolfo, Italy
Massimo Latour , Italy
Bang Yeon Lee , Republic of Korea
Eul-Bum Lee , Republic of Korea
Zhen Lei , Canada
Leonardo Leonetti , Italy
Chun-Qing Li , Australia
Dongsheng Li , China
Gen Li, China
Jiale Li , China
Minghui Li, China
Qingchao Li , China
Shuang Yang Li , China
Sunwei Li , Hong Kong
Yajun Li , China
Shun Liang , China
Francesco Liguori , Italy
Jae-Han Lim , Republic of Korea
Jia-Rui Lin , China
Kun Lin , China
Shibin Lin, China

Tzu-Kang Lin , Taiwan
Yu-Cheng Lin , Taiwan
Hexu Liu, USA
Jian Lin Liu , China
Xiaoli Liu , China
Xuemei Liu , Australia
Zaobao Liu , China
Zhuang-Zhuang Liu, China
Diego Lopez-Garcia , Chile
Cristiano Loss , Canada
Lyan-Ywan Lu , Taiwan
Jin Luo , USA
Yanbin Luo , China
Jianjun Ma , China
Junwei Ma , China
Tian-Shou Ma, China
Zhongguo John Ma , USA
Maria Macchiaroli, Italy
Domenico Magisano, Italy
Reza Mahinroosta, Australia
Yann Malecot , France
Prabhat Kumar Mandal , India
John Mander, USA
Iman Mansouri, Iran
André Dias Martins, Portugal
Domagoj Matesan , Croatia
Jose Matos, Portugal
Vasant Matsagar , India
Claudio Mazzotti , Italy
Ahmed Mebarki , France
Gang Mei , China
Kasim Mermerdas, Turkey
Giovanni Minafò , Italy
Masoomah Mirrashid , Iran
Abbas Mohajerani , Australia
Fadzli Mohamed Nazri , Malaysia
Fabrizio Mollaioli , Italy
Rosario Montuori , Italy
H. Naderpour , Iran
Hassan Nasir , Pakistan
Hossein Nassiraei , Iran
Satheeskumar Navaratnam , Australia
Ignacio J. Navarro , Spain
Ashish Kumar Nayak , India
Behzad Nematollahi , Australia

Chayut Ngamkhanong , Thailand
Trung Ngo, Australia
Tengfei Nian, China
Mehdi Nikoo , Canada
Youjun Ning , China
Olugbenga Timo Oladinrin , United Kingdom
Oladimeji Benedict Olalusi, South Africa
Timothy O. Olawumi , Hong Kong
Alejandro Orfila , Spain
Maurizio Orlando , Italy
Siti Aminah Osman, Malaysia
Walid Oueslati , Tunisia
SUVASH PAUL , Bangladesh
John-Paris Pantouvakis , Greece
Fabrizio Paolacci , Italy
Giuseppina Pappalardo , Italy
Fulvio Parisi , Italy
Dimitrios G. Pavlou , Norway
Daniele Pellegrini , Italy
Gatheeshgar Perampalam , United Kingdom
Daniele Perrone , Italy
Giuseppe Piccardo , Italy
Vagelis Plevris , Qatar
Andrea Pranno , Italy
Adolfo Preciado , Mexico
Chongchong Qi , China
Yu Qian, USA
Ying Qin , China
Giuseppe Quaranta , Italy
Krishanu ROY , New Zealand
Vlastimir Radonjanin, Serbia
Carlo Rainieri , Italy
Rahul V. Ralegaonkar, India
Raizal Saifulnaz Muhammad Rashid, Malaysia
Alessandro Rasulo , Italy
Chonghong Ren , China
Qing-Xin Ren, China
Dimitris Rizos , USA
Geoffrey W. Rodgers , New Zealand
Pier Paolo Rossi, Italy
Nicola Ruggieri , Italy
JUNLONG SHANG, Singapore




Nikhil Saboo, India
Anna Saetta, Italy
Juan Sagaseta , United Kingdom
Timo Saksala, Finland
Mostafa Salari, Canada
Ginevra Salerno , Italy
Evangelos J. Sapountzakis , Greece
Vassilis Sarhosis , United Kingdom
Navaratnarajah Sathiparan , Sri Lanka
Fabrizio Scozzese , Italy
Halil Sezen , USA
Payam Shafigh , Malaysia
M. Shahria Alam, Canada
Yi Shan, China
Hussein Sharaf, Iraq
Mostafa Sharifzadeh, Australia
Sanjay Kumar Shukla, Australia
Amir Si Larbi , France
Okan Sirin , Qatar
Piotr Smarzewski , Poland
Francesca Sollecito , Italy
Rui Song , China
Tian-Yi Song, Australia
Flavio Stochino , Italy
Mayank Sukhija , USA
Piti Sukontasukkul , Thailand
Jianping Sun, Singapore
Xiao Sun , China
T. Tafsirojjan , Australia
Fujiao Tang , China
Patrick W.C. Tang , Australia
Zhi Cheng Tang , China
Weerachart Tangchirapat , Thailand
Xiabin Tao, China
Piergiorgio Tataranni , Italy
Elisabete Teixeira , Portugal
Jorge Iván Tobón , Colombia
Jing-Zhong Tong, China
Francesco Trentadue , Italy
Antonello Troncone, Italy
Majbah Uddin , USA
Tariq Umar , United Kingdom
Muahmmad Usman, United Kingdom
Muhammad Usman , Pakistan
Mucteba Uysal , Turkey

Ilaria Venanzi , Italy
Castorina S. Vieira , Portugal
Valeria Vignali , Italy
Claudia Vitone , Italy
Liwei WEN , China
Chunfeng Wan , China
Hua-Ping Wan, China
Roman Wan-Wendner , Austria
Chaohui Wang , China
Hao Wang , USA
Shiming Wang , China
Wayne Yu Wang , United Kingdom
Wen-Da Wang, China
Xing Wang , China
Xiuling Wang , China
Zhenjun Wang , China
Xin-Jiang Wei , China
Tao Wen , China
Weiping Wen , China
Lei Weng , China
Chao Wu , United Kingdom
Jiangyu Wu, China
Wangjie Wu , China
Wenbing Wu , China
Zhixing Xiao, China
Gang Xu, China
Jian Xu , China
Panpan , China
Rongchao Xu , China
HE YONGLIANG, China
Michael Yam, Hong Kong
Hailu Yang , China
Xu-Xu Yang , China
Hui Yao , China
Xinyu Ye , China
Zhoujing Ye, China
Gürol Yildirim , Turkey
Dawei Yin , China
Doo-Yeol Yoo , Republic of Korea
Zhanping You , USA
Afshar A. Yousefi , Iran
Xinbao Yu , USA
Dongdong Yuan , China
Geun Y. Yun , Republic of Korea

Hyun-Do Yun , Republic of Korea
Cemal YİĞİT , Turkey
Paolo Zampieri, Italy
Giulio Zani , Italy
Mariano Angelo Zanini , Italy
Zhixiong Zeng , Hong Kong
Mustafa Zeybek, Turkey
Henglong Zhang , China
Jiupeng Zhang, China
Tingting Zhang , China
Zengping Zhang, China
Zetian Zhang , China
Zhigang Zhang , China
Zhipeng Zhao , Japan
Jun Zhao , China
Annan Zhou , Australia
Jia-wen Zhou , China
Hai-Tao Zhu , China
Peng Zhu , China
QuanJie Zhu , China
Wenjun Zhu , China
Marco Zucca, Italy
Haoran Zuo, Australia
Junqing Zuo , China
Robert Černý , Czech Republic
Süleyman İpek , Turkey

Contents

Research on the Influence of Natural Wind Pressure in Deep Mines on Ventilation Stability

Enmao Wang , Xiaoping Li , Qiming Huang, and Gang Wang 




Research Article (12 pages), Article ID 8789955, Volume 2022 (2022)

Prevention and Control of Spontaneous Combustion of Residual Coals in Acid-Soaked Goaf in Gas Drainage Condition

Cunli Qin, Qiming Huang , Shibin Wang, Jun Li, Shuang Ju, and Gang Wang 



Research Article (15 pages), Article ID 1668952, Volume 2022 (2022)

Laboratory Study on Changes in Gas Desorption Properties of Anthracite after Cyclic Loading

Tie Li , Dong Wang, Mei-Hua Liu, Liang Chen , and Hao Liu 

Research Article (11 pages), Article ID 7714303, Volume 2021 (2021)

Study on Gas Control Methods Optimization for Mining Safety

Liwen He , Yingcheng Dai, Sheng Xue , Chunshan Zheng, Baiqing Han, and Xin Guo 

Research Article (13 pages), Article ID 4594330, Volume 2021 (2021)

Moisture Content on Methane Desorption Characteristics in Coal and Its Effect on Outburst Prediction

Peng Li, Yaolin Cao, Xuelong Li , Fakai Wang , Zhongguang Sun , Qinke Huang, and Deyou Chen


Research Article (10 pages), Article ID 6797786, Volume 2021 (2021)

Deformation Mechanism of the Coal ahead of Fully Mechanized Caving Face under High-Intensity Mining Condition

Can Zhao, Liang Chen , Bing Wu, Jingui Zhang, Dahe Yan, Yang Li, and Zhiheng Cheng

Research Article (10 pages), Article ID 7713584, Volume 2021 (2021)

Influence of Long Boreholes Layout and Drilling Length on Gas Drainage Based on Multifield Coupling Model of Gas-Bearing Coal

Renjun Feng 


Research Article (16 pages), Article ID 1473769, Volume 2021 (2021)

LNMR Study on Microstructure Characteristics and Pore Size Distribution of High-Rank Coals with Different Bedding

Jiajia Liu , Jianmin Hu , Mengqi Shen , Ming Yang , and Yingxiang Fang 


Research Article (8 pages), Article ID 8542630, Volume 2021 (2021)

Goaf Gas Control Improvement by Optimizing the Adjacent Roadway Large-Diameter Boreholes

Wei Wang , Zongxiang Li, and Hongming Yu

Research Article (13 pages), Article ID 1933010, Volume 2021 (2021)

Reasonable Scope of Kilometer Drilling in Lower Layer of Extrathick Coal Seam: A Case Study of Tingnan Coal Mine, China

Delong Zou and Xiang Zhang 

Research Article (17 pages), Article ID 2044717, Volume 2021 (2021)

Research Article

Research on the Influence of Natural Wind Pressure in Deep Mines on Ventilation Stability

Enmao Wang ¹, Xiaoping Li ², Qiming Huang³ and Gang Wang ^{3,4}

¹College of Energy and Mining Engineering, Shandong University of Science and Technology, Qingdao 266590, China

²Jining No. 3 Coal Mine of Yanzhou Coal Mining Company Limited, Jining 272069, China

³College of Safety and Environmental Engineering, Shandong University of Science and Technology, Qingdao, 266590, China

⁴Shandong University of Science and Technology,

Mine Disaster Prevention and Control-Ministry of State Key Laboratory Breeding Base, Qingdao 266590, China

Correspondence should be addressed to Xiaoping Li; superhero777777@163.com

Received 4 October 2021; Accepted 28 December 2021; Published 27 February 2022

Academic Editor: Peng Liu

Copyright © 2022 Enmao Wang et al. This is an open access article distributed under the Creative Commons Attribution License, which permits unrestricted use, distribution, and reproduction in any medium, provided the original work is properly cited.

Deep mines are greatly affected by changes in natural wind pressure because of their large buried depths and long ventilation paths. Changes in natural wind pressure do affect the air flow of the underground ventilation system, and even change the direction of individual branches. If the dynamic changes of natural wind pressure are not monitored constantly, it is very likely to cause disasters such as gas overrun and may even lead to heavy casualties. In this paper, the changes of natural wind pressure and the air volume entering the mine are measured on-site in the 630 mining area in the south wing of Tangkou Coal Mine. Then, compare the change law of natural wind pressure with the change law of ventilation air volume. Finally, through numerical simulation by FLUENT, the change of internal flow in the gob where there is a loosely closed condition is simulated. Through research, the annual natural wind pressure change and the change of air intake in the 630 mining area of the south wing of Tangkou Coal Mine were obtained; The influence of changes in external conditions on the ventilation air volume of deep mines is obtained; The importance of the influence of natural wind pressure on the stability of the deep mine ventilation system is verified.

1. Introduction

Mine ventilation is a fundamental measure to change coal mine safety. It is used to remove and dilute the dust and gas in the mine to ensure the normal breathing of underground operators. This is very important for improving the economic benefits of the mining area and promoting the stable and healthy development of the mining area.

Numerous researchers have studied natural wind pressure theoretically and numerically. The real research on natural wind pressure originated around 1940 [1–3]. At that time, American researchers began to explore natural wind pressure indoors. By systematically applying the thermal and dynamic principles, they discovered the law of changes in indoor natural wind pressure. However, due to the rudimentary technical equipment and the weak research foundation, the research at that time was not perfect. Around

1970, in order to satisfy the needs of mine production, researchers began to study the influence of natural wind pressure on mines and explain the mechanism of natural wind pressure causing pressure changes in the ventilation system [4–7]. This laid the foundation for airflow research. Later, natural wind pressure calculation algorithm [8–10] was applied to explain the influencing factors and degree of natural wind pressure, discuss the main action section of underground natural wind pressure, and propose methods and ventilation system management concepts on how to use or limit the impact of natural wind pressure on the main action section. With the development of science and technology, the calculation method of natural wind pressure has been constantly improved, and the calculation equation of natural wind pressure has been derived using methods such as thermodynamics, CFD, coupled thermal pressure and thermal air pressure [11–16]. Nowadays, with the extensive

application and development of mathematical modeling and computer numerical simulation [16–19], the study of natural wind pressure has entered the stage of research and design. Through the analysis and integration of a large amount of on-site measurement data, the natural wind pressure change law and network solution algorithm algorithm are combined into the computer program to achieve the automatic computation of natural wind pressure in the computer.

The mine ventilation system [20–23] generally consists of a ventilation shaft network, ventilation power equipment, air flow monitoring and control facilities, etc. The system stability of mine ventilation is based on the concept of system stability in cybernetics, but it is slightly different. The system stability in cybernetics mainly refers to the ability of the system to return to the original equilibrium state after being deviated from the equilibrium state by the instantaneous external force, while the system stability of mine ventilation refers to the change of various parameters in the system with the change of the continuous external force, ventilation structure or ventilation parameters [24–26]. Among numerous research results, the stability theory of a former Soviet scholar Lyapounov [27] is the most prominent. In his theory, the system stability of ventilation can be measured by mathematical statistics. At present, researchers use the standard deviation of mathematical statistics to analyze the change of air volume in mine roadways. Combined with the ventilation network solution model, they can determine the degree of stability of the mine ventilation system and the location in the roadway that affects the stability of the mine ventilation system [28]. Moreover, they use the ventilation system network solver tool [29] to analyze the network airflow stability of the mine ventilation system by establishing the network airflow stability coefficient matrix and analyzing the overall stability index of the network airflow, the network airflow change range index and the network change influence range index. In addition, they use the method of numerical computation to derive general formulas for stability analysis of any ventilation network through inductive analysis.

Currently, most studies on mine natural wind pressure and ventilation system stability stay in shallow mines. For deep mines, the influence of natural wind pressure on the stability of the ventilation system is more significant and complex. In order to study the influence of natural wind pressure on the ventilation system in deep mines, the deep mine, Tangkou Coal Mine in China, is taken as the research background in this paper.

2. Overview of Tangkou Coal Mine

As shown in Figure 1, Tangkou Coal Mine is located about 10 km west of Jining City, Shandong Province, China. The mine is separated from Yunhe Mine by the connecting line of the T₅₋₉ and A₂₄₋₁₆ boreholes in the north, separated from Daizhuang Coal Mine by Jining Fault in the east, connected to Jining security coal pillar in the southeast, separated from Xinhe Mine by Jiexiang Fault and its third branch. The area of the mine field is 72.2189 km².

In this mine, vertical shaft development and zoned extraction ventilation are adopted. Air enters from the north service shaft, north main shaft and south service shaft, and returns from the north return air shaft and south return air shaft. The existing production level is –990 m, the designed production capacity is 3 million t/a, and the approved production capacity in 2015 is 4.8 million t/a. The main coal mining method is the retreating longwall method where the roof is completely collapsed or filled with gangue. In general, the blasting technology is adopted for the rock roadway, and the comprehensive excavation technology is applied for the coal roadway.

The ventilation method of the mine is zoned extraction ventilation. The ventilator room in the north of the mine is equipped with two FBCDZ-10-N₃₂ counter-rotating axial flow ventilators with a motor power of 2 × 560 kW. The southern ventilator room is equipped with two GAF33.5-18-1FB hydraulic movable blade adjustable axial flow ventilators with a motor power of 1,800 kW. The required air volume of the mine is 21,466 m³/min, the actual total air intake volume of the mine is 22,929 m³/min, and the total return air volume is 24,061 m³/min. The effective air volume of the mine is 21,470 m³/min, the effective air volume rate is 93.64%, and the equivalent orifice of the mine is 10.41 m². At present, there is sufficient air volume at each mining operation site, no diffusion ventilation, no old waste ventilation, no windless and breeze operation, no unreasonable series ventilation, and no production exceeding ventilation capacity. The mine ventilation diagram is shown in Figure 2.

3. Measurement and Analysis of Natural Wind Pressure

3.1. Calculation Equation of Natural Wind Pressure in Mine.

As shown in Figure 3, as the atmospheric pressure and temperature change with the seasons, the ground air enters the mine and exchanges heat with various underground heat sources, resulting in different air temperatures in various sections of the underground. At the same time, the increase in atmospheric pressure with the depth and the self-compression of airflow during the flow process will cause the density of the air to change, resulting in an energy difference by the imbalance of the gravity of the air column in the air inlet section and the air return section, which promotes the air to flow along the roadway.

The density of air is a variable that depends on the change process of the gas state, which is related to the pressure, temperature and humidity. The main change processes include isovolumetric process, isobaric process, isothermal process, and polytropic process. The following is a comparative analysis of each change process of the gas.

3.1.1. Isobaric Process. When P is a constant, $1/\rho T = R/P$ is a constant. In the isobaric process, P does not change, and v is proportional to T . Because $dP=0$, the change in pressure energy is:



FIGURE 1: Location of tangkou coal mine.

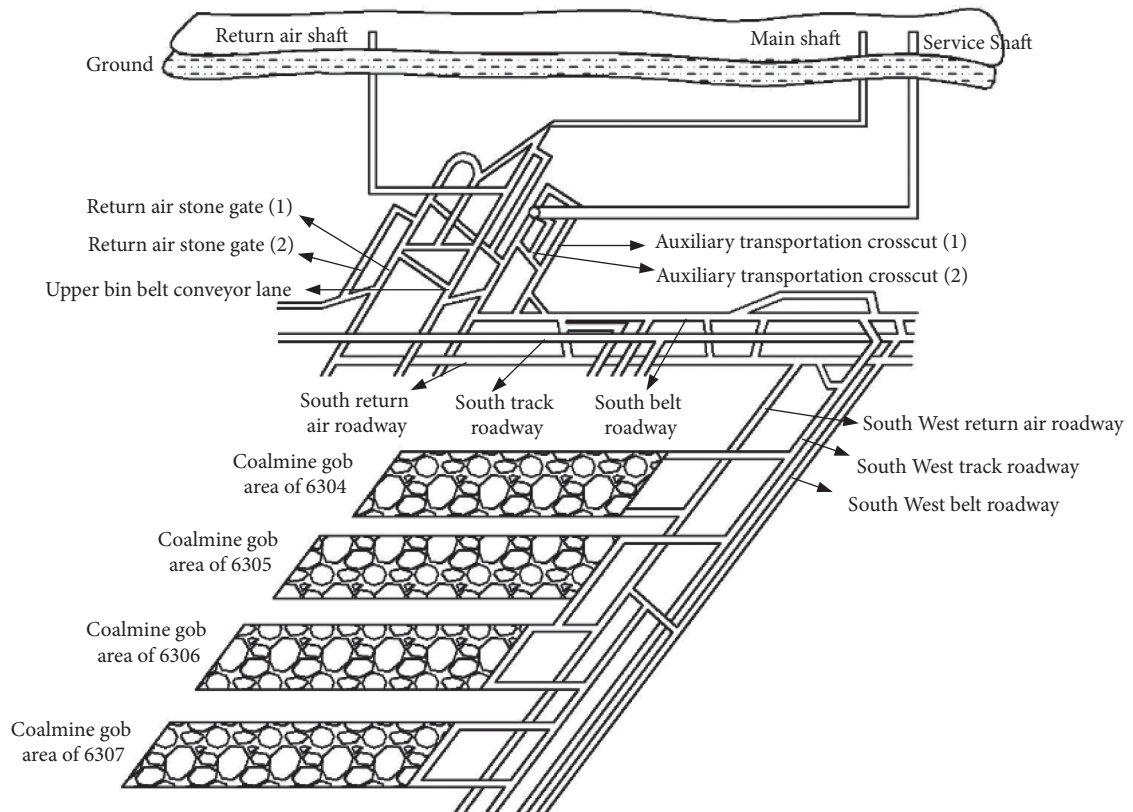


FIGURE 2: Three-dimensional schematic diagram of ventilation system in south wing shaft area.

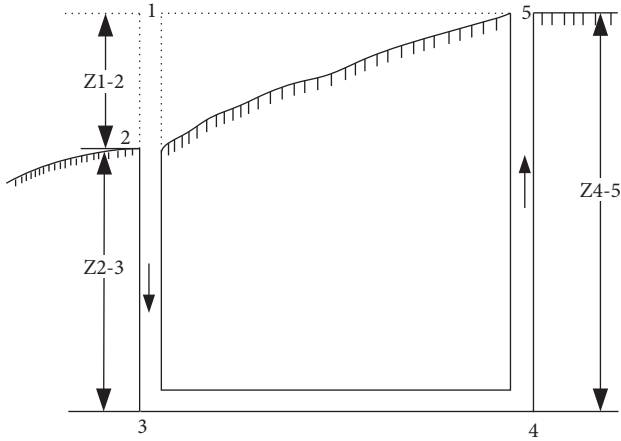


FIGURE 3: Schematic diagram of natural ventilation in mine.

$$\int_2^1 \frac{dP}{\rho} = 0. \quad (1)$$

3.1.2. Isovolumetric Process. In the isovolumetric process, the gas volume V does not change, and then the air density ρ does not change. Hence, the change in pressure energy is:

$$\int_2^1 \frac{dP}{\rho} = \int_2^1 \frac{P_1^{1/n}}{\rho_1} \frac{dP}{P^{1/n}} = \frac{n}{n-1} \cdot \frac{P_1}{\rho_1} \left[\left(\frac{P_1}{P_2} \right)^{n-1/n} - 1 \right] = \frac{n}{n-1} \left(\frac{P_1}{\rho_1} - \frac{P_2}{\rho_2} \right), \quad (4)$$

where the polytropic index n can be calculated from the measured data P_1 , P_2 , T_1 , T_2 of the mine, and the specific calculation is shown in equation (5).

$$n = \frac{\ln(P_2/P_1)}{\ln(P_2/P_1) - \ln(T_1/T_2)} = \frac{\ln(P_2/P_1)}{\ln(\rho_2/\rho_1)}, \quad (5)$$

where T_1 , T_2 are the absolute temperature of the gas at the beginning and end, respectively, K ; P_1 , P_2 are the pressure of the gas at the beginning and end, respectively, Pa .

3.2. Measurement of Natural Wind Pressure in Tangkou Coal Mine. The indirect measurement method is adopted to measure the natural wind pressure in the south wing shaft area of Tangkou Coal Mine. The indirect measurement method is that a precision barometer records the pressure, temperature, humidity and time every 5 minutes at the wellhead of the air inlet well, and another precision barometer enters the well to perform pressure, temperature, humidity and time at the designated measurement location. After the measurement, the natural wind pressure is calculated by the formula. In order to obtain a more comprehensive change in the natural wind pressure throughout the year and reduce errors caused by meteorological changes, according to the actual situation of the south wing shaft area of Tangkou Coal Mine, the most representative day of each season is selected for measurement. Moreover,

$$\int_2^1 \frac{dP}{\rho} = \frac{(P_1 - P_2)}{\rho}. \quad (2)$$

3.1.3. Isothermal Process. In the isothermal process, T is a constant, and then $P/\rho = RT$ is a constant. P is inversely proportional to ρ . Hence, the change in pressure energy is:

$$\int_2^1 \frac{dP}{\rho} = \int_2^1 \frac{P_1}{\rho_1} \frac{dP}{P} = \frac{P_1}{\rho_1} \ln \frac{P_1}{P_2}. \quad (3)$$

3.1.4. Polytropic Process. For the polytropic process ($P/\rho^n = \text{constant}$), the variation law of P with V is shown in Figure 4, where n is the polytropic index, which can be any real number. The value of n is different under different state change laws. When $n=0$, it is an isostatic process; when $n=1$, it is an isothermal process; when $n=k$, it is an adiabatic process (After the air enters the well, there is no heat exchange between the air and various heat sources in the well); when $n=\infty$, it is an isovolumetric process.

Because of the fact $1/\rho = (P_1/P)^{1/n} 1/\rho_1$, the change in pressure energy is:

the data measured on the selected four days are taken as the main research object. Other data are only used as references. The measured data of the four seasons of spring, summer, autumn and winter are shown in Table 1.

The spring in Jining is the period of atmospheric circulation adjustment, in which it is prone to drought and windiness, and warms up quickly. During the three months of spring, March, April and May, the temperature in Jining gradually rises. The three months of summer, June, July and August are the hottest period in Jining. The temperature changes during the three months of autumn, September, October, and November, are the fastest compared to those in spring, summer and winter. The surface temperature of the three months of winter, December, January and February, is the lowest in the whole year. The change of surface temperature will inevitably bring about the change of underground temperature, which in turn will lead to the change of natural wind pressure in the mine.

In order to obtain a more accurate evolution law of the natural wind pressure in the south wing shaft area of Tangkou Coal Mine in spring, according to the actual production situation, the natural wind pressure is measured every 3 hours at 3:00, 6:00, 9:00, 12:00, 15:00, 18:00, 21:00, 24:00, 8 times a day. The measurement results of the natural wind pressure of Tangkou Coal Mine are shown in Figure 5.

Figure 5 clearly shows that the changes in natural wind pressure on one representative day in each of the four

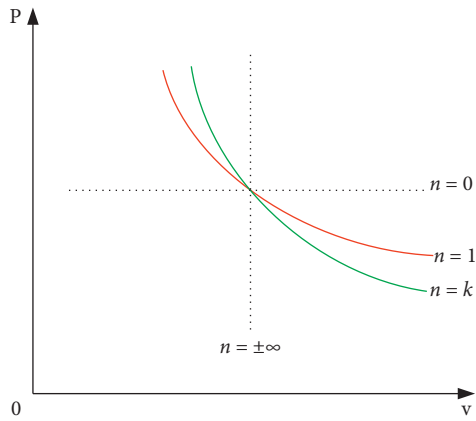


FIGURE 4: (P-V) diagram of isothermal process.

seasons. Firstly, the natural wind pressure decreases gradually from 3:00 to 15:00, and increases gradually from 15:00 to 3:00 the next day. Secondly, the time of the day when the natural wind pressure is the highest is 3:00, and the time of the day when the natural wind pressure is the lowest is 15:00. Finally, in spring, the highest natural wind pressure is 411 MPa, and the lowest natural wind pressure is 375 MPa; in summer, the highest natural wind pressure is -10.6 MPa, and the lowest natural wind pressure is -59.3 MPa; in autumn, the highest natural wind pressure is 195.2 MPa, and the lowest natural wind pressure is 166.7 MPa; in winter, the highest natural wind pressure is 495.5 MPa, and the lowest natural wind pressure is 457.2 MPa.

In order to more intuitively show the changing trend of the natural wind pressure throughout the year, the change trend of the natural wind pressure of the year in the south wing shaft area of Tangkou Coal Mine is obtained with the most representative day of each season of the year taken as the seasonal natural wind pressure, as shown in Figure 6.

Figure 6 shows that the natural wind pressure in the south wing shaft area of Tangkou Coal Mine fluctuates sinusoidally throughout the year with large fluctuations. The natural wind pressure in the south wing shaft area of Tangkou Coal Mine reaches a maximum of about 500 Pa in winter, and a minimum of about -75 Pa in summer. And thus the range of the natural wind pressure fluctuation is 575 Pa. The natural wind pressure is positive in spring, autumn and winter, i.e., the direction of natural wind pressure is consistent with the blowing direction of the ventilator, which is conducive to mine ventilation. It is negative in summer, i.e., the direction of natural wind pressure is opposite to the blowing direction of the ventilator, which hinders mine ventilation.

4. Analysis of Influence of Natural Wind Pressure on Air Supply Volume

4.1. Evolution of Natural Wind Pressure and Ventilator Air Volume. In the normal working state of the mine, the ventilation of the entire mine relies on the mine ventilator, and the function of the mine ventilator depends on the characteristic curve of the ventilator. When the wind

pressure and ventilator air volume at the new operating point are greater than those at the previous operating point, it indicates that the change of the natural wind pressure is beneficial to the air supply of the mine ventilator. When the wind pressure and ventilator air volume at the new operating point is less, indicating that the change of the natural wind pressure hinders the air supply of the mine ventilator.

Based on the influence mechanism of natural wind pressure on mine ventilation, the influence of natural wind pressure on the stability of ventilator air volume in the south wing shaft area of Tangkou Coal Mine is studied. The method of measuring the natural wind pressure on the most representative day of each season is also adopted. The natural wind pressure is measured every 3 hours at 3:00, 6:00, 9:00, 12:00, 15:00, 18:00, 21:00, 24:00, 8 times a day. The measurement data of the air volume of the main ventilator in the south wing shaft area of Tangkou Coal Mine are shown in Figure 7.

Figure 7 indicates that the fluctuation of the natural wind pressure have a certain impact on the air supply volume of the ventilator. In general, the change of the air volume of the ventilator is consistent with the change of the natural wind pressure. When the natural wind pressure is small, the air supply volume of the ventilator is small. When the natural wind pressure is higher, the air supply volume of the ventilator is greater. With the horizontal line where the median value is located taken as the central axis, it can be seen that from 0:00 to 24:00 on one representative day in each of the four seasons, both the natural wind pressure and the air volume of the ventilator first increase, then decrease and then increase. Although the change trends of the natural wind pressure and the supply air volume of the ventilator are basically the same, the inflection points of the changes are slightly different, with a difference of 0~4 h. The change of the air supply volume of the ventilator will affect the stability of the entire ventilation system, and bring hidden safety hazards to underground production.

4.2. Correlation Analysis of Natural Wind Pressure and Ventilator Air Volume. In order to further analyze the influence of natural wind pressure on the air volume of the ventilator, the correlation between the natural wind pressure and the air volume of the ventilator in Tangkou Coal Mine is analyzed by using the correlation analysis method in the field of mathematics. In this correlation analysis method, Pearson's correlation reflects the degree of linear relationship between two variables and its coefficient is between -1 and 1. The Pearson correlation coefficient between two variables is defined as the quotient of the covariance and standard deviation between the two variables, as shown in equation (6):

$$\rho_{X,Y} = \frac{\text{cov}(X,Y)}{\sigma_X \sigma_Y} = \frac{E[(X - \mu_X)(Y - \mu_Y)]}{\sigma_X \sigma_Y}, \quad (6)$$

where ρ is the overall correlation coefficient.

By estimating the covariance and standard deviation of the data sample, the Pearson correlation coefficient can be obtained, as shown in equation (7):

TABLE 1: Measured data of four seasons in shaft area.

Season	Measuring position	Absolute pressure HPa	Dry temperature °C	Absolute partial pressure of saturated water vapor HPa	Relative humidity %	Density kg/ m ³
Spring	Service shaft mouth	1022.81	17.2	20.12	93	1.219444
	Service shaft bottom	1139.46	22.6	27.42	89	1.332117
	Main shaft mouth	1016.18	23.4	28.78	87	1.183332
	Main shaft bottom	1124.2	28.2	38.25	92	1.284983
Summer	Service shaft mouth	1003.29	33	52.62	62.7	1.128109
	Service shaft bottom	1110.13	35.5	57.83	72.3	1.235861
	Main shaft mouth	991	26.7	35.04	94.1	1.137544
	Main shaft bottom	1095.26	30.7	44.18	99.9	1.237327
Autumn	Service shaft mouth	1012.78	24.8	31.3	72.7	1.174801
	Service shaft bottom	1120.69	27.4	36.5	68.2	1.288849
	Main shaft mouth	1002.75	24.7	31.12	91.1	1.160983
	Main shaft bottom	1107.25	28.9	39.82	96.1	1.261101
Winter	Service shaft mouth	1024.73	10.2	12.45	92	1.255323
	Service shaft bottom	1141.15	15.4	17.48	87	1.371615
	Main shaft mouth	1018.83	15.8	17.84	78	1.222741
	Main shaft bottom	1128.4	26	33.61	87	1.301952

$$r = \frac{\sum_{i=1}^n (X_i - \bar{X})(Y_i - \bar{Y})}{\sqrt{\sum_{i=1}^n (X_i - \bar{X})^2} \sqrt{\sum_{i=1}^n (Y_i - \bar{Y})^2}} \quad (7)$$

As shown in Table 2, according to the calculated r value, the correlation between two variables is divided into 8 levels from highly negative correlation to highly positive correlation.

Through the SPSS software, the measured data of the natural wind pressure and ventilator air volume of Tangkou Coal Mine throughout the year are substituted into the Pearson model, and the correlation coefficient between the natural wind pressure and the air volume of the ventilator is obtained, as shown in Table 3.

As shown in Table 3, the Pearson's correlation between the natural wind pressure and the air volume of the ventilator is a moderately positive correlation in spring, a highly positive correlation in summer, a weak positive correlation in autumn, and a weak negative correlation in winter. Through the analysis of the correlation results obtained, in the temperate monsoon climate of Tangkou Coal Mine, for deep mines, the natural wind pressure in spring and summer has a very significant influence on the air volume of the ventilator, while the natural wind

pressure in autumn and winter has a lower degree of influence on the air volume of the ventilator.

5. Verification of Shaft Bottom Airflow Characteristics through Numerical Simulation

5.1. Model Establishment and Mesh Division. In order to verify that the influence of natural wind pressure on the stability of the ventilation system poses a hazard threat to underground production, with the ventilation air volume of each season taken as the parameter and the 630 mining area in the south wing shaft area of Tangkou Coal Mine taken as the background, the model is established through the Solidworks software, as shown in Figure 8. In this model, each gob has an air intake roadway and an air return roadway. In addition, the dimensions of this model are summarized in Table 4.

The entire gob is divided into Submap quadrilateral grids through the ICEM in the software FLUENT [30–33]. The result of mesh division is shown in Figure 9.

After the mesh division, the boundary conditions of the model are set as follows. The surfaces between the gobs are

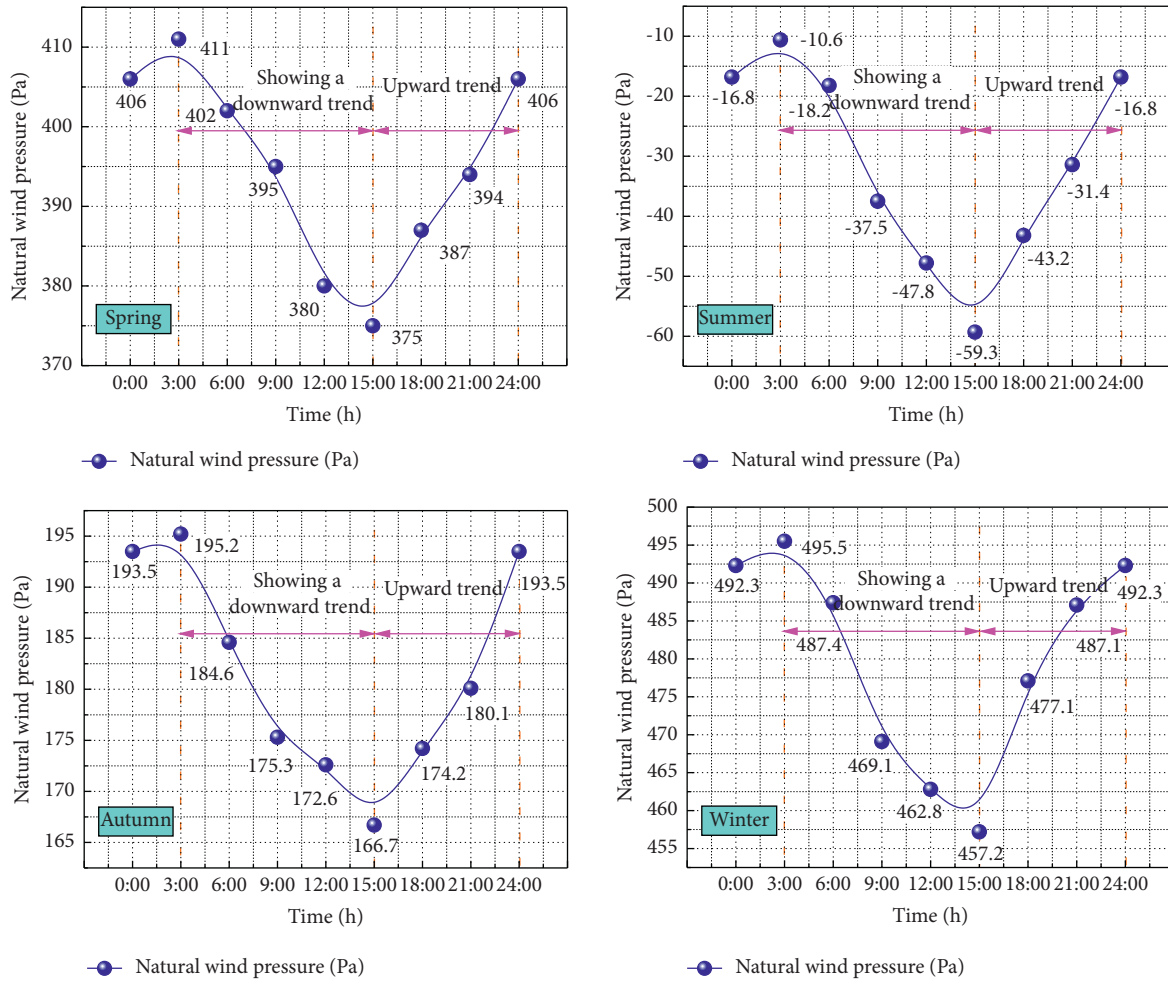


FIGURE 5: Changes in natural wind pressure on one representative day in each of the four seasons.

set to walls without ventilation. The contact surface between the working face and the gob is set to interior, the contact surface between the air intake roadway and the working face is set to interior, and the contact surface between the air return roadway and the working face is set to interior. The air inlet is set as pressure-inlet, and the air outlet is set as pressure-outlet. The air inlet pressure values of the 6304, 6305, 6306 and 6307 gobs are given, the internal pressure value of each gob is given, and the return air outlet is set as a free outlet. The boundary conditions of each area in the gob are set to Fluid. The boundary conditions of the coal pillars are set to wall, and set to porous media for FLUENT solution. The air inlet is set to air.

5.2. Simulation Results and Analysis of U-Shaped Ventilation.

Figure 10 clearly shows the pressure distribution in the gob at three different inlet absolute pressures of 112,400 Pa, 112,000 Pa and 111,800 Pa. It indicates that when the absolute pressure of the air inlet is the largest, the influence on the gob is the greatest. As the absolute pressure of the air inlet decreases, the degree of influence on the gob gradually decreases. When the absolute pressure of the air inlet is 111,800 Pa, it basically only has a certain influence on the part of the gob near the air inlet, and has no influence on the inside of the gob.

Figure 11 shows the simulation results of transverse slices at different air inlet pressures. It is indicated that whether the absolute pressure of the air inlet is 112,400 Pa, 112,000 Pa or 111,800 Pa, the bottom part of the gob is affected more than the top part for the affected area. As the height increases, the affected area gradually decreases. When the absolute pressure of the air inlet is 112,400 Pa, the pressure at the top part of the gob near the working face is close to 112,400 Pa. When the absolute pressure of the air inlet is 111,800 Pa, the pressure at the top part of the gob near the working face becomes 111,570 Pa, and the degree of change is small relative to the absolute pressure of 112,400 Pa.

Figure 12 shows the simulation results of longitudinal slices at different air inlet pressures. Obviously, the internal pressure in each gob is affected more near the air inlet, and less near the air outlet. When the absolute pressure of the air inlet is 112,400 Pa, the interiors of the 6304 and 6307 gobs are basically affected. Since the 6305 and 6306 gobs are relatively long along the stoping direction, their parts far away from the working surface are basically unaffected.

Figures 11 and 12 indicate that the 6304, 6305, 6306 and 6307 gobs all have large areas of air leakage. The readings of the U-shaped tubes measured in the airtight area of the gob

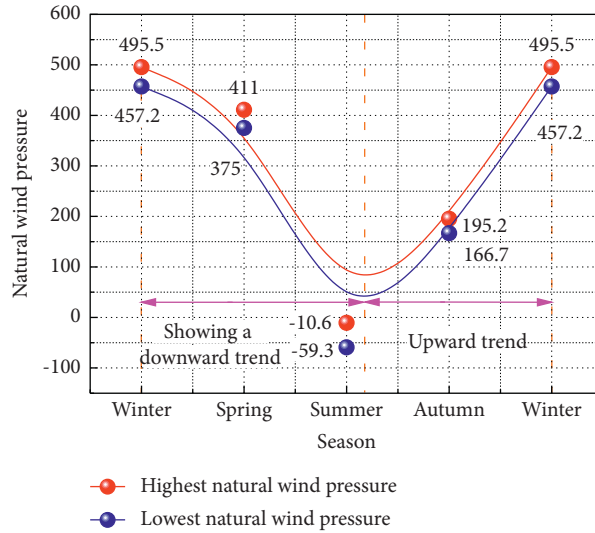


FIGURE 6: Change of natural wind pressure in south wing shaft area of tangkou coal mine.

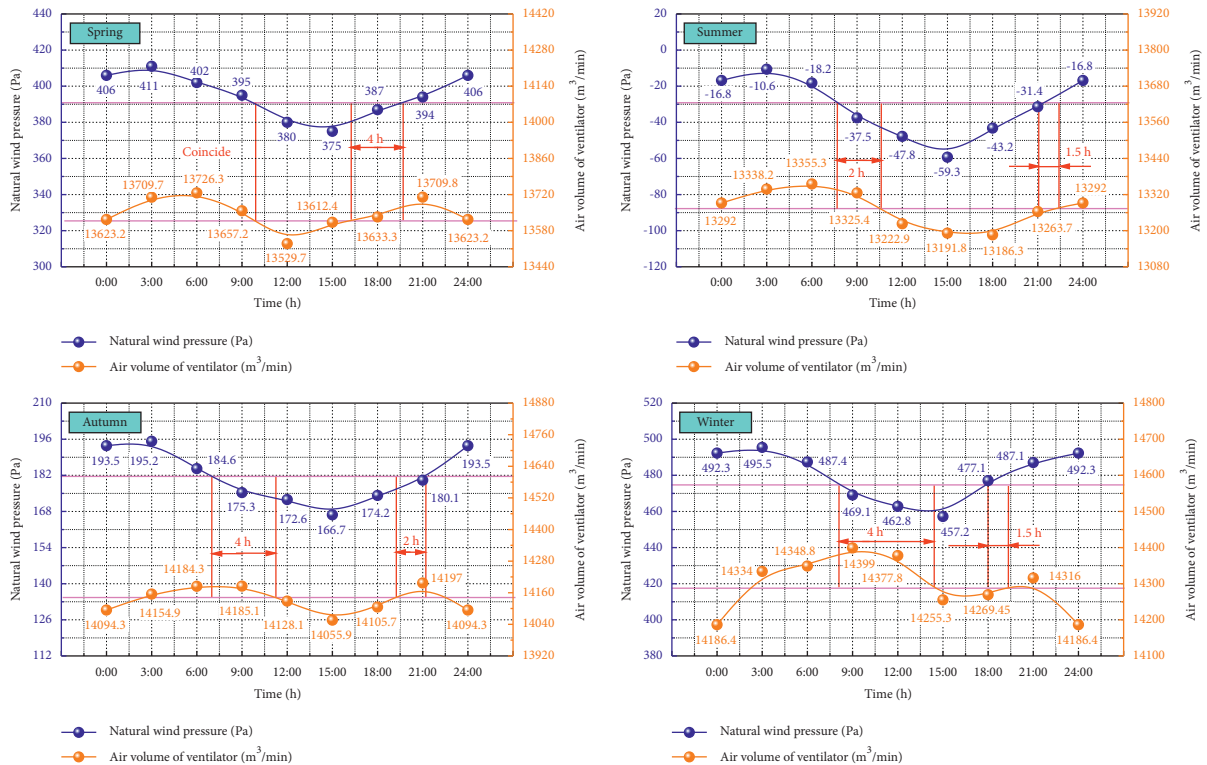


FIGURE 7: Changes of natural wind pressure and ventilator air volume on one representative day in each of four seasons.

are basically 0, and thus the pressure inside the airtight space is the same as the pressure outside the airtight space, which also indicates large areas of air leakage in the 630 gob, as shown in Figure 13. The change of the working face pressure outside the gob has a certain impact on the gob, and it can be inferred that the instability of the ventilation system would have a certain impact on the gob. When the pressure outside the gob is greater than the pressure inside the gob, air leakage may occur and even cause fire in the gob. When the pressure outside the gob is lower than the pressure inside the gob, the

gas inside the gob will rush into the working face, which may cause harmful gas in the working face to exceed the limit, endangering the lives of underground personnel.

The air intake roadway in the 6304 gob is obviously affected by the change of natural wind pressure. In order to explore the impact of this change on the gob, the FLUENT simulation software is used to simulate the 6304 gob. The simulation results are shown in Figures 14 and 15.

Figures 14 and 15 indicate that when the airflow enters the working face from the air intake roadway, part of the

TABLE 2: Correlation evaluation criteria based on r value.

r value	-1~-0.8	-0.8~-0.5	-0.5~-0.3	-0.3~0	0~0.3	0.3~0.5	0.5~0.8	0.8~1
Correlation	Highly negative correlation	Moderately negative correlation	Low negative correlation	Weak negative correlation	Weak positive correlation	Low positive correlation	Moderately positive correlation	Highly positive correlation

TABLE 3: Pearson correlation coefficient between natural wind pressure and ventilator air volume.

Season	Pearson correlation coefficient	Significance	Number of cases
Spring	0.666	0.071	8
Summer	0.823	0.012	8
Autumn	0.283	0.497	8
Winter	-0.225	0.591	8

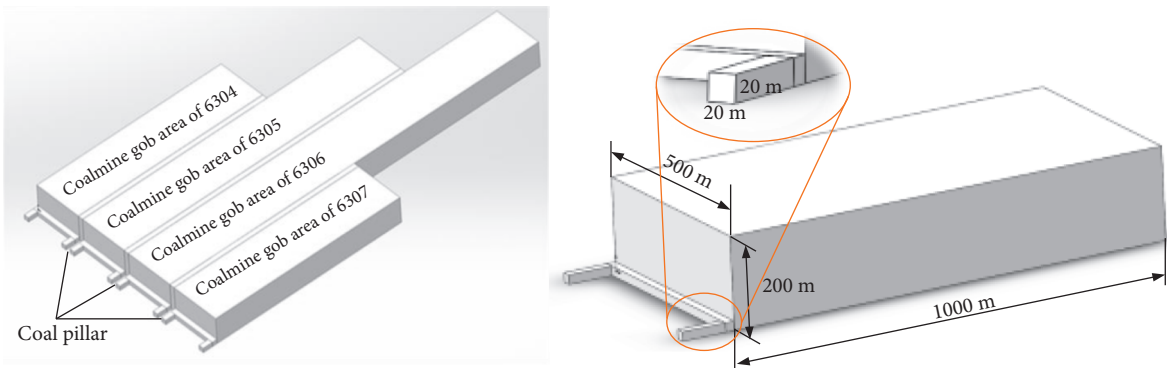


FIGURE 8: Deep mine model established through solidworks.

TABLE 4: Summary of dimensions of each part of model.

Gob	6304	6305	6306	6307
Length of working surface/m	100	100	100	100
Length in stoping direction/m	400	500	800	400
Height/m	60	60	60	60

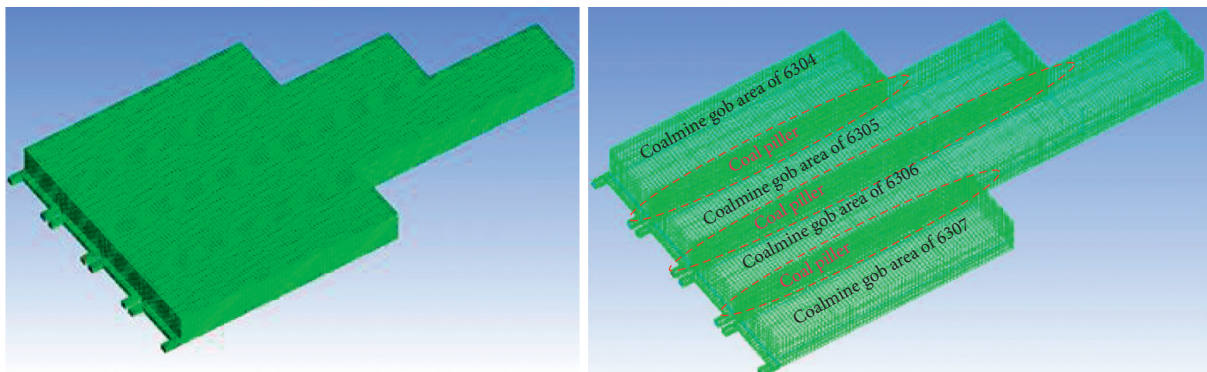


FIGURE 9: Mesh division of model.

airflow enters the gob. The airflow in the gob close to the return air roadway is forced into the return air roadway under the action of the pressure difference, and no airflow enters the working face.

According to the results of the numerical simulation using the ventilation data of each season in Tangkou Coal Mine, the sealing effect of the gob in Tangkou Coal Mine is poor. Under different ventilation conditions, the states of the

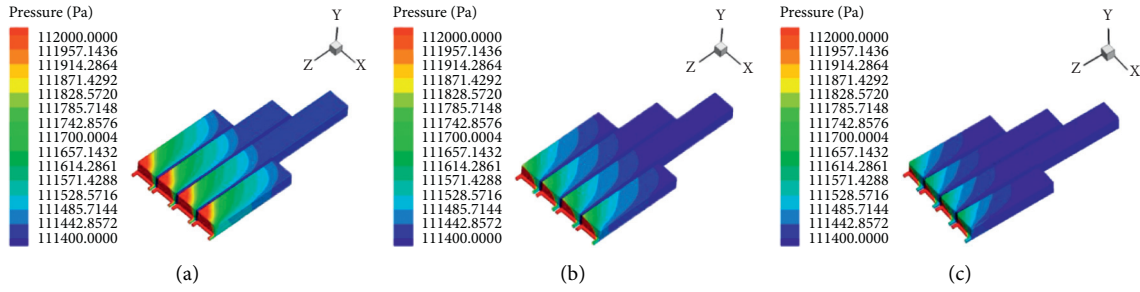


FIGURE 10: Simulation results at different air inlet pressures. (a) At air inlet pressure of 112,400 Pa. (b) At air inlet pressure of 112,000 Pa. (c) At air inlet pressure of 111,800 Pa.

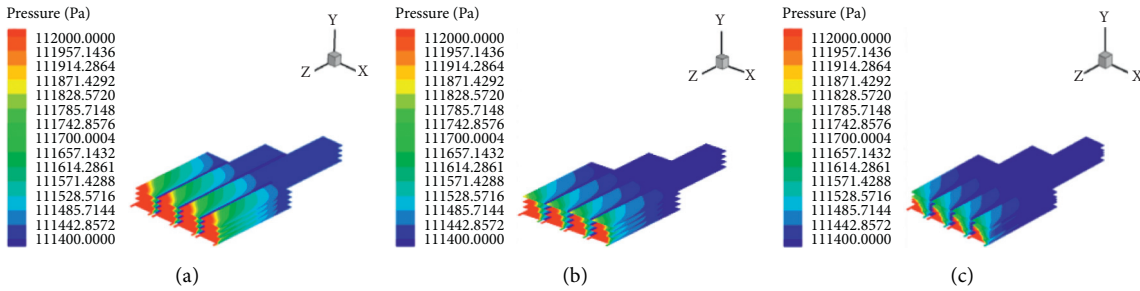


FIGURE 11: Simulation results of transverse slices at different air inlet pressures. (a) At air inlet pressure of 112400 Pa. (b) At air inlet pressure of 112000 Pa. (c) At air inlet pressure of 111800 Pa.

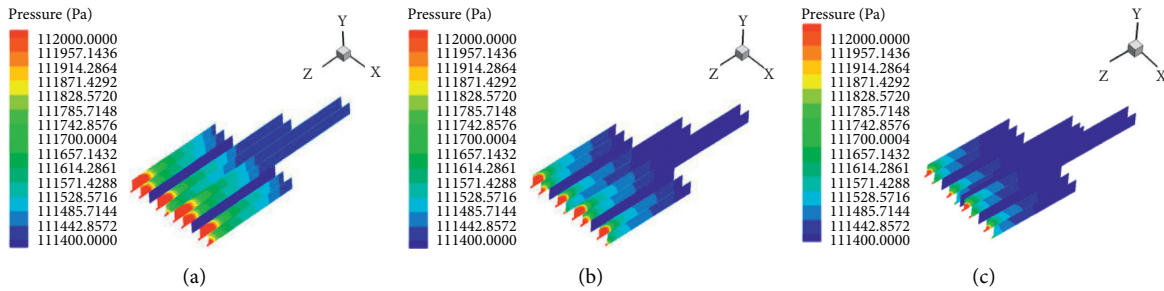


FIGURE 12: Simulation results of longitudinal slices at different air inlet pressures. (a) At air inlet pressure of 112,400 Pa. (b) At air inlet pressure of 112,000 Pa. (c) At air inlet pressure of 111,800 Pa.

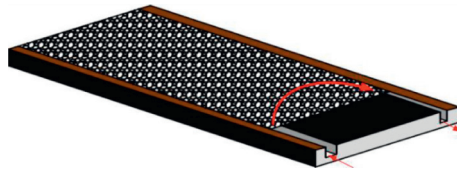


FIGURE 13: Flow field pattern inside gob.

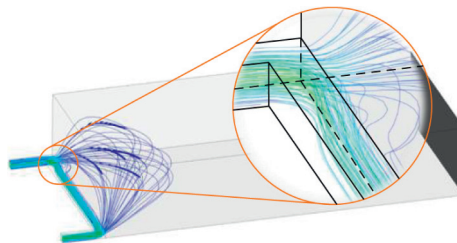


FIGURE 14: Airflow in gob 6304.

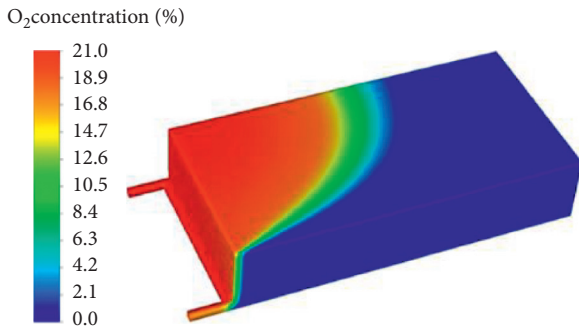


FIGURE 15: Oxygen concentration in gob 6304.

“three zones” inside the gob are different. This indicates that for deep shaft coal mines, changes in natural wind pressure have a close influence on the stability of the ventilation system.

6. Conclusions

In this paper, with the south wing shaft area of Tangkou Coal Mine taken as the research background, the influence of natural wind pressure on the stability of the ventilation system is studied through field measurement, and the importance of the stability of the ventilation system to the deep shaft coal mine is verified through numerical simulation. Through analysis and discussion, the following conclusions are drawn:

- (1) In different seasons, the change trends of natural wind pressure and ventilator air volume are basically the same, and fluctuations in natural wind pressure will cause synchronous changes in ventilator air volume. The changes of natural wind pressure and ventilator air volume in a one-year cycle present a sinusoidal law.
- (2) Based on the sensitivity analysis of natural wind pressure, the air intake roadway in the gob is significantly affected by natural wind pressure, while the return air roadway is less affected by natural wind pressure.
- (3) In the temperate monsoon climate zone, the natural wind pressure in spring and summer has a more significant influence on the air volume of the ventilator than that in autumn and winter, and the natural wind pressure has a linear relationship with the air volume of the ventilator throughout the year..

Data Availability

The Underlying data can be found in the project “Stability of Deep Shaft Ventilation System and Research on Fire Prevention and Control Technology for Large Area Gobs.”

Conflicts of Interest

The authors declare that they have no conflicts of interest.

References

- [1] L. Gong, H. He, and D. Zou, “Treatment of natural ventilation pressure in mine ventilation network flow calculation,” *Mining Safety & Environmental Protection*, vol. 42, no. 6, pp. 113–116, 2015.
- [2] J. Yuan and L. R. Glicksman, “Transitions between the multiple steady states in a natural ventilation system with combined buoyancy and wind driven flows,” *Building and Environment*, vol. 42, no. 10, pp. 3500–3516, 2006.
- [3] B. Lishman and A. W. Woods, “On transitions in natural ventilation flow driven by changes in the wind,” *Building and Environment*, vol. 44, no. 4, pp. 666–673, Article ID 05.012, 2009.
- [4] J. Yuan and L. R. Glicksman, “Multiple steady states in combined buoyancy and wind driven natural ventilation: the conditions for multiple solutions and the critical point for initial conditions,” *Building and Environment*, vol. 43, pp. 62–69, Article ID 11.035, 2006.
- [5] H. Ma, Y. Zhang, and X. Zhou, “Automatic calculation and application of ventilation network with natural wind pressure,” *Metal Mine*, vol. 1, no. 475, pp. 157–161, 2016.
- [6] C. Liu, M. Zhong, C. Shi, P. Zhang, and X. Yian, “Temperature profile of fire-induced smoke in node area of a full-scale mine shaft tunnel under natural ventilation,” *Applied Thermal Engineering*, vol. 110, pp. 382–389, Article ID 08.147, 2016.
- [7] P. Liu, J. Fan, D. Jiang, and J. Li, “Evaluation of underground coal gas drainage performance: mine site measurements and parametric sensitivity analysis,” *Process Safety and Environmental Protection*, vol. 148, pp. 711–723, Article ID 01.054, 2021.
- [8] T. Larsen and P. Heiselberg, “Single-sided natural ventilation driven by wind pressure and temperature difference,” *Energy and Buildings*, vol. 40, no. 6, pp. 1031–1040, Article ID 07.012, 2006.
- [9] A. Fontanini, U. Vaidya, and B. Ganapathysubramanian, “A stochastic approach to modeling the dynamics of natural ventilation systems,” *Energy and Buildings*, vol. 63, pp. 87–97, Article ID 03.053, 2013.
- [10] Y. Li and A. Delsante, “Natural ventilation induced by combined wind and thermal forces,” *Building and Environment*, vol. 36, no. 1, pp. 50–71, Article ID S0360-1323(99)00070-0, 2001.
- [11] M. Hu and W. Xu, “Study on influence of mine natural ventilation pressure to stability of mine ventilation network,” *Coal Engineering*, vol. 11, pp. 72–74, 2008.
- [12] W. Zhong, C. G. Fan, J. Ji, and J. P. Yang, “Influence of longitudinal wind on natural ventilation with vertical shaft in a road tunnel fire,” *International Journal of Heat and Mass Transfer*, vol. 57, no. 2, pp. 671–678, 2013.
- [13] P. Liu, A. Liu, S. Liu, and L. Qi, “Experimental evaluation of ultrasound treatment induced pore structure and gas desorption behavior alterations of coal,” *Fuel*, vol. 307, Article ID 121855, 2021.
- [14] M. Tang and Y. Ding, “The reliability of ergonomics in the ventilation system of an underground metal mine,” *Procedia Engineering*, vol. 26, pp. 1705–1711, Article ID 11.2357, 2011.
- [15] Y. Han, W. Cheng, H. Liu, G. Wang, and Y. Hu, “Treatment methods for natural wind pressure in mines with zonal ventilation system with diagonal branches — a case study of Wudong Coal Mine,” *Energy Sources Part A Recovery Utilization and Environmental Effects*, vol. 5, pp. 1–13, Article ID 1673512, 2019.

- [16] B. He, "Safety issues and stability discussion of coal mine ventilation system," *Safety In Coal Mines*, vol. 5, no. 43, pp. 134–136, 2012.
- [17] J. Han, C. Ding, S. Jiang, and H. Zhang, "Mathematical model of reliability evaluation on air volume of ventilation system in volume adjustment by frequency conversion," *Journal of Safety Science and Technology*, vol. 12, no. 3, pp. 143–148, 2016.
- [18] P. Liu, L. Fan, J. Fan, and F. Zhong, "Effect of water content on the induced alteration of pore morphology and gas sorption/diffusion kinetics in coal with ultrasound treatment," *Fuel*, vol. 306, no. 10, Article ID 121752, 2021.
- [19] F. Chen, H. Ma, and J. yan, "Ventilation stability analysis at a lifting pressure coal face," *Coal Technology*, vol. 27, no. 8, pp. 71–72, 2008.
- [20] Z. Zuo, "The impact of natural wind pressure on the mine ventilation system and countermeasures," *Shanxi Coking Coal Science & Technology*, vol. 9, no. 9, pp. 43–46, Article ID 09.002, 2013.
- [21] Y. Han, H. Cai, and C. Xu, "Study on mechanism of natural ventilation pressure and effect on mine with multiple downcast shafts," *Coal Technology*, vol. 36, no. 6, pp. 139–142, 2017.
- [22] J. Tsutsumi, T. Katayama, and M. Nishida, "Wind tunnel tests of wind pressure on regularly aligned buildings," *Journal of Wind Engineering and Industrial Aerodynamics*, vol. 43, no. 1–3, pp. 1799–1810, Article ID 0167-6105(92)90592-X, 1992.
- [23] G. R. Hunt and P. P. Linden, "The fluid mechanics of natural ventilation-displacement ventilation by buoyancy-driven flows assisted by wind," *Building and Environment*, vol. 34, no. 6, pp. 707–720, Article ID S0360-1323(98)00053-5, 1999.
- [24] G. van Moeseke, E. Gratia, S. Reiter, and A. De Herde, "Wind pressure distribution influence on natural ventilation for different incidences and environment densities," *Energy and Buildings*, vol. 37, no. 8, pp. 878–889, Article ID 11.009, 2005.
- [25] L. Han, S. Lan, and K. Jiang, "New iterative method of ventilation system's wind quantity for electric machines," *Journal of Chongqing University*, vol. 18, no. 5, pp. 57–63, 1995.
- [26] N. Khan, Y. Su, and S. B. Riffat, "A review on wind driven ventilation techniques," *Energy and Buildings*, vol. 40, no. 8, pp. 1586–1604, Article ID 02.015, 2008.
- [27] A. Zhou, K. Wang, L. Wu, and Y. Xiao, "Influence of gas ventilation pressure on the stability of airways airflow," *International Journal of Mining Science and Technology*, vol. 28, no. 2, pp. 297–301, Article ID 09.004, 2018.
- [28] S. Yun, "Database design of three dimensional simulation and optimization system for mine ventilation network," *Applied Mechanics and Materials*, vol. 347–350, pp. 3065–3068, Article ID 347-350.3065, 2013.
- [29] J. Liu and H. Yoshino, "Performance evaluation of hybrid ventilation system in a full-scale test house," in *Proceedings of the 21st AIVC Annual Conference*, p. 4, Innovations in Ventilation Technology, Hague, Netherlands, September 2000.
- [30] B. Taraba, V. Slovak, Z. Michalec, J. Chura, and A. Taufer, "Development of oxidation heat of the coal left in the mined-out area of a longwall face: modelling using the fluent software," *Journal of Mining and Metallurgy, Section B: Metallurgy*, vol. 44, no. 1, pp. 73–81, Article ID JMMB0801073T, 2008.
- [31] J. Wang, X. Bao, and Y. Ding, "Numerical simulation on gob air leakage flow field by fluent," *Shandong Coal Science and Technology*, vol. 1, pp. 86–87, 2009.
- [32] H. Lin, S. Li, L. Suo, M. Huang, and P. Zhao, "Numerical simulation on reasonable position of strike high roadway with FLUENT," *Journal of Liaoning Technical University*, vol. 33, no. 2, pp. 172–176, 2014.
- [33] A. Slezak, J. M. Kuhlman, L. J. Shadle, J. Spenik, and S. Shi, "CFD simulation of entrained-flow coal gasification: coal particle density/sizefraction effects," *Powder Technology*, vol. 203, no. 1, pp. 98–108, Article ID 03.029, 2010.

Research Article

Prevention and Control of Spontaneous Combustion of Residual Coals in Acid-Soaked Goaf in Gas Drainage Condition

Cunli Qin,¹ Qiming Huang ,¹ Shibin Wang,² Jun Li,¹ Shuang Ju,² and Gang Wang ^{1,3}

¹College of Safety and Environmental Engineering, Shandong University of Science and Technology, Qingdao 266590, China

²College of Energy and Mining Engineering, Shandong University of Science and Technology, Qingdao 266590, China

³Shandong University of Science and Technology,

Mine Disaster Prevention and Control-Ministry of State Key Laboratory Breeding Base, Qingdao 266590, China

Correspondence should be addressed to Qiming Huang; skdhuang@163.com

Received 20 October 2021; Accepted 31 December 2021; Published 25 February 2022

Academic Editor: ZOU Quanle

Copyright © 2022 Cunli Qin et al. This is an open access article distributed under the Creative Commons Attribution License, which permits unrestricted use, distribution, and reproduction in any medium, provided the original work is properly cited.

With the increase of mine mining intensity, the scope of goaf continues to expand, a large amount of coal remains in goaf, and the spontaneous combustion fire of coal is particularly serious. In addition, the spontaneous combustion of coal under the condition of gas mining is not clear. At once, spontaneous combustion can induce gas explosion, resulting in the waste of manpower and material resources, bringing hidden dangers to the mine safety production. In order to prevent and control the fire caused by spontaneous combustion of left coal under the condition of gas mining, in this paper by means of laboratory test, field measurement, and numerical simulation, the law of spontaneous combustion of residual coal under gas mining is studied. The index gas of coal spontaneous combustion was determined by temperature-programmed experimental device. Secondly, the distribution of the stope working face, goaf, and O₂ is discussed. It is of great significance to study the spontaneous combustion rule of three belts in goaf under acid leaching condition and then to discuss the best position of injection idling opening and put forward targeted precontrol measures, which is of great significance to guarantee the safety of mine production. The results show that CO begins to appear when the temperature rises to 40 °C, and its concentration increases exponentially with the increase of coal temperature, which can reflect the degree of coal oxidation in goaf. Therefore, CO should be selected as the indicator gas in the working face. Under the influence of negative drainage pressure, the dangerous area will be enlarged. The optimal drainage volume of high drainage roadway is 90 m³/min, and the optimal air intake volume of working face is 1400 m³/min. The area 0–34 m away from the working face is scattered zone, 34–135 m away is spontaneous combustion zone, and 135 m away is asphyxiation zone. When the position of the idler is 50 m behind the working face, the reduction of the oxidation zone is the largest.

1. Introduction

As the mining depth of coal mines increases gradually, gas disasters caused by spontaneous combustion in goaf will become more serious, further increasing the risk of gas explosion and leading to graver consequences, especially in goafs with high gas content and spontaneous combustion risk. A gas explosion will rapidly outburst if its conditions meet. However, spontaneous coal combustion develops very slowly, during which gas drainage directly affects the evolution of spontaneous coal combustion in the goaf [1–3]. In addition, due to high

mining intensity and great roof-caving height, residual coals and air leakage coexist in the goaf, further worsening spontaneous combustion risk and seriously threatening the safe production of coal [4, 5]. Furthermore, an increase in goaf temperature enhances spontaneous coal combustion risk, severely restricting the advance of fully mechanized mining technology [6–10]. Therefore, to solve spontaneous coal combustion in goafs, it is of great practical significance to study the prevention and control of spontaneous coal combustion in goaf in the conditions of gas drainage to ensure safe and efficient production in underground mines.

Scholars and engineers from various countries have started research on the prevention and control of spontaneous combustion of coal under the conditions of gas drainage in the goaf. Observation of the distribution of the three spontaneous combustion zones (heat dissipation zone, oxidation/temperature rising zone, and choking zone) in the goaf to determine the scope of the “three zones” is an important basis for fire prevention and extinguishment of the goaf [11–14]. With the theory of flow field applied to the flow field in the gob, numerical simulation has become an effective approach to study the distribution of gas volume fractions and optimize inert gas injection parameters [15]. Some researchers set such important parameters of gob’s permeability, resistance coefficient, gas source term, oxygen dissipation, and the like, as constants, establishing the 2D model to solve the flow field in the goaf and the optimal technical parameters for preventing fires due to spontaneous coal combustion and further compare the simulated flow field with the actual one in the gob [16]. Relevant scholars have further refined and in-depth studied the relevant theories of spontaneous coal combustion in key areas under gas drainage. Based on the above research results in various periods, they comprehensively applied prevention and control measures for spontaneous combustion of coal in the goaf under gas drainage and made outstanding contributions to the safe and efficient production of the coal industry [17–20]. Jiang et al. [21] established a model for the migration of gas and air mixture in the goaf and carried out a numerical simulation study on the 3D flow field of a fully mechanized caving mining field. They showed that gas accumulates seriously in the goaf area without drainage and there is a high-risk zone for coexisting gas and spontaneous coal combustion hazard in the possible spontaneous combustion zone. Czech experts Taraba B and Michalec Z [22] aimed at the problem of spontaneous combustion in the goaf of a longwall working face in gas drainage conditions, established a longwall working face model, and studied the impact of the mining speed in the working face on gas emission. They found that there is generally an area suitable for initiation and development of the self-heating process in the goaf. The location and the maximum temperature that can be reached in this area will greatly affect the advancement of the working face. The slower the advancement of the working face, the higher the highest temperature in the area, and the smaller the depth. Yuan et al. [23] applied computational fluid dynamics to analyze different ventilation schemes. They considered the gas flow in the goaf a porous medium laminar flow and simulated the gas flow in the goaf. In addition, they simulated the turbulent flow in the roadway, obtained the contour maps of airflow velocity and velocity vector diagrams, discussed areas prone to spontaneous combustion in the goaf, and optimized the ventilation system of the mine with coexisting disasters of gas and spontaneous coal combustion. Wang et al. [24, 25] developed a new type of composite material to control spontaneous coal combustion in coal mines. The material is a foam gel composed

of composite foaming agent (CFA) and high-water absorbent gel (HWAG) and produced via physical and mechanical agitation. It uses the comprehensive properties of the foam and gel to control spontaneous coal combustion in coal mines. The foam gel can effectively block air leakage, prolong the moisturizing time of coal, significantly enhance the cooling effect of water on coal, and effectively reduce the oxidation reaction rate and heating rate of coal to control spontaneous coal combustion in coal mines. Their results have guiding significance for the prevention and control of spontaneous combustion in the goaf similar to the fully mechanized caving working face.

To sum up, under the influence of high ground temperature and acidic soaking water, the spontaneous combustion characteristics of residual coals in the goaf under gas drainage conditions and the distribution of three spontaneous coal combustion zones in the goaf are still unclear. The fire prevention and extinguishing technologies in such mine goafs are still lacking. Therefore, in this study, we took No.204 working face of Gaojiabao Coal Mine as the research object, analyzed CH_4 and O_2 distribution laws in the working face of the goaf, discussed the influence of drainage volume and air intake on CH_4 concentration in the high-level drainage roadway and O_2 concentration in the goaf floor, and comprehensively determined the optimal drainage volume and air intake volume. In view of the characteristics of the acidic soaking water and high ground temperature, we applied the programmed temperature rising experiment to simulate the primary oxidation/secondary oxidation processes of the residual coals in the goaf and determine the index gas. In addition, we adopted numerical simulation techniques to determine the three spontaneous combustion zones in the goaf and the optimal inert gas injection location and carried out on-site engineering practice applications to solve the spontaneous combustion problem of residual coals under gas drainage conditions, with the hope to provide a reference for similar mines.

2. Overview of the Working Face

The underground No.204 working face is a V-shaped area located in the west of No.203 working face with 7 m distance to its clean coal pillar. The specific location is shown in Figure 1. At the east of the No.204 working face is located the No.205 return air trough that is being excavated. The roadway roof elevation of No.204 working face is +78.122 m–+152.338 m. The working face is mined using the fully mechanized inclined longwall top coal caving and retreating method and adopts the fully caving method to manage the roof. It belongs to category 4 and Type II spontaneous combustion coal seam with a spontaneous combustion period of 37 days. The coal mine is identified as a high CH_4 mine with a relative gas emission of $1.2 \text{ m}^3/\text{t}$, absolute gas emission of $7.18 \text{ m}^3/\text{min}$, maximum absolute gas emission of $2.7 \text{ m}^3/\text{min}$, maximum absolute gushing volume of $0.19 \text{ m}^3/\text{min}$, relative emission of carbon dioxide (CO_2) of $1.53 \text{ m}^3/\text{t}$, and the absolute CO_2 emission of $9.13 \text{ m}^3/\text{min}$.

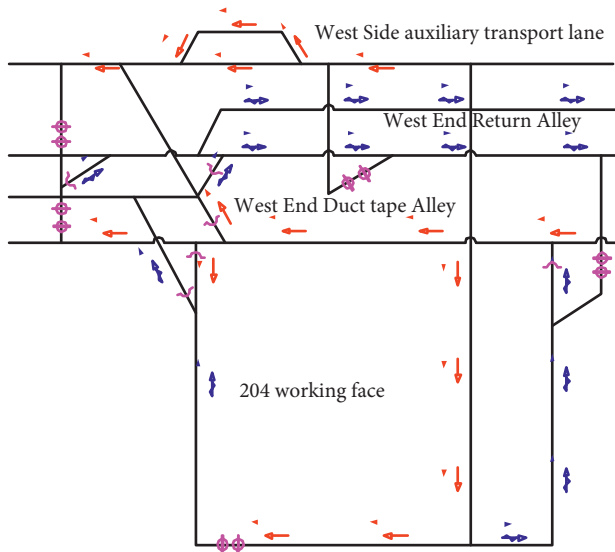


FIGURE 1: Schematic diagram of the specific location of working face.

3. Programmed Temperature Rising Experiments

3.1. Programmed Temperature Rising Device. The experiment is carried out with an oxidation simulation experiment system, as shown in Figure 2. The system is composed of a gas preheating subsystem, a heat transfer coal sample tank, a programmed temperature control chamber, a gas collection and analysis device, and a multichannel data collection subsystem. The gas preheating subsystem can provide preheated dry air to the coal sample tank; the programmed temperature control chamber can provide constant temperature, track temperature increasing, or increase temperature based on the predefined program. During the test, the coal sample tank is placed in the programmed temperature control chamber with a constant flow of dry air entering from the bottom of the coal sample tank. The gas at the outlet is collected for subsequent concentration measurement.

The specific experimental steps are as follows.

3.1.1. Filling the Sample. Put 50 g samples to be tested into the sample tank, and cover a layer of asbestos with a thickness of 2–3 mm evenly above the coal sample, filter the air flow to prevent blocking the gas path, tighten the sample tank with screws at both ends, and seal both ends of the sample tank and the inlet and outlet joint with high temperature resistant raw material belt.

3.1.2. Connecting the Device. Check the connection of power supply, temperature control system, and air supply system to ensure the correct connection of the circuit. The test tube of the coal sample is vertically placed into the main body of the temperature programmed chamber. Adjust the required gas flow, detect the patency of the gas path, and prepare to start the experiment.

3.1.3. Adjusting the Temperature. According to the requirements of the experiment, the temperature control table is used to set the heating program. The change of temperature is another factor that has a great influence on the oxidation process of the original coal samples, and it also has a nonlinear relationship with the coal oxidation rate. The coal oxidation reaction rate is in accordance with the Arrhenius equation; coal molecular structure of surface is active and lively changes along with the change of temperature; the higher the temperature, the faster the reaction speed; studies have shown that the temperature rises every 10°C. The reaction rate will increase by an order of magnitude. Therefore, the programmed heating rate of each experiment is guaranteed to be the same to enhance the comparability of experimental results. At the same time, in order to ensure that the temperature rise is 1.0 °C/min within the precision range of temperature control equipment, analyze the composition and concentration of gas every 10°C. Turn on the power control switch and program heating switch, and the equipment begins to control heating according to the set value of heating program.

3.2. Experiment Design. Fresh coal samples were collected at the freshly exposed coal wall of the No.204 underground working face in Gaojiabao Coal Mine. A certain amount of coal samples was selected, crushed at room temperature, and sieved. Samples with a particle size of 40–80 mesh (0.18–0.38 mm) were used in the experiments. They were placed in a tightly sealed container with desiccants on the top to eliminate water. Samples were soaked in different solutions for 5 days and then air-dried at 23 °C for 24 h. After that, samples were placed at different preoxidation conditions (40 °C, 55 °C, and 70 °C) to simulate the primary oxidation/secondary oxidation process of the residual coals in the goaf of No.204 working face. In addition, coal samples were presoaked in the H₂S-dissolved water solution for 5 days and then air-dried for 24 h to simulate the affecting process of H₂S on the residual coals in the goaf of the working face. Specific experimental conditions are set as shown in Table 1. Alkanes such as CO₂ and C₂H₄ will also be produced in the process of temperature programmed experiment, but CO₂ will also be produced in the heating process, which does not belong to chemical reaction. Secondly, alkanes such as C₂H₄ are produced in a small amount during the experiment, while CO and CH₄ are produced in a large amount and have obvious change rules. Therefore, this paper only discusses the variation of CO and CH₄ gas production under temperature programmed condition.

3.3. Analysis of Experiment Results. Figures 3–6 show the changes in O₂ consumption, CO production, CO₂ production, and CH₄ production of different pretreated coal samples, respectively. It can be seen from Figure 3 that, at different temperatures, coal samples that have been air-dried for 24 h after soaking in acidic aqueous solution consume the least O₂. At 40–110 °C, the overall changing trend of oxygen consumption of the coal samples is not obvious. At 110–170 °C, the O₂ consumption by coal samples is greatly reduced. The O₂

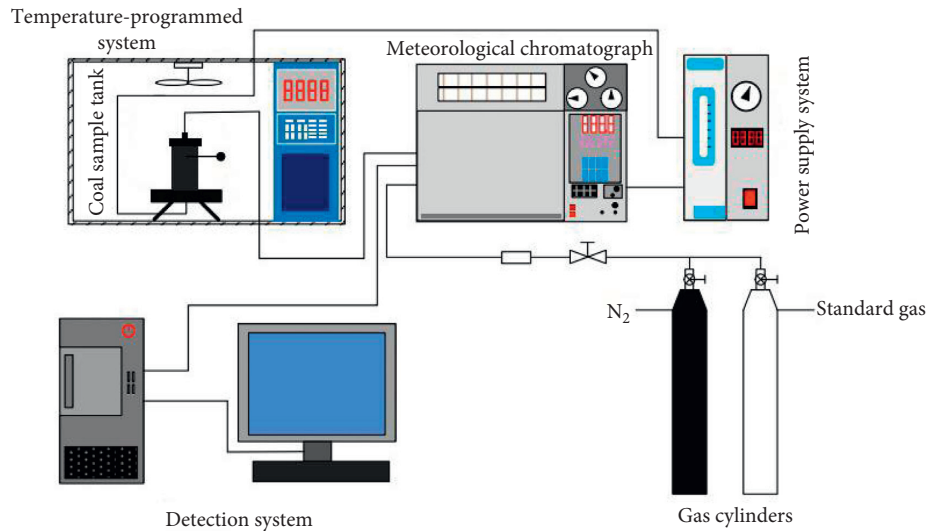


FIGURE 2: Schematics of the programmed temperature rising experiment system of coal samples.

TABLE 1: Experimental scheme design conditions setting.

Serial number	Processing conditions	For the wind speed	Heating rate
1	Raw coal		
2	Five-day immersed	Air dry for 24 h	
3	Soak in weakly acidic water	Air dry for 24 h	
4	Preoxidation to 40°C	50 mL/min	1.0°C/min
5	Preoxidation to 55°C		
6	Preoxidation to 70°C		

consumption by coal samples preoxidized at 70 °C shows an overall downward trend. The O₂ consumption is 19.02 ppm by 24 h air-dried coal samples after soaking in acidic aqueous solution, 19.78 ppm by 24 h air-dried coal samples after soaking in water, 19.88 ppm by coal samples preoxidized at 70 °C, 19.94 ppm by coal samples preoxidized at 55 °C, 20.9 ppm by coal samples preoxidized at 40 °C, and 21.05 ppm by raw coal samples. Among them, the 24 h air-dried coal samples after soaking in acidic aqueous solution consume least O₂, while raw coal sample has the greatest risk of spontaneous combustion due to oxidation.

It can be seen from Figure 4 that, at low temperature, that is, 40–80 °C, the CO production of all coal samples is low, about 40–50 ppm, indicating that coal samples with different pretreatment conditions have relatively small differences at low temperatures. When the temperature rises to 90 °C, samples enter a high temperature stage. As the temperature rises, CO production begins to change significantly. At 90–120 °C, the amount of CO produced by coal samples begins to diverge although at a slowly increasing rate. At 120–180 °C, the amount of CO produced by coal samples shows a rapid increase trend. At 180–200 °C, the CO production of coal samples slows down and reaches the maximum at 200°C. The CO production of coal samples under different pretreatment conditions and raw coal samples reaches more than 20,000 ppm, which is 400–500 times the CO production at the initial temperature. The maximum CO is produced by the air-dried coal samples weak acidic aqueous solution, reaching 24698 ppm. The order of CO

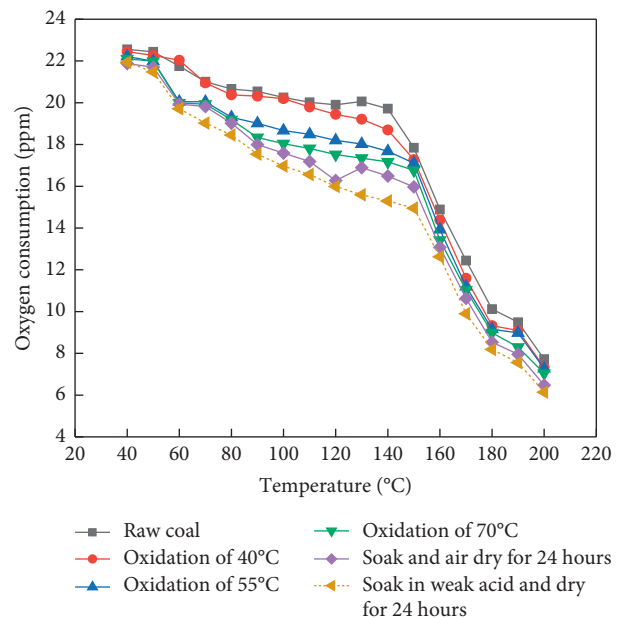


FIGURE 3: Changes in O₂ consumption of different pretreated coal samples.

production is 24 h air-dried coal samples after soaking in acidic aqueous solution > 24 h air-dried coal samples after soaking in water > coal samples preoxidized at 70°C > coal samples preoxidized at 55°C > coal samples preoxidized at 40°C > raw coal samples.

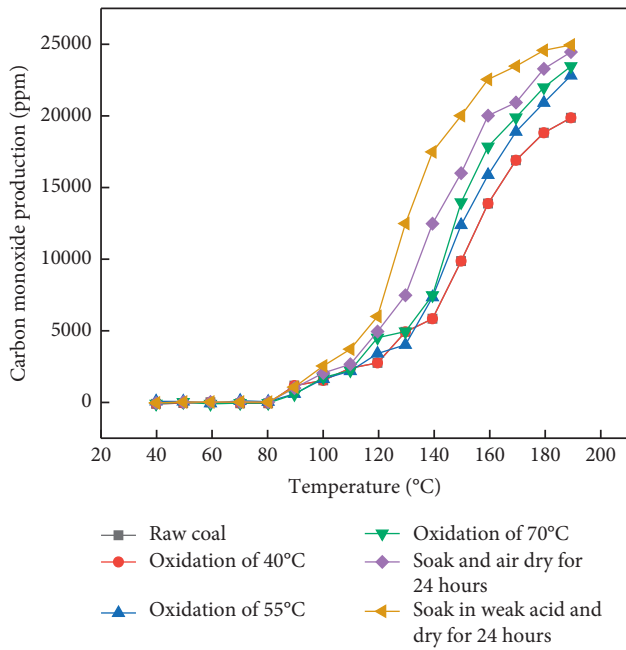


FIGURE 4: CO production of different pretreated coal samples.

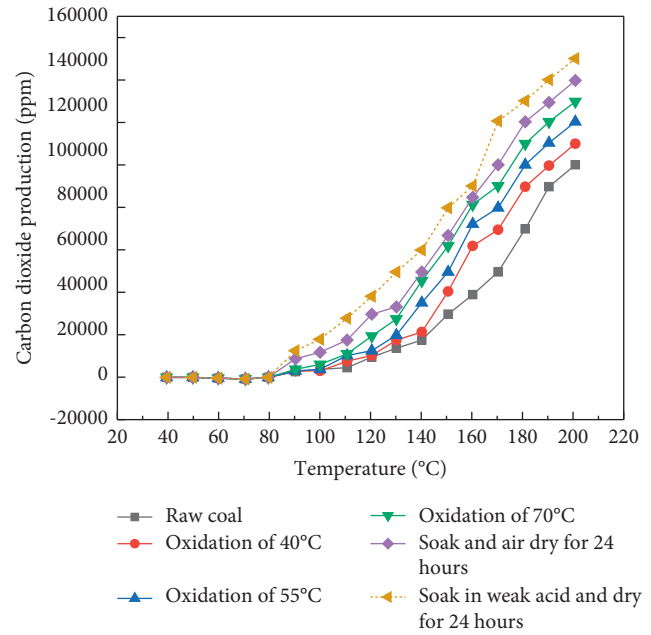


FIGURE 5: CO₂ production of different pretreated coal samples.

It can be seen from Figure 5 that, at low temperature, that is, 40–80°C, all coal samples produce relatively low CO₂, about 400–600 ppm, and the difference between different coal samples is small. When the temperature rises to 90°C, the CO₂ production of different coal samples begins to diverge significantly, and the coal samples enter a rapid heating phase. At 90–140°C, CO₂ production increases at a relatively slow rate. When the temperature rises to 150°C, the CO₂ production starts to rise rapidly until it reaches the maximum at 200°C. The amount of CO₂ reaches 144333 ppm by 24 h air-dried coal samples after soaking in acidic aqueous solution. At different temperatures, the CO₂ production by 24 h air-dried coal samples after soaking in acidic aqueous solution is always the highest among all samples at different temperatures. The order of CO₂ production is 24 h air-dried coal samples after soaking in acidic aqueous solution > 24 h air-dried coal samples after soaking in water > coal samples preoxidated at 70°C > coal samples preoxidated at 55°C > coal samples preoxidated at 40°C > raw coal samples.

As can be seen from Figure 6, the amount of CH₄ gas produced by coal samples in the process of coal oxidation and spontaneous combustion increases significantly compared with that of raw coal and presents an upward trend. The CH₄ production of coal samples soaked in water during the whole process is at the maximum, followed by that soaked in water. The order of CO₂ production is as follows: air drying 24 h for acid-soaked coal sample > air drying 24 h for soaked coal sample > preoxidation 70 °C > preoxidation 55°C > preoxidation 40°C > raw coal.

3.4. Determination of Index Gas of Spontaneous Coal Combustion in an Acidic Environment. Coal spontaneous combustion symbol gas refers to the gas that can mark the spontaneous combustion of coal. The oxidation and thermal

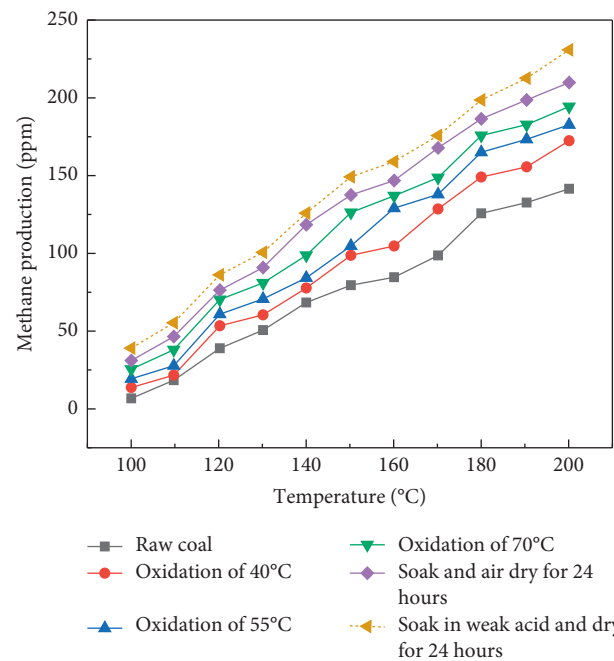


FIGURE 6: CH₄ production of different pretreated coal samples.

accumulation of coal will release alkanes, olefin, CO₂, CO, and other components. The release of gas is affected by time, concentration, type of coal, geological conditions, temperature, oxygen concentration, and other related conditions. Therefore, in order to accurately predict coal spontaneous combustion, a reasonable gas which can reflect the temperature and state of coal spontaneous combustion is selected.

It can be seen from Figure 3 that CO is present in the atmosphere at 80 °C although at a relatively low

concentration. Throughout the entire experiment period, CO concentration continues to rise with the increase of coal temperature, showing a single increasing exponential relationship. It can be seen from the gas production from coal oxidation that the absolute amount of CO production is the largest among all gas products. The first abrupt CO concentration change in coal samples occurs at 80 °C, and the second abrupt CO concentration change occurs at 120 °C.

CH₄ production is accompanied by the coal sample temperature rising. At temperatures below the critical temperature, about 70–90°C, desorption occurs. At temperatures higher than the critical temperature, CH₄ concentration increases significantly and exponentially. It can be seen from Figure 5 that CH₄ is produced at 100–140°C although at relatively low concentration, indicating that the coal samples of Gaojiapu Coal Mine contain a small amount of CH₄. Since then, CH₄ concentration increases continuously with the increase of coal temperature because the adsorption capacity of the intermolecular Van der Waals force on CH₄ gradually weakens with the increase of temperature. Since CH₄ is the main component of coal-bed gas, it cannot be used as an index gas for spontaneous coal combustion. The analysis shows that CO begins to appear when the temperature rises to 40 °C, and its concentration increases exponentially with the increase of coal temperature, which can reflect the degree of coal oxidation in the goaf [26]. The critical temperature of CH₄ generation is about 100 °C. Compared with CO, CH₄ shows a significant time difference and temperature difference. Therefore, CO should be selected as the index gas for No.204 working face.

4. Determination of the Three Spontaneous Combustion Zones in Goaf

4.1. Layout of the Measuring Points for the Beam Tube Monitoring System in the Goaf. The gas concentration distribution in the goaf is observed using the buried pipe extraction method. The measurement range is about 200 m away from the working surface, with measuring points set at an interval of 50 m to keep 3 measuring points in the air inlet side, return air side, and central area of the goaf. The gas components in the goaf are extracted from each measurement point of the buried pipes and simultaneously tested.

A total of 5 monitoring pipelines are arranged in the transportation trough, return air trough, and the back of the No.204 working face, with one monitoring point set at an interval of 50 m for each pipeline, as shown in Figure 7. Each monitoring point is equipped with a beam tube device and a gas sample collection device. As the working surface advances, sensors and beam tubes will be buried in the goaf.

Each measuring point is sealed with plastic when no gas is taken out and placed in a hidden place for protection. Because it is too complicated to connect the measuring point with the mine beam tube monitoring system, it is necessary to use a portable air pump for manual sampling and analysis. Every day, a special person is organized to take gas at each measuring point with a balloon (balloon) and send it to the ground chromatographic station for gas chromatographic analysis, instead of using portable instruments. The gas

composition of goaf is pumped by buried beam tube for analysis and determination. The beam pipe is laid using 3-inch steel tube as a protective sleeve to prevent it from being crushed by falling rock. In order to distinguish different measuring points, identification marks should be made at the exhaust port of the beam tube, the diameter of the beam tube is 8 mm, and the filter probe should be used at the end of the beam tube. Each beam tube is responsible for the gas sample of a measuring point. In order to prevent extrusion, the pipelines laid at the two grooves should be as close to the coal wall as possible, and the probe should be fixed below the coal wall to prevent the probe from being hit during coal mining. The lead is pulled out of a 3-inch steel tube.

According to the plan, a total of 15 observation points were arranged. Figure 8 shows the observed oxygen concentration distribution at different locations in the goaf. It can be seen from Figure 7 that as the working face advances and the depth of the goaf increases, the oxygen concentration in the goaf shows an overall downward trend. At the depth of 58 m in the goaf on the return air side, the oxygen concentration drops to 14%, after which the oxygen concentration declines significantly faster, indicating that oxidation of the floating coal in the goaf is more serious. The oxygen concentration on the inlet side decreases more slowly than on the return side and remains at a high level within 82 m from the working face. The oxygen concentration decreases to about 14%. This is due to the wind pressure difference being greater on the inlet side, resulting in significant air leakage. With the continuous advancement of the working face, the depth of the measuring points buried in the goaf gradually increases. Due to the reduction of air leakage intensity, relatively increased opportunity for the floating coal to react with oxygen, and the effect of oxygen consumption in the coal bed, oxygen concentration gradually decreases [27].

Gas samples are drawn through the buried pipes and boreholes in the mined-out area for testing to investigate the changes in coal parameters in the mined-out area. According to the observation data of the mined-out area, CO change law in the mined-out area of No.204 working face is obtained, as shown in Figure 9. From the changing trend of CO concentration contour in the goaf, it can be seen that, with the continuous advancement of the working face, the depth of the measuring point buried in the goaf continues to deepen and CO concentration changes with an overall trend of increasing before decreasing. When the depth of the measurement point in the goaf on the return air side enters 20 m, CO concentration shows an upward trend, indicating that the floating coals in the goaf begin to be oxidized. The CO concentration increases rapidly after 60 m, indicating that the floating coal is in the oxidation/temperature rising zone. Therefore, during the advancing process of No.204 working face, 100 m from the return air side is a key area for fire prevention. In summary, it can be concluded that the distribution of oxygen concentration in the goaf of No.204 working face is relatively wide on the air inlet side, and the oxygen concentration is still maintained at about 14% at 80 m from the working face. As the working face continues to advance, the oxygen concentration in the goaf on the inlet

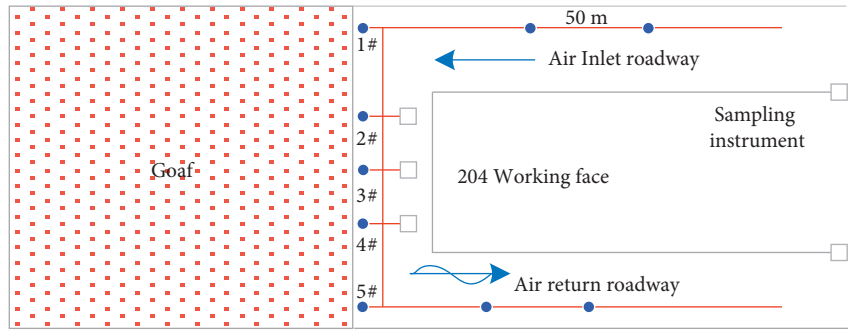


FIGURE 7: Layout of temperature and gas concentration measurement points in No.204 goaf.

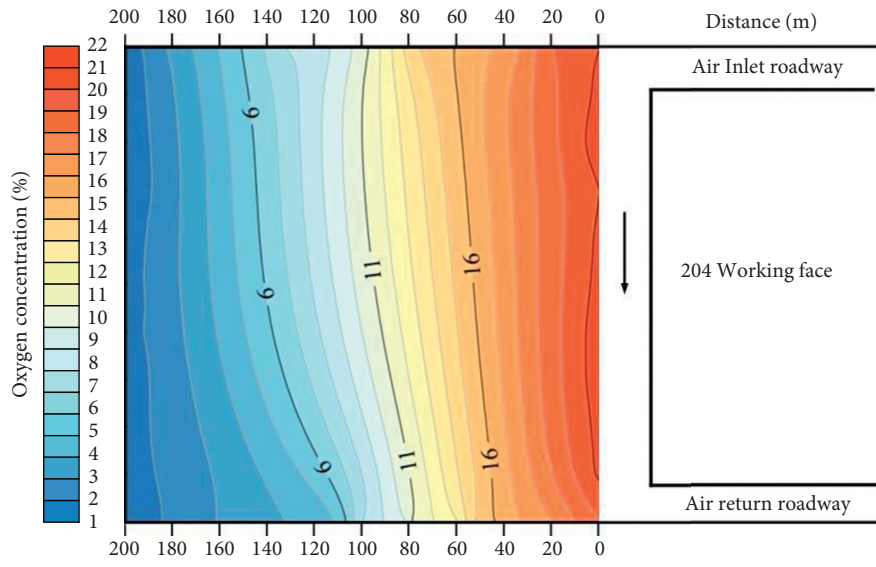


FIGURE 8: Distribution of O₂ concentration in the goaf.

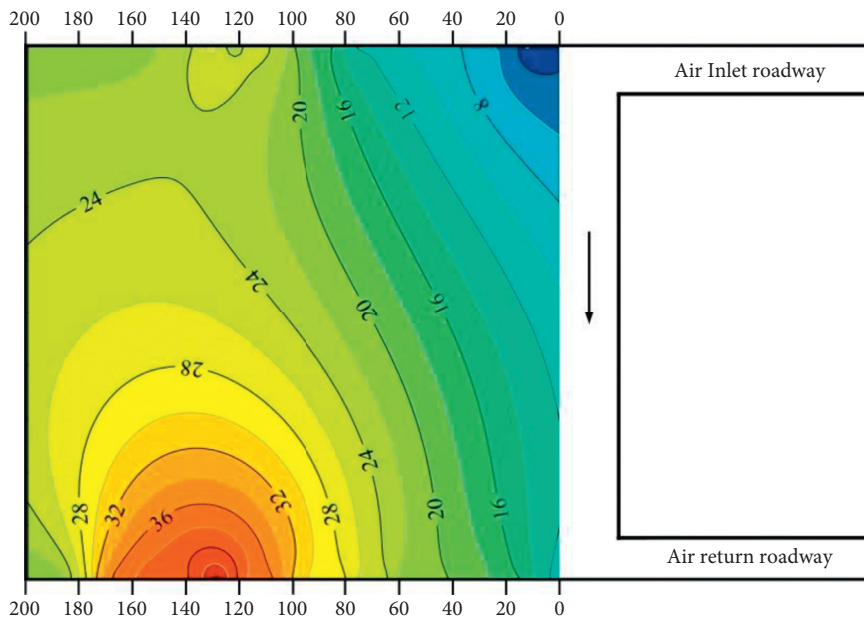


FIGURE 9: Distribution of O₂ and CO concentration on the inlet side of the goaf.

side gradually decreases. At 150 m from the working face, the oxygen concentration drops to about 7%. The distribution range of oxygen concentration on the return air side is relatively shallow. At 20 m from the working face, the oxygen concentration is maintained at about 18%, and when it is 150 m deep into the goaf, the oxygen concentration drops to about 5%. The oxygen concentration distribution in the middle of the goaf area generally decreases from the air inlet side to the return air side. The oxygen concentration at the same buried distance is higher on the inlet side than on the return air side.

4.2. Numerical Simulation of the Three Spontaneous Combustion Zones. 3D mesh model of the fully mechanized goaf in the No.204 working face of Gaojiabao Coal Mine is established. The working face width is 10 m, the air inlet and return roadway is 10 m long, and the cross section is $5\text{ m} \times 5\text{ m}$. The goaf is 26 m high, 220 m long, and 200 m wide. The model is shown in Figure 10.

4.3. “Three-Zone” Simulation Results and Analysis. It can be seen from Figures 11 and 12 that the range of the heat dissipation zone is about 0–34 m behind the working face. The width of the heat dissipation zone is greater on the side of the air inlet roadway than that the return air roadway of the goaf and the maximum depth of the heat dissipation zone is up to 34 m behind the working face on the side of the air inlet roadway of the working face and is only 20 m in the return air roadway.

The distribution range of the heat dissipation zone in the goaf of No.204 working face is within 0–34 m from the working face in the goaf. Due to the relatively large air leakage at the air inlet side of the goaf, the heat dissipation zone is relatively deep. By contrast, due to the oxygen consumption of the remaining coal on the return air side, the heat dissipation zone is shallow. The choking zone in the deep part of the mined-out area is more than 100–135 m away behind the working face, as shown in Figure 13. As a result, there is a heat dissipation zone at 0–34 m from the working face, an oxidation/temperature rising zone at 34–135 m, and a choking zone beyond 135 m.

4.4. Mechanism of Spontaneous Combustion of Coal under Gas Extraction. During the mining of coal seam with high gas and easy spontaneous combustion, the air leakage in goaf is aggravated due to gas extraction, which leads to spontaneous combustion of floating coal in goaf. At the same time, due to the spontaneous combustion of floating coal in goaf, “internal fire wind pressure” is formed locally in goaf, which intensifies the oxygen supply power of floating coal spontaneous combustion in goaf. On the other hand, the spontaneous combustion of floating coal has become the ignition source of gas combustion and explosion, which seriously affects the safe extraction of mine gas. Due to the influence of gas extraction, mining activities around a large area of goaf increase, and harmful gases in a large area of goaf flood into the mine caused by spontaneous combustion

or other disasters, resulting in increased risk of personal injury or other production accidents. With the increase of the goaf area, the goaf is divided by different forms of coal pillars such as mining area coal pillar, isolated island coal pillar, corner coal pillar, and so on, and there are many kinds of insufficient mining areas. Because of the thick hard rock strata in the overburden in most areas, there is a hidden danger of mine earthquake caused by sudden instability of overburden in large area [28]. When the mine earthquake occurs, high-pressure airflow rushes out from the goaf and destroys the goaf sealed, threatening personal safety, and it is easy for air leakage to cause natural ignition. With the gradual increase of mining depth, the geothermal gradient increases, the temperature of raw rock increases, the natural starting temperature of coal is high, and the ignition period is shortened. The stress of surrounding rock is large, and the coal body is easy to be crushed and broken. With the increase of mining intensity, the scope of mined-out area is getting larger and larger. No coal pillar mining leads to the connection between mined-out areas, and there are many air leakage channels. In addition, there are many remaining coal in mined-out areas in fully mechanized caving mining [29].

4.5. Influence of High-Level Drainage Parameters on Gas and Spontaneous Coal Combustion. Figure 14 shows the gas concentration distribution at the end of the high-level drainage roadway under different drainage volumes, and Table 2 shows the specific gas drainage data.

It can be seen from Figure 14 and Table 2 that when the drainage volume increases gradually, the gas concentration and scalar quantity both show a trend of first increasing before decreasing. When the drainage volume increases from $80\text{ m}^3/\text{min}$ to $90\text{ m}^3/\text{min}$, the gas drainage range and gas drainage rate of high-level drainage roadways increase, and the gas concentration and scalar quantity also increase. However, with the continuous increase of the drainage volume, the extraction range continues to expand, and the extraction channel is connected to the caving zone of the goaf. The negative pressure pumps make the gas flow from the working face to the high-level drainage roadways, which reduces the gas scalar quantity. Thus, when the drainage volume is $90\text{ m}^3/\text{min}$, the gas drainage volume and gas scalar quantity are moderate, and the gas scalar volume accounts for 70.23% of the total emission volume.

Figure 15 shows the O_2 concentration field of the goaf floor under different drainage conditions. It can be seen from Figure 15 that, with the increase of gas drainage in the high-level drainage roadway, the O_2 volume fraction contour moves to the inside of the goaf, indicating that the width of the oxidation/temperature rising zone increases [30]. When the drainage rate is $80\text{ m}^3/\text{min}$, the average width of the oxidation/temperature rising zone in the goaf is 40.24 m, and the maximum width is 50.11 m; when the drainage volume is $90\text{ m}^3/\text{min}$, the average width of the oxidation/temperature rising zone in the goaf is 63.1 m, and the maximum width is 70.2 m; when the drainage volume reaches $130\text{ m}^3/\text{min}$, the average width of the oxidation/temperature rising zone in the goaf is 85.1 m, and the

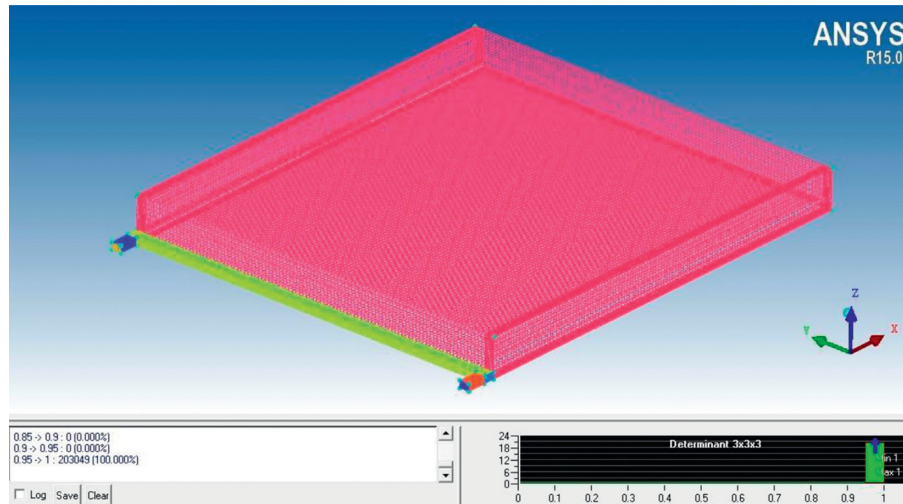
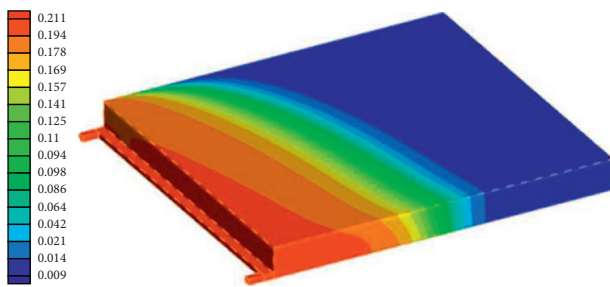


FIGURE 10: 3D goaf model of the working face.

FIGURE 11: Overall O₂ concentration distribution in the goaf.

maximum width reaches 91 m. Overall, with the increase of the gas drainage volume, the width of the oxidation/temperature rising zone in the goaf increases, and the dangerous area will be enlarged under the influence of the negative pressure of the extraction. Comprehensively considering the effect of gas extraction, the optimal gas extraction amount of the high-level drainage roadway is 90 m³/min.

4.6. Influence of Air Intake on the Three Spontaneous Combustion Zones in the Goaf. Figure 16 shows the field distribution of gas concentration in the high-level drainage roadway area under different air intake conditions. Table 3 shows the specific data. It can be seen from Figure 14 that when the air intake is 1400 m³/min, the gas concentration and scalar quantity increase correspondingly. The reason is that the increase in air volume causes a slight increase in air leakage, which carries away a large amount of gas in the goaf. When the air volume reaches 1800 m³/min, the concentration and scalar quantity of gas in the high-level drainage roadway are significantly reduced. The reason is that the air leakage channel of the working face is connected to the drainage channel of the high-level drainage roadway. Under the influence of negative suction pressure, the air that leaked into the working face flows into the high-level drainage roadway through the air leakage fissure, which causes the concentration and scalar quantity of drainage gas to decrease [31].

Figure 16 shows the O₂ concentration field of the goaf floor under different air intakes. With the increase of the air intake of the working face, the width of the oxidation/temperature rising zone on the air inlet side of the goaf increases, reaching 107.3 m at the maximum, while the width of the oxidation/temperature rising zone on the return air side barely changes. The results show that the increase of the air intake has a greater impact on the width of the oxidation/temperature rising zone on the air intake side. Therefore, the optimal air intake of the working face is 1400 m³/min.

4.7. Simulation Results and Analysis of the Influence of Different Inert Gas Injection Positions on the Three Spontaneous Combustion Zones in the Goaf. If the position of the inert gas inlet is too close to the working face, the oxygen concentration in the upper corner will be too low under the influence of air leakage in the goaf. Meanwhile, the inert gas flow route is short, and the effect of reducing the oxygen concentration in the middle and rear of the goaf is not obvious. If the distance between the opening of inert gas injection and the working face is too far, the effect of inert gas inerting oxidation zone in goaf cannot be achieved effectively. In order to determine a reasonable position of compound inerting gas injection and analyze the influence of different inerting positions on nitrogen injection effect, four different positions of inert gas injection port are selected. Since the buried depth of inert gas injection pipeline exceeds 50 m, it is highly likely to be crushed and destroyed by residual coal, so the maximum buried depth of inert gas injection pipeline is set as 60 m. That is, the simulated injection idler is located 30 m, 40 m, 50 m, and 60 m behind the working face. Figure 17 shows the numerical simulation results of the three spontaneous combustion zones in the goaf at different injecting sites when setting the injecting flow rate at 600 m³/h.

It can be seen from Figure 17 that, before injection, the maximum extension depth of the heat dissipation zone on the air inlet side reaches 33 m behind the working face. When the injection site is 30 m behind the air inlet side of the

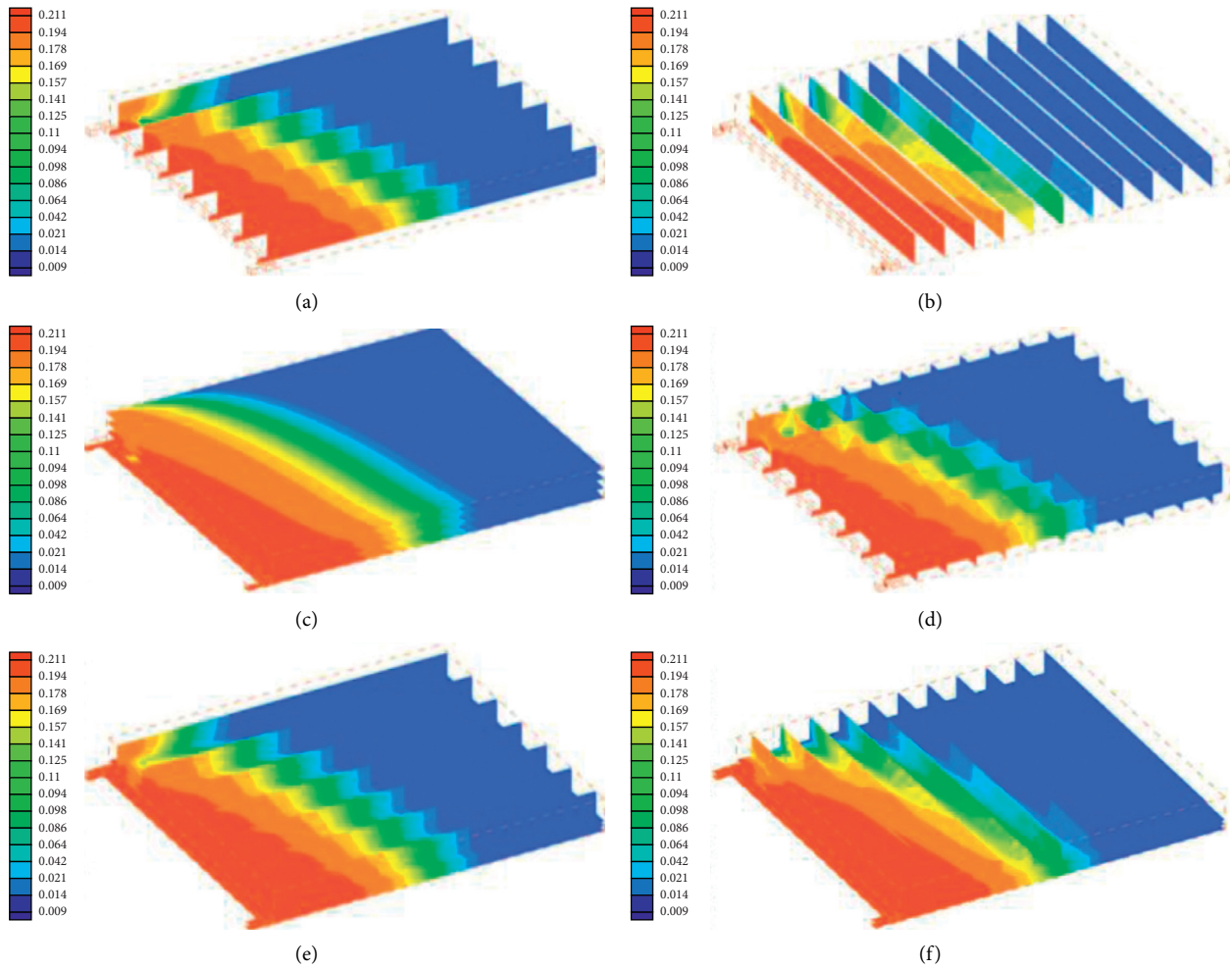


FIGURE 12: Distribution of O₂ concentration in each axis of the goaf. (a) Tangential O₂ concentration distribution along the axis X. (b) Tangential O₂ concentration distribution along the axis Y. (c) Tangential O₂ concentration distribution along the axis Z. (d) Tangential O₂ concentration distribution along the axis XY. (e) Tangential O₂ concentration distribution along the axis YZ. (f) Tangential O₂ concentration distribution along the axis XZ.

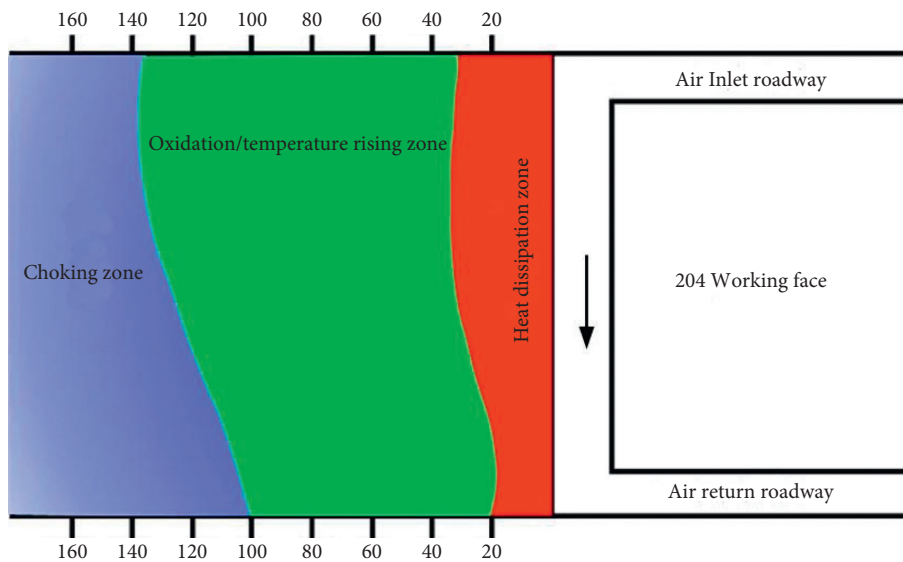


FIGURE 13: Distribution of three spontaneous combustion zones in the goaf.

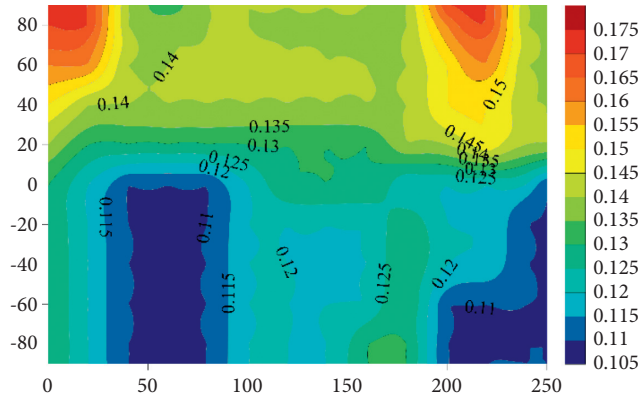


FIGURE 14: CH₄ concentration field in high-level drainage roadway under different drainage conditions.

TABLE 2: Gas drainage data of high drainage roadway under drainage volume conditions.

Drainage volume (m ³ .min ⁻¹)	Air intake (m ³ .min ⁻¹)	Gas drainage in high drainage roadway		
		Volume fraction (%)	Scalar quantity (m ³ .min ⁻¹)	Proportion of gushing volume (%)
80	1400	15.3	11.30	26.63
90	1400	32.1	29.23	70.23
110	1400	16.7	16.83	41.02
130	1400	9.4	11.61	17.41

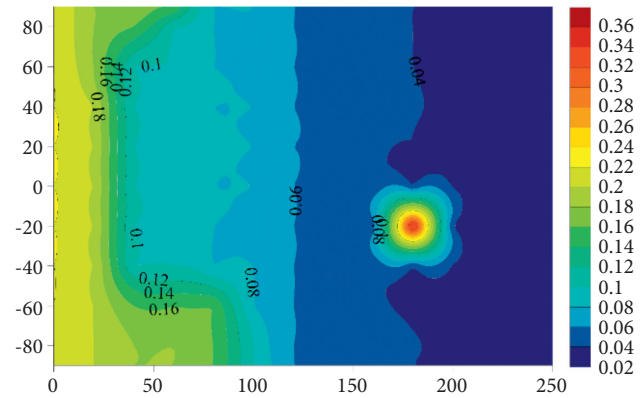


FIGURE 15: O₂ concentration field in high-level drainage roadway under different drainage conditions.

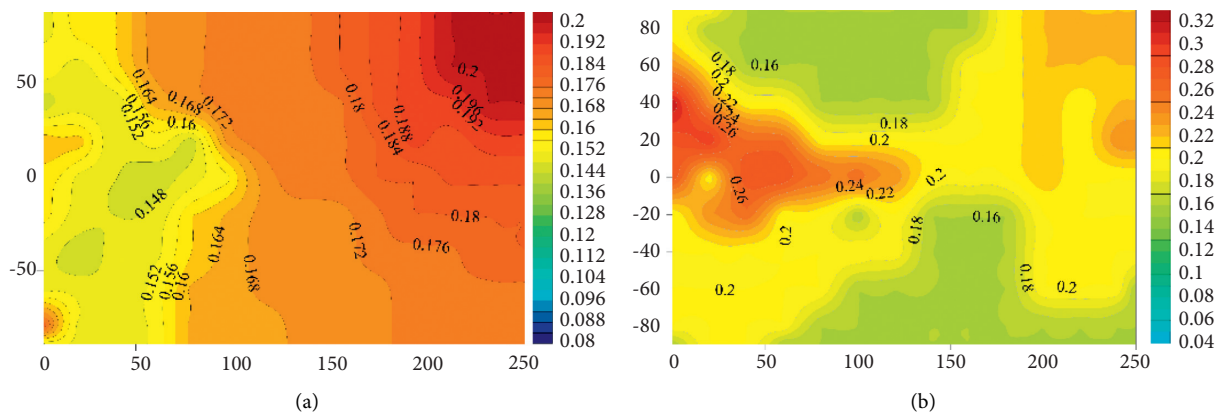


FIGURE 16: O₂ concentration field in the goaf floor under different air intake conditions. (a) Inlet air volume at 1400 m³/min. (b) Inlet air volume at 1800 m³/min.

TABLE 3: Gas drainage data of high-level drainage roadway under different air intake conditions.

Air intake ($\text{m}^3 \cdot \text{min}^{-1}$)	Mixing amount ($\text{m}^3 \cdot \text{min}^{-1}$)	Gas drainage in high drainage roadway		
		Volume fraction (%)	Scalar quantity ($\text{m}^3 \cdot \text{min}^{-1}$)	Proportion of gushing volume (%)
1400	90	32.3	29.07	69.71
1800	90	11.2	10.08	24.17

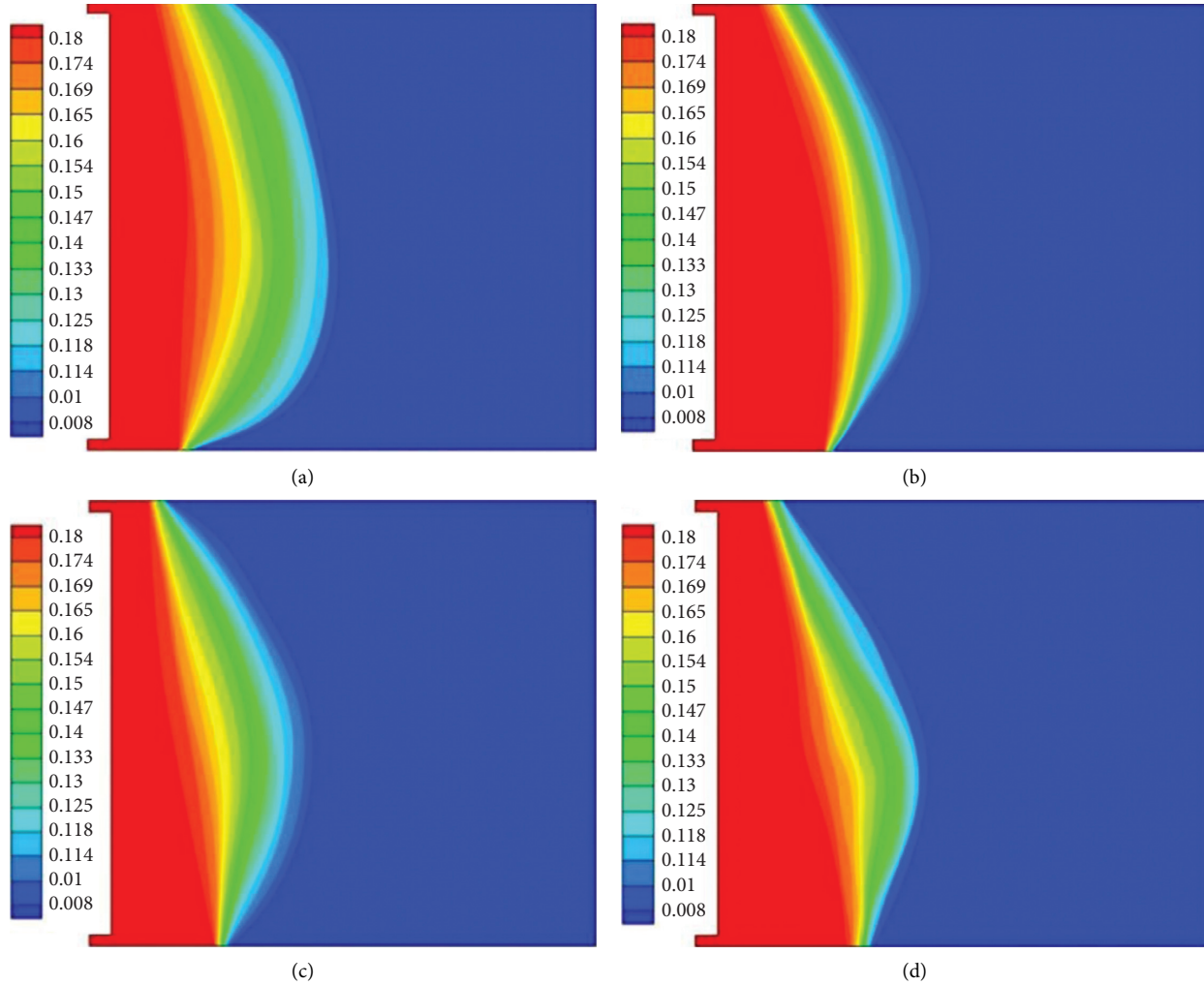


FIGURE 17: The distribution of O_2 concentration in the goaf under different inert gas injection sites. (a) Distribution of O_2 concentration in the goaf at $X = 30$ (m). (b) Distribution of O_2 concentration in the goaf at $X = 40$ (m). (c) Distribution of O_2 concentration in the goaf when $X = 50$ (m). (d) Distribution of O_2 concentration in the goaf when $X = 60$ m.

working face, the heat dissipation zone, oxidation/temperature rising zone, and choking zone converge near the injection site, and the width of oxidation/temperature rising zone behind the goaf significantly declines. After injection at this position, the maximum depth of the oxidation/temperature rising zone in the goaf is 104 m and reduces about 22.3%. When the injection site is 40 m behind the working face, the phenomenon of three-zone convergence also occurs at the injection area. Moreover, due to the influence of the injection, the heat dissipation zone near the injection site changes significantly. The maximum depth of the oxidation zone is 95 m, and the maximum width of the oxidation/

temperature rising zone reduces by 39 m or 29.1%. With the injection depth continuously increasing to make the injection site locate at 50 m behind the working face, the maximum width of the oxidation/temperature rising zone is 92 m, and the maximum reduction is 31.3%. When the injection site is 60 m inside the goaf, the inert gas mainly flows to the back of the goaf. The maximum depth of the oxidation/temperature rising zone is 94 m, and the reduction rate is 29.8%. When the injecting site is 50 m behind the working face, the reduction of the oxidation/temperature rising zone is the largest. It is basically consistent with the on-site measurement results.

4.8. Influence Law of Spontaneous Combustion of Residual Coal under Gas Drainage Condition in the Goaf. When the drainage volume increases gradually, both gas concentration and scalar quantity show a trend of increasing before decreasing. When the gas drainage range and gas drainage rate of the high-level drainage roadway increase, the gas concentration and scalar quantity also increase. However, with the increase of the extraction volume, the extraction range continues to expand, the extraction channel is connected to the caving zone of the goaf, and the gas is extracted from the working face to the high-level extraction roadway due to the negative pressure, which reduces the gas scalar quantity. In addition, with the increase of gas drainage in the high-level drainage roadway, the O₂ volume fraction contour will move to the inner goaf with the increase of the drainage, thereby affecting the width of the oxidation/temperature rising zone.

The change of air intake will affect the change of gas concentration and scalar quantity. This is because increased air volume will lead to a slight increase in air leakage, and a large amount of gas in the goaf is carried away by the air leakage. When the air volume is large enough, the gas concentration and scalar quantity of high-level drainage roadways will decrease slightly, mainly because the air leakage channel of the working face is intersected and connected with the drainage tunnel of the high-level drainage roadway. Under the influence of negative suction pressure, the air leaked from the working face flows into the high-level drainage roadway through the air leakage fissure, leading to decreased gas drainage concentration and scalar quantity. Under different air intakes, the O₂ concentration of the goaf floor increases with the air intake of the working face, which in turn affects the width of the oxidation/temperature rising zone.

5. Spontaneous Combustion Prevention and Control Technology at the Working Face and Its Effectiveness Analysis

5.1. Prevention and Control Technical Solution. At present, the mine fire prevention and fire extinguishing technologies mainly include grouting, ammonia injection, gel injection, and other conventional measures. In the process of implementation, it is found that due to the influence of geological conditions, the fluidity of grout in goaf is limited, which leads to the poor coverage of goaf. After nitrogen is injected into the goaf, the retention time of nitrogen in the goaf is short due to cracks and air leakage in the surrounding rock. Gel injection or other materials have high cost and complex process and affect production. In recent years, liquid CO₂ injection in goaf has a remarkable effect on mine fire prevention and control. Therefore, combined with the actual situation of mine production, this paper analyzes the effect of CO₂ fire prevention, in order to provide reference for other mine fire prevention methods.

The direct injection method is adopted, which is to press CO₂ into the goaf at the working face along the grouting

pipeline using the liquid CO₂ self-vaporization pressure. Before the liquid CO₂ is injected, the air in the pipeline is vented, and the CO₂ concentration reaches >97%. When injecting liquid CO₂, the laying position of the injection pipelines is the same as that of the N₂ injection pipelines. The injection site is set at 50 m in the goaf on the side of the transportation trough, and the injection flow rate of liquid CO₂ is 35–45 m³/h. The injected liquid CO₂ flows into the goaf of the working face and is strictly controlled to prevent high-concentration CO₂ from flowing into the working face. When the CO₂ concentration in the wind flow on the working face reaches 1%, stop pressing.

A set of inhibitor spraying and pressure injection systems are installed in each of the two troughs of No.204 working face, and full-time personnel are arranged to spray the broken coal bodies on the coal walls of the two roadways during the mining process of the working face. The material used for spraying the inhibitor is industrial grade MgCl₂, and the concentration of inhibitor solution is calculated using the following equation:

$$\rho = \frac{T}{C} \times 100\% = \frac{T}{T + W}, \quad (1)$$

where C is the amount of inhibitor solution, kg; T is the amount of inhibitor, kg; and W is the amount of water, kg.

After calculation, the optimal inhibitor concentration is 17%. Therefore, MgCl₂ is mixed with water in a ratio of 15% to 20%. The prepared solution is sprayed to the broken coal walls of the two roadways. The pipeline is Φ25 mm high-pressure hose laid from the rear beam of the support bracket at the return air corner of the working face to the rear beam of the end bracket with a three-way stop valve installed every 20 m. The pipeline outlet is connected to the inhibitor injection pump and the pipeline inlet is connected to a φ13 mm hose and spray gun.

5.2. Engineering Practice Effect Analysis. As shown in Figure 18, after implementing the strengthened fire prevention measures during the mining cease period at No.204 working face, CO concentration at each measurement point gradually decreases to 11 ppm at the corner of the return air, to 4 ppm at the corner of the inlet air, and to a normal value at the No.204 working face. As shown in Figure 19, the gas concentration in the upper corner and the return air lane showed an obvious decreasing trend. During the mining, the gas concentration in each area of the working face is within a reasonable range, and the gas concentration in the upper corner is always stable at 0.1%–0.5%, which is within a reasonable range, indicating the measures have achieved a good application effect.

6. Conclusion

The absolute amount of CO produced is the largest among all gas products. The temperature of CO concentration in coal sample was 80 °C for the first time and 120 °C for the second time. When the temperature of coal sample is about

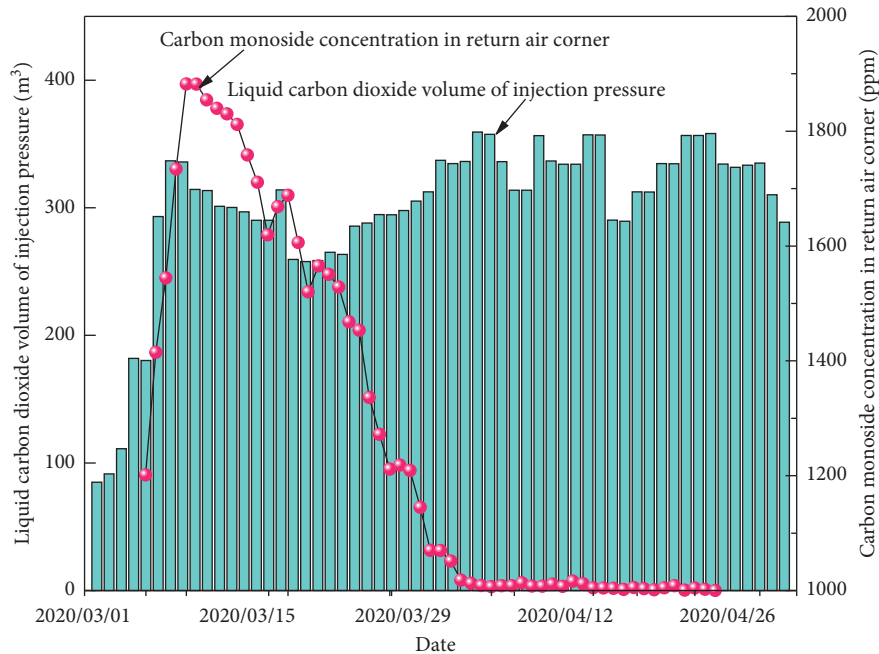


FIGURE 18: Distribution of CO concentration in the goaf under different inert gas injection sites.

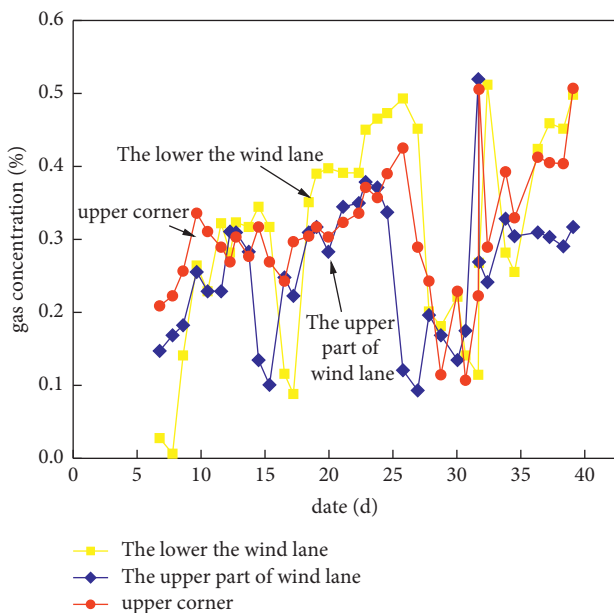


FIGURE 19: Gas extraction situation.

70–90 °C, the desorption phenomenon occurs. When the temperature exceeds the critical temperature, the gas concentration increases obviously, showing an exponential relationship. CH₄ gas is produced when the temperature of coal is 100–140°C, but its concentration is relatively small. Since then, the concentration of CH₄ gas increases continuously with the rise of coal temperature, because the adsorption capacity of intermolecular Van der Waals force on CH₄ decreases gradually with the rise of temperature.

When the temperature rises to 40 °C, CO begins to appear, and its concentration increases exponentially with the increase of coal temperature. The critical temperature of CH₄ is about 100 °C. Compared with CO gas, CH₄ has significant time difference and temperature difference. Therefore, CO should be selected as the indicator gas in the working face.

With the increase of pumping amount, the width of oxidation heating zone in goaf increases, and the dangerous zone will be enlarged under the influence of negative pumping pressure. The optimal pumping volume of high-level roadway is 90 m³/min. With the increase of air inlet volume, the width of oxidation heating zone on the inlet side of goaf increases obviously, while the width of oxidation heating zone on the return side of goaf changes very little. The optimal air inlet volume of working face is 1400 m³/min.

The area 0–34 m away from the working face is scattered zone, 34–135 m away is spontaneous combustion zone, and 135 m away is asphyxiation zone. The oxidation zone has the largest reduction range, and the CO concentration at the corner of the return air and the corner of the inlet air decreases to 11 PPM and 4 PPM, and the CO gas concentration at the 204 working face decreases to the normal value. It proves that the measures adopted to strengthen the fire extinguishing measures are effective, and good application effect has been achieved.

Data Availability

The raw/processed data required to reproduce these findings cannot be shared at this time as the data also form part of an ongoing study.

Conflicts of Interest

The authors declare that they have no conflicts of interest.

References

- [1] G.. Zhou, *Mechanism of Using Liquid-State Carbon Dioxide against Fire and its Key Techniques Development and Application*, Xi'an University of Science and Technology, Xi'an,China, 2019.
- [2] G.. Li, *Study on Spontaneous Coal Combustion Law and Key Prevention Technology in Goaf under Gas Drainage Condition*, Shandong University of Science and Technology, Qingdao,-China, 2019.
- [3] X.. Huang, *Research on Fire Control Technology of Residual Pillar Mining with Spontaneous Combustion in Mine*, China University of Mining and Technology, Beijing,China, 2015.
- [4] Y.. Wang, *Research on Prevention and Treatment Technology of Spontaneous Combustion in Goaf of Close-Distance Coal Seams*, China University of Mining and Technology, Beijing,China, 2015.
- [5] H. Fujitsuka, R. Ashida, M. Kawase, and K. Miura, "Examination of low-temperature oxidation of low-rank coals, aiming at understanding their self-ignition tendency," *Energy and Fuels*, vol. 28, no. 4, pp. 2402–2407, 2014.
- [6] Y. Song, B. Jiang, and M. Qu, "Molecular dynamic simulation of self- and transport diffusion for CO₂/CH₄/N₂ in low-rank coal vitrinite," *Energy and Fuels*, vol. 32, no. 3, pp. 3085–3096, 2018.
- [7] Y. Song, B. Jiang, J. P. Mathews, G. Yan, and F. Li, "Structural transformations and hydrocarbon generation of low-rank coal (vitrinite) during slow heating pyrolysis," *Fuel Processing Technology*, vol. 167, no. 4, pp. 535–544, 2017.
- [8] S. Sun, P. He, G. Wang et al., "Shape characterization methods of irregular cavity using Fourier analysis in tunnel," *Mathematics and Computers in Simulation*, vol. 187, pp. 191–214, 2021.
- [9] R.-L. Du, K. Wu, D.-A. Xu, C.-Y. Chao, L. Zhang, and X.-D. Du, "A modified Arrhenius equation to predict the reaction rate constant of Anyuan pulverized-coal pyrolysis at different heating rates," *Fuel Processing Technology*, vol. 148, pp. 295–301, 2016.
- [10] J. Li, Q. Huang, G. Wang, E. Wang, S. Ju, and C. Qin, "Experimental study of effect of slickwater fracturing on coal pore structure and methane adsorption," *Energy*, vol. 239, Article ID 122421, 2022.
- [11] T. Xu, D. Wang, H. Xin, and X. Qi, "Experimental study on the temperature rising characteristic of spontaneous combustion of coal," *Journal of Mining & Safety Engineering*, vol. 29, no. 4, pp. 575–580, 2012.
- [12] J. Deng, J. Zhao, Y. Zhang, and R. Geng, "Study on spontaneous coal combustion characteristic temperature of growth rate analysis," *Procedia Engineering*, vol. 84, pp. 796–805, 2014.
- [13] X. Chen, X. Yi, and J. Deng, "Experiment study of characteristic self-heating intensity of coal," *Journal of China Coal Society*, vol. 5, p. 017, 2015.
- [14] J. Deng, J. Zhao, and Y. Zhang, "Micro-characteristics of spontaneous combustion of second oxidation with different rank coals," *Journal of China Coal Society*, vol. 41, no. 5, pp. 1167–1172, 2016.
- [15] H. Usui and S. Ishikawa, "The evaluation of spontaneous combustion characteristics and properties of raw and upgraded Indonesian low rank coals," *Coal Preparation*, vol. 22, pp. 81–91, 2002.
- [16] J. Deng, Q. Li, X. Yang, and S. Min, "Experimental study on the thermal properties of coal during pyrolysis, oxidation, and re-oxidation," *Applied Thermal Engineering*, vol. 22, pp. 81–91, 2016.
- [17] X. Li, *Experimental Study on Characteristic Parameters of Spontaneous Combustion of Soaked and Air-Dried Coal*, China University of Mining and Technology, Xuzhou,China, 2014.
- [18] T. Jia, S. Wang, and H. Yu, "Experiments on the precipitation and oxidation characteristics of alkanes in spontaneous combustion of coal," *Journal of Liaoning Technical University*, vol. 31, no. 06, pp. 830–833, 2012.
- [19] M. Wang, Q. Li, and F. Meng, "Study on comprehensive fire prevention technology for goaf during the stopping period of medium-and-thick coal seam," *China Coal*, vol. 47, no. 07, pp. 39–45, 2021.
- [20] K. Jiang, Y. Wang, and G. Reng, "Study on the optimization simulation and application of technical parameters of CO₂ injection for fire prevention in goaf in 8059 working face of Yaoqiao Coal Mine," *Mining Safety & Environmental Protection*, vol. 48, no. 03, pp. 74–78+84, 2021.
- [21] J. Si, J. Zhang, and G. Chen, "Experimental study on the coexistent characteristics of both gas drainage and spontaneous coal combustion in goaf," *Journal of North China Institute of Science and Technology*, vol. 16, no. 04, pp. 1–5, 2019.
- [22] W. Cui, Q. Meng, Q. Feng, L. Zhou, Y. Cui, and W. Li, "Occurrence and release of cadmium, chromium, and lead from stone coal combustion," *International Journal of Coal Science & Technology*, vol. 06, no. 04, pp. 586–594, 2019.
- [23] Z. Li, H. Jia, Q. Bi, Y. Wen, and D. Wang, "Study on relevance between gas source strength and spontaneous combustion in goaf of top coal caving," *Journal of China Coal Society*, vol. 37, no. s1, pp. 120–125, 2012.
- [24] M. Więckowski, N. Howaniec, and S. Adam, "Effect of flow rates of gases flowing through a coal bed during coal heating and cooling on concentrations of gases emitted and fire hazard assessment," *International Journal of Coal Science & Technology*, vol. 07, no. 01, pp. 107–121, 2020.
- [25] B. Taraba and Z. Michalec, "Effect of longwall face advance rate on spontaneous heating process in the gob area - CFD modelling," *Fuel*, vol. 90, no. 8, pp. 2790–2797, 2011.
- [26] J. Li, Q. Huang, G. Wang, and E. Wang, "Influence of active water on gas sorption and pore structure of coal," *Fuel*, vol. 239, Article ID 122400, 2022.
- [27] C. Fan, L. Yang, G. Wang, Q. Huang, X. Fu, and H. Wen, "Investigation on coal skeleton deformation in CO₂ injection enhanced CH₄ drainage from underground coal seam," *Frontiers of Earth Science*, vol. 09, pp. 01–11, 2021.
- [28] C. Fan, S. Li, D. Elsworth, J. Han, and Z. Yang, "Experimental investigation on dynamic strength and energy dissipation characteristics of gas outburst prone coal," *Energy Science & Engineering*, vol. 08, no. 04, pp. 1015–1028, 2020.
- [29] Z. Zhou, Z. Li, C. Gao et al., "Peridynamic micro-elastoplastic constitutive model and its application in the failure analysis of rock masses," *Computers and Geotechnics*, vol. 132, 2021.
- [30] A. Liu, S. Liu, G. Wang, and D. Elsworth, "Continuous compaction and permeability evolution in longwall gob materials," *Rock Mechanics and Rock Engineering*, vol. 53, no. 12, pp. 5489–5510, 2020.
- [31] A. Liu, S. Liu, G. Wang, and D. Elsworth, "Predicting fugitive gas emissions from gob-to-face in longwall coal mines: coupled analytical and numerical modeling," *International Journal of Heat and Mass Transfer*, vol. 150, pp. 119–392, 2020.

Research Article

Laboratory Study on Changes in Gas Desorption Properties of Anthracite after Cyclic Loading

Tie Li ^{1,2}, Dong Wang,^{1,2,3,4} Mei-Hua Liu,^{3,4} Liang Chen ⁵, and Hao Liu ⁶

¹State Key Laboratory of High-Efficiency Mining and Safety of Metal Mines, Ministry of Education, University of Science and Technology Beijing, Beijing 100083, China

²School of Civil and Resource Engineering, University of Science and Technology Beijing, Beijing 100083, China

³China Coal Research Institute, Beijing 100013, China

⁴National Key Lab of Coal High Efficient Mining and Clean Utilization (China Coal Research Institute), Beijing 100013, China

⁵School of Safety Engineering, North China Institute of Science and Technology, Beijing 101601, China

⁶College of Aerospace Engineering, Chongqing University, Chongqing 400044, China

Correspondence should be addressed to Liang Chen; chenliangncist@21cn.com and Hao Liu; liuhaocqu@cqu.edu.cn

Received 3 July 2021; Revised 18 October 2021; Accepted 15 November 2021; Published 26 December 2021

Academic Editor: Dawei Yin

Copyright © 2021 Tie Li et al. This is an open access article distributed under the Creative Commons Attribution License, which permits unrestricted use, distribution, and reproduction in any medium, provided the original work is properly cited.

Coal mass is subjected to cyclic loading during pulsating hydraulic fracturing (PHF), and changes in its gas desorption properties affect gas drainage. Therefore, it is of great importance to correctly understand the influences of cyclic loading on the gas desorption properties of coal mass. Firstly, loading tests with different frequencies and amplitudes were performed on anthracite from Qinshui Basin (Shanxi Province, China) using a fatigue testing machine. Secondly, gas desorption tests were performed to determine the associated curves for each test group at different equilibrium pressures, and the initial desorption capacity and diffusion coefficient of the gas were calculated. Finally, the influence of different loading conditions on the gas desorption laws were analyzed. The test results demonstrate that a greater loading frequency increases the ratio of the initial desorption capacity so that the desorption rate of coal samples is higher, and the gas desorption properties become increasingly better in the initial stage. However, variations in the amplitude have minimal impact on the ratio of the initial desorption capacity. When the amplitude is too large in the initial stage, the diffusion coefficient decreases and the gas desorption properties worsen. In addition, the above test results are used to discuss the selection of the amplitude and frequency in the PHF process from a macroperspective. The contained research results provide an important theoretical basis for the field application of PHF technologies in coal mines.

1. Introduction

Coal and gas outburst are one of the major disasters that significantly threatens safe production in coal mines, with China being one of the countries with the most serious coal and gas outburst disasters in the world [1–3]. To date, with increased mining depths and intensities in coal mines, hazard factors such as high *in situ* stresses, gas pressures, and gas contents readily induce rock and gas dynamic disasters, which further affects safe production in coal mines and threatens the lives of underground workers [4–7]. After many field practices, it has been proven that gas drainage is an effective means to prevent and control gas disasters in

coal mines and to develop and utilize gas in coal seams [8–10].

The permeability of coal seams is a key parameter that influences gas drainage effects [11, 12]. However, the permeability of coal seams in China is generally low, which mostly ranges from 10^{-4} to 10^{-3} mD at 3 to 4 orders of magnitude lower than those in the United States and Australia [13–15]. Existing studies show that technologies such as hydraulic slotting, fracturing, and flushing can effectively increase the permeability of coal seams, which improves the gas drainage effects [16–22]. Nevertheless, in recent years, it has been found that the engineering application of traditional hydraulic technologies requires the

consumption of significant water resources to achieve the desired effects [19, 23]. Moreover, it is difficult to apply such technologies in areas with water shortages [24, 25]. To solve this problem, Li et al. [26] proposed the pulsating hydraulic fracturing (PHF) approach based on traditional hydraulic fracturing technologies. This method continuously injects pulsating water with a certain frequency into coal seams and produces a cyclic loading, unloading, and loading effect by controlling the pulsating water pressure. With an increasing number of cycles, fatigue failure gradually occurs in coal mass and some new pores and fractures are formed. These coalesce with preexisting pores to form an interconnected fracture network, which provides channels for gas migration and greatly improves the permeability of coal seams [27]. Xu et al. [28] and Ni et al. [29] separately performed PHF tests in Daxing Coal Mine in Tiefsa coalfield, Liaoning Province, and in Changping Coal Mine in Qinshui coalfield, Shanxi Province, China. The field test results showed that the technology can safely and reliably improve gas drainage effects.

During gas drainage from coal seams, gas is first desorbed from the coal matrix and diffused into fractures before flowing into drainage boreholes under seepage effects [30, 31]. Gas desorption is another important factor that impacts drainage effects. If coal mass has a strong gas desorption capacity, coalbed methane (CBM) adsorbed at the inner surface of pores in the coal matrix changes from an adsorbed state to a free state as much as possible, and the ability of CBM diffusion from the matrix and micropores to the fractures is improved [32]. Su et al. [33] demonstrated that pore structures in the coal mass significantly influence gas desorption properties. In the PHF process, pore structures in the coal matrix are likely to change to some extent under cyclic loading. Xie *et al.* [34] also proved such a perspective as they compared and analyzed pore structures in coal mass before and after PHF using a scanning electron microscope and found the preexisting pores after PHF, which change from small to large. However, the effects of cyclic loading on gas desorption properties have been rarely investigated to date. Therefore, to further understand the dynamics of gas migration in PHF processes, it is of great scientific importance to study the change laws of the desorption properties in coal mass under cyclic loading.

Based on the above research status, loading tests with different frequencies and amplitudes were performed on anthracite from Qinshui Basin, Shanxi Province, China, by utilizing a fatigue testing machine. Furthermore, gas desorption curves for each test group at different equilibrium pressures were obtained through gas desorption tests, and the initial desorption capacity and diffusion coefficient of the gas were calculated. Finally, this study analyzed the effects of different loading conditions on gas desorption laws and provides a discussion of the selection of the amplitude and frequency in the PHF process from a macroperspective. Therefore, the research results offer an important theoretical basis for field applications of PHF technologies in coal mines.

2. Materials and Methods

2.1. Coal Sample Preparation. Anthracite from the Qinshui Basin, Shanxi Province, China, was used for the coal samples in the tests. The coal samples were collected from a freshly exposed working face underground before being sealed and packed immediately and sent to the laboratory as fast as possible to prevent oxidation. The basic properties of the coal samples are shown in Table 1.

This study performed cyclic loading and methane desorption tests after processing the crushed coal samples into briquettes because the anisotropy of the coal sample could affect the test results. The briquettes were processed according to the following two primary steps:

- (1) Preparation of pulverized coal: The coal blocks were ground into small powder particles using a crusher and a grinder and were screened repeatedly with standard sieves of 0.2 and 0.25 mm. Thus, pulverized coal particles with particle sizes of 0.2–0.25 mm were obtained.
- (2) Compression molding: Pulverized coal of 200 g was placed into a mold with a diameter of 50 mm and pressed for 20 min to shape the sample with a material testing machine at 200 t under a molding pressure of 100 MPa. The pressure was increased to a preset value within 10 min at a loading speed of 20 kN/min. The deviation in pressures caused the final molding pressure to be 197 kN.

2.2. Cyclic Loading Tests. To study the influences of cyclic loading with different frequencies and amplitudes on the gas desorption properties in anthracite, this research designed seven groups of loading conditions, as shown in Table 2.

During cyclic loading, the specimens were molded under pressure for 20 min together with the mold and were placed on the fatigue testing machine (Figure 1). Sine waves were applied on the coal samples for 6 h in total following the loading conditions in Table 2. After loading, the mold and specimen were removed, and the mold was opened with a wrench to retrieve the final specimen.

This paper mainly analyzes the effect of loading frequency and loading amplitude on the coal desorption performance. The loading frequencies were set to 4, 7, and 10 Hz, and the loading amplitudes were set to 10–20, 12–18, and 14–16 MPa. For each experimental condition, three desorption tests were performed at different equilibrium pressures (0.5, 1, 0, and 1.5 MPa).

2.3. Gas Desorption Tests. In accordance with the Determination Method of Methane Adsorption Capacity in Coal (MT/T752-2004), the steps for the desorption tests are shown as follows:

- (1) Loading samples: The coal samples that were subjected to cyclic loading were crushed with a hammer to obtain particles sized at 1–3 mm after screening.

TABLE 1: Basic properties of the coal samples.

Property	Type	Proximate analysis (wt.%)		
		M_{ad}	A_{ad}	V_{daf}
Value	Anthracite coal	1.89	8.59	9.41

M_{ad} , moisture content; A_{ad} , ash yield; V_{daf} , volatile matter.

TABLE 2: Loading conditions for cyclic loading tests.

Test number	Test condition		Loading time (h)
	Loading frequency (Hz)	Amplitude of loading pressure (MPa)	
1	10		
2	7	12–18	
3	4		
4	7	10–20	6
5	7	14–16	
6	—	15	
7	—	—	—

Notes: Group Nos. 1–5 are the test groups that change the frequency or amplitude alone; group No. 6 is the control group with a constant frequency and amplitude; group No. 7 represents the blank control group without cyclic fatigue loading.

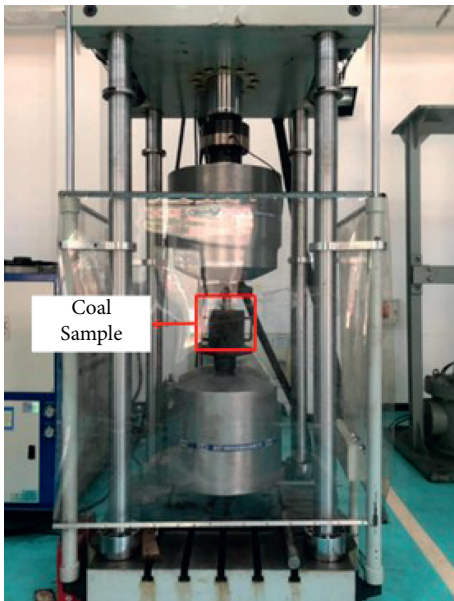


FIGURE 1: Fatigue testing machine.

Coal samples of 100 g in each test group were placed into numbered coal sample tanks.

- (2) Gas filling and leakage detection: High-purity methane was filled to the three preset pressures of 0.5, 1.0, and 1.5 MPa (pressure for adsorption equilibrium in the stable state) for each coal sample tank. The coal sample tanks were then placed into water to check for leakage. If there were no bubbles, the tank was qualified; otherwise, the tank was tightened or its sealing rings were replaced.
- (3) Equilibrium adsorption: The qualified coal sample tanks after leak detection were placed in a constant temperature water bath at 30°C for adsorption equilibrium for more than 24 h. The measured gas

pressures, room temperatures, and atmospheric pressures of the correspondingly numbered coal sample tanks were recorded.

- (4) Desorption tests: The coal sample tank valve was opened rapidly. When the pressure gauge dropped to zero, the tank was rapidly connected to an electronic flowmeter interfaced with a computer to constantly record the gas desorption capacities at different moments within 2 h. After 2 h of desorption, the valve of the coal sample tank was quickly tightened.
- (5) Laboratory test results under the pressure of adsorption equilibrium were obtained by repeating steps (1)–(4).

After completing the desorption tests, the final obtained desorption capacity was converted into a volume under standard conditions as

$$Q_t = \frac{273.15}{101325(273.15 + t_w)} * (P_{atm} - 9.81h_w - P^0) * Q'_t, \quad (1)$$

where Q_t , Q'_t , and t_w represent the volume (mL) in the standard state converted from the total gas desorption capacity, total gas desorption capacity (mL) measured during the tests, and room temperature (°C) in the test, respectively; and P_{atm} , h_w , and P^0 indicate the atmospheric pressure (Pa) in the laboratory, height (mm) of a liquid column in the apparatus for desorption when reading data, and the saturated steam pressure (Pa) at the temperature t_w , respectively.

3. Results and Discussion

3.1. Analysis on Characteristics of Desorption Curves at Different Equilibrium Pressures. Figures 2 and 3 show the desorption curves of the briquette samples at the select equilibrium pressures (0.5, 1.0, and 1.5 MPa) under different loading conditions. Because the production process of

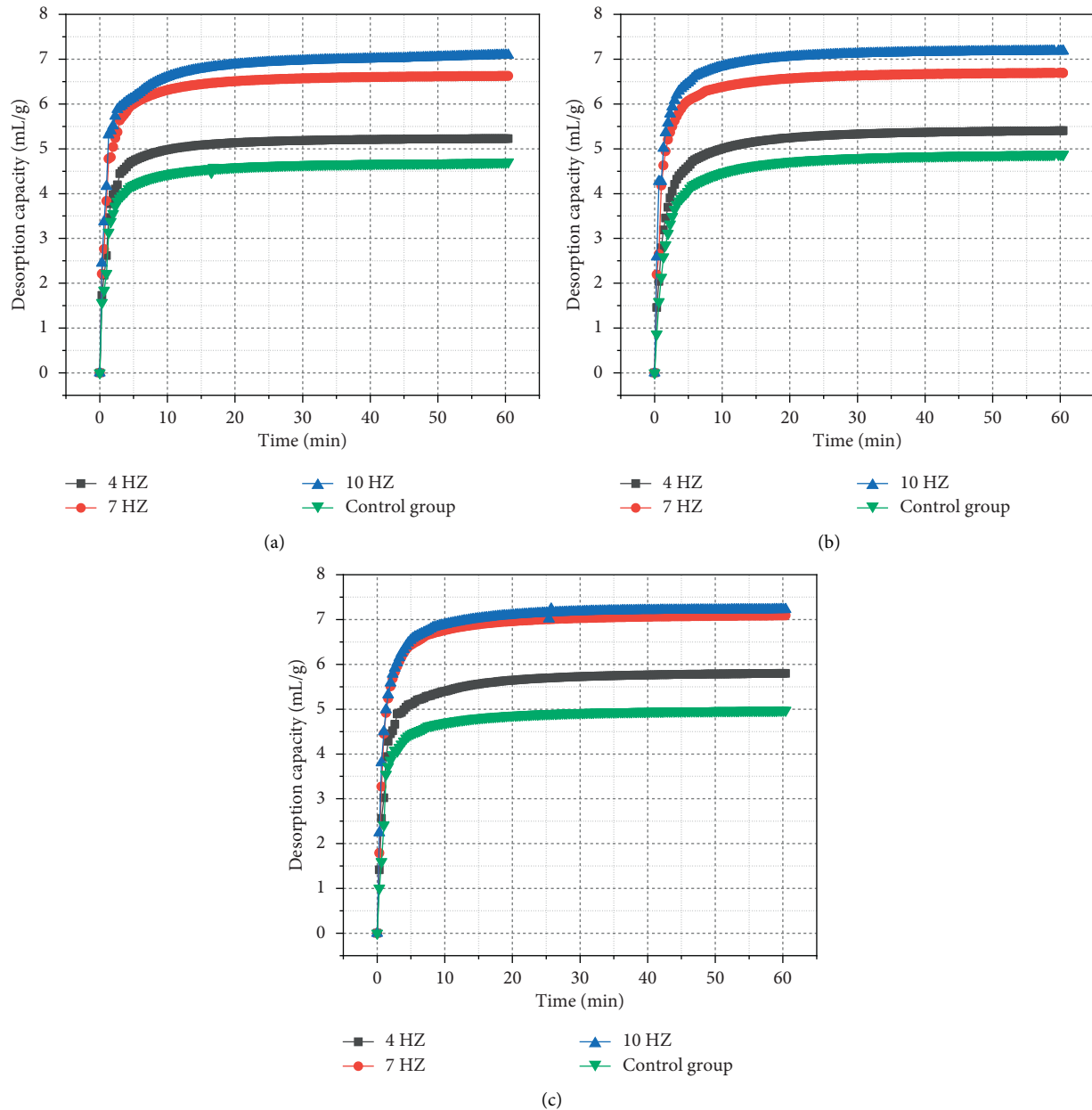


FIGURE 2: Desorption curves of the samples under different loading frequencies. (a) Equilibrium pressure of 0.5 MPa. (b) Equilibrium pressure of 1.0 MPa. (c) Equilibrium pressure of 1.5 MPa.

briquettes is different from that of common briquettes, the adsorption curves have certain differences from those of most coal mass analyses, but the general laws that govern this process are similar. The trends of the desorption curves for briquettes under different loading conditions are consistent. With an increasing desorption time, the desorption capacity from the briquette samples continuously increases and the initial desorption rate is rapid. After passing the early growth stage, the desorption rate drops sharply after 10 min and then becomes gentler. A faster initial gas desorption rate gives a quicker desorption rate attenuation. This is because when a coal sample tank is opened, the gas equilibrium state with a high concentration in the coal sample tank is broken

instantly, and gas is desorbed from the adsorbed state. A higher equilibrium pressure gives a larger gas desorption capacity. However, due to the samples used in the tests, the curves are nearly flat in the later stage and the desorption capacities within 60 min are not significantly different at various equilibrium pressures.

Comparing the curves in Figures 2 and 3 indicates that the desorption capacities of the samples within 60 min are different for the various loading frequencies and amplitudes. As the frequency increases, the desorption capacity within 60 min rises slightly with an obvious difference. However, the amplitude has little influence and the desorption capacity shows a small difference under various amplitudes (except

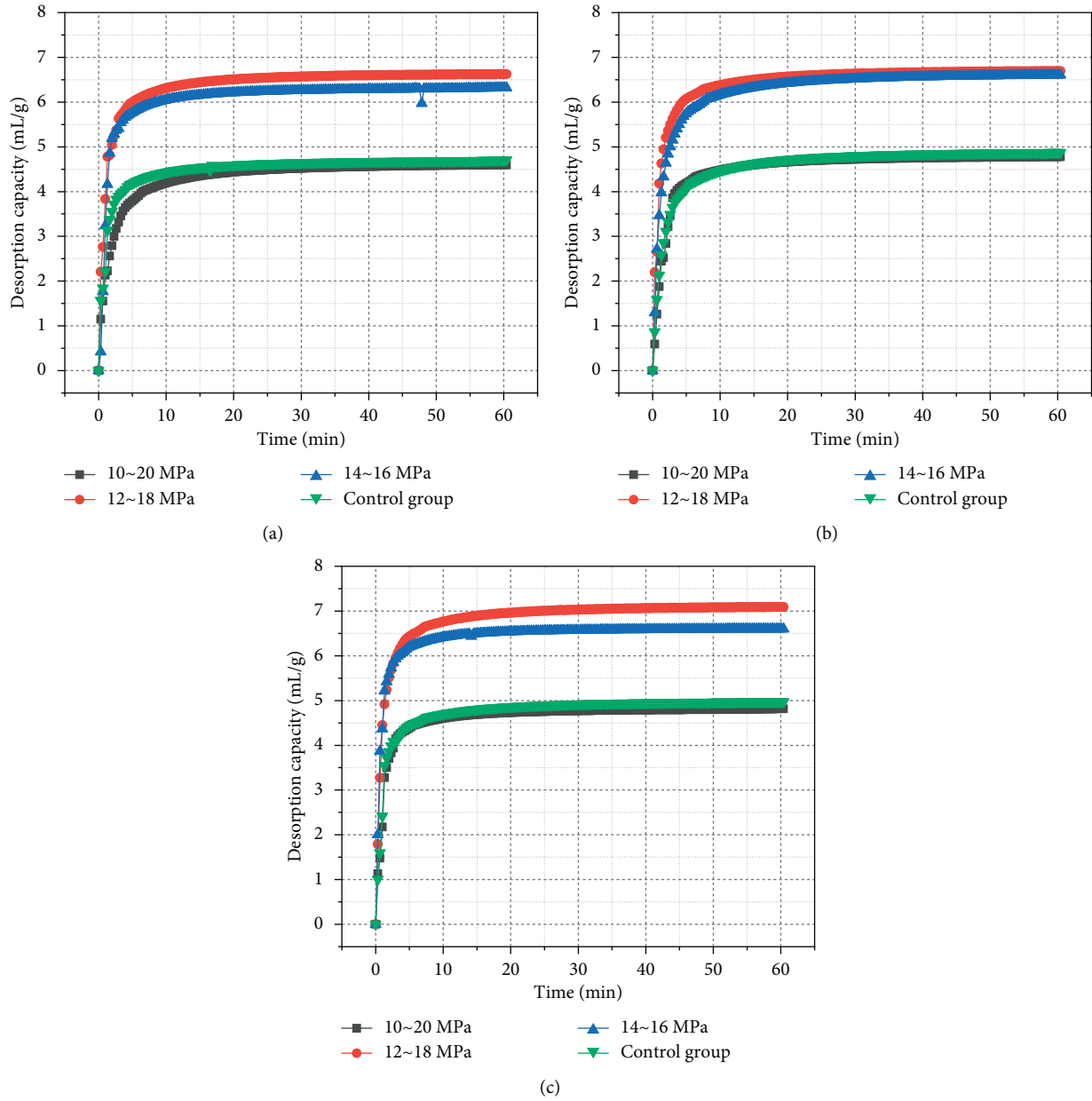


FIGURE 3: Desorption curves of the samples under different loading amplitudes. (a) Equilibrium pressure of 0.5 MPa. (b) Equilibrium pressure of 1.0 MPa. (c) Equilibrium pressure of 1.5 MPa.

for the test group under the amplitude of 10–20 MPa). After desorption on the pore surface, the adsorbed gas in the coal needs to enter the pore and fissure system of the coal body through diffusion, which then flows to the drainage hole via seepage. Therefore, the gas desorption characteristics significantly impact the gas drainage effect of the coal seam, which is discussed in Section 3.4.

3.2. Analysis on the Effects of Loading Frequency for Gas Desorption Parameters. The gas desorption curves in Section 3.1 indicate that the associated process in coal mass has a fast initial gas desorption that then attenuates quickly. Therefore, it is important to study the initial desorption capacity and

diffusion coefficient. Combining pore volumes in each stage with the initial gas desorption capacity and diffusion coefficient allows studying the influences of a changing loading frequency on the gas desorption parameters. Taking the desorption capacity within 1 min in the early stage in the test as the initial desorption capacity allows investigating the relationship between the initial desorption rate and the characteristics of pores in the coal mass. The statistical results of the desorption capacities at different equilibrium pressures in each test group are given in Table 3.

Table 3 indicates that changes in the loading conditions influence the Q_1/Q_{60} value. With a greater loading frequency, the ratio of the cumulative desorption capacity within 1 min to that within 60 min increases. The Q_1/Q_{60}

TABLE 3: Cumulative desorption capacity from the briquettes under different loading frequencies.

Loading conditions		Equilibrium pressure (MPa)	Desorption capacity within 1 min ($Q_1/\text{mL}\cdot\text{g}^{-1}$)	Desorption capacity within 60 min ($Q_{60}/\text{mL}\cdot\text{g}^{-1}$)	Q_1/Q_{60} (%)
Frequency (Hz)	Amplitude (MPa)				
4	12–18	0.5	2.62	5.23	50.07
7			3.83	6.62	57.90
10			4.16	7.09	58.70
—	15		2.22	4.70	47.18
4	12–18	1.0	2.79	5.40	51.65
7			4.18	6.69	62.48
10			4.27	7.18	59.48
—	15		2.13	4.87	43.77
4	12–18	1.5	3.02	5.80	52.10
7			4.24	6.75	62.78
10			4.50	7.22	62.27
—	15		2.41	4.97	48.56

values in the test groups under the frequencies of 4 and 7 Hz are 50.07–52.1% and 57.90–65.78%, respectively. The Q_1/Q_{60} value for the test group under 10 Hz is slightly different from that for the test group under 7 Hz, which ranges from 58.7 to 62.27%. However, the Q_1/Q_{60} value is in the range of 43.7–48.56% in the control group. Loading sine waves with different frequencies increases the gas desorption capacity by 16–34% in the early stage. The greater loading frequency (namely, the greater volume and specific surface area of pores) increases the ratio of the initial desorption capacity so that the desorption rate of the samples is larger. In addition, a greater equilibrium pressure causes a larger Q_1/Q_{60} value. The increased ratio of the initial desorption capacity indicates that, in the initial stage, the desorption capacity is large and the desorption rate is greater.

The initial gas desorption capacity is calculated based on the relational expression between the initial gas diffusion coefficient and the square root of time proposed by Barrer [35] as

$$Q_i = A\sqrt{t}, \quad (2)$$

where Q_i , A , and t represent the initial gas desorption capacity, initial gas diffusion coefficient, and desorption time, respectively. In the test, gas desorption data within 2.64 min were used as the initial gas desorption capacity and the square root of time was regarded as the abscissa. Thus, the adsorption-desorption fit curves of the briquette samples at the selected equilibrium pressures (0.5, 1.0, and 1.5 MPa) under different loading frequencies are drawn, as shown in Figure 4. The fitting results are summarized in Table 4.

The fitting results indicate the curves have high fitting correlations with an R^2 coefficient that reaches 0.98. The gas diffusion coefficient in the early stage is correlated with the pore characteristics in the coal samples, equilibrium pressure, and final gas desorption capacity. With a greater loading frequency, the gas diffusion coefficient gradually increases in the early stage. The diffusion coefficients in the test groups at frequencies of 4, 7, and 10 Hz are 2.6160–3.0828, 3.6011–3.7156, and 3.9855–4.0510, respectively, in the early stage, in which the maximum value is found in the test group under a frequency of 10 Hz. In the

control group under loading with a stable pressure, the diffusion coefficient ranges from 2.1588 to 2.6301. Applying sine waves with different frequencies increases the diffusion coefficient by 12–60% in the early stage, indicating that, with a larger loading frequency, the gas desorption properties become increasingly better in the early stage.

3.3. Analysis on Influences of Loading Amplitude on Gas Desorption Parameters. The data for the cumulative desorption capacities within 1 and 60 min when changing the loading amplitude are shown in Table 5.

Amplitude changes have minimal influence on the ratio of the initial desorption capacity. The Q_1/Q_{60} value is maximized and reaches 57.90–62.78% in the test group under an amplitude of 12–18 MPa, while that in the test group under an amplitude of 14–16 MPa is approximately 52% at the equilibrium pressures of 0.5 and 1.0 MPa. However, the Q_1/Q_{60} value reaches 66.17% at the equilibrium pressure of 1.5 MPa. Compared with the control group (43.77–48.56%), the Q_1/Q_{60} value increases by approximately 32%. The Q_1/Q_{60} value is the minimum in the test group under an amplitude of 10–20 MPa, which is the only test group with a value smaller than the control group at around 93% of the control group. The adsorption-desorption fitting curves of the briquette samples at the selected equilibrium pressures (0.5, 1.0, and 1.5 MPa) under different loading amplitudes are shown in Figure 5. A statistical analysis of fitting results is demonstrated in Table 6. The fitting results for each curve are highly linearly correlated and with an R^2 coefficient above 0.97.

With a decreasing loading amplitude, the gas diffusion coefficient gradually increases in the early stage. The diffusion coefficients in the test groups under the amplitudes of 14–16, 12–18, and 10–20 MPa are 3.2429–4.0132, 3.6011–3.7156, and 1.9808–2.5511 MPa, respectively. Compared with the effects of the loading frequency, changes in the loading amplitude lead to small changes in the diffusion coefficient. Compared with the diffusion coefficient in the control group, those in the test groups with amplitudes of 12–18 and 14–16 MPa increase by

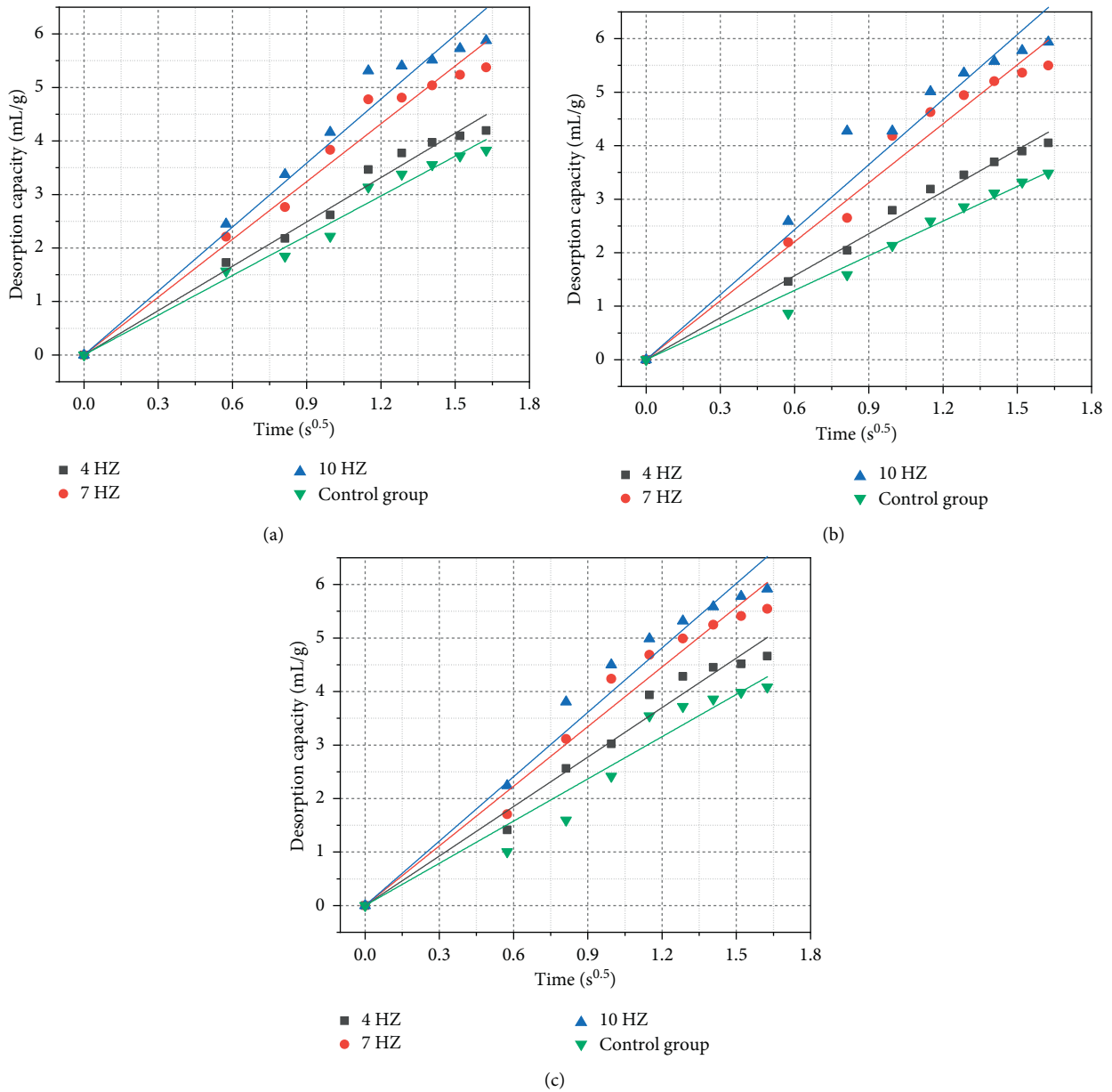


FIGURE 4: Fit curves for the diffusion coefficient of the samples in the early stage under different loading frequencies. (a) Equilibrium pressure of 0.5 MPa. (b) Equilibrium pressure of 1.0 MPa. (c) Equilibrium pressure of 1.5 MPa.

TABLE 4: Fit results for the relationship between the desorption capacity of the briquette samples within 2.64 min and the square root of time under different loading frequencies.

Loading conditions		0.5 MPa		1.0 MPa		1.5 MPa	
Frequency (Hz)	Amplitude (MPa)	A_1	R^2	A_2	R^2	A_3	R^2
4	12-18	2.7635	0.9969	2.6160	0.9984	3.0828	0.9951
7		3.6011	0.9946	3.6742	0.9945	3.7156	0.9939
10		3.9855	0.9938	4.0510	0.9908	4.0128	0.9938
—	15	2.4768	0.9962	2.1588	0.9965	2.6301	0.9875

TABLE 5: Cumulative desorption capacities of briquettes under different loading amplitudes.

Loading conditions Frequency (Hz)	Amplitude (MPa)	Equilibrium pressure (MPa)	Desorption capacity within 1 min ($Q_1/\text{mL}\cdot\text{g}^{-1}$)	Desorption capacity within 60 min $Q_{60}/\text{mL}\cdot\text{g}^{-1}$	Q_1/Q_{60} (%)
7	10~20	0.5	2.13	4.60	46.37
	12~18		3.83	6.62	57.90
	14~16		3.24	6.32	51.19
	15		2.22	4.70	47.18
7	10~20	1.0	1.88	4.78	39.27
	12~18		4.18	6.69	62.48
	14~16		3.46	6.60	52.43
	15		2.13	4.87	43.77
7	10~20	1.5	2.22	4.91	45.16
	12~18		4.24	6.75	62.78
	14~16		4.37	6.60	66.17
	15		2.41	4.97	48.56

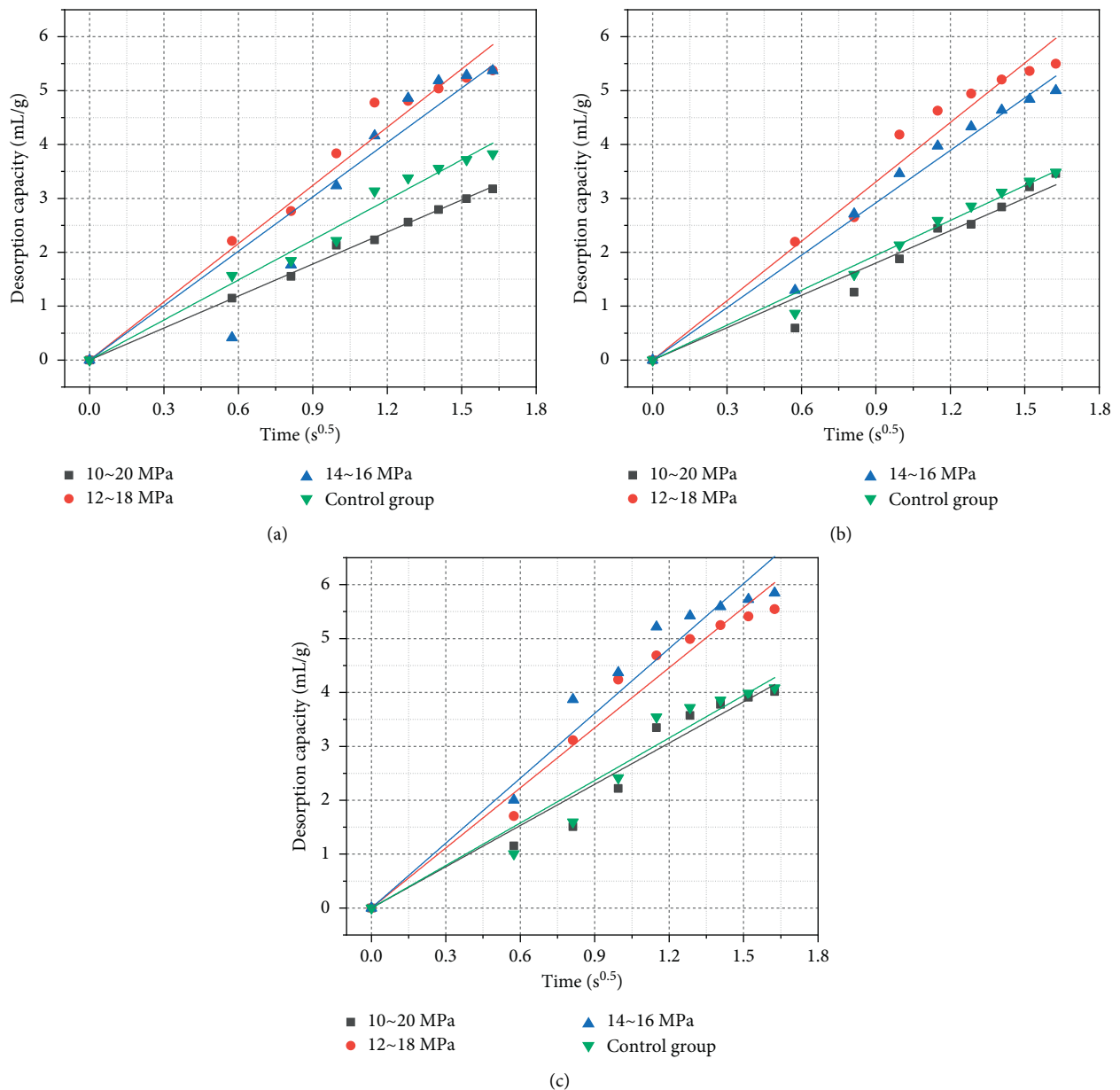


FIGURE 5: Fitting curves of the diffusion coefficients of the samples in the early stage under different loading amplitudes. (a) Equilibrium pressure of 0.5 MPa. (b) Equilibrium pressure of 1.0 MPa. (c) Equilibrium pressure of 1.5 MPa.

TABLE 6: Fitting results for the relationship between the desorption capacity of the briquette samples within 2.5 min and the square root of time under different loading conditions.

Loading conditions		0.5 MPa		1.0 MPa		1.5 MPa	
Frequency (Hz)	Amplitude (MPa)	A_1	R^2	A_2	R^2	A_3	R^2
7	10–20	1.9808	0.9993	2.0010	0.9884	2.5511	0.9894
	12–18	3.6011	0.9946	3.6742	0.9945	3.7156	0.9939
	14–16	3.3655	0.9721	3.2429	0.9956	4.0132	0.9915
—	15	2.4768	0.9962	2.1588	0.9965	2.6301	0.9875

36–45%, while that in the test group under an amplitude of 10–20 MPa is only approximately 0.8% of the control group. Applying sine waves with certain amplitudes can increase the gas diffusion coefficient in the early stage. However, when the amplitude is too large in the early stage, the diffusion coefficient is reduced and the gas desorption properties worsen.

3.4. Implications When Selecting Frequency and Amplitude during PHF. During PHF in underground coal mines, the ultimate goal is to improve the gas drainage [36, 37]. Research shows that, at larger frequencies, the gas desorption properties of the coal samples are increasingly enhanced. Therefore, after PHF, more adsorbed methane is converted into free molecules and diffuses into fractures. When there is more free methane in the fractures, the pressure gradient increases. According to Darcy's law, a larger pressure gradient inevitably increases the gas flow per unit time [38]. Therefore, more methane flows into the drainage boreholes. In addition, the results from Section 3.3 demonstrate that a greater loading amplitude can improve the gas desorption properties to a certain extent, but there is an optimum. In sum, in field construction, the PHF effects can be enhanced by increasing the frequency and adopting an optimal amplitude.

4. Conclusions

This study performed loading tests with different frequencies and amplitudes on anthracite from Qinshui Basin, Shanxi Province, using a fatigue testing machine. This research developed gas desorption curves in each test group at different equilibrium pressures through gas desorption tests and calculated the initial gas desorption capacity and diffusion coefficient. Finally, the influences of different loading conditions on the gas desorption laws were analyzed. The conclusions are drawn as follows:

- (1) Applying sine waves of different frequencies increases the gas desorption capacity by 16–34% in the early stage. A greater loading frequency increases the ratio of the initial desorption capacity so that the desorption rate of the samples is larger. The diffusion coefficient increases by 12–60% in the early stage, indicating the gas desorption properties become increasingly better with the loading frequency.
- (2) The influence laws of the changing amplitude on the ratio of the initial desorption capacity are minimal.

For the test groups under amplitudes of 12–18 and 14–16 MPa, a smaller frequency increases the Q_1/Q_{60} value by about 32%, while the Q_1/Q_{60} value in the test group under an amplitude of 10–20 MPa is only about 93% of the control group. Applying sine waves with certain amplitudes can increase the gas diffusion coefficient in the early stage. However, when the amplitude is too large, the diffusion coefficient reduces and the gas desorption properties worsen.

- (3) In the PHF process for underground coal mines, the fracturing effects can be enhanced by increasing the frequency. However, economic costs need to be considered when selecting the proper frequency. In addition, when the amplitude is 12–18 MPa, the gas diffusion coefficient is the largest in the early stage. Therefore, the amplitudes in this range are selected for PHF. The research results provide an important theoretical basis for the field applications of PHF technologies in coal mines. This paper mainly analyzed the effects of the loading frequency and amplitude on the gas desorption characteristics. The relationship between the loading frequency and balance force is not considered and will be addressed in future studies.

Data Availability

All the data, models, and codes generated or used during this study appear in the manuscript.

Conflicts of Interest

The authors declare that there are no conflicts of interest regarding the publication of this article.

Acknowledgments

This work was supported by the National Natural Science Foundation of China (Grant nos. 52074120 and 51674016) and the Fundamental Research Funds for the Central Universities (3142019005).

References

- [1] L. Qi, X. Tang, Z. Wang, and X. Peng, "Pore characterization of different types of coal from coal and gas outburst disaster sites using low temperature nitrogen adsorption approach," *International Journal of Mining Science and Technology*, vol. 27, no. 2, pp. 371–377, 2017.

- [2] J. Sobczyk, "A comparison of the influence of adsorbed gases on gas stresses leading to coal and gas outburst," *Fuel*, vol. 115, pp. 288–294, 2014.
- [3] Q. Zou, H. Liu, Y. Zhang, Q. Li, J. Fu, and Q. Hu, "Rationality evaluation of production deployment of outburst-prone coal mines: a case study of Nantong coal mine in Chongqing, China," *Safety Science*, vol. 122, Article ID 104515, 2020.
- [4] F. H. An and Y. P. Cheng, "An explanation of large-scale coal and gas outbursts in underground coal mines: the effect of low-permeability zones on abnormally abundant gas," *Natural Hazards and Earth System Sciences*, vol. 14, no. 8, pp. 2125–2132, 2014.
- [5] E. Su, Y. Liang, Q. Zou, M. Xu, and A. P. Sasmito, "Numerical analysis of permeability rebound and recovery during coalbed methane extraction: implications for CO₂ injection methods," *Process Safety and Environmental Protection*, vol. 149, pp. 93–104, 2021.
- [6] H. Liu, H. Liu, and Y. Cheng, "The elimination of coal and gas outburst disasters by ultrathin protective seam drilling combined with stress-relief gas drainage in Xinggong coal-field," *Journal of Natural Gas Science and Engineering*, vol. 21, pp. 837–844, 2014.
- [7] K. Jin, Y. Cheng, Q. Liu et al., "Experimental investigation of pore structure damage in pulverized coal: implications for methane adsorption and diffusion characteristics," *Energy and Fuels*, vol. 30, no. 12, Article ID 10383, 2016.
- [8] J. Dong, Y. Cheng, K. Jin et al., "Effects of diffusion and suction negative pressure on coalbed methane extraction and a new measure to increase the methane utilization rate," *Fuel*, vol. 197, pp. 70–81, 2017.
- [9] T. Liu, B. Lin, W. Yang, C. Zhai, and T. Liu, "Coal permeability evolution and gas migration under non-equilibrium state," *Transport in Porous Media*, vol. 118, no. 3, pp. 393–416, 2017.
- [10] E. Su, Y. Liang, Q. Zou, F. Niu, and L. Li, "Analysis of effects of CO₂ injection on coalbed permeability: implications for coal seam CO₂ sequestration," *Energy and Fuels*, vol. 33, no. 7, pp. 6606–6615, 2019.
- [11] Z. Pan and L. D. Connell, "Modelling permeability for coal reservoirs: a review of analytical models and testing data," *International Journal of Coal Geology*, vol. 92, pp. 1–44, 2012.
- [12] T. Xia, F. Zhou, J. Liu, S. Hu, and Y. Liu, "A fully coupled coal deformation and compositional flow model for the control of the pre-mining coal seam gas extraction," *International Journal of Rock Mechanics and Mining Sciences*, vol. 72, pp. 138–148, 2014.
- [13] T. Liu, B. Lin, and W. Yang, "Impact of matrix-fracture interactions on coal permeability: model development and analysis," *Fuel*, vol. 207, pp. 522–532, 2017.
- [14] Q. Liu, Y. Cheng, H. Zhou, P. Guo, F. An, and H. Chen, "A mathematical model of coupled gas flow and coal deformation with gas diffusion and klinkenberg effects," *Rock Mechanics and Rock Engineering*, vol. 48, no. 3, pp. 1163–1180, 2015.
- [15] E. Su, Y. Liang, X. Chang, Q. Zou, M. Xu, and A. P. Sasmito, "Effects of cyclic saturation of supercritical CO₂ on the pore structures and mechanical properties of bituminous coal: an experimental study," *Journal of CO₂ Utilization*, vol. 40, Article ID 101208, 2020.
- [16] Q. Zou, Q. Li, T. Liu, X. Li, and Y. Liang, "Peak strength property of the pre-cracked similar material: implications for the application of hydraulic slotting in ECBM," *Journal of Natural Gas Science and Engineering*, vol. 37, pp. 106–115, 2017.
- [17] Y. Zhao, B. Lin, T. Liu, Q. Li, and J. Kong, "Gas flow field evolution around hydraulic slotted borehole in anisotropic coal," *Journal of Natural Gas Science and Engineering*, vol. 58, pp. 189–200, 2018.
- [18] A. Abdollahipour, M. F. Marji, A. Y. Bafghi, and J. Gholamnejad, "DEM simulation of confining pressure effects on crack opening displacement in hydraulic fracturing," *International Journal of Mining Science and Technology*, vol. 26, no. 4, pp. 557–561, 2016.
- [19] Y. Lu, Z. Ge, F. Yang, B. Xia, and J. Tang, "Progress on the hydraulic measures for grid slotting and fracking to enhance coal seam permeability," *International Journal of Mining Science and Technology*, vol. 27, no. 5, pp. 867–871, 2017.
- [20] Y. Liang, Y. Cheng, Q. Zou, W. Wang, Y. Ma, and Q. Li, "Response characteristics of coal subjected to hydraulic fracturing: an evaluation based on real-time monitoring of borehole strain and acoustic emission," *Journal of Natural Gas Science and Engineering*, vol. 38, pp. 402–411, 2017.
- [21] J. Chen, X. Li, H. Cao, and L. Huang, "Experimental investigation of the influence of pulsating hydraulic fracturing on pre-existing fractures propagation in coal," *Journal of Petroleum Science and Engineering*, vol. 189, Article ID 107040, 2020.
- [22] J. A. Wang and H. D. Park, "Fluid permeability of sedimentary rocks in a complete stress-strain process," *Engineering Geology*, vol. 63, no. 3, pp. 291–300, 2002.
- [23] Y. Lu, X. Chen, J. Tang et al., "Relationship between pore structure and mechanical properties of shale on supercritical carbon dioxide saturation," *Energy*, vol. 172, pp. 270–285, 2019.
- [24] Z. Jiang, Q. Li, Q. Hu et al., "Underground microseismic monitoring of a hydraulic fracturing operation for CBM reservoirs in a coal mine," *Energy Science and Engineering*, vol. 7, no. 3, pp. 986–999, 2019.
- [25] Q. Zou, H. Liu, Z. Cheng, T. Zhang, and B. Lin, "Effect of slot inclination angle and borehole-slot ratio on mechanical property of pre-cracked coal: implications for ECBM recovery using hydraulic slotting," *Natural Resources Research*, vol. 29, 2019.
- [26] Q. Li, B. Lin, and C. Zhai, "The effect of pulse frequency on the fracture extension during hydraulic fracturing," *Journal of Natural Gas Science and Engineering*, vol. 21, pp. 296–303, 2014.
- [27] L. Chen, P. Li, G. Liu, W. Cheng, and Z. Liu, "Development of cement dust suppression technology during shotcrete in mine of China-A review," *Journal of Loss Prevention in the Process Industries*, vol. 55, pp. 232–242, 2018.
- [28] J. Xu, C. Zhai, and L. Qin, "Mechanism and application of pulse hydraulic fracturing in improving drainage of coalbed methane," *Journal of Natural Gas Science and Engineering*, vol. 40, pp. 79–90, 2017.
- [29] G. Ni, X. Hongchao, L. Zhao, Z. Lingxun, and N. Yunyun, "Improving the permeability of coal seam with pulsating hydraulic fracturing technique: a case study in Changping coal mine, China," *Process Safety and Environmental Protection*, vol. 117, pp. 565–572, 2018.
- [30] H. Liu, B. Lin, and C. Jiang, "A new method for determining coal seam permeability redistribution induced by roadway excavation and its applications," *Process Safety and Environmental Protection*, vol. 131, pp. 1–8, 2019.
- [31] H. Guo, Y. Cheng, L. Yuan, L. Wang, and H. Zhou, "Unsteady-state diffusion of gas in coals and its relationship with coal pore structure," *Energy and Fuels*, vol. 30, no. 9, pp. 7014–7024, 2016.

- [32] L. Si, Z. Li, Y. Yang, and R. Gao, "The stage evolution characteristics of gas transport during mine gas extraction: its application in borehole layout for improving gas production," *Fuel*, vol. 241, pp. 164–175, 2019.
- [33] E. Su, Y. Liang, and Q. Zou, "Structures and fractal characteristics of pores in long-flame coal after cyclical supercritical CO₂ treatment," *Fuel*, vol. 286, Article ID 119305, 2021.
- [34] X. Jingna, X. Jun, N. Guanhua, S. Rahman, S. Qian, and W. Hui, "Effects of pulse wave on the variation of coal pore structure in pulsating hydraulic fracturing process of coal seam," *Fuel*, vol. 264, Article ID 116906, 2020.
- [35] R. M. Barrer and D. E. W. Vaughan, "Sorption and diffusion of rare gases in heulandite and stilbite," *Surface Science*, vol. 14, no. 1, pp. 77–92, 1969.
- [36] M. Mastalerz and A. Drobnik, "Coalbed methane," in *Future Energy*, T. M. Letcher, Ed., , Elsevier, Amsterdam, Netherlands, 3rd edition, 2020.
- [37] J. Blunski, T. Ertekin, and J. Wang, "Hydraulic fracturing mechanisms in coal: a review," *International Journal of Oil, Gas and Coal Technology*, vol. 14, no. 3, pp. 247–263, 2017.
- [38] A. Mitra, S. Harpalani, and S. Liu, "Laboratory measurement and modeling of coal permeability with continued methane production: part 1-laboratory results," *Fuel*, vol. 94, pp. 110–116, 2012.

Research Article

Study on Gas Control Methods Optimization for Mining Safety

Liwen He ¹, Yingcheng Dai,¹ Sheng Xue ^{2,3}, Chunshan Zheng,^{2,3}
Baiqing Han,⁴ and Xin Guo ^{2,3}

¹College of Environment and Resources, Xiangtan University, Xiangtan 411100, China

²Institute of Energy, Hefei Comprehensive National Science Center, Hefei 230031, China

³School of Safety Science and Engineering, Anhui University of Science and Technology, Huainan 232001, China

⁴China National Coal Xinji Group Corporation, Huainan 232001, China

Correspondence should be addressed to Sheng Xue; sheng.xue@aust.edu.cn

Received 29 July 2021; Revised 27 August 2021; Accepted 16 November 2021; Published 21 December 2021

Academic Editor: Peng Liu

Copyright © 2021 Liwen He et al. This is an open access article distributed under the Creative Commons Attribution License, which permits unrestricted use, distribution, and reproduction in any medium, provided the original work is properly cited.

Effective gas control is of significance for safe efficient coal mining in Haizi Coal Mine and other mines with similar geological conditions. This study concentrates on gas control theories and techniques in multiple coal seams of Haizi Coal Mine (No. 7, No. 8, No. 9, and No. 10 coal seam from top to bottom). To minimize risk of high gas emission and outburst hazard, No. 10 seam was mined first as a protective seam prior to the mining of its overlying outburst-prone No. 7, No. 8, and No. 9 seam. Four gas drainage measures were determined for gas control, including cross-measure boreholes into overlying coal seams, surface goaf wells, roof boreholes, and roof gas drainage roadway. These gas control measures, if implemented through entire coal seam extraction, would be possibly uneconomic. An investigation was undertaken to analyze effects of those four measures on gas emission, methane concentration, and gas drainage quantity in No. 2 1024 mining panel of No. 10 seam. Results indicate that the highly expensive gas drainage measure of a roof roadway has poor drainage performance and could be effectively replaced by roof boreholes. When adopting the optimized combination of gas drainage measures, drainage efficiency of No. 7 seam, No. 8 seam, and No. 9 seam could reach 58.64% and decrease gas pressure to be below 0.74 MPa. Outcomes of this study could provide beneficial guidance not only for gas drainage design optimization in Haizi Coal Mine but also for other multiple-seam mines with similar mining and geological conditions, for increasing gas drainage efficiency and guaranteeing mining safety.

1. Introduction

Due to the specific conditions of energy demand in Chinese economic development, coal has been and will continue to be the dominant energy resource in China. Hence, safe production and sustainable development of coal industry are of significance. However, coal mine safety remains to be a key obstacle in mining activities. According to statistics, 3985 gas incidents occurred in Chinese coal mines in the period from 2001 to 2013 when coal industry developed rapidly [1]. Therefore, preventing the occurrence of gas disasters is of great necessity.

Most coal mines in China have multiple coal seams. To minimize the risk of high gas emission and coal and gas outburst, a less outburst-prone seam is often mined first as a protective seam prior to the mining of its overlying or

underlying seams. Meanwhile, these relieved overlying or underlying seams are called protected seam as these seams experience substantial stress relief and permeability enhancement which both could help preventing mining hazards [2]. This protective seam mining method has been widely applied and delivered large amount of benefits on guaranteeing mining safety [3, 4]. Gas drainage measures are always adopted in combination with this method. Popular gas drainage measures include surface gas wells, underground gas boreholes, and tunnels or combination of the above. Starting in the 1970s, Chinese coal mines adopted the protective mining method with various gas drainage measures depending on localized geological and mining conditions, e.g., cross-measure boreholes were used to drain gas from relieved protected seams in No. 4 Mine of Yangquan Coal Group in Shanxi Province, Wudanggou Coal Mine in

Inner Mongolia, and Dayong Coal Mine in Guizhou Province [5]. In Yutianbao Coal Mine of Nantong Mining Area and Xieqiao Coal Mine in Huainan City, the cross-measure borehole method in the intake airflow lane of mining panel is also adopted, in which the drilling-site construction is convenient and the maintenance time and workload of lane do not increase [6–11]. Moxinpo Coal Mine in Chongqing City and Luling Coal Mine in Anhui Province chose to drill drainage boreholes in the roadway located outside protective layer. This method is widely used for panel in coal seams of various dip angle and mining methods [12, 13].

Over the years, the protective mining method combined with various gas drainage measures has been studied and applied in various coal seam conditions [14–19]. In general, taking more comprehensive gas drainage measures could lead to better gas control. However, implementation of comprehensive gas drainage measures is quite expensive, particularly in current weak coal market. It is therefore important to optimize these gas drainage measures without compromising gas control effectiveness. Taking Haizi Coal Mine as an example, this study discusses on-site investigation results of optimization of gas drainage measures combined with the multiple-seam protective mining method, for providing references on conducting safe efficient gas drainage and coal mining in large amount of coal mines similar to Haizi Coal Mine.

2. Site Conditions

Haizi Coal Mine of Huaibei Mining Company is located about 40 km north of Huaibei City, Anhui Province, China (Figure 1). This mine adjoins another coal mine named Linhuan in the southeast (separated by a Fault) and is bounded by the Daluujia Fault in the west. Recoverable mining area is about 11 km long and 2.6 km wide, covering an area of approximately 26.7 km².

There are 10 coal seams in the mining area, numbered from top to bottom as No. 1 to No. 10 seam. Generalized stratigraphic column is shown in Figure 2. Four seams including No. 7 seam, No. 8 seam, No. 9 seam, and No. 10 seam are mainly extracted. Gas pressure of those four coal seams is 1.6 MPa, 0.8 MPa, 0.85 MPa, and 0.6 MPa, respectively. Gas contents of them are 12 m³/t, 8.7 m³/t, 9 m³/t, and 5 m³/t, respectively. The thickness of those four coal seams is 0.5 m, 1.1 m, 0.7 m, and 9 m, respectively.

Coal mine risk assessment shows that except for No. 10 seam, the other three extraction seams (No. 7 seam, No. 8 seam, and No. 9 seam) are both outburst-prone. No. 10 seam belongs to the igneous intrusion area, and it does not have outburst-prone. Therefore, in this multiple-seam mining, No. 10 seam is mined first as the protective seam, for decreasing risk of outburst and high gas emission during mining activities of its adjacent overlying seams.

This study concentrates on the No. 2 1024 panel of No. 10 seam. No. 2 1024 panel is located in the east wing of No. 2 102 Mining Area as shown in Figure 3. Its upper border is the goaf of No. 2 1022 panel, while its lower border is the planned No. 2 1026 panel. The eastern border is safety coal

pillar of No. 2 102 Mining Area, and the western border is nonrecoverable area of No. 2 102 Mining Area. Its elevation is between −593 m and −657 m. The panel is 550 m long and 185 m wide with an area of around 101750 m². Thickness of the coal seam is 2.7 m with an average dip angle of 20° in No. 2 1024 panel.

3. Gas Drainage Design of No. 2 1024 Panel

3.1. Design Principle. Protective seam mining is one of the most economic and effective method in mitigating coal and gas outburst risk of multiple coal seam group. Mining the protective No. 10 seam in Haizi Coal Mine will significantly affect the stress and gas conditions in protected overlying seams of No. 7, No. 8, and No. 9. As the protective seam being mined, three roof zones in vertical direction will be formed, namely, caved zone, fractured zone, and subsidence zone [20, 21]. Stress in the protected seams will decrease, fractures generate, and permeability increases, and finally gas desorbs and pressure drops. As a result, coal and gas outburst risk in protected seams is reduced, as shown in Figure 4 [19, 22, 23].

It should be noted that there is a hard igneous rock layer in the overlying strata of No.7 seam. This will prolong the subsiding time of overlying strata and the fracture closure time in the fractured zone. This extra time is good for gas drainage if drainage boreholes are in place prior to the extraction of protective No. 10 seam.

3.2. Gas Drainage Design. Effective gas drainage is essential to Haizi Coal Mine as a complex outburst-prone mine. Four gas drainage measures are initially designed for No. 2 1024 panel, including cross-measure boreholes into the protected seams, surface goaf wells, roof boreholes, and a roof gas drainage roadway. These methods are popularly used in coal mines. Detailed design of these measures is described below.

Cross-measure boreholes serve two purposes in Haizi Coal Mine. One is preventing excessive gas from adjacent seams into No. 2 1024 panel. Another one is draining gas released from overlying protected seams to reduce or eliminate the outburst risk. Figure 5 illustrates principle of gas emission in protected coal seams and gas extraction methods using cross-measure boreholes.

Some of the boreholes are designed to only pass through No. 7 seam and No. 8 seam by 0.5 m, while the others will be drilled past No. 9 seam by 0.5 m. As these overlying seams are soft and of low permeability, boreholes with 94 mm diameter are adopted to minimize risk of borehole collapse and closure. Bottom of the boreholes is spaced 10 m. A cross section of cross-measure boreholes is shown in Figure 6.

Surface wells are frequently used to capture goaf gas. Typically, with the advance of a panel in a protective seam, “three horizontal zones” are also formed in overlying strata, namely, intact zone, separation zone, and recompaction zone (Figure 7). With the development of working face, bending subsidence zone also goes with it. In the development process, the overlying protected coal seam in bending subsidence zone will be broken, permeability

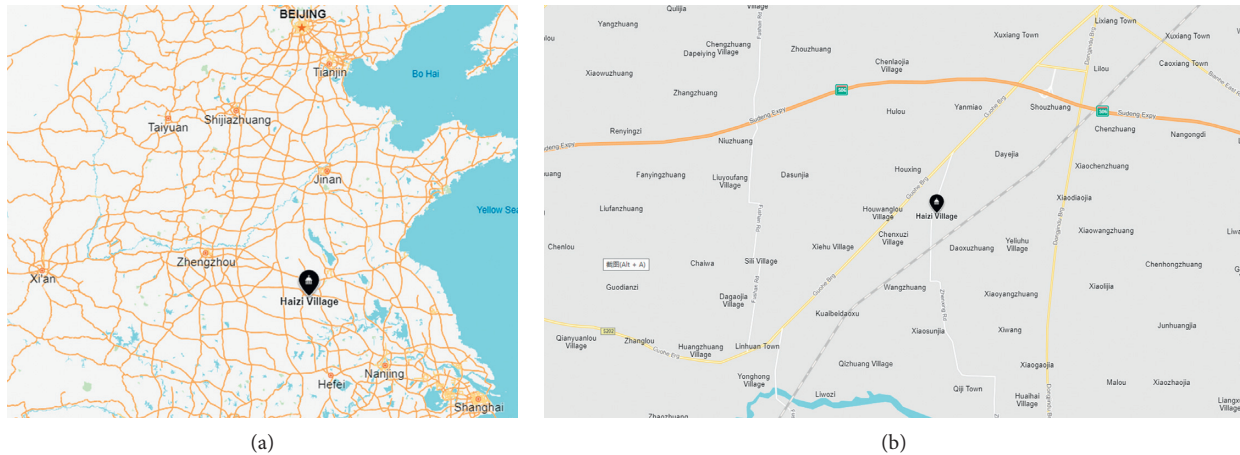


FIGURE 1: Location of Haizi Coal Mine.

experiences increase, and a large amount of gas emits out. Fracture network becomes flow channels of gas, and gas could be drained by surface wells.

Each of those two wells consists of four sections, as shown in Figure 9.

- (1) *Surface Pipe*. Use a $\phi 311$ mm bit to drill the well. Cement it with a $\phi 245 \times 10$ mm casing to prevent water in quaternary aquifer from getting into the underground from new strata to bedrock.
- (2) *Bedrock Pipe*. Use a $\phi 216$ mm bit to drill well to the position 2–5 m above No. 7 seam roof and cement it.
- (3) *Perforated Pipe*. Adopt a $\phi 152$ mm bit to drill well through No. 7 seam, No. 8 seam, and No. 9 seam to 4–5 m above the top of No. 10 seam. Put a $\phi 139.7 \times 9.17$ mm casing in this section. Its purpose is to prevent well from collapsing in No. 8 seam and No. 9 seam under the influence of No. 10 seam mining. Meanwhile, the well is gas passage from No. 7 seam, No. 8 seam, and No. 9 seam and goaf of No. 10 seam.
- (4) *Wooden Plug*. Finally, use a $\phi 94$ mm bit to drill the well to No. 10 seam floor and block it up with a $\phi 95$ mm wooden plug. Its purpose is to prevent water flowing into mining panel when the panel passes well.

Roof boreholes are drilled into the roof of protective seam from ventilation roadway of mining area. The boreholes are under suction pressure and used to capture roof gas which may otherwise flow into longwall mining face.

Highly located drilling site is placed in No. 2 1024 ventilation roadway and is constructed in every 80–110 meters. There is 2.5 m rock pillar between floor of drilling sit and coal seam roof. A 108 mm diameter bit is used to drill borehole up to 6 m, and then a 89 mm diameter bit is adopted to drill the other borehole section. Borehole depth is drilling field spacing plus 40 meters, and borehole position is at 3.5 meters from coal seam roof. It is determined that bottom position of borehole is about 30 meters from coal seam roof according to drainage situation in Haizi Coal

Mine. Five boreholes are constructed in each drilling site, as shown in Figure 10.

A special roof roadway parallel with panel gateroads is designed in the fractured zone of roof of protective seam. This roadway is used to capture goaf gas. In the initial stage of panel mining from its starting position, some boreholes are required to be drilled downward from the roadway into panel caving zone to obtain effective gas drainage as at this time the fractured zone of roof may not extend to roadway area. The best position of roadway for effective gas drainage is in the range of about 20 m in roof of protective seam and 20 m inside the panel gateroad in Haizi Coal Mine. One end of the roadway is 50 m inside the panel starting line, and a total of 9 boreholes of 94 mm in diameter are designed at the end of roadway. Those boreholes are drilled downward into protective No. 10 seam and are arranged in fan pattern, as shown in Figure 11.

4. Gas Drainage Design Optimization in No. 2 1024 Mining Panel

During mining process of No. 2 1024 panel, investigations are undertaken to study effects of different gas drainage measures on gas emission, methane concentration at working face, and gas drainage quantity. Four different combinations of gas drainage measures are adopted. In Case 1, all of above four gas control measures are implemented; in Case 2, the roof boreholes are not used while the other three measures being implemented; in Case 3, the roof gas tunnel and accompanying boreholes are not adopted when the other three measures are in operations, and in Case 4, the cross-measure boreholes are closed and the other three measures are implemented. The panel gas emission, methane concentration at working face, and gas drainage quantity of each drainage case are monitored by using gas sensor and orifice plate flowmeter. According to the daily data report of coalmine, variations of these monitored parameters are shown in Figures 12–15.

As indicated in Figures 12–15, for the case roof boreholes being not adopted, the panel relative and absolute gas emission

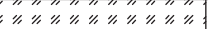
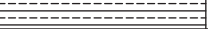
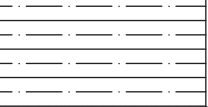

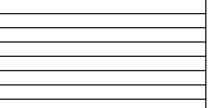
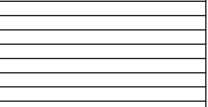




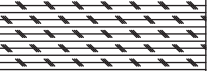

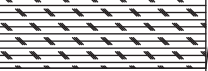

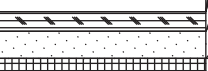

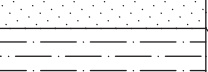

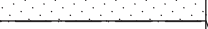
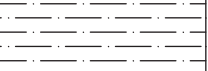
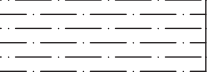

Rock name	Columnar	Thickness (m)	Lithology description
Alluvium		20	Yellow powder sandstone and clay.
Sand clay		21	Yellow clay and a small amount of sand, there is the conglomerate in this bottom.
Mud-sand stone		79	Reddish-brown,consisting of sand and clayey.
Glutenite		79	Reddish-brown mud bonded sand,gravel based.
Shale		198	Red and brown.
Sandshale		234	The upper part is gray and purple sandshale,middle part is grey-green sandstone.
Gritstone		34	Gray medium-grain sandstone.
No.3 seam		0.8	
Packsand		4.5	
No.4 seam		0.7	
Sandshale		7.5	
No.7 seam		0.5	
Sandstone		18.8	The upper part is sandshale,middle part is fine-grained sandstone.
No.8 seam		1.1	
Mudstone		10.7	Gray fine-grained sandstone and dark gray mudstone.
No.9 seam		0.7	
Sandstone		35.8	Grey lithology.
Sandy mudstone		39.2	Consisting of mudstone,siltstone and dark grey mudstone.
No.10seam		9	
Medium sandstone		58.8	Consisting of fine-grained and medium-grained sandstone.
Sandy mudstone		161.2	Consisting of mudstone,sandstone and siltstone.
Limestone		62.4	Belong to the Ordovician aquifer,containing a great amount of water.

FIGURE 2: Generalized stratigraphic column of Haizi Coal Mine.

increases substantially before decreasing slowly. Meanwhile, gas drainage quantity in surface wells and cross-measure boreholes increases. The growth of gas drainage quantity from roof gas

drainage tunnel and accompanying boreholes also slightly becomes bigger. However, there are no significant changes being observed in methane concentration.

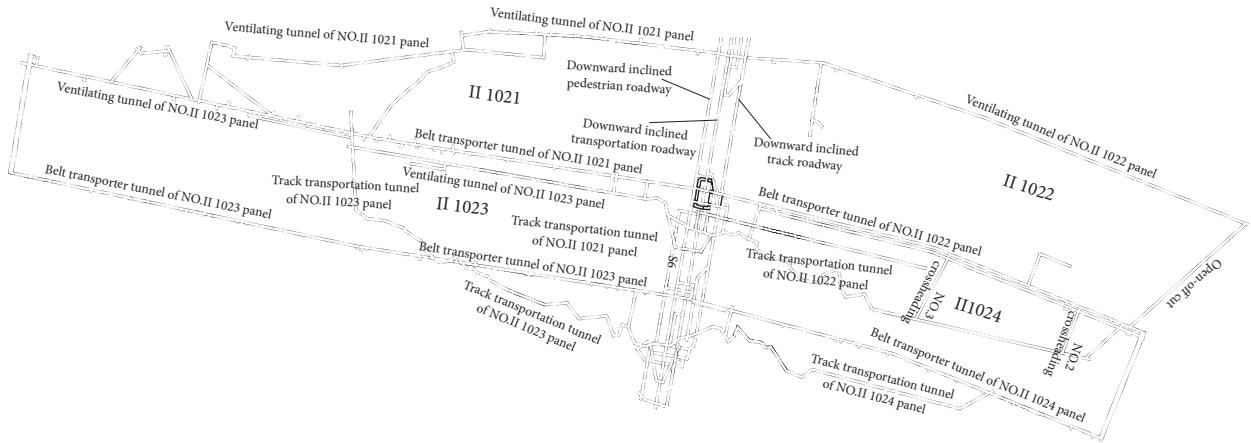


FIGURE 3: General layout of the No. 2 102 Mining Area.

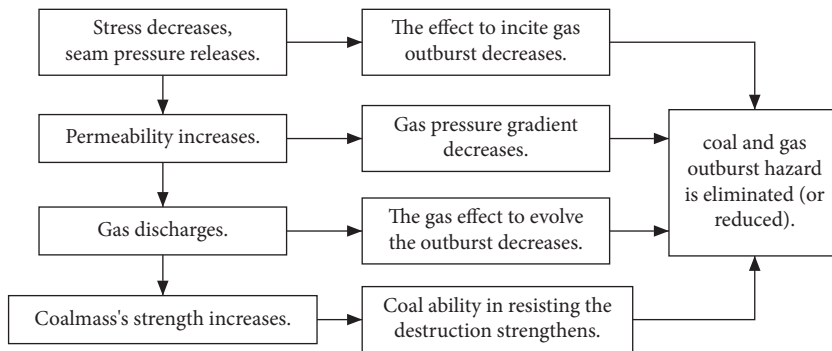


FIGURE 4: Outburst prevention principle with the protective seam mining.

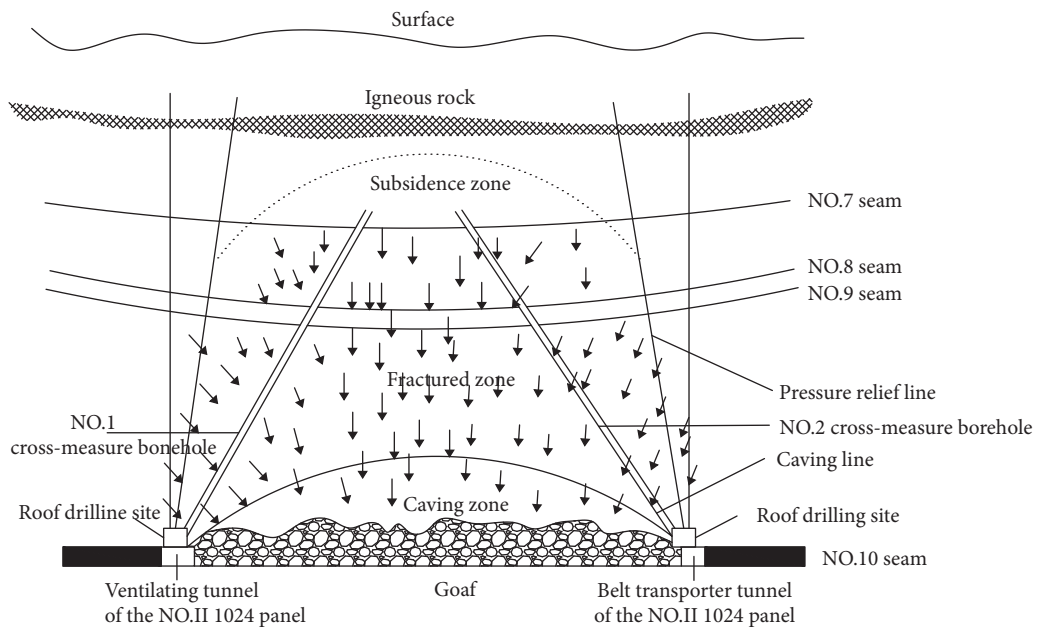


FIGURE 5: Diagram illustrating principle of gas emission in protected coal seam and gas drainage methods with cross-measure boreholes.

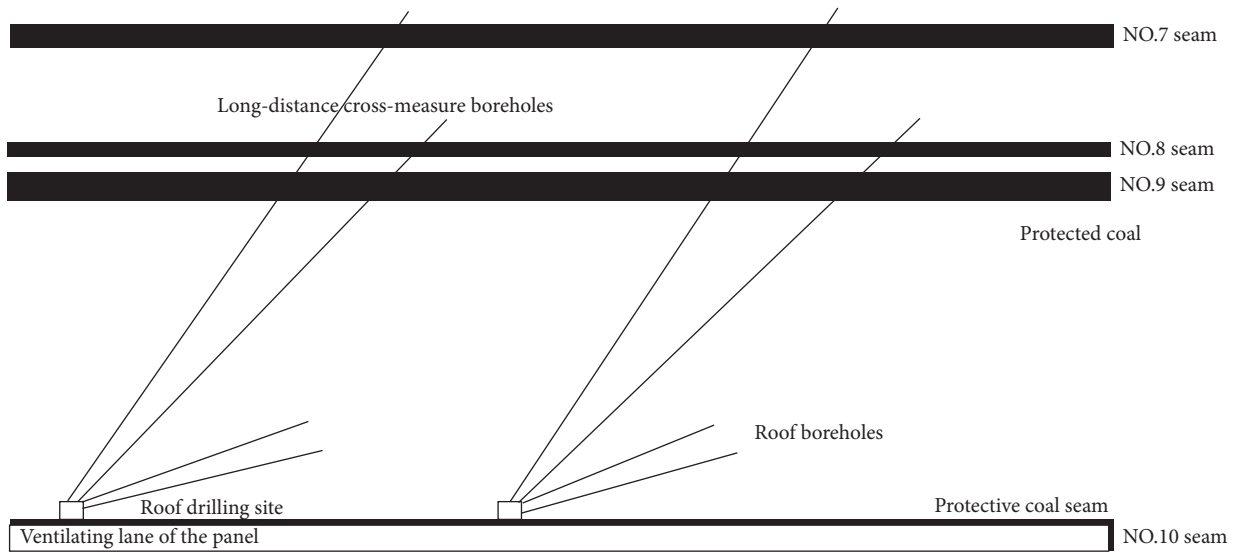


FIGURE 6: Cross section of the cross-measure boreholes in No. 2 1024 panel.

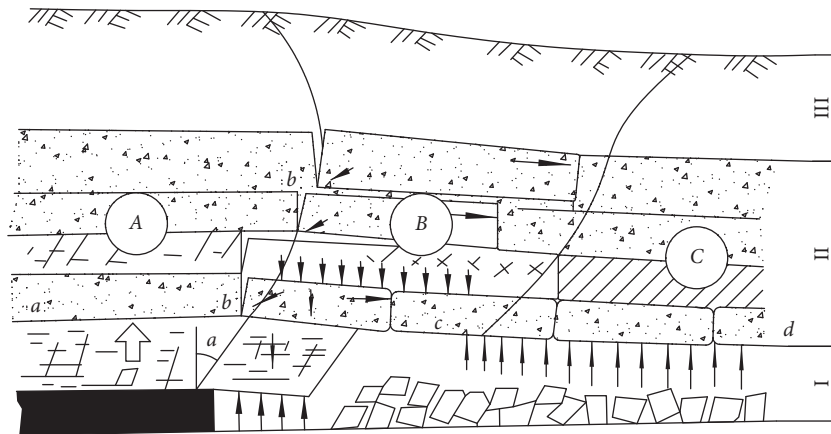


FIGURE 7: Subareas of overlying strata along advancing direction in mining panel. (A) Intact zone (a-b). (B) Separation zone (b-c). (C) Recompaction zone (c-d). (I) Caved zone. (II) Fractured zone. (III) Bending subsidence zone. The gas drainage method with surface wells is a major means of gas control in Haizi Coal Mine. First well is designed to be 100–150 m away from open-off cut and located in the middle of mining panel. Space between surface wells is 300 m. Two surface wells are designed in No. 2 1024 panel. The schematic diagram of surface borehole’s layout is shown in Figure 8.

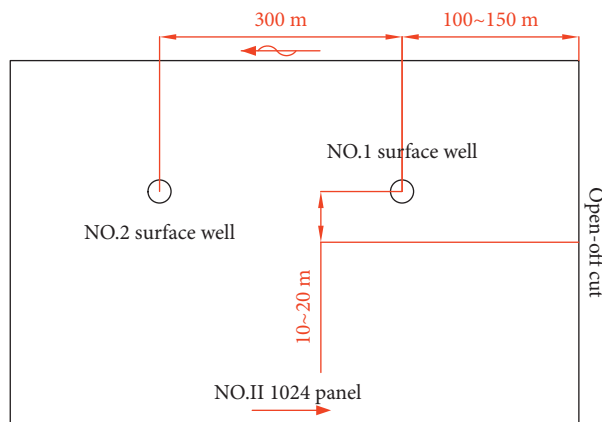


FIGURE 8: Schematic diagram of surface well’s layout.

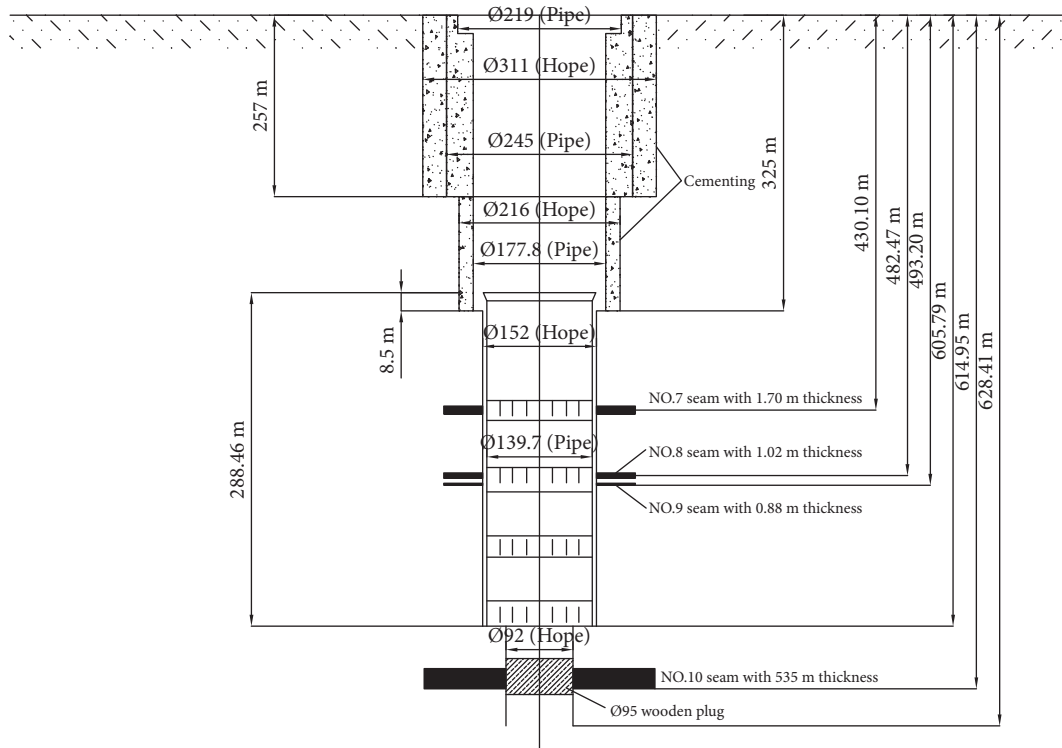


FIGURE 9: Schematic diagram of surface well's structure in No. 2 1024 panel.

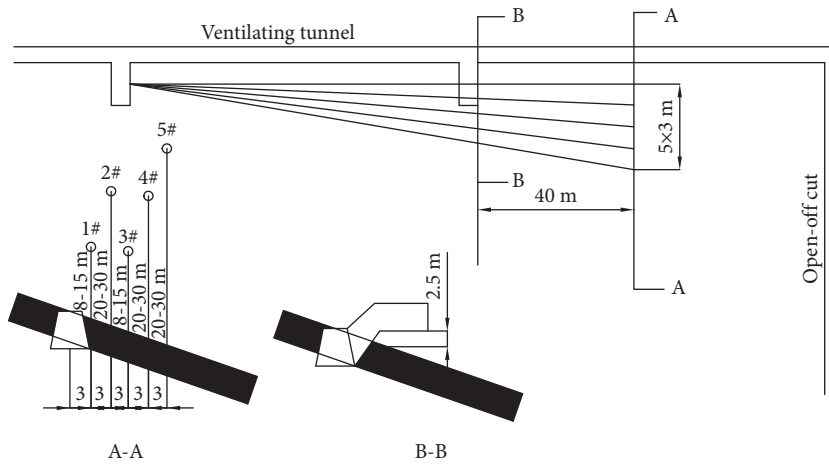


FIGURE 10: Roof borehole layout in No. 2 1024 panel.

In the case that roof gas drainage tunnels are closed, relative gas emission quantity is observed to increase in medium period of drainage but being relatively flat in other periods. Absolute gas emission quantity relatively reduces. Gas drainage quantity has no obvious change, but methane concentration decreases obviously in this case.

In the case that cross-measure boreholes being not used, both relative and absolute gas emission quantities do not obviously change. Gas drainage quantity of other drainage boreholes and methane concentration also experiences small change.

According to above analysis, effects of roof gas drainage tunnel and its accompanying boreholes on drainage performance in mining panel are limited. Methane concentration drops when they are closed. In comparison, cross-measure borehole is the main measure to drain gas from No. 7 seam, No. 8 seam, and No. 9 seam because its gas drainage quantity is large. Therefore, it is determined to replace roof gas drainage tunnel and its accompanying boreholes with horizontal long roof boreholes.

Taking into account high excavation cost and low gas drainage quantity of roof gas drainage tunnel in the early

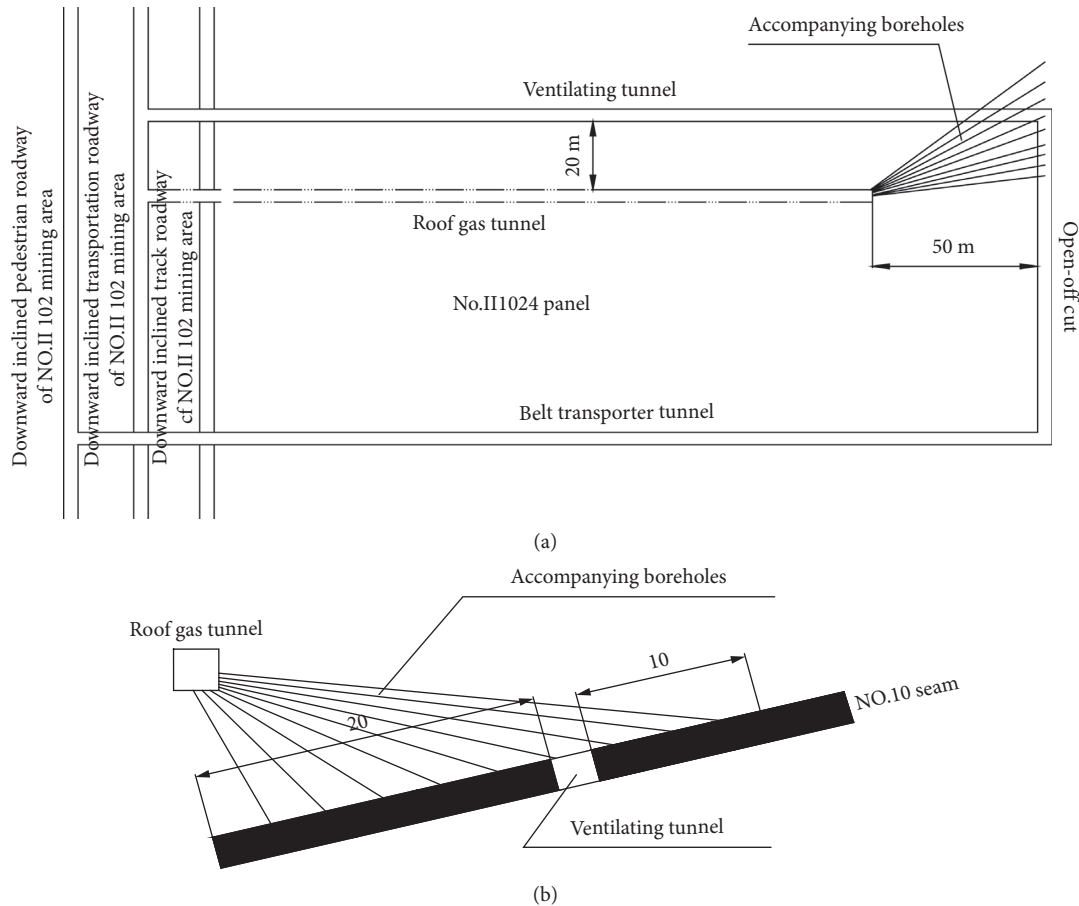


FIGURE 11: Roof gas drainage roadway and accompanying boreholes in No. 2 1024 panel: (a) plan view; (b) vertical cross section.

drainage stage, tests on horizontal long roof boreholes (replacing roof gas drainage tunnel) are carried out in No. 2 1023 panel, as shown in Figure 16. Boreholes are about 30 m distance from coal seam roof. They are parallel to ventilating lane and drilled in the direction of open-off cut. There are 6 boreholes in total, and their diameter is 108 mm while their length being 440 m. Testing results show that gas drainage concentration is 15–90% and gas drainage quantity is stable at $8 \text{ m}^3/\text{min}$. Thus, drainage effect of horizontal long roof boreholes is good.

After implementing aforementioned optimized gas drainage measures, residual gas pressure of No. 7 seam, No. 8 seam, and No. 9 seam was measured. Firstly, the borehole should be well sealed:

- (1) The sealing material includes piezometric tube, injection pipe, reflux pipe, cement, and polyurethane foam.
- (2) Pressure test section of the piezometric tube is located at the top of borehole, and its front end is protected by steel mesh to prevent pipe plugging.
- (3) Cement slurry and UEA expansion agent are used for borehole sealing. In order to completely seal the borehole, a certain amount of UEA expansion

agent is added in the cement slurry, and the expansion of UEA is used to fill borehole space after solidification and contraction of cement slurry. The ratio of cement, UEA expansion agent, and water is 100 : 8 : 110. The position of injection pipe is shown in Figure 17. First, the gap between piezometric tube, injection pipe, and borehole wall is sealed with polyurethane for about 1.5 m, and then the injection pipe is used for pumping cement slurry until the slurry returns through reflux pipe.

- (4) After 48 hours of solidification of slurry, pressure gauge is installed and pressure-measurement construction is completed.

The residual gas pressure in sealed borehole was measured by using pressure gauge. Results show that gas drainage efficiency of No. 7 seam, No. 8 seam, and No. 9 seam reached 58.64%, resulting in a significant reduction of gas pressure to be below 0.74 MPa (Figure 18). According to “Provisions for the Prevention and Control of Coal and Gas Outburst” in China, it is verified that the optimization of gas drainage scheme was effective. It has demonstrated that this optimization could effectively reduce gas emission and

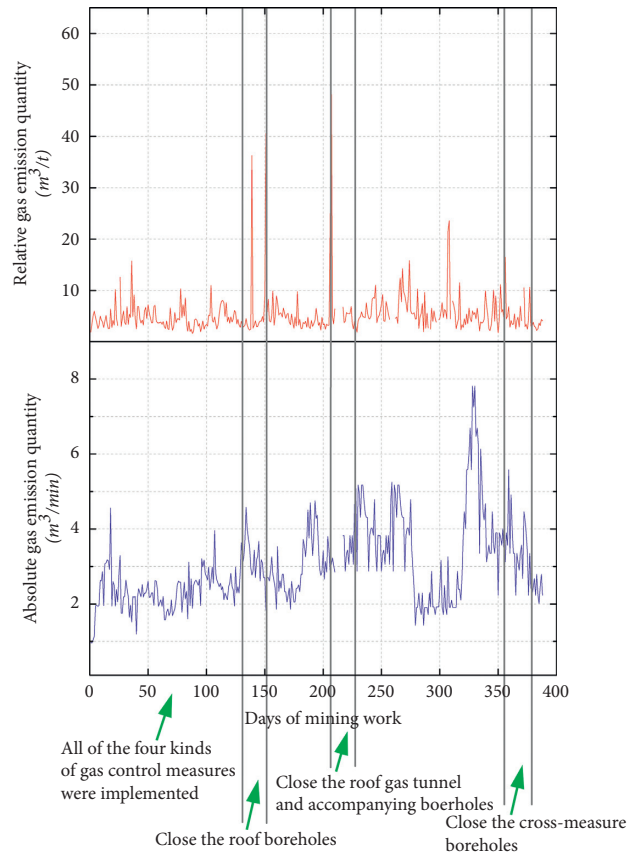


FIGURE 12: Variations of absolute and relative gas emission quantity during mining work when using different gas drainage measures in No. 2 1024 panel.

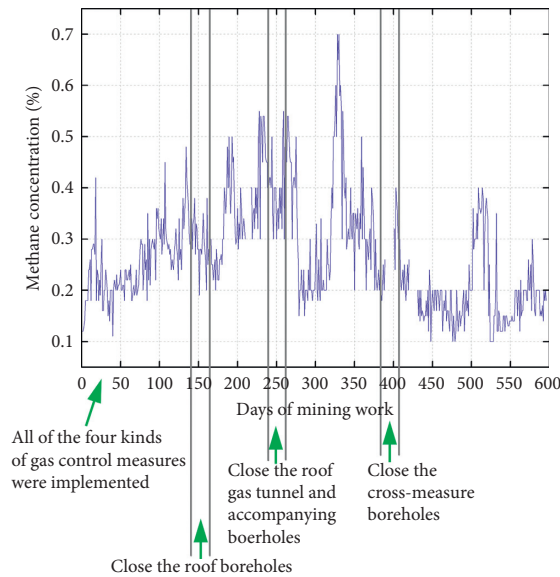


FIGURE 13: Variations of methane concentration in mining area when using different gas drainage measures in No. 2 1024 panel.

realize mining safety in the mining process of No. 10 seam. Furthermore, it can effectively reduce gas pressure and gas content of the protected seam (No. 7 seam, No. 8 seam, and

No. 9 seam) after No. 10 seam being mined, and it will be conducive to the safety production of No. 7 seam, No. 8 seam, and No.9 seam.

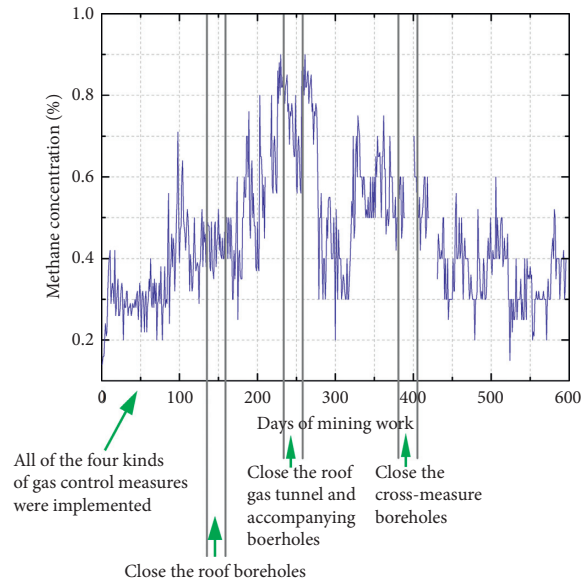


FIGURE 14: Variations of methane concentration when using different gas drainage measures in No. 2 1024 panel (particularly, at the corner of working face).

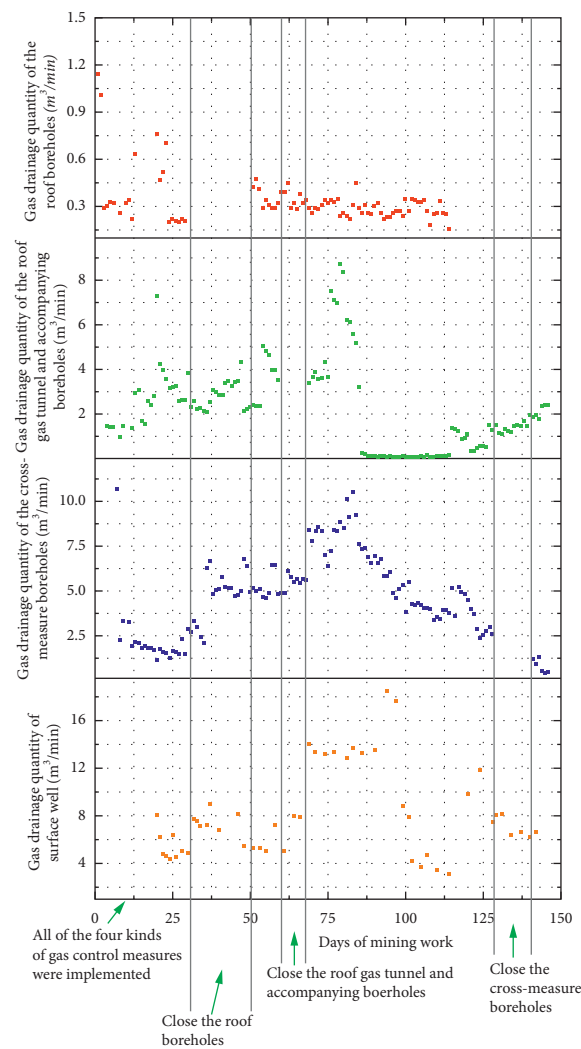


FIGURE 15: Variation of gas drainage quantity when using different gas drainage measures in No. 2 1024 panel.

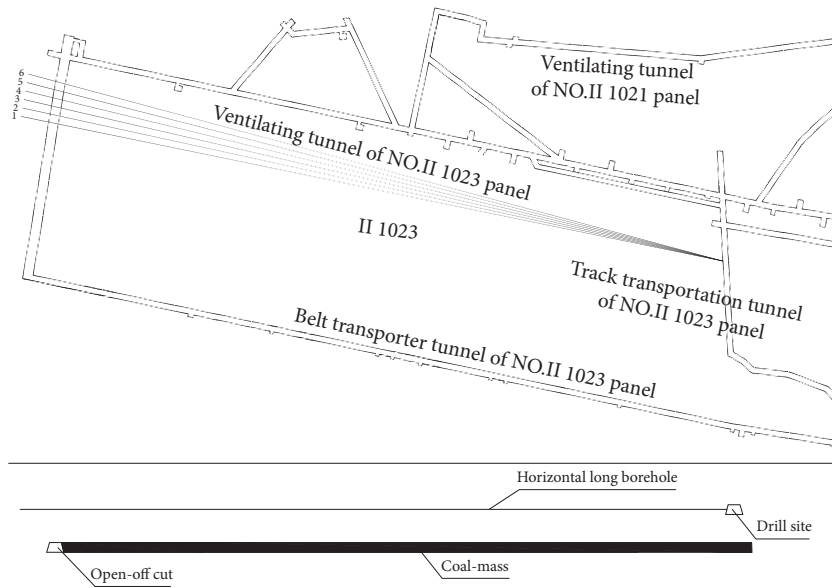


FIGURE 16: Schematic diagram of horizontal long borehole design in the roof.

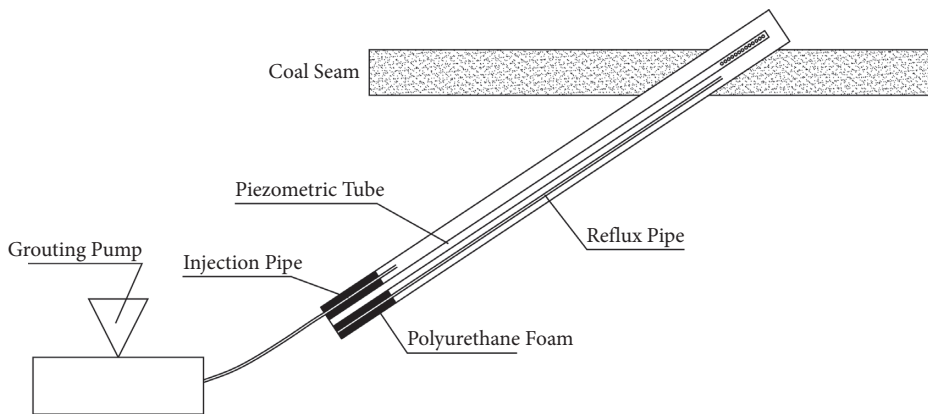


FIGURE 17: Schematic diagram of borehole sealing for measuring residual gas pressure.

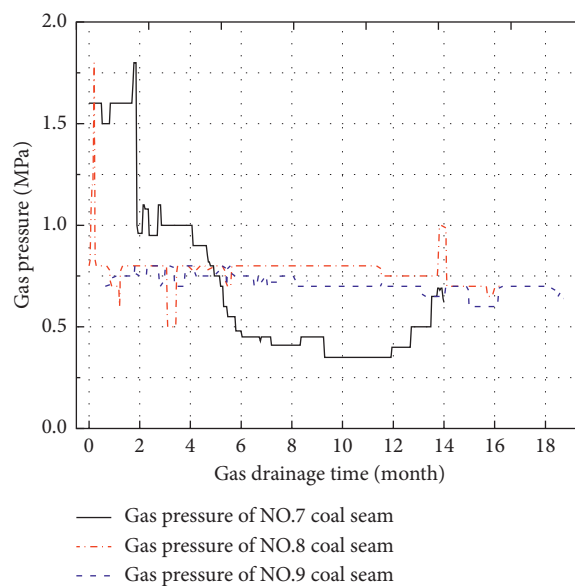


FIGURE 18: Variations of gas pressure in No. 7, No. 8, and No. 9 coal seams.

5. Conclusions

This study focuses on gas drainage design optimization in the mining process of No. 2 1024 panel for mining safety in Haizi Coal Mine. Four gas drainage measures are discussed for gas control, i.e., cross-measure boreholes into overlying seams, surface goaf wells, roof boreholes, and gas drainage roof roadway. Optimization on combinations of above measures is conducted and following conclusions could be obtained: drainage performance of roof gas drainage roadway with accompanying boreholes is poor. It could be replaced by horizontal long roof boreholes as the latter shows better drainage outcomes and could achieve safe mining and low costs. In No. 2 1023 panel, when adopting roof boreholes (replacing roof gas drainage roadway), gas drainage concentration ranges from 15% to 90%, when the drainage quantity being stable at 8 m³/min. Furthermore, after implementing optimized combination of gas drainage measures, the drainage efficiency of No. 7 seam, No. 8 seam, and No. 9 seam increases to 58.64%, resulting in a significant reduction of gas pressure to be below 0.74 MPa.

Outcomes of this study could help eliminating risk of coal and gas outburst in upper far-distance protected coal seams (No. 7 seam, No. 8 seam, and No. 9 seam) through optimization of gas drainage design in the mining process of the lower protective coal seam (No. 10 seam). For other coal mines that have similar geological conditions with Haizi Coal Mine, it is expected to deliver some guidance on their gas drainage design, for enhancing gas drainage performance and ensuring mining safety.

Data Availability

The data used for conducting classifications are available from the corresponding author authors upon request.

Conflicts of Interest

The author(s) declare that there are no conflicts of interest with respect to the research, authorship, and/or publication of this article.

Acknowledgments

This study was financially supported by the University Synergy Innovation Program of Anhui Province (No. GXXT-2021-018), National Natural Science Foundation of China (Nos. 51904013 and 51934007), Institute of Energy, Hefei Comprehensive National Science Center (No. 21KZS218), Youth Science and Technology Talents Support Program (2020) by Anhui Association for Science and Technology (No. RCTJ202005), Open Research Fund of State Key Laboratory of Coal Resources and Safe Mining, CUMT (No. SKLCRSM20KF003), and Anhui Oversea Returnees Innovation Project Funding (No. 2019LCX001).

References

- [1] M. M. Wu and Y. Zhong, "Statistics analysis of our country's coal mine fatal accidents from 2012 to 2013," *Coal Technology*, vol. 10, pp. 296–299, 2014.
- [2] B. Q. Lin and J. G. Zhang, *Theory and Technology about Gas Drainage in the Coal Mine*, China Mining University Press, Xuzhou, China, 1995.
- [3] D. Deb, "Analysis of coal mine roof fall rate using fuzzy reasoning techniques," *International Journal of Rock Mechanics and Mining Sciences*, vol. 40, no. 2, pp. 251–257, 2003.
- [4] S. Kong, P. Yang, X. Fang et al., "Analysis of characteristics of safety accidents in university laboratory and research on the causes of accidents," *E3S Web of Conferences*, vol. 257, Article ID 03050, 2021.
- [5] X. Tong, H. Wen, X. Cheng et al., "Characteristics of pressure relief gas extraction in the protected layer by surface drilling in huainan," *Advances in Civil Engineering*, vol. 2021, Article ID 9966843, 11 pages, 2021.
- [6] L. Y. Qing, "Gas control mode of outburst coal seams in huainan coal mining area," *Coal Technology*, vol. 35, 2016.
- [7] C. Guo and L. Wenke, "On comprehensive gas control technology in mining of protective layer in linhuan coal mine," *Mineral Engineering Research*, vol. 32, 2017.
- [8] W. Xudong and Y. Xing, "Gas drainage effect and parameter optimization of long borehole along roof strike based on cfd numerical simulation," *Mining Safety & Environmental Protection*, vol. 46, 2019.
- [9] H. Zhang, "Application of coal seam gas drainage technology with advanced pressure-relief in gas control of Xingyu coal mine," *Shanxi Chemical Industry*, vol. 38, 2018.
- [10] Z. Wang, Y. Sun, Y. Wang, J. Zhang, and Z. Sun, "A coupled model of air leakage in gas drainage and an active support sealing method for improving drainage performance," *Fuel*, vol. 237, pp. 1217–1227, 2019.
- [11] X. Wu, "Application and analysis of mined-out area high gas drainage drilling technology," *Mechanical Management and Development*, vol. 31, 2016.
- [12] H. Y. Ma, Z. F. Wang, and H. M. Yang, "Study on effective drainage radius of downward borehole drilled through strata in sijiazhuang mine," *Coal Engineering*, vol. 5, 2011.
- [13] L. Sheng, "Study on high level gas drainage gateway layout along roof strike in high gassy mechanized coal mining face," *Coal Science and Technology*, vol. 45, 2017.
- [14] H. Wang, Y. Cheng, and L. Yuan, "Gas outburst disasters and the mining technology of key protective seam in coal seam group in the Huainan coalfield," *Natural Hazards*, vol. 67, no. 2, pp. 763–782, 2013.
- [15] G. L. Dai, "Forecast of the gas effused from the face in protective seam," *Journal of China Coal Society*, vol. 32, pp. 382–385, 2007.
- [16] V. Leisle and R. Kovalski, "Assessing the well yield during methane drainage in coal mines," *Ecology Environment and Conservation*, vol. 23, 2017.
- [17] W. Zhang, "Numerical simulation on stress evolution and deformation of overlying coal seam in lower protective layer mining," *Alexandria Engineering Journal*, vol. 59, pp. 3623–3633, 2020.
- [18] Q. Dong and Hong, "Study on numerical simulation of pressure-relief law of coal-rock masses and gas in outburst coal seams under thick key stratum," *Zhongzhou Coal*, vol. 7, 2015.
- [19] H. Yang and W. Qiu, "Numerical simulation research on mining stress field of overlying coal-rock seam under far

- distance lower protective seam mining,” *Industry and Mine Automation*, vol. 43, 2017.
- [20] W. Sun and S. Wu, “A study of crack initiation and source mechanism in the Brazilian test based on moment tensor,” *Engineering Fracture Mechanics*, vol. 246, no. 4, Article ID 107622, 2021.
- [21] D. Huang, “A numerical simulation method for time-dependent growth of cracks in rocks and its validation,” *Chinese Journal of Rock Mechanics and Engineering*, vol. 36, pp. 1623–1633, 2017.
- [22] M. V. Bastawrous and M. I. Hussein, “Closed-form existence conditions for band-gap resonances in a finite periodic chain under general boundary conditions,” 2021, <https://arxiv.org/abs/2108.00828>.
- [23] B. Huo, Y. Tai, X. Meng, and T. Kuang, “Deformation and failure mechanism of full seam chamber with extra-large section and its control technology,” *Open Geosciences*, vol. 12, no. 1, pp. 390–405, 2020.

Research Article

Moisture Content on Methane Desorption Characteristics in Coal and Its Effect on Outburst Prediction

Peng Li,^{1,2} Yaolin Cao,^{1,2} Xuelong Li^{3,4} , Fakai Wang⁵ , Zhongguang Sun^{4,6} ,
Qinke Huang,³ and Deyou Chen³

¹China Coal Technology and Engineering Group Shenyang Research Institute Co. Ltd, Fushun 113122, China

²State Key Laboratory of Coal Mine Safety Technology, Fushun 113122, China

³College of Energy and Mining Engineering, Shandong University of Science and Technology, Qingdao, Shandong 266590, China

⁴State Key Laboratory of Coal Mine Disaster Dynamics and Control, College of Resources and Environmental Science, Chongqing University, Chongqing 400044, China

⁵College of Mining Engineering, Guizhou Institute of Technology, Guiyang 550000, China

⁶State Key Laboratory of the Gas Disaster Detecting, Preventing and Emergency Controlling, Chongqing 400037, China

Correspondence should be addressed to Xuelong Li; lixlumt@126.com

Received 30 August 2021; Accepted 1 December 2021; Published 21 December 2021

Academic Editor: Shun Liang

Copyright © 2021 Peng Li et al. This is an open access article distributed under the Creative Commons Attribution License, which permits unrestricted use, distribution, and reproduction in any medium, provided the original work is properly cited.

Facts have proved that coal and gas outbursts require rapid desorption in a short period of time. Due to the limitation of experimental conditions, the methane desorption characteristics in the first few seconds (0–60 s) in coals with different moisture contents have not been fully studied at present. In this article, the initial desorption characteristics of methane in coals with different moisture contents were investigated using a self-developed experimental setup. In order to collect enough methane pressure data for analysis and calculation, a self-developed real-time data acquisition system with a time interval of about 10 ms was used in the experiment to calculate the initial gas desorption amount and the initial gas velocity diffusion index (ΔP). Experiments show that coal with low water content and methane outburst is more dangerous than coal with high water content and outburst; and the degree of outburst of coal and methane decreases exponentially with the increase of moisture content.

1. Introduction

Gas is a by-product of coal formation [1]. Coal seam gas exists in coal seams in several forms such as adsorption on the surface of micropores and macropores; adsorption on the molecular structure of coal; free gas in fissures and macropores; and dissolving in coal fissure water [2–4]. Outburst is a dynamic phenomenon in which coal and gas are violently ejected from the face coal seam, causing certain economic losses and casualties. It gets worse as mining goes deeper in the coal seam [5, 6]. Outburst accidents frequently occur during deep coal mining. Based on the statistical research on a large number of experimental data of gas adsorption and desorption characteristics in coal, scholars have established coal seam outburst prediction indicators, for example, the index value K_V of prominent risk prediction

using gas emissions [7]. The V -index of gas emission is the gas desorption amount of coal in the interval of 35–70 s under atmospheric pressure [8–10]. The gas desorption indices (K_1 and Δh_2) of coal cuttings have been widely used in China. K_1 is the gas desorption amount in 1 min, Δh_2 is the gas desorption amount in the interval of 3–5 min under atmospheric pressure [11]. Moreover, the Δp index has been widely adopted worldwide. In addition, Norbert proposed that the time constant T reflects the rate of pressure drop in front of briquette work [12].

Therefore, it is of great significance to study the desorption characteristics of water to gas in coal for the prevention and control of outbursts. A large number of existing experimental studies have shown that the diffusion rate of anthracite decreases with the increase of water content, while the diffusion rate of asphalt shows a U-shaped

distribution that first decreases and then increases with the increase of water content [13]. The desorption and diffusion experiments of methane and carbon dioxide show that the moisture content in the coal matrix has a more significant effect on the gas desorption rate, and the effect of moisture content on the methane diffusion rate is greater than that on carbon dioxide diffusion rate [14]. The results show that the initial desorption rate, diffusion capacity, and gas desorption capacity of coal after pulsating water injection are higher than static pressure, and the gas desorption diffusion effect is better than that of static pressure water injection [15]. Both the gas desorption and desorption rates of the coal samples decreased with the increase of the moisture content of the coal samples [16]. Adsorption-water-desorption experiments were carried out and it was concluded that the desorption rate decreased with decreasing critical pore size [17]. The analysis of the outburst prevention effect of coal seam water injection shows that the higher the water content of the coal seam, the smaller the outburst risk [18]. Research [19] shows that the cumulative degassing rate of dry and wet coal samples is similar to the Langmuir adsorption isotherm, adding water inhibits the desorption rate of coal, and the desorption rate of dry coal is greater than that of water.

In this paper, the self-developed test equipment was used to study the methane desorption characteristics in the first tens of seconds (0–60 s) under different water contents from three aspects: gas pressure, initial desorption gas amount, and initial gas diffusion rate. High-purity methane was used in the experiments. The influence of different moisture content on outburst risk is analyzed. Experimental studies have shown that coal and methane bursts with low moisture content are more dangerous than high moisture content.

2. Experimental Setup and Procedure

Experimental setup is shown in Figure 1. It is mainly composed of a pressure container (5), a constant temperature water bath (11), a vacuum system (1), an inflation system (7–10), and a self-developed real-time data acquisition system (4). The container (5) is connected to the diffusion space (3) through the electromagnetic valve (6). The charging system of the test platform is equipped with a pressure regulating valve (8) to adjust the charging pressure to reach the set test adsorption gas pressure.

The experimental platform adopts a real-time dynamic data acquisition system. In order to obtain enough gas pressure data during the initial desorption process, the data acquisition time interval is set to be about 10 ms. The ultimate pressure of the test device is almost absolute vacuum level (less than 10 mm Hg). For an isobarometer, we degas the diffusion space to a pressure below 10 mm Hg when the sample is not loaded. After stopping the vacuum pump and vacuuming for 5 minutes, the increase of space pressure should be less than 1 mm Hg. Otherwise, the experimental equipment should be overhauled until the air tightness meets the requirements.

Coal material was sampled from Quanlun coal mine of Shandong energy group Guizhou Co., Ltd., in Guizhou province of China. The geographical location of the Quanlun

coal mine is shown in Figure 2. The coal mine is rich in coal seams to be mined, and the geological occurrence is simple (Figure 3). The coal lumps are ground and screened to reach an ideal particle size of 0.20 mm–0.25 mm. The coal sample weighs 3.5 g. The approximate analysis of coal samples was as follows: moisture content $M_{ad}=1.50\%$, volatile content $V_{daf}=7.06\%$, ash content $A_{ad}=16.92\%$, total sulfur content $S_{t,d}=0.56\%$, porosity $n=10.49\%$, and average porosity size $r=9.3$ nm.

We placed the test coal sample in container (5). After 1.5 h evacuation, we turned off the vacuum pump (1) while injecting high-purity methane into the vessel. The coal sample was adsorbed for 1.5 h. When the pressure remains constant, the electromagnetic valve (2) opens and the electromagnetic valves (6, 7) close. The vacuum pump (1) was opened to degassing the diffusion space (including the instrument gas piping). Then, we stopped the vacuum pump, closed the electromagnetic valve (2), opened the electromagnetic valve (6), so that the coal sample container and diffusion space are connected, and started the data acquisition. At 10 s, we closed the electromagnetic valve (6) and recorded the diffusion space real-time pressure data. At 45 s, we connected the coal sample container and diffusion space and once again read the diffusion space real-time pressure data.

When the coal sample container is filled with coal samples, we injected high-purity methane with a certain pressure. The experiments were carried out under the equilibrium methane pressure of 0.100 MPa and the pretreatment contents of 0.5%, 1%, 2%, 4%, 6%, 8%, and 10% of the water balance. The pressure regulating valve (8) is used to regulate the set methane pressure.

Steps of moisture balance pretreatment of coal samples are as follows (as shown in Figure 4): Firstly, we weighted a certain amount of air-dried coal sample (with a precision of 0.1 mg). Second, we placed the coal sample in a container and evenly added appropriate amount of distilled water. Third, we placed the container containing the quantitative sample in a moisture-proof sealed container (25°C, relative humidity in a humidified environment of 97%), filled it with a sufficient amount of potassium sulfate supersaturated solution, and weighed every 24 hours. Until two consecutive weighing, the weight change does not exceed 2% of the sample weight. Formula is as follows:

$$M_0 = \left(1 - \frac{G_2 - G_1}{G_2} \right) \times M_{ad} + \frac{G_2 - G_1}{G_2} \times 100, \quad (1)$$

where M_0 is the moisture balance content, %; G_1 is the sample mass after adding water to balance, g; G_2 is the sample mass after adding water for equilibrium, g; M_{ad} is the original sample moisture content, %.

In order to eliminate the influence of the coal sample's own volume on the diffusion space, the mass of the coal sample was measured by an analytical balance, and the density was measured by the paraffin dipping method.

Since the gas adsorption/desorption properties of coal are extremely temperature-sensitive, the entire vessel was placed in a constant temperature water bath (11) with a

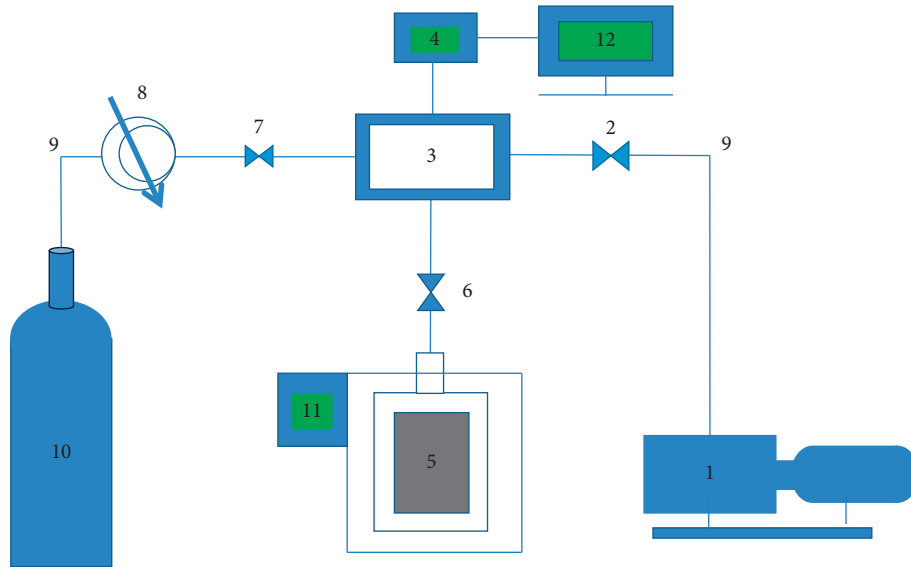


FIGURE 1: Experimental setup. Denoted elements are as follows: 1, vacuum pump; 2, 6, 7, electromagnetic valves; 3, diffusion space; 4, pressure transducer and real-time data acquisition system (DAS); 5, coal sample container; 8, pressure regulating valve; 9, gas piping; 10, gas cylinder; 11, constant temperature water bath; 12, computer.



FIGURE 2: The geographical location of the Quanlun coal mine.

water temperature of 25°C (298.15 K) throughout the experiment.

In order to ensure the reliability of the experimental device, the air tightness of the instrument was tested. The pressure change of the diffusion space in the experimental device was less than 10 Pa, which met the test pressure requirements of the methane diffusion process.

3. Results and Discussion

3.1. Initial Gas Pressure of Desorbed Gas. According to the measurement range of the pressure sensor (0–0.100 MPa), the real-time test methane pressure data collected by the pressure sensor and the real-time data acquisition system include the following: high range 45 s pressure data → 60 s pressure data P_2 , and low range of 0 s pressure data → 10 s pressure data P_1 . In order to simplify the analysis of the test data, the methane pressure data of the coal sample container for 10 s–45 s do not need to be collected or directly

eliminated during the experimental. The intermediate time (the 10 s–45 s diffusion space' pressure is constant) and the coal sample methane pressure data collected by pressure transducer and real-time data acquisition system (0 s pressure data → 10 s pressure data; 45 s pressure data → 60 s pressure data) are combined and analyzed. Figure 5 shows an example of pressure changes.

Figure 5 shows that the gas pressure increases sharply at the initial time and then slowly rises. Changes in methane pressure at different times are different. The pressure rise rate of the diffusion space pressure from 45 s to 60 s is lower than that of the diffusion space pressure of 0 s to 10 s. The reason is that the methane adsorbed on the microporous surface of the coal matrix is rapidly desorbed into free methane under the action of pressure gradient and concentration gradient [16–19].

Figure 6 shows the change curve of methane desorption pressure when the coal sample container is filled with coal particles with different moisture contents. It can be seen

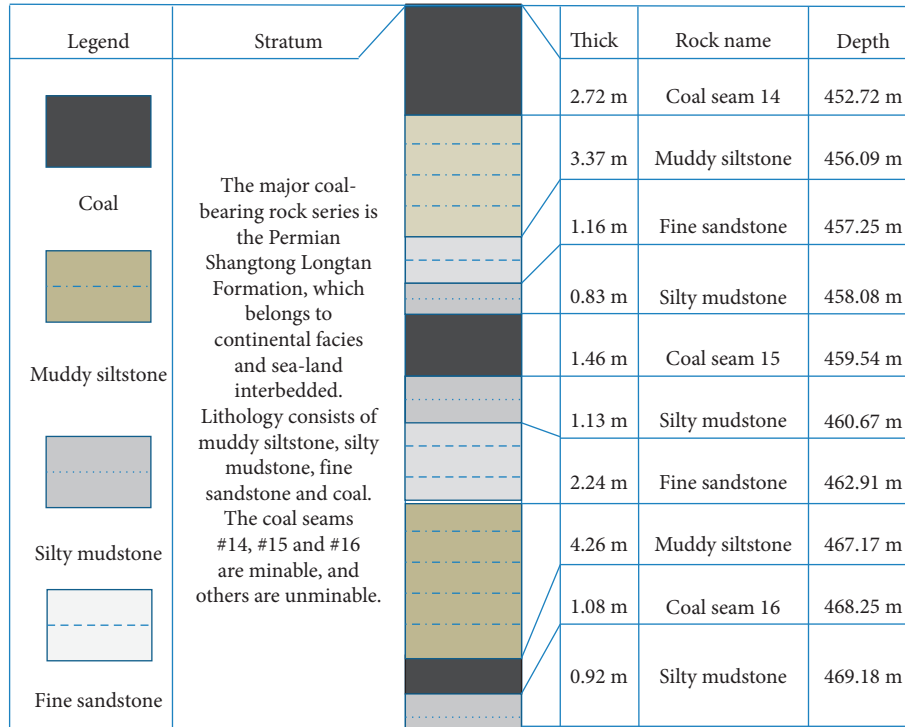


FIGURE 3: Coal seam histogram.

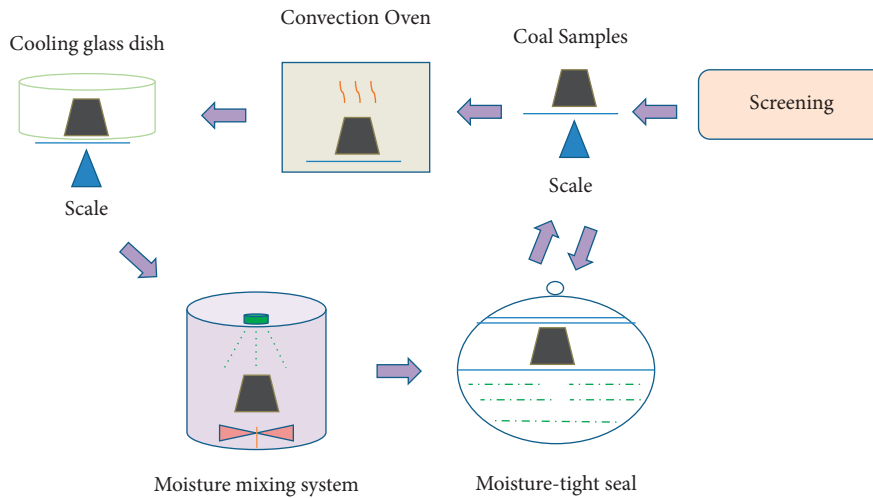


FIGURE 4: Preparation of coal samples and its moisture balance.

from the figure that the desorption pressure curve of methane with low water content is always higher than that of high water content, indicating that the diffusion space pressure of methane in coal increases at a higher rate than that with low water content. That is, the methane content in the coal with lower moisture pressure will remain higher for a longer period of time. Therefore, a large amount of methane is desorbed into free gas after coal exposure, contributing to the generation of sufficient outburst energy. The results of this paper are consistent with the actual outstanding situation and many laboratory research results [13, 14].

3.2. Initial Desorbed Methane Amount of Coal Sample. The amount of methane diffusing (n) through the electronic valve (6) is mainly composed of two components: the gas flux from the pore volume (n_1) and the gas flux from the coal particles (n_2).

The gas mass flow rate (m) at the electronic valve (6) is calculated using the collected gas desorption pressure data using the following formula [18]:

$$m = \frac{P\sigma^*}{\sqrt{T}} \sqrt{\frac{2\gamma}{\gamma - 1} \left[\left(\frac{P_2}{P}\right)^{2/\gamma} - \left(\frac{P_2}{P}\right)^{\gamma+1/\gamma} \right]}, \quad (2)$$

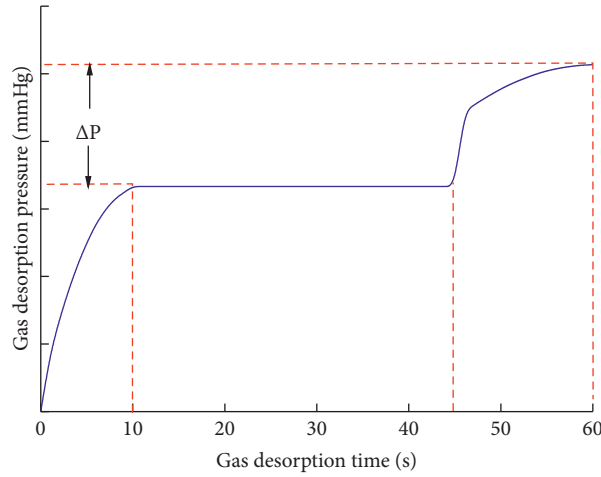


FIGURE 5: An example of pressure variation.

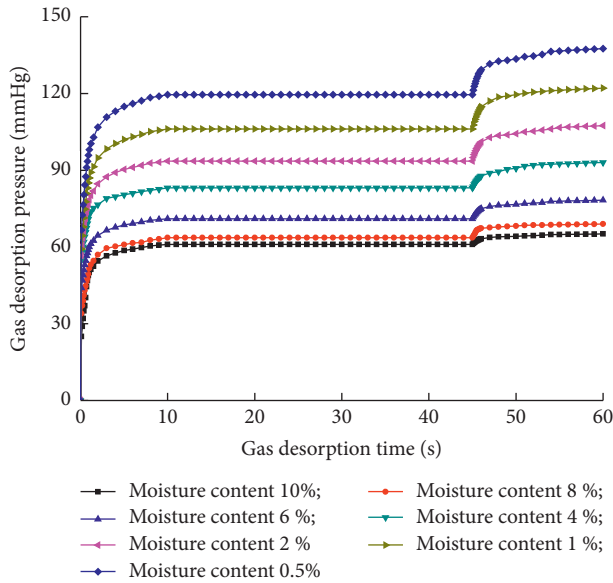


FIGURE 6: Methane desorption pressure curves of coal samples.

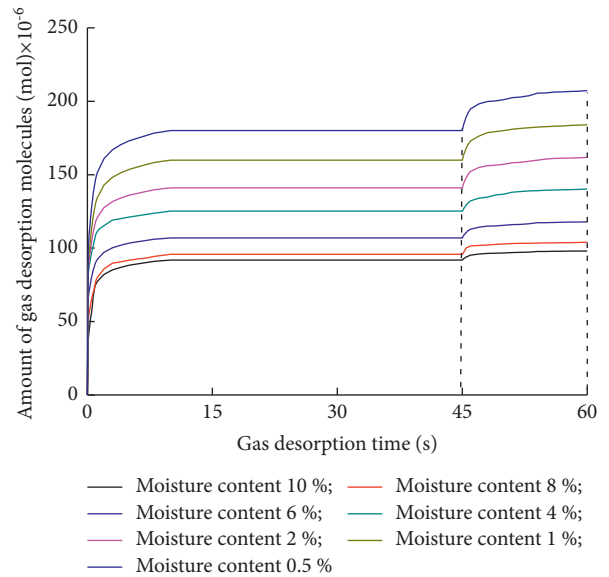


FIGURE 7: The relationship between the total amount of methane desorbed.

where P and T are the absolute pressure and temperature, respectively; γ is the adiabatic exponent; σ^* is the cross-sectional area; and R is the gas constant. The amount of methane flowing through the electronic valve (6) can be calculated:

$$n = \frac{1}{M} \int_0^{t_0} m dt = \frac{PV}{298.15ZR}, \quad (3)$$

where M is the methane molar mass; R is the methane molar constant; V is the container diffusion space; and Z is the methane compressibility.

The results of the experimental data analysis are shown in Figure 7. It can be seen from the figure that the total amount of desorbed methane increases with time at an extremely fast rate at the initial time. Then, their growth rates are decreasing over time.

From a microscopic point of view, the adsorption of water and methane by coal is due to the interaction of water and methane molecules with coal-based molecules. The maximum adsorption potential of methane on the coal surface is -2.704 kJ/mol, and the maximum adsorption potential of water on the coal surface is -24.0 kJ/mol. The larger the adsorption potential is, the more the adsorbable molecules are adsorbed [20–23]. Therefore, the presence of moisture in coal can significantly affect the adsorption capacity of coal for methane. Moisture mainly affects the adsorption of methane by coal in three aspects [24–27]: First, part of the free water combined with the coal surface occupies a certain space on the coal surface, thereby reducing the adsorption space of methane molecules and reducing the coal surface. Adsorption capacity. Methane adsorption.

Secondly, due to the certain vapor pressure of water, there is a small amount of gaseous water molecules in the coal micropores, which hinders the adsorption of methane molecules on the surface of coal, thereby reducing the amount of methane adsorption by coal. Third, water prevents methane molecules from entering the micropores. Since the specific surface area of pores is the main surface for coal adsorption [28], water will form capillary resistance in the micropores of coal [29, 30]. Especially when the pressure pores between the internal and external environments are not enough to overcome the capillary resistance, the methane molecules are prevented from entering the pores, thereby reducing the amount of methane adsorbed in the coal. In general, water will reduce the amount of adsorbed gas in the coal sample, thereby reducing the initial desorption pressure of methane.

The gas flux (n_1) from the container volume is equal to the gas increase in the diffusion space volume and can be calculated:

$$\Delta n = \frac{V}{298.15R} \left(\frac{P_2}{Z_2} - \frac{P_1}{Z_1} \right), \quad (4)$$

where P_1 and P_2 are the coal-methane absolute pressure; V is the container diffusion space; and Z is the compressibility factor. The velocity of gas desorbed from coal particles (v) in unit time Δt is calculated as

$$v = \frac{\Delta n}{\Delta t}. \quad (5)$$

The experimental data analysis is shown in Figure 8. As can be seen from the figure, the methane desorption rate decreases very rapidly with time from the initial time. Then, the desorption rate decline rate keeps decreasing. The trend line has an unstable wave curve in the time period of 0.4–1.2 s, and at the same moisture content, they are similar in time of 45–49 s. For the experimental data with a water content of 10%, the desorption gas velocity is slightly larger than that after the unstable fluctuation curve. Then, the total amount of desorbed methane is still increasing rapidly. The total desorbed methane gap between the 0–10 s and 45–60 s time periods increased with time. They have similar trends in the moisture content of other coal samples.

3.3. Initial Velocity Diffusion of Coal-Methane. The index (ΔP) of initial velocity diffusion of coal gas (abbreviated as IVDCG) is an index widely used worldwide to judge the outburst danger. It has been proved that with the increase of the IVDCG value, the outburst accidents probability increases significantly, and the critical value is 10 mmHg.

Yang and Liu [31] showed that when the coal particle size is smaller than the limit size, the coal particles are basically composed of pores. The limit particle size of coal samples varies with the degree of coal metamorphism, and the particle size ranges from about 0.5 to 10 mm [32]. Therefore, the mass flow of methane at the initial velocity measurement will be proportional to its concentration gradient, which follows Fick's law.

$$J = -D \frac{\partial C}{\partial X}, \quad (6)$$

where J is the methane diffusion velocity, $m^3/(m^2 \cdot s)$; D is the methane diffusion coefficient, m^2/s ; C is the methane concentration, m^3/t ; and X is the distance from the center of the particle, m .

The experimental research results of many scholars show the adsorption isotherm when coal-methane conforms to the Langmuir adsorbs equation [33, 34]:

$$W = \frac{abP}{1 + bP} \times \frac{1}{1 + 0.31M_0}, \quad (7)$$

where W is at a certain temperature, mL/g; P is the gas adsorption equilibrium pressure, MPa; a is an adsorption constant, mL/g; b is an adsorption constant, MPa^{-1} ; and M_0 is the moisture balance content, %.

To further analyze the experimental data, it is assumed that (1) the coal is composed of spherical particles with an average radius R of 0.125 mm; (2) the coal particles are uniform; and (3) the methane flow conforms to the law of mass conservation and the principle of continuity.

The approximate solution of desorption of coalbed methane by coal particles under the first-order boundary condition can be calculated [35]:

$$\frac{C - C_p}{C_0 - C_p} = \frac{2R(-1)^n}{\pi n \pi} \sin \frac{n\pi r}{R} \exp \left(-n^2 \pi^2 \frac{Dt}{R^2} \right). \quad (8)$$

According to the determination method of the outburst hazard identification index ΔP , the following formula can be obtained:

$$\Delta P = \frac{3.5}{27\rho(4/3\pi R^3)} \int_0^{60} \int \int ((C_0 - C_p) dV) dt, \quad (9)$$

where ρ is the particle density and C_p is the methane concentration.

The approximate solution of the outburst risk discrimination index ΔP is obtained by formulas (7) and (8):

$$\Delta P = \frac{3.5}{27\rho} \left(\frac{abP}{1 + bP} \times \frac{1}{1 + 0.31M_0} - C_p \right) \left\{ \sum_{n=1}^{\infty} \frac{6}{\pi^2 n^2} \left[\exp \left(-\pi^2 n^2 \frac{60D}{R^2} \right) - \exp \left(\pi^2 n^2 \frac{10D}{R^2} \right) \right] \right\}. \quad (10)$$

It can be seen from formula (9) that the moisture content has a great influence on the determination of the outstanding

risk judgment index. Without considering the influence of adsorption temperature and adsorption pressure, the

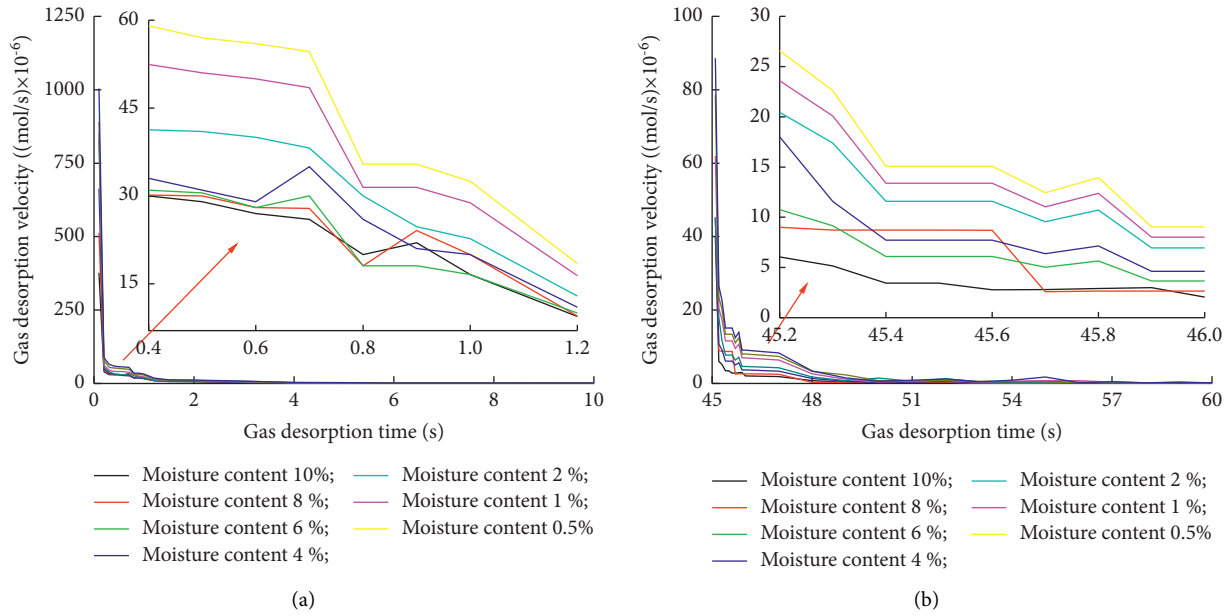


FIGURE 8: The relationship between desorption velocity and time of methane in coal. (a) Time range 0 s–10 s; (b) time range 45 s–60 s.

methane diffusion coefficient D of coal is constant, so the index value of different coal samples will be significantly affected by moisture content. The greater the amount of methane adsorbed, the greater the effect of moisture content on IVDCG. Under the condition of constant equilibrium gas adsorption pressure and the same coal sample, the lower the water content, the larger the index ΔP ; the higher the water content, the smaller the index ΔP . In addition, IVDCG has a certain relationship with the adsorption constant of coal. According to the outburst risk judgment index IVDCG, the final adsorption capacity of coal can be estimated.

Table 1 indicates that the moisture content has a significant effect on the measurement of IVDCG. The higher the moisture content, the lower the IVDCG. In order to study the change of IVDCG with moisture content, regression analysis was carried out on the measured IVDCG of methane in coal samples with different moisture contents.

The regression analysis results of the test data are shown in Table 2. The regression analysis showed that the R -square of the exponential function in the fitting curve of the test data was the largest, so it could be concluded that the measured data of IVDCG decreased exponentially, while the moisture content of the coal samples increased. It can be seen from Figure 9 that when the equilibrium moisture content is reduced by 9.5%, the reduction rate of the outburst risk judgment index ΔP is 34.9%. So, we know that IVDCG is significantly affected by moisture content. With the increase of equilibrium moisture content in coal samples, the decrease of IVDCG decreases. It can be concluded that the experimental data show that IVDCG is greatly affected by the equilibrium moisture content.

The relationship between outburst risk judgment index IVDCG and the equilibrium moisture content of coal samples is shown in Figure 9. References [28–30] have demonstrated that IVDCG directly varies significantly with

TABLE 1: Index ΔP measurement results.

CH ₄	M _{ad} (%)	0.5	1	2	4	6	8	10
	ΔP (mmHg)	17.9	15.8	13.8	10.0	7.3	5.4	4.1

TABLE 2: The regression analysis results.

Model	Fitting formula	Adj. R -square
Linear	$\Delta P = 17.07 - 1.43 * M_{ad}$	0.9464
Exponential	$\Delta P = 18.07 * \exp(-M_{ad}/5.6) + 1.08$	0.9978
Logarithmic	$\Delta P = 15.66 - 4.68 * \ln(M_{ad})$	0.9735
Power	$\Delta P = 15.59 * M_{ad}^{-0.47}$	0.8953

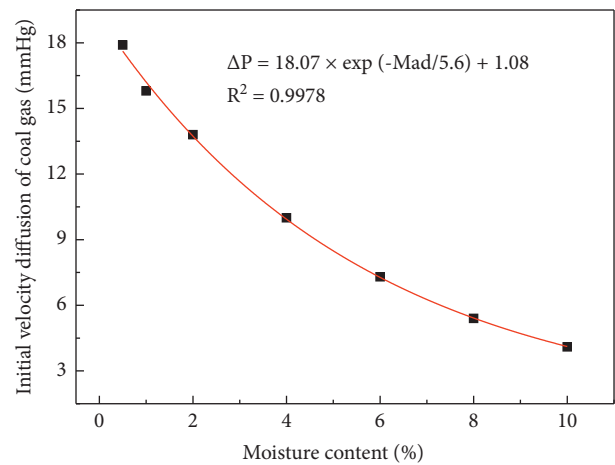


FIGURE 9: The relationship between IVDCG and equilibrium moisture content.

the humidity of coal samples, but there is no experimental data and description for coals with different moisture contents. It can be seen from Figure 9 that this relationship

TABLE 3: Indicator thresholds.

Coal seam	ΔP (mmHg)	ΔP (mmHg)
The critical value	≥ 10	< 10
Outburst risk	Danger	Safe

can be fully described by the exponential function equation of $\Delta P = k \exp(-A * M_{ad}) + B$ (k is the moisture influence coefficient, its value indicates the degree of moisture affecting IVDCG; A is the attenuation of IVDCG, whose value represents the effect of moisture on the rate of decline; B is a constant).

According to the outburst critical value of IVDCG (as shown in Table 3) [11], when the moisture content of the experimental coal sample in the adsorption of methane is higher than 4%, the coal seam should be identified as nonoutburst coal seam. Under methane adsorption pressure of 0.1 MPa, it is confirmed that the outburst risk in low moisture content is much greater than that in high moisture content.

In addition, studies have shown that the outburst risk judgment index IVDCG (ΔP) has a certain relationship with the adsorption constants (a and b) [36]. Therefore, the initial rate of methane diffusion can be used to approximate the final coal adsorption capacity.

The outburst risk judging index ΔP is an index of the coal ability to absorb gas under standard atmospheric pressure (0.1 MPa) and the gas desorption rate when it is suddenly exposed to air. The diffusion performance of coal to gas is the result of the combined effect of coal's physical and mechanical properties and impurities in coal. Under the condition of the same moisture content, the greater the IVDCG, the greater the outburst risk [13].

Index ΔP is one of the outburst prediction indicators, and the critical value is 10 mmHg. When $\Delta P \geq 10$ mmHg, the coal seam has outburst risk; when $\Delta P < 10$ mmHg, the coal seam has no outburst risk and is relatively safe.

According to the exponential function equation obtained from the test, it can be seen that with the increase of the moisture content of the coal sample, the index ΔP of IVDCG decreases exponentially. Especially when the moisture content of coal samples increases to more than 4%, the index ΔP of IVDCG will decrease below the critical value of 10 mmHg. It can be seen that in the coal samples using water injection measures to measure IVDCG, with the increase of coal sample moisture, the index ΔP of IVDCG decreases, thus covering the outburst risk information, which will lead to inconsistent actual results [37–40].

Due to the small amount of data in this experiment, the correction of the experimental data will continue to be carried out in future research.

4. Conclusions

- (1) The greater the methane adsorption capacity, the greater the effect of moisture content on IVDCG. Under the condition of constant equilibrium methane adsorption pressure, the lower the moisture content, the larger the index ΔP ; the higher the moisture content, the smaller the index ΔP .

- (2) The rate of desorption of methane decreases with time at a great rate at the initial time. Then, the desorption rate keeps decreasing. For the experimental data with a moisture content of 10%, the desorption gas velocity is slightly larger than that after the unstable fluctuation curve. However, the total amount of desorbed methane is still increasing rapidly. The total desorbed methane gap between the 0–10 s and 45–60 s time periods increases with time.
- (3) Outburst judgment index IVDCG is greatly affected by moisture content. The relationship between IVDCG and equilibrium moisture content can be fully described by the exponential function equation of $\Delta P = ke - A M_{ad} + B$. As the equilibrium moisture content increases, the exponential ΔP decreases exponentially.
- (4) When the moisture content increases to more than 4%, the index ΔP of IVDCG will decrease to below the critical value of 10 mmHg, so the coal seam should be identified as a nonoutburst.
- (5) When determining the outburst judgment index ΔP , the moisture content should be consistent with the moisture content on-site. If the critical value (10 mmHg) is adopted, the critical value of the response index should be adjusted according to the actual moisture content after water injection.

Data Availability

The data used to support the findings of this study are available from the corresponding author upon request.

Conflicts of Interest

The authors declare that they have no conflicts of interest.

Acknowledgments

This work was financially supported by the National Natural Science Foundation of China (52104204), the Cultivation and Exploration and Innovation Project of New Academic Seedlings of Guizhou Institute of Technology (GZLGXM-04), the Natural Science Foundation of Chongqing China (cstc2019jcyj-msxmX0633, cstc2019jcyj-bsh0041, and cstc2020jcyj-msxmX0972), the Natural Science Foundation of Shandong Province (ZR2021QE170), the Science Innovation and Entrepreneurship Special Funded Projects of China Coal Technology and Engineering Group (2020-TD-ZD007), and the Science and Technology Planning Project of Jiulongpo District (2020-02-005-Y), which are gratefully acknowledged.

References

- [1] A. Tahmasebi, J. Yu, Y. Han, and X. Li, "A study of chemical structure changes of Chinese lignite during fluidized-bed drying in nitrogen and air," *Fuel Processing Technology*, vol. 101, pp. 85–93, 2012.

- [2] K. Kotarska, W. Dziemianowicz, and A. Wierczyńska, "The effect of detoxification of lignocellulosic biomass for enhanced methane production," *Energies*, vol. 14, no. 18, pp. 1–14, 2021.
- [3] X. Li, S. Chen, Q. Zhang, X. Gao, and F. Feng, "Research on theory, simulation and measurement of stress behavior under regenerated roof condition," *Geomechanics and Engineering*, vol. 26, pp. 49–61, 2021.
- [4] U. Hee, V. Lee, and Z. Semenovich, "About possibilities to improve current outburst hazard prediction based on updated mechanism of coal and gas outburst," *Mining Report*, vol. 152, no. 2, pp. 161–170, 2016.
- [5] B. B. Beamish and P. J. Crosdale, "Instantaneous outbursts in underground coal mines: an overview and association with coal type," *International Journal of Coal Geology*, vol. 35, no. 1–4, pp. 27–55, 1998.
- [6] A. Fisne and O. Esen, "Coal and gas outburst hazard in Zonguldak Coal Basin of Turkey, and association with geological parameters," *Natural Hazards*, vol. 74, no. 3, pp. 1363–1390, 2014.
- [7] X. l Li, S. j Chen, S. m Liu, and Z. h Li, "AE waveform characteristics of rock mass under uniaxial loading based on Hilbert-Huang transform," *Journal of Central South University*, vol. 28, no. 6, pp. 1843–1856, 2021.
- [8] C. Wang, D. Song, C. Zhang, L. Liu, Z. Zhou, and X. Huang, "Research on the classification model of coal's bursting liability based on database with large samples," *Arabian Journal of Geosciences*, vol. 12, no. 13, p. 411, 2019.
- [9] S. M. Liu, X. L. Li, D. K. Wang, and D. Zhang, "Investigations on the Mechanism of the Microstructural Evolution of Different Coal Ranks under Liquid Nitrogen Cold Soaking," *Energy Sources, Part A: Recovery, Utilization, and Environmental Effects*, vol. 32, pp. 1–17, 2020.
- [10] R. Dhuot, "La genèse précoce des différences sociales dans les habitudes alimentaires," *Research Gate*, vol. 15, Article ID 02069319, 2018.
- [11] National Mine Safety Administration, *Regulation of Coal and Gas Outburst Prevention and Control*, China coal industry publishing home, China: beijing, 2019.
- [12] S. Norbert, A. Pajdak, K. Kozieł, and L. T. P. Braga, "Methane emission during gas and rock outburst on the basis of the unipore model," *Energies*, vol. 12, no. 10, pp. 1999–2022, 2019.
- [13] D. Wu, Y. Zhao, Y. Cheng, and F. An, "ΔP index with different gas compositions for instantaneous outburst prediction in coal mines," *Mining Science and Technology*, vol. 20, no. 5, pp. 723–726, 2010.
- [14] J. Sobczyk, "A comparison of the influence of adsorbed gases on gas stresses leading to coal and gas outburst," *Fuel*, vol. 115, pp. 288–294, 2014.
- [15] M. Y. Chen, Y. P. Cheng, H. R. Li, L. Wang, K. Jin, and J. Dong, "Impact of inherent moisture on the methane adsorption characteristics of coals with various degrees of metamorphism," *Journal of Natural Gas Science and Engineering*, vol. 55, pp. 312–320, 2018.
- [16] J. Cordeiro, A. L. Magalhães, A. A. Valente et al., "Experimental and theoretical analysis of the diffusion behavior of chromium(III) acetylacetonate in supercritical CO₂," *The Journal of Supercritical Fluids*, vol. 118, pp. 153–162, 2016.
- [17] X. Du, Y. Cheng, Z. Liu et al., "CO₂ and CH₄ adsorption on different rank coals: a thermodynamics study of surface potential, Gibbs free energy change and entropy loss," *Fuel*, vol. 283, Article ID 118886, 2021.
- [18] L. Xu, C. Jiang, and S. Tian, "Experimental study of the gas concentration boundary condition for diffusion through the coal particle," *Journal of Natural Gas Science and Engineering*, vol. 21, pp. 451–455, 2014.
- [19] S. Wang, D. Elsworth, and J. Liu, "Rapid decompression and desorption induced energetic failure in coal," *Journal of Rock Mechanics and Geotechnical Engineering*, vol. 7, no. 3, pp. 345–350, 2015.
- [20] H. Zhu, Y. Zhang, S. Fang, Y. Huo, H. Wang, and G. Cheng, "Methane adsorption influence and diffusion behavior of coking coal macromolecules under different moisture contents," *Energy & Fuels*, vol. 34, no. 12, pp. 15920–15935, 2020.
- [21] H. Ullah, G. Liu, B. Yousaf et al., "Hydrothermal dewatering of low-rank coals: influence on the properties and combustion characteristics of the solid products," *Energy*, vol. 158, pp. 1192–1203, 2018.
- [22] H. Mu, Y. Bao, D. Song, and D. Su, "Investigation of strong strata behaviors in the close-distance multiseam coal pillar mining," *Shock and Vibration*, vol. 202114 pages, Article ID 1263275, 2021.
- [23] J. Zang, K. Wang, and Y. Yu, "Effects of particle size on diffusion kinetics in Chinese anthracites during CH₄ desorption," *Processes*, vol. 8, no. 5, p. 514, 2020.
- [24] Z. J. Pan, L. D. Connell, M. Camilleri, and L. Connelly, "Effects of matrix moisture on gas diffusion and flow in coal," *Fuel*, vol. 89, no. 11, pp. 3207–3217, 2010.
- [25] X. Jingna, X. Jun, N. Guanhua, S. Rahman, S. Qian, and W. Hui, "Effects of pulse wave on the variation of coal pore structure in pulsating hydraulic fracturing process of coal seam," *Fuel*, vol. 264, Article ID 116906, 2020.
- [26] F. Wang, X. Li, B. Cui et al., "Experimental study on adsorption promotion and desorption restrain of gas-containing coal in low-temperature environment," *Arabian Journal of Geosciences*, vol. 14, no. 12, pp. 1124–1212, 2021.
- [27] J. Jiang, Y. Cheng, J. Mou, K. Jin, and J. Cui, "Effect of water invasion on outburst predictive index of low rank coals in dalong mine," *PLoS One*, vol. 10, no. 7, Article ID 0132355, 2015.
- [28] S. Alexander and D. Yuliya, "Geophysical criterion of pre-outburst coal out squeezing from the face space into the working," *International Journal of Mining Science and Technology*, vol. 29, no. 3, pp. 152–159, 2019.
- [29] W. Haidong, T. Yang, W. Deyue, S. Xin, and G. Jiahui, "Experimental study on mechanical properties of briquette coal samples with different moisture content," *Geofluids*, vol. 2021, pp. 1–11, 2021.
- [30] K. Yamakawa and K. Fukutani, "Nuclear spin conversion of H₂, H₂O, and CH₄ interacting with diamagnetic insulators," *Journal of the Physical Society of Japan*, vol. 89, no. 5, Article ID 051016, 2020.
- [31] Y. Yang and S. Liu, "Estimation and modeling of pressure-dependent gas diffusion coefficient for coal: a fractal theory-based approach," *Fuel*, vol. 253, pp. 588–606, 2019.
- [32] Y. Liang, F. Wang, X. Li, C. Jiang, L. Li, and Y. Chen, "Study on the influence factors of the initial expansion energy of released gas," *Process Safety and Environmental Protection*, vol. 117, pp. 582–592, 2018.
- [33] B. Guo, Y. Li, F. Jiao, T. Luo, and Q. Ma, "Experimental study on coal and gas outburst and the variation characteristics of gas pressure," *Geomechanics and Geophysics for Geo-Energy and Geo-Resources*, vol. 4, pp. 355–368, 2018.
- [34] C. Wang, S. Yang, J. Li, X. Li, and C. Jiang, "Influence of coal moisture on initial gas desorption and gas-release energy characteristics," *Fuel*, vol. 232, pp. 351–361, 2018.
- [35] Z. Wang, X. Tang, G. Yue, B. Kang, C. Xie, and X. Li, "Physical simulation of temperature influence on methane sorption and

- kinetics in coal: benefits of temperature under 273.15 K,” *Fuel*, vol. 158, pp. 207–216, 2015.
- [36] K. Jin, Y. Cheng, T. Ren et al., “Experimental investigation on the formation and transport mechanism of outburst coal - gas flow: implications for the role of gas desorption in the development stage of outburst,” *International Journal of Coal Geology*, vol. 194, pp. 45–58, 2018.
- [37] Y. Zhou, H. Li, J. Huang et al., “Influence of coal deformation on the Knudsen number of gas flow in coal seams,” *Energy*, vol. 233, Article ID 121161, 2021.
- [38] M. Pillalamarry, S. Harpalani, and S. Liu, “Gas diffusion behavior of coal and its impact on production from coalbed methane reservoirs,” *International Journal of Coal Geology*, vol. 86, no. 4, pp. 342–348, 2011.
- [39] E. S. Alias, M. Mukhtar, and R. Jenal, “Instrument development for measuring the acceptance of UC&C: a content validity study,” *International Journal of Advanced Computer Science and Applications*, vol. 10, no. 4, pp. 187–193, 2019.
- [40] B. Nie, X. Liu, L. Yang, J. Meng, and X. Li, “Pore structure characterization of different rank coals using gas adsorption and scanning electron microscopy,” *Fuel*, vol. 158, pp. 908–917, 2015.

Research Article

Deformation Mechanism of the Coal ahead of Fully Mechanized Caving Face under High-Intensity Mining Condition

Can Zhao,¹ Liang Chen ,² Bing Wu,¹ Jingui Zhang,³ Dahe Yan,⁴ Yang Li,⁵ and Zhiheng Cheng⁵

¹China University of Mining and Technology-Beijing, Beijing 100083, China

²Safety Branch, China Coal Research Institute, Beijing 100013, China

³Shenmu Energy Bureau of Shaanxi Province, Shenmu 719300, China

⁴Shaqu No. 1 Mine of Huajin Coking Coal Co., Ltd., Liulin 033300, China

⁵North China Institute of Science and Technology, Beijing 101601, China

Correspondence should be addressed to Liang Chen; 3303178898@qq.com

Received 17 September 2021; Revised 22 November 2021; Accepted 25 November 2021; Published 16 December 2021

Academic Editor: Qian Chen

Copyright © 2021 Can Zhao et al. This is an open access article distributed under the Creative Commons Attribution License, which permits unrestricted use, distribution, and reproduction in any medium, provided the original work is properly cited.

In order to study the coal deformation and failure mechanism in fully mechanized caving face under the high-intensity mining, based on the equivalent mechanical model of transversely isotropic cylindrical coal with fractures, the equivalent equations for axial, radial, and volume strains of coal sample loaded in linear elastic and plastic stages were derived in this paper. The equivalent mechanical model shows good reliability through the conventional triaxial experiment. Taking the N1206 workface in Yuwu coal mine of Luan group as the example, we have simulated the stress concentration factor of the coal body ahead of the working face with FLAC and divided three regions according to stress distribution in coal mining. Mathematical equations were derived to express the horizontal and vertical stress, which provide theoretical guidance of the stress paths in triaxial experiment about real mining stress environment simulation. Experimental results show that the volume strain's value is about 0.4% in the coal mass deformation progress of axial compression increasing slowly area. In axial compression increasing rapidly area, the volume strain's value varies from 0.41% to 0.27%, and the radial strain changes from compression deformation to expansion deformation gradually. The volume strain of coal sample increases sharply in axial compression releasing rapidly area; meanwhile, there are good linear relationships between Poisson's ratio and axial strain and radial strain.

1. Introduction

China's coal seam gas is richly endowed, and its reserves are roughly comparable to those of natural gas. Gas flow in coal seams is a complex process of mutual coupling between gas transport and solid deformation of coal seams [1]. With the further extension of coal mining depth, the pressure gradient of coal seam gas is larger than that of shallow coal seam, and the gas content in coal seam also increases gradually [2], which makes the working face more prone to gas gushing and coal and gas protrusion and other power disaster accidents. Therefore, this coal seam gas has become an important factor to restrict the safe and efficient production of coal mines [3]. Intensive study on the deformation and

failure mechanism of coal body ahead of fully mechanized caving face is helpful to make the corresponding fracture and seepage fields of coal body clear [4–6]. It has important theoretical guiding significance and engineering application value for the gas control and coal and gas outburst prevention in high gas working face [7, 8].

With the advance of the working face, the front coal body would successively become the original rock stress area, the stress concentration area, and the pressure relief area, where the elastic deformation and plastic deformation gradually occur until the coal-body fracture. At present, the relevant research at home and abroad focuses on the determination of “three areas” of coal body ahead of working face. Xie et al. [9] studied the distribution law of mining-induced stress of

coal body ahead of fully mechanized caving by establishing a mechanical model of coal body damage in working face. The isotropic damage model established by Hansen and Schreyer [10, 11] was used to study the damage characteristics of coal body. Pu and Miao [12] used RFP software to simulate the distribution characteristics of support pressure ahead of fully mechanized caving face, and the scope of “three zones” of fully mechanized caving working face was divided. Jiang and Hu [13, 14] used the microseismic monitoring system to determine the width of the “three zones” of coal body ahead of the working face. In addition, Su and Huang et al. [15, 16] simulated the in situ stress field through deformation and failure tests of coal samples under different stress paths, and the deformation and failure laws of coal body ahead of the working face were also studied. Jianping et al. [17] used a triaxial test platform with gas-contained coal and rock samples to study the transformation law of strain and permeability of coal body under load.

Due to the differences between the loading and unloading paths of triaxial test and the real stress state of coal body ahead of the working face, how to improve the accuracy of the test and then quantitatively judge the deformation of coal body still needs to lucubrate, especially for the deformation characteristics study of coal body ahead of fully mechanized caving face under high-intensity mining condition. Based on equivalent pore-fracture mechanical model of cylindrical coal sample, the stress-strain equation of coal sample when loaded in the plastic stage is derived in this paper. The horizontal stress and vertical stress distributions of coal body in the relief zone, stress concentration zone, and normal pressure zone ahead of fully mechanized caving working face are obtained by using numerical simulation. According to the real working face stress distribution in different stages, the GCTS triaxial instrument is then used to load and unload simultaneously the axial pressure and confining pressure to the coal sample. The deformation characteristics of coal body and the development of fractures under the real stress environment of fully mechanized caving face are emphatically studied. The research results provide a reference for the study of coal and gas solid-gas coupling law, which is of great significance to realize the coming of coal and gas in the high-strength fully mechanized caving face.

2. Theoretical Analysis of Deformation of Coal Sample under Loading

As a typical sedimentary rock, coal seam has obvious stratification [18], and this porous medium consists of cracks and the coal matrix which contains a solid skeleton and pores [19]. Considering the coal body as transverse isotropic material and the pores as isotropic material, Xue [20] proposed a pore-crack equivalent mechanical model as shown in Figure 1, and the equivalent radial strain, equivalent axial strain, and equivalent volume strain of coal samples during linear elastic deformation are derived.

In the linear elastic deformation stage, the equivalent displacements $\tilde{\varepsilon}_x$, $\tilde{\varepsilon}_y$, and $\tilde{\varepsilon}_z$ along x , y , and z directions of the equivalent coal and rock mass model would have the relationship shown in the following equation:

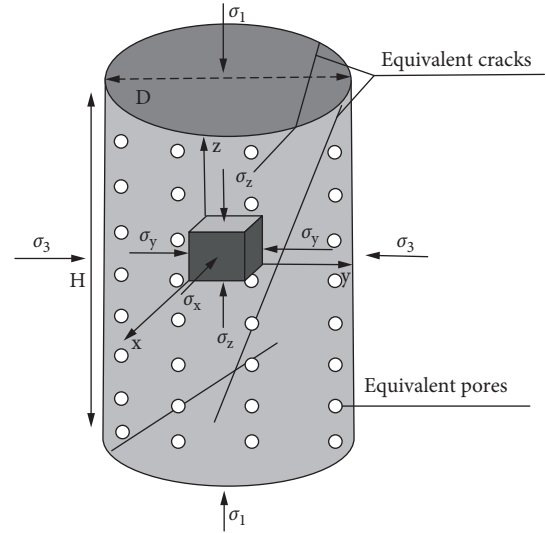


FIGURE 1: Equivalent mechanical model of the coal containing pores and cracks [20].

$$\begin{cases} \tilde{\varepsilon}_x = \frac{(\delta_{\phi x} + \delta_{\tau x} + \delta_{ox})}{D}, \\ \tilde{\varepsilon}_y = \frac{(\delta_{\phi y} + \delta_{\tau y} + \delta_{oy})}{D}, \\ \tilde{\varepsilon}_z = \frac{(\delta_{\phi z} + \delta_{\tau z} + \delta_{oz})}{H}, \end{cases} \quad (1)$$

where $\delta_{\phi x}$, $\delta_{\phi y}$, and $\delta_{\phi z}$ are the pore displacements of coal samples along x , y , and z directions, respectively. $\delta_{\tau x}$, $\delta_{\tau y}$, and $\delta_{\tau z}$ are the displacements of coal matrix, respectively. D is the diameter of the cylindrical coal sample, mm; H is the height of the coal sample, mm.

Therefore, the equivalent volume strain of the media in the elastic stage is

$$\tilde{\varepsilon}_v = \tilde{\varepsilon}_x + \tilde{\varepsilon}_y + \tilde{\varepsilon}_z. \quad (2)$$

However, in coal's conventional triaxial mechanical test, the coal would experience the compaction stage, elasticity stage, and volume expansion stage from the initial stress loading to the failure, successively. The linear elastic deformation is only a part of the process and further analysis of the subsequent plastic deformation is required.

When the coal-rock mass enters the plastic deformation stage, its strain state is not only related to the loading and unloading stress state but also related to the loading and unloading path, where the plastic constitutive relation between incremental stress and incremental strain can only be established. According to increment theory [19], there must be a small increment in the total strain $d\varepsilon_{ij}$ containing the elastic strain increment $d\varepsilon_{ij}^e$ and the plastic strain increment $d\varepsilon_{ij}^p$, when a small increment in the external load existed, where $d\varepsilon_{ij} = d\varepsilon_{ij}^e + d\varepsilon_{ij}^p$.

According to the characteristics of pore-crack structure, it is considered that the whole deformation of coal body consists of coal matrix deformation, pore deformation, and crack deformation on the surface of coal body. The strain increment at each place in the coal body $d\varepsilon_{ij}$ includes the matrix deformation increment $d\varepsilon_{ij}^{\phi}$, the main fracture deformation increment $d\varepsilon_{ij}^r$, and the pore deformation increment inside the coal body $d\varepsilon_{ij}^o$. Since most of the deformable pores are compacted after the compaction stage of coal and rock mass, the pore deformation at this stage is ignored. Therefore, the plastic stage strain increment includes the matrix deformation increment of coal body and the main fracture deformation increment of coal body.

$$d\varepsilon_{ij} = d\varepsilon_{ij}^{\phi} + d\varepsilon_{ij}^r. \quad (3)$$

In the plastic deformation stage, elastic strain $\varepsilon_{ij}^{\phi e}$ and plastic strain $\varepsilon_{ij}^{\phi p}$ occur in the coal-rock matrix. According to the increment theory,

$$d\varepsilon_{ij}^{\phi} = d\varepsilon_{ij}^{\phi e} + d\varepsilon_{ij}^{\phi p}. \quad (4)$$

When elastic deformation occurs in the coal-rock matrix, the generalized Hooke's law is still satisfied. The elastic strain increment along x , y , and z directions is

$$\begin{cases} d\varepsilon_x^{\phi e} = \frac{(d\sigma_3 - \nu_x d\sigma_1 - \nu_x d\sigma_3)}{E_x}, \\ d\varepsilon_y^{\phi e} = \frac{(d\sigma_3 - \nu_x d\sigma_1 - \nu_x d\sigma_3)}{E_x}, \\ d\varepsilon_z^{\phi e} = \frac{(d\sigma_3 - 2\nu_z d\sigma_3)}{E_z}. \end{cases} \quad (5)$$

The constitutive equations of plastic strain increment along x , y , and z directions of coal matrix are obtained by applying the incremental theory when the coal transformed

to the plastic strain, as shown in equation (6). Parameter $d\lambda$ is a nonnegative scalar proportional coefficient, which is related to the loading path and $d\lambda = 3d\varepsilon_i/2d\sigma_i$.

$$\begin{cases} d\varepsilon_x^{\phi p} = \frac{1}{3}d\lambda(\sigma_3 - \sigma_1), \\ d\varepsilon_y^{\phi p} = \frac{1}{3}d\lambda(\sigma_3 - \sigma_1), \\ d\varepsilon_z^{\phi p} = \frac{2}{3}d\lambda(\sigma_1 - \sigma_3). \end{cases} \quad (6)$$

Combined with equations (5) and (6), it can be concluded that the displacements of coal-rock mass matrix

along x , y , and z directions when it transformed to the plastic stage are

$$\begin{cases} d\delta_x^{\phi} = \left[\frac{(d\sigma_3 - \nu_x d\sigma_1 - \nu_x d\sigma_3)}{E_x} + \frac{1}{3}d\lambda(\sigma_3 - \sigma_1) \right] \left(D - \sum_{i=1}^n \frac{h_i}{\sin \theta} \right), \\ d\delta_y^{\phi} = \left[\frac{(d\sigma_3 - \nu_x d\sigma_1 - \nu_x d\sigma_3)}{E_x} + \frac{1}{3}d\lambda(\sigma_3 - \sigma_1) \right] \left(D - \sum_{i=1}^n \frac{h_i}{\sin \theta} \right), \\ d\delta_z^{\phi} = \left[\frac{(d\sigma_3 - 2\nu_z d\sigma_3)}{E_z} + \frac{2}{3}d\lambda(\sigma_1 - \sigma_3) \right] \left(D - \sum_{i=1}^n \frac{h_i}{\cos \theta} \right). \end{cases} \quad (7)$$

When the coal is in the plastic state, especially in the volume expansion stage, the constitutive equation would be obtained by using the D-P criterion as the yield condition of the coal expansion [20–23], where τ is the shear stress of coal body, σ_m means normal stress, and α and k are the test constants only related to the internal friction angle and cohesion of coal body, as shown in the following equation (8):

$$\begin{cases} f(\sigma_m, \tau) = -\tau + \alpha\sigma_m^2 + k\sigma_m, \\ \tau = \frac{\sqrt{2}}{3}(\sigma_1 - \sigma_3), \\ \sigma_m = \frac{1}{3}(\sigma_1 + 2\sigma_3). \end{cases} \quad (8)$$

When studying the displacement caused by the crack on the coal surface, the normal stress and shear stress on the equivalent crack surface of the coal body can be obtained according to equation (8). When the coal body is in the plastic state, the nonlinear changes would occur on the normal stiffness, tangential stiffness parallel to the crack, and angular stiffness perpendicular to the crack on the surface of a single crack, and corresponding instantaneous increments are dk_n , $dk_{f//}$, and $dk_{f\perp}$ respectively. As shown in Figure 2, the displacement increments of multiple groups of cracks along x , y , and z directions are

$$\begin{cases} d\delta_x^\tau = 0, \\ d\delta_y^\tau = \sum_{i=1}^n \left\{ \frac{1}{3}\sigma_1 \left(\frac{\sqrt{2} \sin \theta h_i}{dk_n} - \frac{\cos \theta l_i}{dk_{f//}} \right) - \frac{1}{3}\sigma_3 \left(\frac{\sqrt{2} \sin \theta h_i}{dk_n} + \frac{2 \cos \theta l_i}{dk_{f//}} \right) \right\}, \\ d\delta_z^\tau = \sum_{i=1}^n \left\{ \frac{1}{3}\sigma_1 \left(\frac{\sqrt{2} \cos \theta h_i}{dk_n} + \frac{\sin \theta l_i}{dk_{f//}} \right) + \frac{1}{3}\sigma_3 \left(\frac{2 \sin \theta l_i}{dk_{f//}} - \frac{\sqrt{2} \cos \theta h_i}{dk_n} \right) \right\}. \end{cases} \quad (9)$$

Therefore, the equivalent displacement strains of coal body in the plastic stage along x , y , and z directions are

$$\begin{cases} \widetilde{d\varepsilon}_x = \frac{d\delta_x^\phi}{D}, \\ \widetilde{d\varepsilon}_y = \frac{(d\delta_y^\phi + d\delta_y^\tau)}{D}, \\ \widetilde{d\varepsilon}_z = \frac{(d\delta_z^\phi + d\delta_z^\tau)}{H}. \end{cases} \quad (10)$$

Therefore, the equivalent volume strain of coal in the plastic stage is

$$\widetilde{d\varepsilon}_V = \frac{d\delta_x^\phi}{D} + \frac{d\delta_y^\phi + d\delta_y^\tau}{D} + \frac{d\delta_z^\phi + d\delta_z^\tau}{H}. \quad (11)$$

3. The Verification by Triaxial Mechanical Test of Coal-Rock Mass

The test coal sample is obtained from the N1206 fully mechanized caving face of No. 3 coal seam, Yuwu coal mine, Luan Group, where the buried depth is 460–510 m and the average dip angle is 3~8°. According to the Specification of Gas Geological Map of No. 3 Coal Seam of Yuwu coal mine [24], the relative gas emission of this mine is

16.93~19.55 m³/t, which is a high gas mine. The porosity of coal seam is 4.54~6.79%, the average bulk density is 1.44 t/m³, the hardness coefficient is 0.45~0.62, and the hardness of coal body is soft. Large block coal samples are selected in the coal body ahead of the working face, and the standard size samples ($\Phi 50 \text{ mm} \times H100 \text{ mm}$) is drilled along the parallel bedding direction. The GCTS triaxial test platform was used to test by the displacement control method. In the period of triaxial tests, the confining pressure was held at 6 MPa, and the axial pressure was loaded at the rate of 0.03% mm/min until failure.

The quality of sample ($\Phi 49.41 \text{ mm} \times H102 \text{ mm}$) is 274.76 g. The density is 1.40 g/cm³ and the porosity of the coal sample is 5.58%. As shown in Figure 3, two main cracks can be observed on the cylindrical surface of the coal sample: the length of fissure 1 is 63 mm, extending upward to the upper end face, and fissure 2 is 44 mm, extending downward to the lower end face. Therefore, the two main cracks have a certain influence on the macroscopic mechanical properties of coal samples. At present, there are few studies on the transverse isotropic mechanical parameters of coal samples with cracks. The mechanical test data of different coal bodies are given according to [25]. The rates of elastic modulus and Poisson's ratio along the vertical bedding direction (E_\perp and ν_\perp) and the parallel bedding direction ($E_{//}$ and $\nu_{//}$) are 2.5~7.7 and 1.8~3.1, respectively. According to the occurrence conditions of No. 3 coal seam, values of rates are 4.8 and 2.1, respectively. It can be seen that E_\perp and $E_{//}$ are 3800 MPa and 792 MPa,

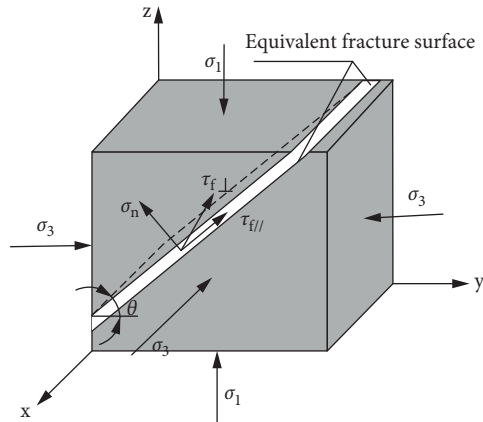


FIGURE 2: Stress analysis of the coal's fracture surface.

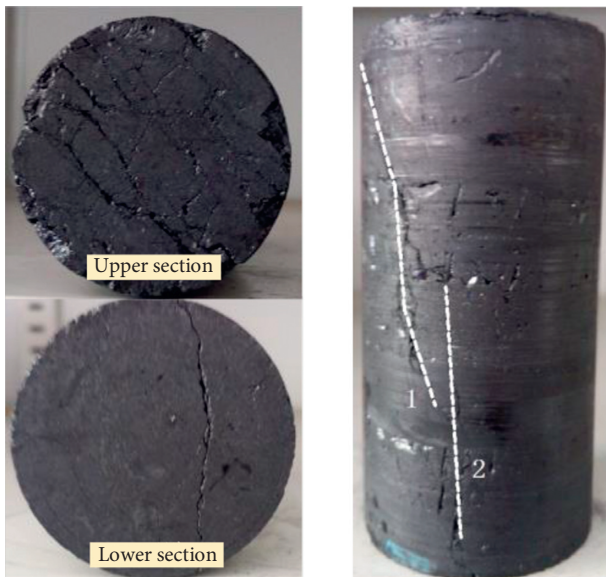


FIGURE 3: Major fracture distribution of coal surface.

respectively, and ν_{\perp} and $\nu_{//}$ are 0.38 and 0.18, respectively, where the elastic modulus corresponding to coal matrix and coal pore medium is 792 MPa and 2900 MPa, respectively, and corresponding Poisson's ratio is 0.32 and 0.18. The details of surface crack parameters of coal are shown in Table 1. Since displacement control was adopted in this test, the axial compression loading rate was 0.03 mm/min, and the corresponding average axial stress rate was 0.013 MPa/min. It can be concluded that the plastic deformation coefficient $d\lambda = 0.023$. According to the value of [26], the internal friction angle of the sample is 39.8° and the average cohesion force is 7.4 MPa.

The stress-strain curve obtained from the test is shown in Figure 4. Based on the anisotropic deformation of the coal, it can be considered that the stress and strain of the coal have a linear relationship in the compaction stage and the elastic deformation stage, and, in the yield stage, the stress and strain show nonlinear-correlation relationship when the coal is in the plastic deformation stage, which is

consistent with the theoretical analysis results in Section 1. In the failure stage of coal mass, the main failure mode is shear dilatation. The confining pressure is 6 MPa and the axial pressure is in the range of 0~15 MPa. Correspondingly, the axial strain, radial strain, and volume strain are 0~0.00299, 0~-0.00126, and 0~-0.00048, respectively, and the sample is in the linear elastic stage. When the axial compression is greater than 15 MPa, it belongs to the plastic stage, and the corresponding axial strain is 0.00299~0.00618.

Due to the displacement controlling loading method, the axial strain still changes linearly before the failure. The radial strain and volume strain are -0.00126~-0.00831 and 0.00048~-0.01042, respectively, which are 5.6 and 22.7 times of the anisotropic strain in the linear elastic stage. Figure 5 shows the stress-strain curves of linear elastic stage and plastic stage calculated by theory, which well verifies the axial, radial, and volume strain curves obtained from the tests. Although it is large in the range of isotropic strain, it can be used to reflect the isotropic deformation law of coal samples in the process of triaxial loading and unloading.

Because of the large dispersion of coal and rock and the large variation of different coal seams, the theoretical results described in the previous section are only applicable to the same coal seam. Therefore, we can later select enough coal and rock samples to achieve generalization of the theoretical analysis.

4. Study on Loading Deformation of Coal Body ahead of Fully Mechanized Caving

4.1. Numerical Simulation and Theoretical Analysis. The structure of Yuwu coal mine is mostly monoclinic in the direction of south and north. The angle of its wings is less than 10° . 3# coal seam is located in the lower part of Permian Shanxi Formation, and its buried depth range is 350~642 m with 6 m thickness coal seam, which is stable coal seam, and its vitrinite reflectance is 2.01~2.94% belonging to mainly lean and lean coal. The relative gas emission of this mine is 16.93~19.55 m^3/t , which is a high gas mine. Taking the N1206 working face of the mine as an example, the working face adopts top coal caving and the machine mining height is 3.3 m, while the coal drawing thickness is 3 m. The working face inclination length is 300 m, and the strike length is 1200 m. The daily coal output of this high-intensity mining is 8800~12000 t, and the buried depth of coal seam in the area is 480 m. The 109 m overburden seam, including 18 layers of strata, above the coal seam is selected as the research object, and the top-down lithology of the overburden seam is followed by mudstone (2.4 m), siltstone (5.3 m), fine-grained sandstone (2.2 m), medium grained sandstone (3.8 m), sandy mudstone (2.3 m), siltstone (5.19 m), mudstone (3.5 m), siltstone (2.5 m), medium-grained sandstone (2.5 m), mudstone (1.4 m), siltstone (4.1 m) sandy mudstone (2.8 m), siltstone (2.6 m) of coarse grained sandstone (2 m), and the sediment layer, interaction (50 m). The numerical model of the fully mechanized caving working face was established by FLAC software with 400 m length (x

TABLE 1: Mechanical property parameters of coal's fracture structure.

Main fractures	Normal stiffness K_n /MPa	Tangential stiffness K_s /MPa	Main fractures distribution	
			Angles ($^\circ$)	Widths (cm)
Fracture 1	3800	1200	71	0.15
Fracture 2	3800	1200	84	0.04

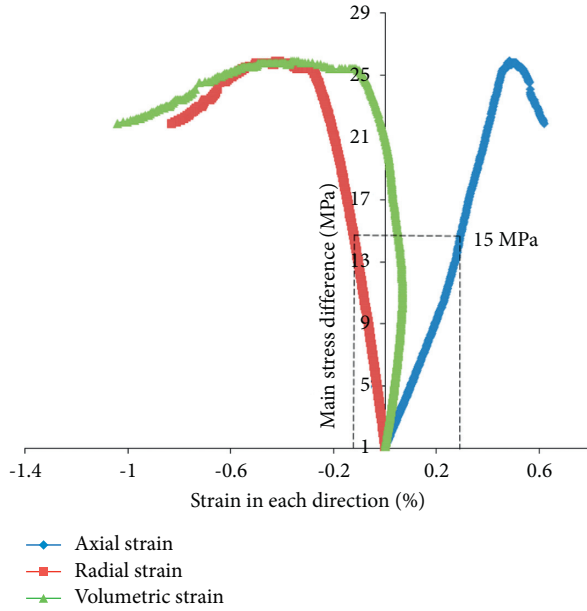


FIGURE 4: Full stress-strain curves of loaded coal sample.

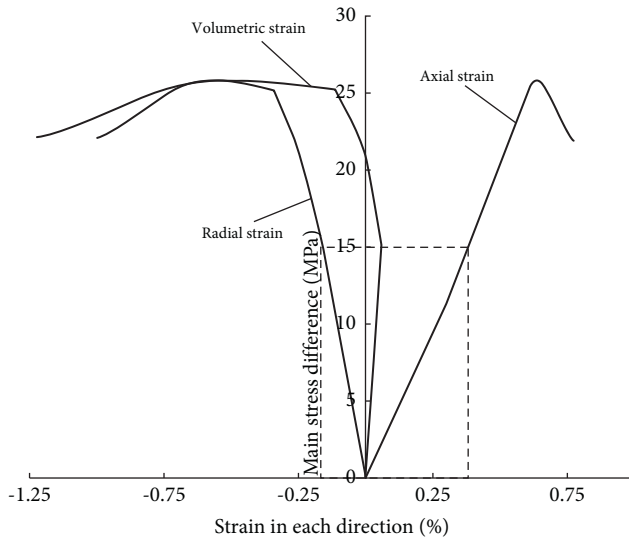


FIGURE 5: The curves of linear elastic and plastic stage.

direction), 400 m width (y direction), and 200 m height (z direction). The loading stress of the overburden of the model is 8.1 MPa, and the failure criterion of coal body is Coulomb mole. Therefore, the stress distribution diagram of the coal body ahead of fully mechanized caving can be obtained, as shown in Figure 6.

Due to the fact that these two roadways have the pressure relief effect on the coal body near the fully mechanized caving working face, the stress will be unloaded at the coal wall near roadways, and the stress concentration phenomenon will not appear when the horizontal stress along X -axis applied on the coal body in front of the working face is greater than that of the initial stress; and one side of the working face along the Y -axis direction is the coal wall of the working face where the stress is completely unloaded; the other side is the initial stress zone without stress concentration. However, the peak value of stress concentration is smaller than that of vertical stress along the Z -axis due to the pressure relief of roadways. With the cylindrical coal sample in this test, stress path in the Y -axis and Z -axis can be used to guide the loading mode of confining pressure and axial pressure in the test to reflect the reality horizontal stress in the field. According to the horizontal stress expressions of mining dynamics of 3 different typical mining conditions of mining unloading proposed by Xie Heping, the common features of 3 typical mining are refined. Although the peak bearing pressure coefficients and the influence range of the 3 typical mining methods are different, the overall bearing pressure curve ramp-up zone can be further divided into the slowly increasing pressure zone and the sharply increasing pressure zone. Therefore, according to Figure 7, the mining stress on the coal body in front of the working face can be divided into three zones: Rapid step-down zone (L_1), rapid pressurization zone (L_2), and slow pressurization zone (L_3). The results show that the stress concentration coefficient at the peak value of vertical stress concentration is 2.23, and the horizontal stress concentration coefficient is 0.65. At the boundary between the slow pressure boost zone and the rapid pressure boost zone, the vertical stress concentration coefficient is 1.16, and the horizontal stress concentration coefficient is 0.92. Therefore, the stress distribution characteristics of the fully mechanized caving working face and the axial pressure and confining pressure values corresponding to each critical point in the simulation test can be obtained, as shown in Figure 7.

According to the actual situation of fully mechanized caving working face, the vertical stress of coal body at point A in front of the working face is the residual strength of coal body R_C , and the horizontal stress is 0, as shown in Figure 8. On the influence of different mining speed and coal seam occurrence conditions, the length of the three zones will change in front of the corresponding fully mechanized caving working face. According to [27], the actual stress distribution curve of the fully mechanized caving face can be simplified as a linear piecewise function of stress and distance. The mining speed of fully mechanized caving face is set as V , and the corresponding time of the three zones is

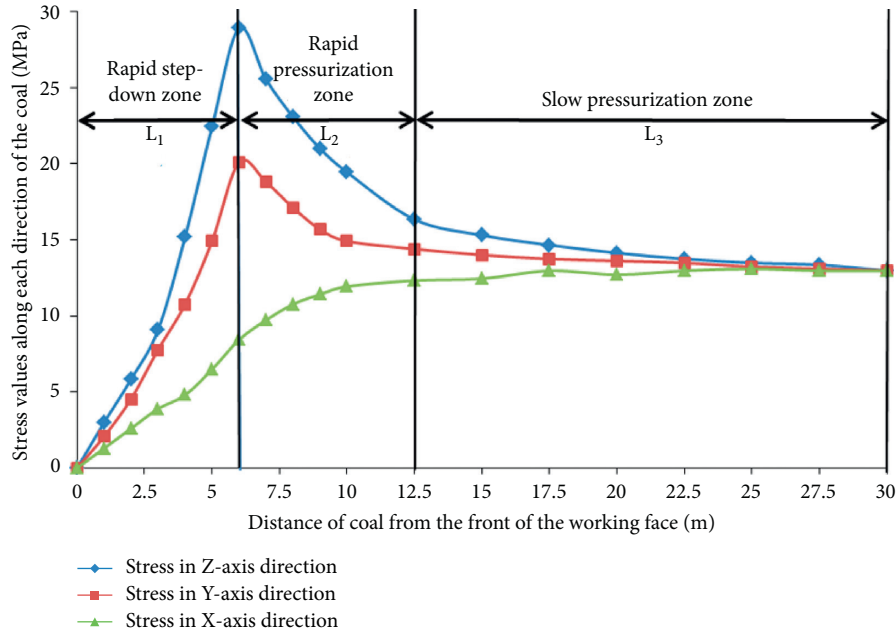


FIGURE 6: Isotropic stress distributions of the coal within 30 m ahead of working face.

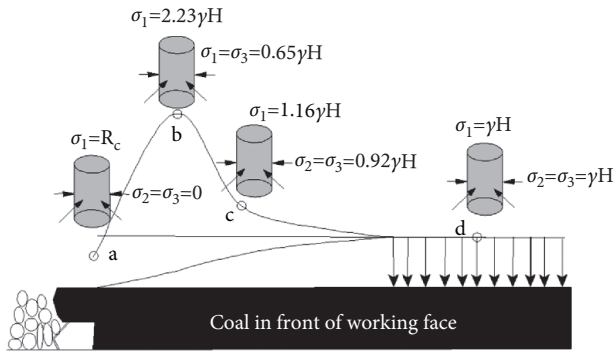


FIGURE 7: Stress distributions of the coal in fully mechanized caving face.

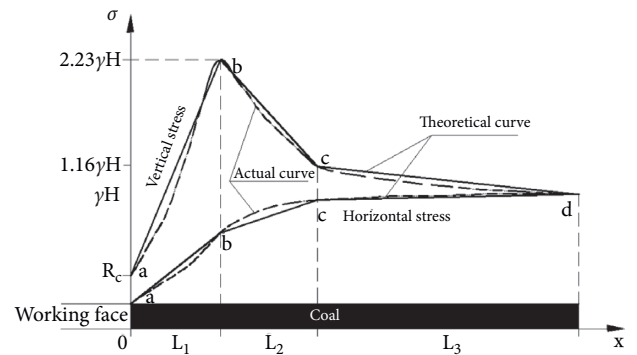


FIGURE 8: The actual stress distribution curve and theoretical curve.

obtained as L_1/V , L_2/V , and L_3/V , respectively. Given that the slopes of the line in the corresponding interval of vertical stress are K_1 , K_2 , and K_3 , the corresponding values are $(2.23\gamma H - R_c)/L_1$, $-1.07\gamma H/L_2$, and $-0.16\gamma H/L_3$, which correspond to the axial compression loading rates of $(R_c - 2.23\gamma H)v$, $1.07\gamma Hv$, and $0.16\gamma Hv$ in different stages of

triaxial test, respectively. To ensure that the test is closer to the real stress state of the actual fully mechanized caving face, the loading rates of confining pressure are $-0.65\gamma Hv$, $-0.27\gamma Hv$, and $-0.08\gamma Hv$, respectively.

Therefore, the vertical stress distribution function can be obtained as follows:

$$\sigma_1 = \begin{cases} \frac{2.23\gamma H - R_c}{L_1}x + R_c, & (0 \leq x < L_1), \\ -\frac{1.07\gamma H}{L_2}x + \frac{1.16\gamma HL_2 - 0.07\gamma HL_1}{L_2}, & (L_1 \leq x < L_1 + L_2), \\ -\frac{0.16\gamma H}{L_3}x + \frac{L_3\gamma H - (L_1 + L_2)0.16\gamma H}{L_3}, & (L_1 + L_2 \leq x < L_1 + L_2 + L_3). \end{cases} \quad (12)$$

The corresponding horizontal stress distribution function is

$$\sigma_3 = \begin{cases} \frac{0.65\gamma H}{L_1}x, & (0 \leq x < L_1), \\ \frac{0.27\gamma H}{L_2}x + \frac{0.65\gamma HL_2 - 0.27\gamma HL_1}{L_2}, & (L_1 \leq x < L_1 + L_2), \\ \frac{0.08\gamma H}{L_3}x + \frac{0.92L_3\gamma H - (L_1 + L_2)0.08\gamma H}{L_3}, & (L_1 + L_2 \leq x < L_1 + L_2 + L_3). \end{cases} \quad (13)$$

4.2. Analysis of Simulation Test Results. The diameter of the test coal sample is 49.31 mm, the height is 100.55 mm, and the mass is 260.62 g. The surface of the sample contains cracks. According to the daily output of N1206 working face (8800 ~ 12000 t), the daily advance would be about 5 m, and the corresponding mining speed is calculated as 0.014 m/min. The correlation coefficient (original rock stress is 10 MPa; the residual strength of coal is 4.7 MPa) is substituted. In the triaxial simulation test, the axial compression loading rates of the coal body in front of fully mechanized caving are 0.023 MPa/min, 0.149 MPa/min, and -0.246 MPa/min in the slow pressurization area, rapid pressurization, and rapid unloading area, and the confining pressure unloading rates at corresponding stages are 0.011 MPa/min, 0.038 MPa/min, and 0.091 MPa/min, respectively. In the process of the test, the axial pressure and confining pressure of the coal sample were first loaded to the original stress, and then the triaxial loading and unloading test guided by the above test parameters could truly reflect the deformation characteristics of the coal body in the “three zones” in front of the fully mechanized caving working face. The stress-strain-Poisson’s ratio variation curve obtained from the test is shown in Figure 9. Subsections I, II, and III, respectively, correspond to slow pressurization area, rapid pressurization, and rapid unloading area.

As seen in Figure 9, the stress-strain curve of the coal sample is consistent with the mechanical deformation characteristics of conventional triaxial mechanical tests. However, it is illuminated that the volume strain of coal body changes little in the slow pressurized region and the rapid pressurized region. In the relief zone, the volume strain shows a sudden increment, which is 6.7 times that of the previous two stages, indicating that the coal deformation in the fully mechanized caving face is mainly volumetric expansion. The trend of different stages is analyzed as follows:

- (1) The slow pressurization stage. Due to the initial rock stress, there existed certain axial and radial strains in the coal. In this stage, the ranges axial strain is from 0.12 to 0.37%, and the volume strain decreases slightly from 0.44% to 0.41%. Poisson’s ratio ranges from 0.23 to 0.035, which indicates that axial compression is the dominant deformation of coal at

this stage, and both axial strain and volume strain belong to linear elastic deformation.

- (2) Rapid pressurization stage. At this stage, the axial strain is 0.37~0.51%, volume strain is 0.42~0.24%, and Poisson’s ratio is 0.035~0.495. Compared with the previous stage, the volume compression strain in this stage gradually decreases, and the axial deformation is always dominant, but the radial strain turns from compression deformation to expansion deformation. As the axial compression increases rapidly and the confining pressure decreases slowly at this stage, the increase rate of axial strain is greater than that of radial strain, and the volume strain is still a compression deformation, gradually changing from linear elastic deformation to plastic yield deformation.
- (3) Rapid pressure relief stage. At this stage, the axial strain is 0.51~0.59%, the volume strain is 0.24%~-0.037, and Poisson’s ratio is 0.035~0.495. At this stage, the coal mass undergoes plastic yield to macroscopic failure. When the volume strain is -0.018, the volume of the sample expands sharply, and the maximum expansion rate is 3.7%. Both volume strain and radial strain are dominated by expansion deformation, and the corresponding expansion velocity increases firstly and then decreases. Due to the rapid unloading of the confining pressure to 0 at this stage, the internal cracks in the coal gradually expanded and coalesced until failure, and the axial pressure of the coal rapidly decreased to the residual strength of 4.7 MPa. The absolute value of the change slope of Poisson’s ratio changes from less than 1 to greater than 1, indicating that the failure mode of coal samples changes from compression shear failure to dilatancy failure [28]. In addition, it can be concluded that Poisson’s ratio has a good linear relationship with the axial strain and radial strain at this stage, as shown in Figure 10. The corresponding expressions are as follows: $\nu = -1.7794, \varepsilon_{\text{radial}} + 0.0044$; $\nu = 12.505, \varepsilon_{\text{axial}} - 6.5166$. It shows that the axial strain and radial strain in this stage also have a linear relationship, which indirectly proves that the displacement along the shear plane occurs when the macroscopic failure of the coal gradually occurs.

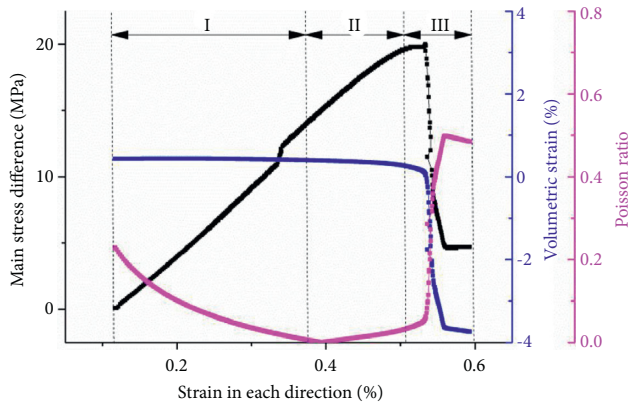


FIGURE 9: The stress-strain-Poisson's ratio curves of coal sample in loading and unloading process.

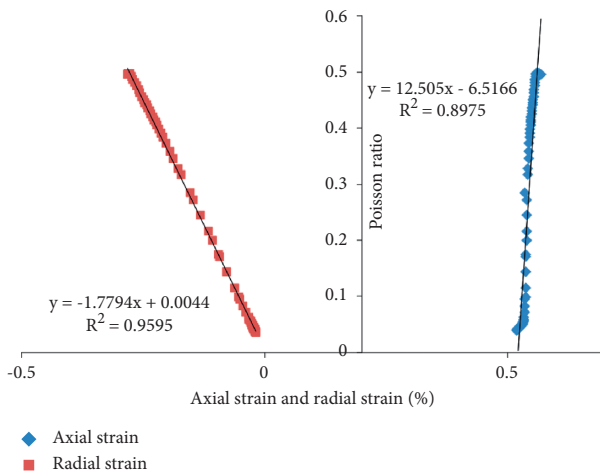


FIGURE 10: Fitting curves among Poisson's ratio and axial strain and radial strain.

5. Conclusions

- (1) The equivalent pore-crack model of transversely isotropic coal pointed out that the plastic stage mainly consists of surface crack deformation and coal matrix deformation, leading to the equivalent axial strain, radial strain, and volume strain equations of coal in the plastic stage under loading condition. The conventional triaxial test proves that this theory can be used to characterize the deformation characteristics of coal.
- (2) Taking the N1206 working face of Yuwu coal mine in Luan as an example, the stress concentration coefficient of the coal body in front of the fully mechanized caving working face is 2.23 with the consideration of mining intensity through numerical simulation. The coal body in front of fully mechanized caving is divided into slow pressurization area, rapid pressurization, and rapid unloading area, and the expressions of vertical stress and horizontal stress in corresponding stages are derived.

- (3) The mining disturbance characteristics of highly intensive fully mechanized caving working face, gained from theoretically analyses, are used to guide the triaxial loading and unloading simulation test, and it is concluded that the axial deformation is dominant in the slow pressurization area. The radial deformation is dominant in the rapidly pressurized region, and the compression deformation turns to the expansion deformation in radial direction. In the rapid unloading area, Poisson's ratio of the coal sample has a linear relationship with the axial strain and radial strain. With the volume expanding rapidly, the internal cracks gradually expand and connect until the failure occurs. When the volume strain is 0.018, the volume deformation increases sharply, and the failure mode changes from compression shear failure to dilatancy failure.
- (4) In this paper, further study is required due to the fact that the influence of gas adsorption and absorption in the process of pressurization and unloading was not considered in the derivation of coal deformation. In addition, considering the large dispersion of raw coal, different locations and larger number of samples should be manufactured in order to make more generalized results.

Data Availability

The data used to support the findings of this study are available from the corresponding author upon request.

Conflicts of Interest

The authors report no potential conflicts of interest.

Acknowledgments

This work was financially supported by the National Natural Science Foundation of China (52074120), Program for Science & Technology Innovation Talents in Universities of Henan Province (19HASTIT047), and Science and Technology Project of Henan Province (182102310012). This support is gratefully acknowledged.

References

- [1] W. Qin, J. Xu, and X. Peng, "Experimental study of coupling between solid and gas during drainage by advance pressure relief in mining-coal seam," *Journal of China University of Mining&Technology*, vol. 41, no. 6, pp. 900–905, 2012.
- [2] G. Hu, J. Xu, H. Wang, Z. Jin, and R. Wu, "Research on a dynamically coupled deformation and gas flow model applied to low-permeability coal," *Journal of China University of Mining&Technology*, vol. 40, no. 1, pp. 1–6, 2011.
- [3] G. Z. Yin, B. He, M. H. Li, J. Cao, H. Qin, and W. P. Li, "Coupling mechanism between flow rate of gas drainage and coal seam abutment stress under mining conditions," *Journal of China Coal Society*, vol. 40, no. 4, pp. 736–741, 2015.
- [4] Y. Xue, J. Liu, P. G. Ranjith, X. Lianga, and S. Wang, "Investigation of the influence of gas fracturing on fracturing characteristics of coal mass and gas extraction efficiency based

- on a multi-physical field model,” *Journal of Petroleum Science and Engineering*, vol. 206, Article ID 109018, 2021.
- [5] Q. Zou, H. Liu, Y. Zhang, Q. Li, J. Fu, and Q. Hu, “Rationality evaluation of production deployment of outburst-prone coal mines: a case study of nantong coal mine in Chongqing, China,” *Safety Science*, vol. 122, Article ID 104515, 2020.
- [6] Q. Zou, H. Liu, Z. Jiang, and X. Wu, “Gas flow laws in coal subjected to hydraulic slotting and a prediction model for its permeability-enhancing effect,” *Energy Sources, Part A: Recovery, Utilization, and Environmental Effects*, pp. 1–15, 2021.
- [7] X. He, *Rheological Dynamics of Coal Rock Containing Gas*, China University of mining and technology press, Xuzhou, China, 1995.
- [8] L. Yuan, “Theory of press-relieved gas extraction and technique system of integrated coal production and gas extraction,” *Journal of China Coal Society*, vol. 36, no. 7, pp. 1067–1074, 2011.
- [9] Z. Chen and H. Xie, “Damage mechanics analysis on the distribution of abutment pressure around a coal face,” *Journal China of Rock Mechanics and Engineering*, vol. 19, no. 4, pp. 436–439, 2000.
- [10] N. R. Hansen and H. L. Schreyer, “A thermodynamically consistent framework for theories of elastoplasticity coupled with damage,” *International Journal of Solids and Structures*, vol. 31, no. 3, pp. 359–389, 1994.
- [11] M. R. Salari, S. Saeb, K. J. Willam, S. J. Patchet, and R. C. Carrasco, “A coupled elastoplastic damage model for geomaterials,” *Computer Methods in Applied Mechanics and Engineering*, vol. 193, no. 27–29, pp. 2625–2643, 2004.
- [12] H. Pu and X. Miao, “Numerical simulation of dynamic falling of overlying rocks and abutment pressure in surrounding rocks for fully-mechanized top-coal caving stope,” *Journal China of Rock Mechanics and Engineering*, vol. 19, no. 4, pp. 3274–3280, 2000.
- [13] H. Shi and F. Jiang, “Study on abutment pressure rule of overlying strata spatial structures based on micro-seismic monitoring,” *Journal China of Rock Mechanics and Engineering*, vol. 27, no. S1, pp. 436–439, 2008.
- [14] G. Hu, *Study on the Characteristics of Strata Behavior and Roof Control in the Large Mining Height Fully-Mechanized Face*, Taiyuan university of technology, Taiyuan, China, 2006.
- [15] C. Su, B. Gao, H. Nan, and X. Li, “Experimental study on acoustic emission characteristics during deformation and failure processes of coal samples under different stress paths,” *Journal China of Rock Mechanics and Engineering*, vol. 28, no. 4, pp. 757–766, 2009.
- [16] G. Yin, Q. Huang, and D. Zhang, “Test study of gas seepage characteristics of gas-bearing coal specimen during process of deformation and failure in geostress field,” *Journal China of Rock Mechanics and Engineering*, vol. 29, no. 2, pp. 336–343, 2010.
- [17] W. Jianping, W. Dengke, and W. Le, “Comparison of permeability between two kinds of loaded coal containing gas samples,” *Journal of China Coal Society*, vol. 29, no. 2, pp. 336–343, 2010.
- [18] S. Zhou and B. Lin, *The Theory of Gas Flow and Storage in Coal Seams*, Coal Industry Publishing House, Beijing, China, 1999.
- [19] Z. Pan and L. D. Connell, “Modelling permeability for coal reservoirs: a review of analytical models and testing data: a review of analytical models and testing data,” *International Journal of Coal Geology*, vol. 92, no. 1, pp. 1–44, 2012.
- [20] D. Xue, *Research on Mechanism of Enhanced Gas Permeability of Coal and Rock under Various Mining Layouts*, China University of Mining and technology (Beijing), Beijing, China, 2013.
- [21] S. Liu and T. Zhang, *Basic Theory of Elasticity and Plasticity*, Huazhong University of Science and Technology, Wuhan, China, press, 2002.
- [22] J. Zheng, *The Correlation between Mining Distressing Law and Gas Migration Ahead of Working Face*, China University of Mining and technology (Beijing), Beijing, China, 2015.
- [23] J. Chen, C. Yang, and Y. Guo, “Study of sealability of caven for natural gas storage in deep salt formation based on compaction-dilatancy boundary of salt,” *Chinese Journal of Rock Mechanics and Engineering*, vol. 28, no. S2, pp. 3302–3308, 2009.
- [24] X. Zhao, Q. Zhang, and G. Dong, *Gas Geological Map Instruction of 3#coal Seam in Yuwu Coal Mine*, China Coal technology Engineering Group Chongqing Research Institute, Chongqing, China, 2010.
- [25] T. Li, X. Wu, and H. Tu, “The measurement and analysis on the mechanical property of coal seam,” *Chinese Journal of Rock Mechanics and Engineering*, vol. 35, no. 2, pp. 328–336, 2013.
- [26] C. Su, B. Guo, and X. Tang, “Research on acoustic emission characteristics of Zhangcun coal samples in two sizes subject to uniaxial compression,” *Journal of China Coal Society*, vol. 4, no. S1, pp. 12–18, 2013.
- [27] D. Xue, H. Zhou, X. Tang, and Y. Zhao, “Mechanism of deformation-induced damage and gas permeability enhancement of coal under typical mining layouts,” *Chinese Journal of Geotechnical Engineering*, vol. 35, no. 2, pp. 328–336, 2013.
- [28] Q. Huang, *Research on Mechanical Characteristics of Gas-Bearing Coal under the Condition of Unloading Confining Pressure*, Chongqing university, Chongqing, China, 2011.

Research Article

Influence of Long Boreholes Layout and Drilling Length on Gas Drainage Based on Multifield Coupling Model of Gas-Bearing Coal

Renjun Feng ^{1,2,3,4}

¹School of Resource & Environment and Safety Engineering, Hunan University of Science and Technology, Xiangtan 411201, Hunan, China

²Work Safety Key Lab on Prevention and Control of Gas and Roof Disasters for Southern Coal Mines, Hunan University of Science and Technology, Xiangtan 411201, Hunan, China

³State Key Laboratory of Gas Disaster Detecting, Preventing and Emergency Controlling, Chongqing 400037, China

⁴China Coal Technology Engineering Group Chongqing Research Institute, Chongqing 400037, China

Correspondence should be addressed to Renjun Feng; fenrenjun2025@163.com

Received 20 June 2021; Revised 28 August 2021; Accepted 9 October 2021; Published 17 November 2021

Academic Editor: ZOU Quanle

Copyright © 2021 Renjun Feng. This is an open access article distributed under the Creative Commons Attribution License, which permits unrestricted use, distribution, and reproduction in any medium, provided the original work is properly cited.

Gas drainage through long seam boreholes is an effective method to prevent gas disasters in coal mines. In this paper, a multifield coupling model of gas migration in gas-bearing coal was first established. Then, a quantitative characterization method of gas drainage effect was put forward. Finally, the extraction effect of long boreholes was obtained under different layouts and drilling lengths. The research results show that, under the arrangement of long boreholes along the seam, the gas pressure around the borehole decreases significantly with the extraction time. There is no extraction blank in the middle of the working face. However, it is easy to cause uneven gas drainage in the combined arrangement of the long boreholes along the seam and the penetrating boreholes. Furthermore, it is found that the drainage volume of the long boreholes along the seam is similar to that of the joint layout under the same drainage time. As the length of the borehole increases, the influencing range of gas drainage increases. When the borehole lengths are 150 m and 240 m, the drainage volumes are about 1.31 and 2.50 times that of the 90 m boreholes, respectively. The research achievements could provide a specific reference for the layout of long boreholes along the bedding and the determination of reasonable parameters for gas drainage on site.

1. Introduction

Gas drainage is an effective way to eliminate the danger of coal and gas outbursts in China at present [1–4]. In recent years, with the development of drilling rig equipment and drilling technology, gas drainage technology with long boreholes has made rapid progress [5–7]. Gas migration significantly affects the gas drainage effect of long boreholes. Therefore, a correct understanding of the law of coal gas migration is of great significance for preventing and controlling coal mine gas disasters and promoting long drilling technology [8–12].

At present, many scholars have studied the multifield coupling model of coal seam gas migration. The coal reservoir is a typical double pore system composed of interlaced fractures and coal matrices [13–15]. Coal seam gas migration

mainly includes two processes: diffusion and seepage. First, the gas is desorbed from the coal matrix and diffused into the fissures under the action of a concentration gradient. This process conforms to Fick's law of diffusion. Then, the gas in the fissure flows to the borehole under the action of the pressure gradient, and this process conforms to Darcy's law [16]. Su et al. [17] described a dual pore model that paralleled coal seam gas migration. The diffusion and seepage of gas in gas drainage are simulated, and the influence of diffusion coefficient on gas pressure evolution and permeability in fractures is analyzed. Dong et al. [18] analyzed the mechanism of negative pressure in gas drainage through a gas-solid coupling model and put forward a method to reduce the negative pressure of drainage to improve gas drainage efficiency. Mora and Wattenbarger [19] summarized the

correct shape factor formulas considering constant drainage rate from a matrix block and constant pressure in the adjacent fractures through numerical simulation. However, the above research mainly analyzed the gas drainage effect in conventional borehole gas drainage. There are few studies on gas drainage with long boreholes along the seam.

On the other hand, to evaluate the effect of long borehole gas drainage, it is necessary to study the reasonable length of the borehole for long borehole drainage [20–22]. If the length of the borehole is too large, due to the attenuation of the negative pressure in the borehole, the gas content at the bottom of the long borehole will be high, making it difficult to reach the drainage index. If the length of the borehole is too short, it will result in low efficiency of gas drainage measures [23–25]. At present, the methods to determine the effective gas drainage radius include on-site measurement and theoretical calculation methods [26, 27]. The on-site measurement mainly determines the residual gas content of the gas after the gas drainage. In terms of theoretical calculations, the effective gas drainage radius is determined mainly based on the gas flow theory in the borehole and the characteristics of coal seam gas seepage. [28, 29] The practice of predecessors in gas drainage has achieved remarkable results. In the case of a short borehole length, the negative pressure of gas drainage in the borehole does not decrease significantly, and there is still a large negative pressure for gas drainage at the bottom of the borehole. After a period of time of extraction, there is little difference in residual gas content before and after the borehole. However, for long boreholes along the bedding, when the negative pressure attenuation is apparent, the residual gas content at the bottom of the borehole is still relatively large. Therefore, it is necessary to study the reasonable length of the borehole for long borehole drainage.

This paper first elaborates and establishes a multifield coupling model of gas migration in coal which considers coal matrix gas diffusion, fissure gas seepage, permeability evolution law, and coal deformation law. Then, the change value of the residual gas content per unit time is used to calculate the gas drainage volume and then quantify the gas drainage effect of the long borehole. Finally, the COMSOL software was adopted, and the fully coupled numerical simulation method was used to analyze the drainage effects of different layouts and lengths of long boreholes along the bedding. The research results are expected to provide a theoretical basis for gas drainage from long boreholes along the bedding.

2. Multifield Coupling Model for Gas-Bearing Coal Seams

2.1. Model Assumptions. The multifield coupling model for gas-bearing coal seams is established based on the following assumptions:

- Coal seam is a homogeneous, isotropic, double-porosity elastic medium
- The influence of water on gas migration in coal seams is ignored
- The coal seam is an isothermal system, and gas is an ideal gas

- The strain of the coal skeleton is infinitesimal [14, 16, 17]

2.2. Effective Stress Principle. In order to better describe the mechanical response of pore and fissure dual media under gas pressure, the effective stress law of dual porous media is introduced when establishing the permeability model [16]:

$$\sigma_{ij}^e = \sigma_{ij} - (\beta_f p_f + \beta_m p_m) \delta_{ij}, \quad (1)$$

where σ_{ij}^e is the effective stress, MPa; σ_{ij} is the total stress, MPa; δ_{ij} is the Kronecker delta (1 for $i=j$ and 0 for $i \neq j$); p_f and p_m are pressure in the fractures and matrix blocks, respectively, Pa; and β_f and β_m are the effective stress coefficients for pore and fracture, respectively.

The effective stress coefficients β_f and β_m of the cracks in (1) can be calculated by the following formulas, respectively:

$$\beta_f = 1 - \frac{K}{K_m},$$

$$\beta_m = \frac{K}{K_m} - \frac{K}{K_s}, \quad (2)$$

where K is the bulk modulus of the coal body, MPa; K_m is the bulk modulus of the coal matrix, MPa; and K_s is the bulk modulus of the coal body skeleton, MPa.

The following formulas can calculate the above three bulk moduli:

$$K = \frac{E}{3(1-2\nu)},$$

$$K_m = \frac{E_m}{3(1-2\nu)}, \quad (3)$$

$$K_s = \frac{K_m}{1-3\phi_m(1-\nu)/[2(1-2\nu)]},$$

where E is the elastic modulus of the coal body, MPa; E_m is the elastic modulus of the coal matrix, MPa; ν is Poisson's ratio of the coal; and ϕ_m is the coal matrix porosity, %.

2.3. Dynamic Evolution Equation of Coal Porosity and Permeability. Palmer and Mansoori [30] proposed a widely used permeability model (PM model) suitable for uniaxial strain conditions. However, the PM model was established based on the coal seam containing only cracks. The coal seam is usually modeled as a dual-porosity medium containing both cracks and pores. Therefore, this study adopts the dual-porosity poroelasticity theory. The revised crack porosity model is shown in the following equation:

$$\frac{\phi_f}{\phi_{f0}} = \frac{\varepsilon_L}{\phi_{f0}} \left(\frac{K}{M} - 1 \right) \left(\frac{p_m}{P_L + p_m} - \frac{p_0}{P_L + p_0} \right) + 1$$

$$+ \frac{1}{M\phi_{f0}} (\beta_f (p_f - p_0) + \beta_m (p_m - p_0)), \quad (4)$$

where ϕ_f is the fracture porosity, %; ϕ_{f0} is the initial fracture porosity, %; ε_L is Langmuir volumetric strain constant; P_L is Langmuir pressure constant; M is the limiting axial

modulus, MPa; and p_0 is the initial pressure in the matrix blocks, Pa.

According to the Kozeny–Carman equation [31, 32], the coal seam permeability k is

$$\frac{k}{k_0} = \left(1 + \frac{1}{M\phi_{f0}} (\beta_f(p_f - p_0) + \beta_m(p_m - p_0)) + \frac{\varepsilon_L}{\phi_{f0}} \left(\frac{K}{M} - 1 \right) \left(\frac{p_m}{P_L + p_m} - \frac{p_0}{P_L + p_0} \right) \right)^3, \quad (5)$$

where k_0 is the coal seam permeability, m^2 .

2.4. Diffusion Equation of Gas in Coal. The mass exchange between the matrix and the fissures in the coal body can be expressed by the following equation:

$$Q_m = D\chi \frac{M_C}{RT} (p_m - p_f), \quad (6)$$

where Q_m is the mass exchange between coal pores and cracks, $\text{kg}/(\text{m}^3 \cdot \text{s})$; χ is the matrix shape factor, m^{-2} ; M_C is the molar mass of methane, kg/mol ; D is gas diffusion coefficient, m^2/s ; R is the universal gas constant, $\text{J}/(\text{mol} \cdot \text{K})$; and T is the coal seam temperature, K.

The following formula can calculate the diffusion coefficient:

$$D = D_0 \exp(-\xi t), \quad (7)$$

where ξ is the attenuation coefficient of the dynamic diffusion coefficient, s^{-1} , and D_0 is the initial gas diffusion coefficient, m^2/s .

According to the Langmuir equation, the gas content per unit volume of coal matrix can be obtained as

$$m_p = \frac{abp_m\rho_c M_C}{(1 + bp_m)V_m} + \phi_m \frac{M_C p_m}{RT}, \quad (8)$$

where m_p is the gas content per unit mass of the coal matrix, kg/m^3 ; ρ_c is the apparent density of the coal, kg/m^3 ; ϕ_m is the matrix porosity, %; a is the Langmuir volume constant, m^3/kg ; b is the reciprocal of Langmuir pressure constant, Pa^{-1} ; and V_m is the molar volume of methane under standard conditions, m^3/mol .

From the conservation of mass, it can be seen that the relationship between the amount of change in matrix gas content and Q_m is

$$\frac{\partial m_p}{\partial t} = -Q_m. \quad (9)$$

Substituting (6) ~ (8) into (9), the governing equation for gas diffusion is

$$\frac{\partial p_m}{\partial t} = -\frac{b\chi V_m (p_m - p_f) (p_m + P_L)^2}{aRT\rho_c + b\phi_m V_m (p_m + P_L)^2} D_0 \exp(-\xi t). \quad (10)$$

2.5. The Seepage Equation of Gas in Coal. According to the law of conservation of mass, the change in gas mass in a fracture is equal to the gas diffused into the fracture by the pore minus the gas flowing into the borehole from the fracture; namely,

$$\frac{M_C}{RT} \frac{\partial \phi_f p_f}{\partial t} = Q_m (1 - \phi_f) - \nabla \left(\frac{M_C}{RT} p_f v_f \right), \quad (11)$$

where v_f is the gas flow velocity in the crack, m/s .

Moreover, the flow of gas in the cracks of the coal body conforms to Darcy's law; then,

$$v_f = -\frac{k}{\mu} \nabla p_f, \quad (12)$$

where μ is the dynamic viscosity of the gas, Pa·s.

By combining the above equations, the governing equation of gas percolation can be obtained as

$$\phi_f \frac{\partial p_f}{\partial t} + p_f \frac{\partial \phi_f}{\partial t} - \nabla \left(p_f \frac{k}{\mu} \nabla p_f \right) = D\chi (p_m - p_f) (1 - \phi_f). \quad (13)$$

2.6. Deformation Equation of Gas-Bearing Coal. The deformation equation of gas-containing coal is composed of the stress balance equation, geometric deformation equation, and stress-strain relationship [33], which can be expressed as

$$Gu_{i,jj} + \frac{G}{1 - 2\nu} u_{j,ji} - \beta_f p_{f,i} - \beta_m p_{m,i} + F_i = 0, \quad (14)$$

where G is the coal's shear modulus, MPa, and u_i is the displacement component in the i -direction.

The above control equations constitute a multifield coupling model for gas-containing coal seams that comprehensively consider the coal skeleton compression effect (effective stress effect) and matrix shrinkage effect. The coupling relationship between the physical fields is shown in Figure 1.

3. Geometric Model and Definite Solution Conditions

3.1. Geometric Model. In order to analyze the effect of gas drainage with long boreholes along the seam, two gas

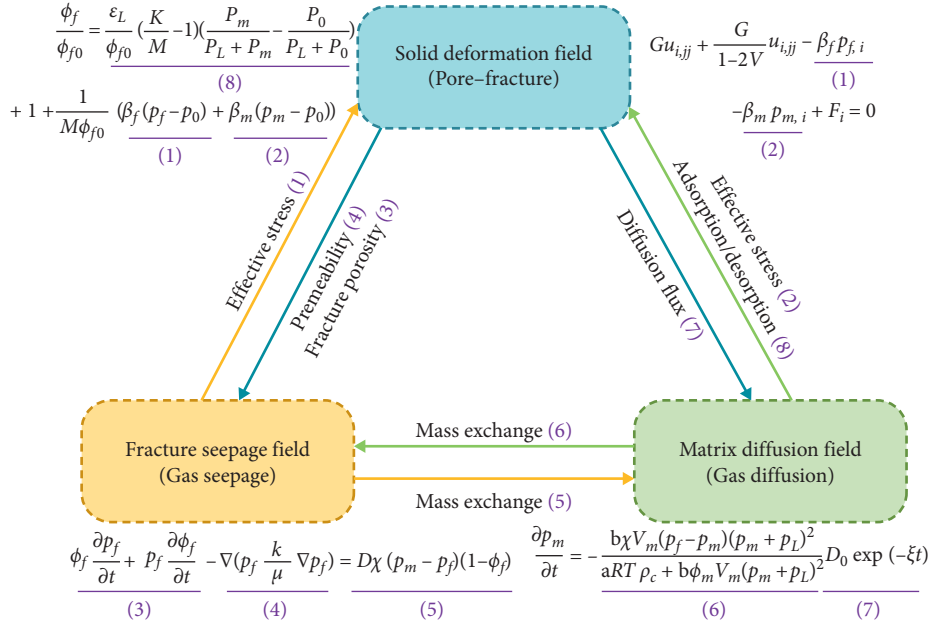


FIGURE 1: Schematic diagram of physics coupling relationship.

drainage schemes under two conditions have been established :

- (1) Gas drainage with long boreholes along the seam
The geometric model is shown in Figure 2. The 240 m long boreholes along the seam were constructed in the direction of the coal seam's inclination in the machine roadway or wind roadway in the working face. The borehole spacing distance is 2 m, and ten long boreholes along the seam were constructed.
- (2) The combination of long boreholes along the seam and penetrating boreholes

The geometric model is shown in Figure 3. The 90 m long boreholes along the seam were constructed in the machine lane and the winding lane in the working face along the direction of the inclination of the coal seam. The borehole spacing distance is 2 m, and 20 long boreholes along the seam were constructed. Moreover, the penetrating boreholes were constructed in the middle of the working face of the bottom-drawing roadway, and the position of the final hole of the penetrating boreholes is shown in Figure 3. The boreholes are spaced 2 m apart in both the strike and inclination directions, and a total of 290 penetrating boreholes have been constructed.

The size of the coal seam under these two drainage schemes is 400×240 m.

The numerical simulation software used in this study is COMSOL Multiphysics. The simulation uses the PDE module and the solid mechanics module in COMSOL to calculate the model. The parameters used in the numerical simulation are shown in Table 1 [17].

3.2. Model Validation. To verify the correctness of the multi-field coupling model of gas-bearing coal seams established in this paper, the use of mathematical models of Liu et al. [16] coal seam gas pressure data was compared to verify. A model consisting of three horizontal coal layers was established. There is a coal seam with a width of 40 meters and a height of 4 meters between the two rock layers. The drill hole is located in the center of the coal seam. The other parameters used in the model are consistent with those in the Liu model. After COMSOL numerical calculation, the experimental results are shown in Figure 4. It can be seen from Figure 4 that the gas-solid coupling model established in this paper is in good agreement with Liu's model.

4. Quantitative Characterization of Gas Drainage Effect in Boreholes

It can be seen from Section 1 that, at time t and $t + \Delta t$, the gas content in the coal seam is

$$m_t = \frac{V_L p_m(t)}{p_m(t) + P_L} \frac{M_c}{V_M} \rho_c + \phi_m \frac{M_c}{RT} p_m(t),$$

$$m_{t+\Delta t} = \frac{V_L p_m(t + \Delta t)}{p_m(t + \Delta t) + P_L} \frac{M_c}{V_M} \rho_c + \phi_m \frac{M_c}{RT} p_m(t + \Delta t). \quad (15)$$

In the formula, m_t and $m_t + \Delta m_t$ represent the gas content in the coal seam when the drainage time is t and $t + \Delta t$, respectively.

According to the above formula, the gas content extracted from the coal seam after the gas drainage of Δt time is as follows:

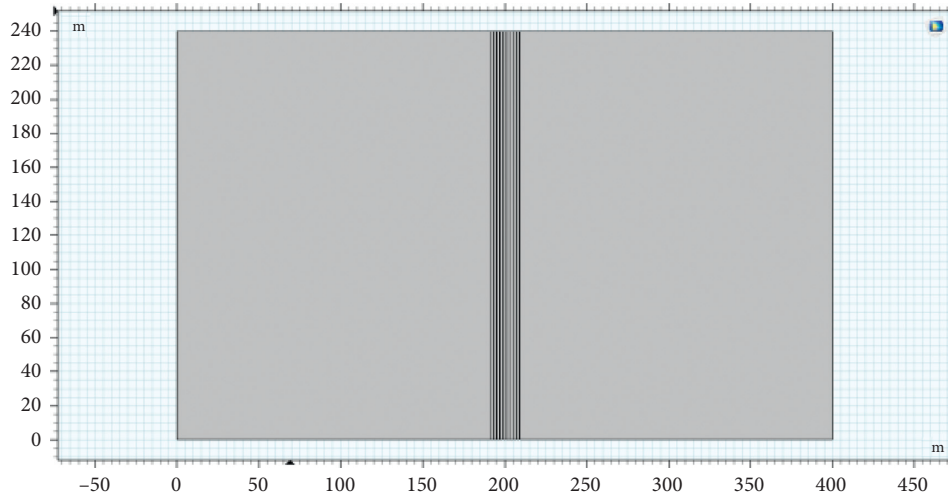


FIGURE 2: The arrangement of long boreholes along the seam.

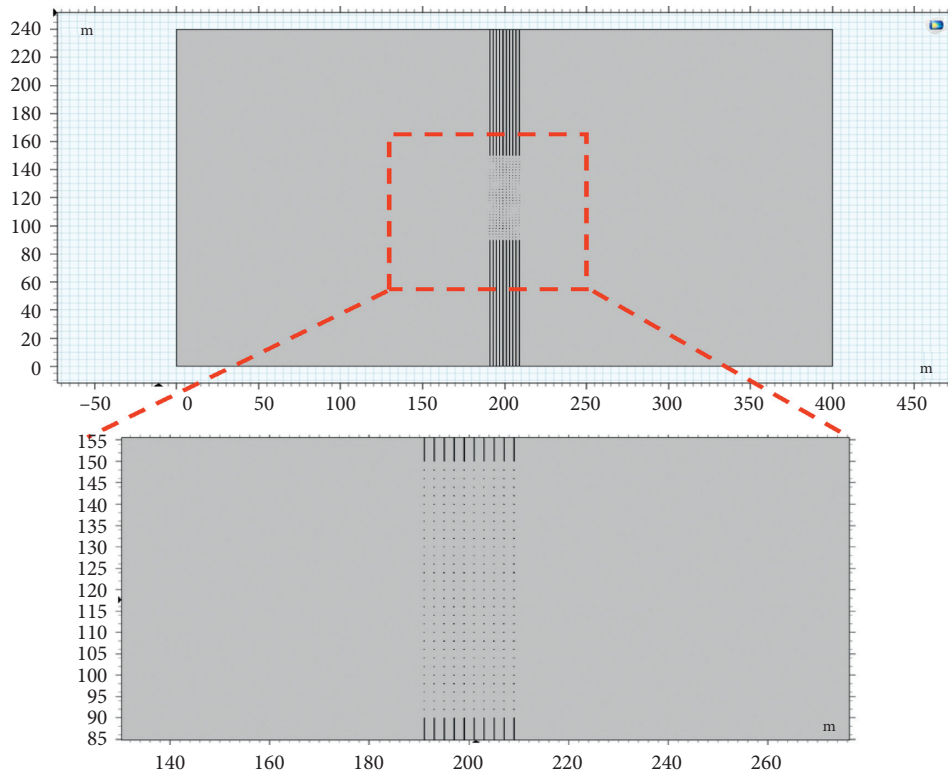


FIGURE 3: Borehole layout method for gas drainage combined with long boreholes along the seam and penetrating boreholes.

$$m_{\Delta t} = \iint_{\Omega} (m_t - m_{t+\Delta t}) dv. \quad (16)$$

Based on the above formula, the gas content extracted within a certain period can be obtained by integration with COMSOL software.

5. Results and Discussion

5.1. Influence of Drilling Layout on the Effect of Gas Drainage.

Figure 5 is a cloud map of coal seam gas content under different drainage times in long boreholes along the seam. It can be seen from Figure 5 that, under the action of negative

TABLE 1: Parameters used in numerical simulation [17].

Parameter	Value
Modulus of elasticity of coal	2713 MPa
Poisson's ratio of coal	0.339
Initial porosity	0.072
Initial gas pressure	1.08 MPa
Initial coal permeability	0.02 mD
Coal initial diffusion coefficient	$1 \times 10^{-12} \text{ m}^2/\text{s}$
Attenuation coefficient	$2 \times 10^{-8} \text{ s}^{-1}$
Langmuir pressure constant	1.8672 MPa^{-1}
Langmuir volume constant	$14.4348 \text{ m}^3/\text{t}$
Coal density	$1250 \text{ kg}/\text{m}^3$
The molar mass of methane	$0.016 \text{ kg}/\text{mol}$
Drainage time	360 d
Time step	1 d
Ambient temperature	293 K

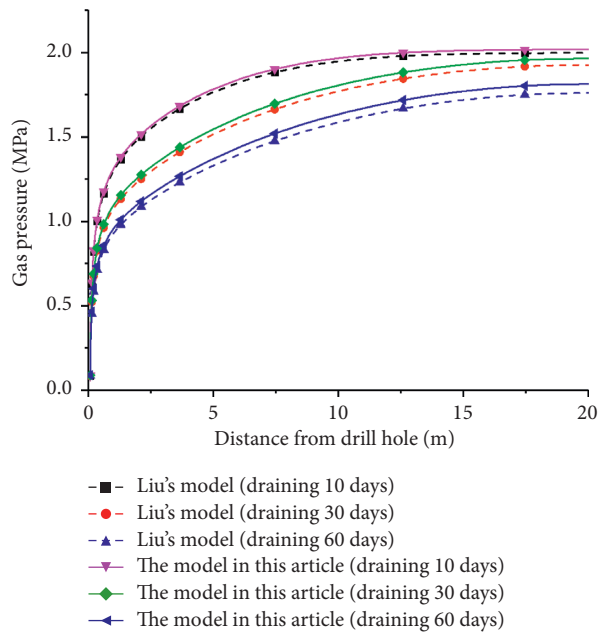


FIGURE 4: Data comparison between the model in this article and Liu's model at different extraction times.

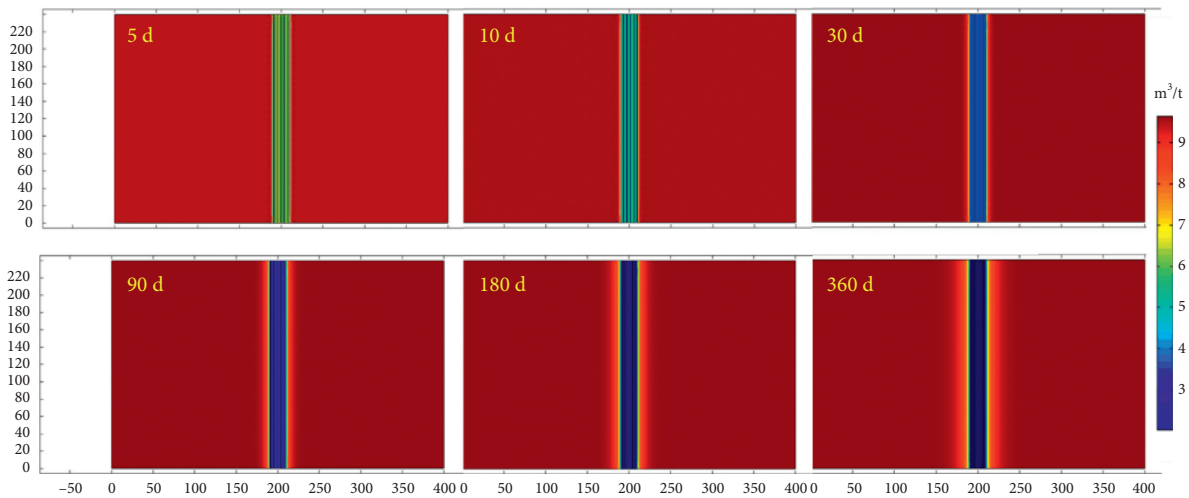


FIGURE 5: Cloud map of coal seam gas content under different drainage time in the case of long boreholes along the seam.

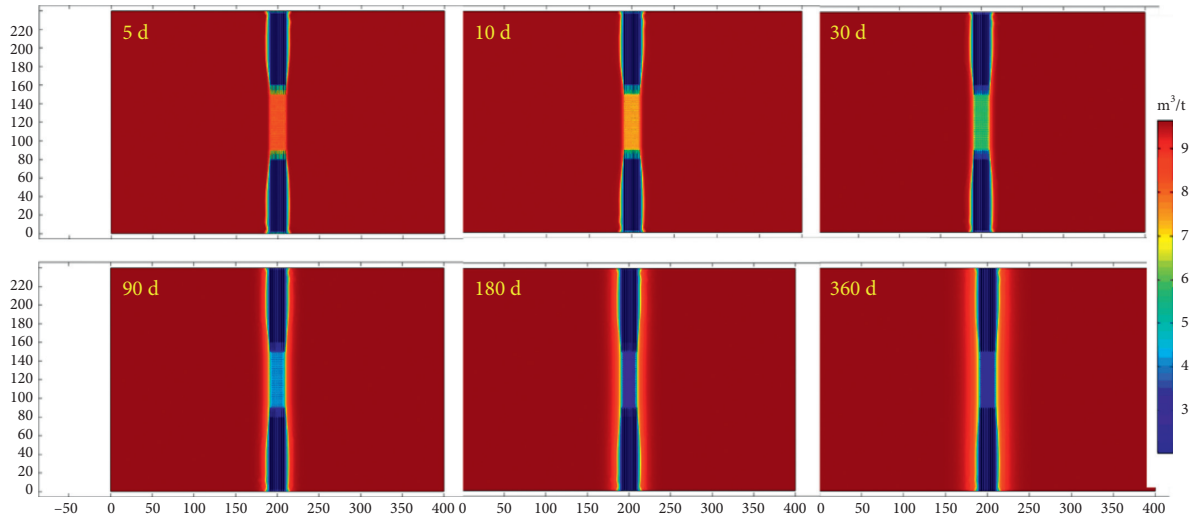
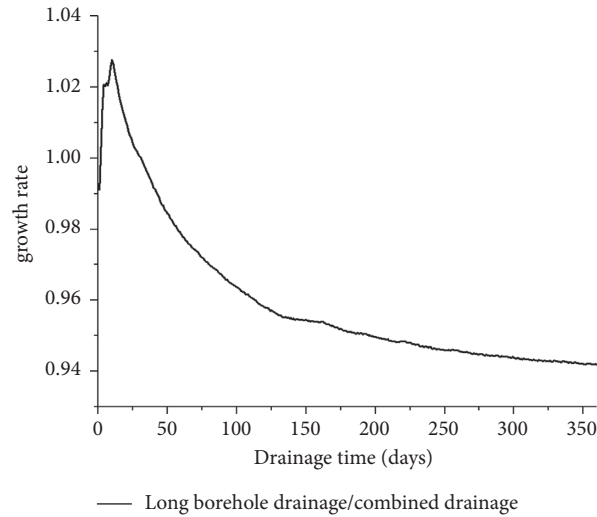


FIGURE 6: Cloud map of coal seam gas content under different drainage times under the combined drainage of long boreholes along the seam and penetrating boreholes.



— Long borehole drainage/combined drainage
 FIGURE 7: Long boreholes drainage growth rate.

pressure in the borehole, the gas pressure around the borehole is significantly lower than that of the distant coal body. Furthermore, because the borehole spacing distance is only 2 m, the gas pressure between the drill holes is significantly reduced, and there is no apparent blank zone. In addition, the length of the borehole reaches 240 meters and runs through the entire working face. Therefore, the contact area between the borehole and the coal body is large, and the drainage effect is good. On the other hand, as the drainage time increases, the gas content around the borehole gradually decreases, and the influence range of borehole drainage gradually increases. For example, after 360 days of drainage, the gas content of the coal body covered by the borehole was significantly reduced to $3 \text{ m}^3/\text{t}$, which was significantly lower than the gas content of 5 days of drainage.

At present, due to limited drilling rig equipment in some domestic mining areas, the construction length of long boreholes along the seam is limited, so there must be a blank

zone of gas drainage in the middle of the working face. To ensure the safety of the working face during the mining period, penetrating boreholes are usually used to extract the coal seam gas in the middle of the working face. The boreholes arrangement in this section is based on the above facts.

Figure 6 is a cloud map of coal seam gas content under different drainage times in combined drainage with long boreholes along the seam and penetrating boreholes. It can be seen from Figure 6 that the distribution of residual gas content in coal seams is different from that in Figure 5. The gas content in long boreholes along the seam drainage area is significantly lower than that of penetrating boreholes drainage area. For example, at five days of drainage, the gas content in the area covered by the long boreholes along the seam has dropped to $4 \text{ m}^3/\text{t}$, while the gas content in the penetrating boreholes covering the coal seam is about $8 \text{ m}^3/\text{t}$. According to the analysis in Section 1, the gas drainage

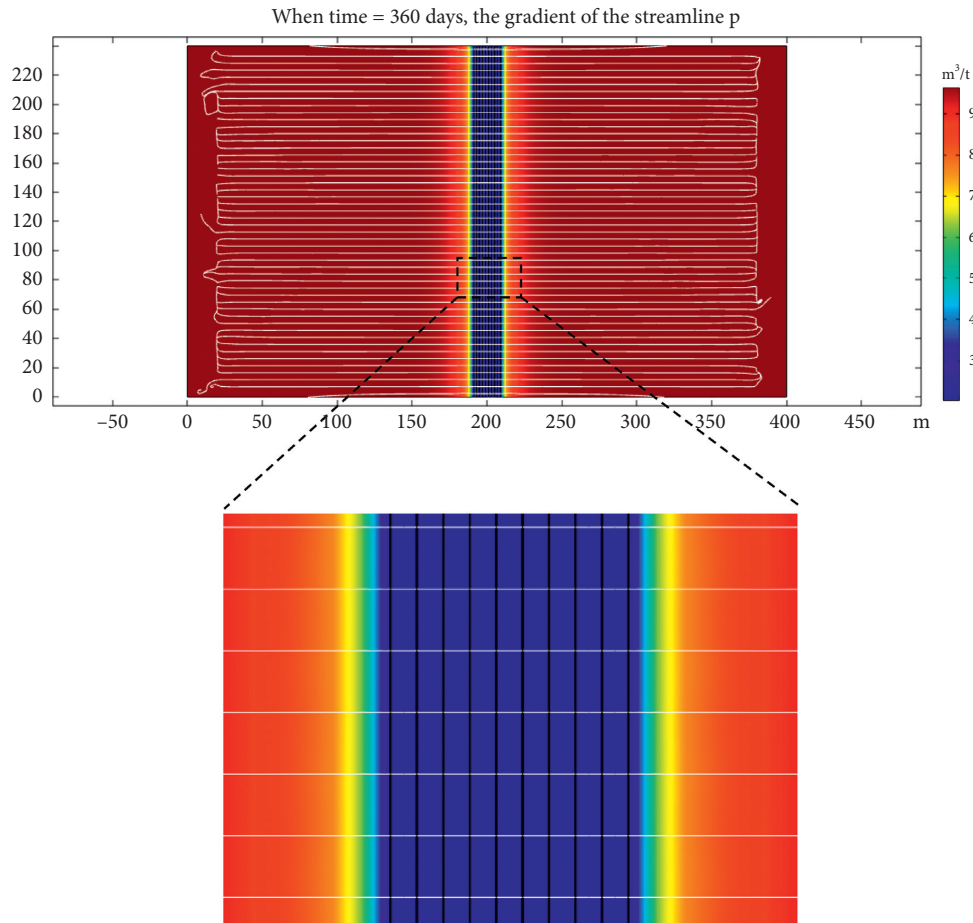


FIGURE 8: Streamline diagram of the long boreholes along the seam.

volume per unit time of a borehole is mainly determined by the permeability and the contact area of the borehole. Therefore, the gas drainage effect of long boreholes along the seam is significantly higher than that of penetrating boreholes. In addition, with the increase of the extraction time, the gas content of the coal body around the borehole is consistent with the previous analysis. One point that needs to be particularly pointed out is that, with the increase of the drainage time, the difference between the gas drainage effect of the long boreholes along the seam and the penetrating boreholes gradually decreases.

For example, at 360 days of drainage, the gas content in the long boreholes along the seam area is about $2.5 \text{ m}^3/\text{t}$, and the gas content in the penetrating boreholes area is also reduced to about $3 \text{ m}^3/\text{t}$.

It can be seen that the drainage effect of the long boreholes along the seam arrangement is significantly higher than that of the combined long boreholes along the seam and penetrating boreholes. However, it is difficult to intuitively compare the drainage effects of the two drilling arrangements based on the distribution cloud map of the residual gas content after coal seam drainage. To solve the problems mentioned above, this paper proposes a quantitative characterization method for the effect of borehole gas drainage in Section 3. Based on this quantitative characterization

method, the gas drainage volume under different borehole layouts can be obtained. This paper takes the combined drainage volume of long boreholes along the seam and penetrating boreholes as the benchmark. It can be concluded that there is an increase in drainage under the condition of long boreholes along the seam relative to the combined drainage, as shown in Figure 7. It can be seen from Figure 7 that the gas drainage volume in the bedding long borehole layout is similar to the gas drainage volume under the combined layout under the same drainage time. For example, in the early stage of drainage, the drainage volume under the long borehole layout is 1.025 times that of the combined drainage, and it gradually decreases in the later stage, down to 0.94 times at the lowest level. In addition, considering the construction cost of tunnel extraction and drilling through layers, it can be considered that the long boreholes along the seam can reduce the pressure and content of coal seam gas faster in the process of gas drainage in coal mines. The danger of gas outbursts in the working face is eliminated, and construction costs are reduced.

Figures 8 and 9 are the streamline diagram of the long boreholes along the seam and the streamline diagram of the combined boreholes through bedding during the 360-day drainage. It can be seen from Figure 8 that the gas migration streamlines of the long boreholes along the seam are

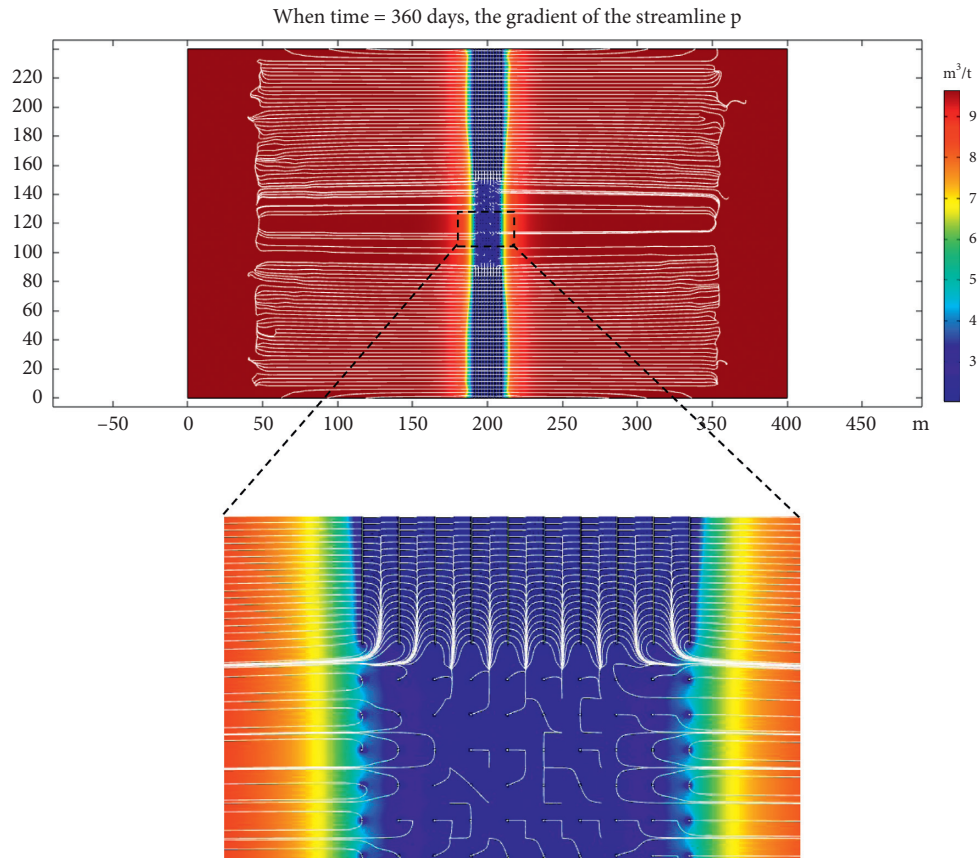


FIGURE 9: Streamline diagram of the combined layout of penetrating boreholes and the long boreholes along the seam.

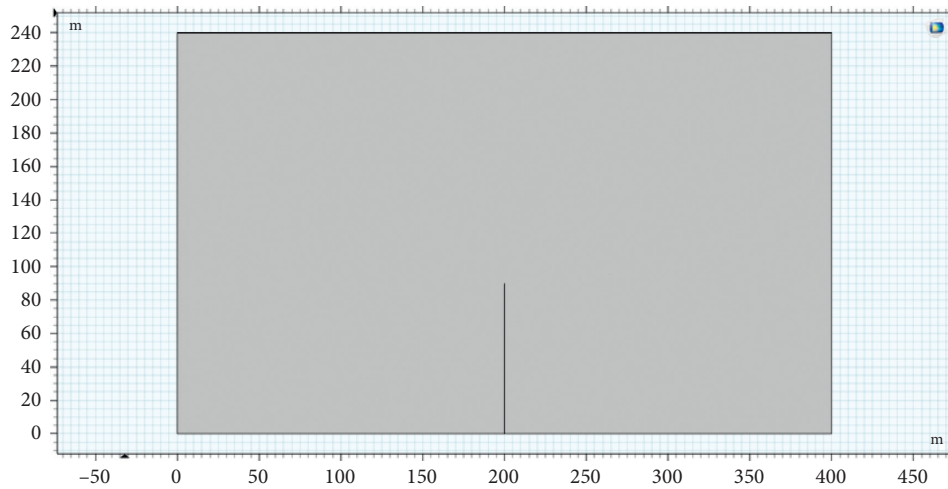


FIGURE 10: 90 m drilling geometry model.

perpendicular to the borehole. The gas flows neatly and orderly to the boreholes, with almost no influence on each other, conforming to radial flow. It can be seen from Figure 9 that the gas streamlines in the long boreholes along the seam area still show a radial flow, while the gas flow in the penetrating boreholes area is messy. In addition, the turbulent gas streamlines interfere with each other at the intersection of the long boreholes along the seam and

penetrating boreholes. The gas migration between boreholes is subject to drainage forces in multiple directions, not conducive to gas drainage.

The above analysis compares and analyzes the drainage effect of the arrangement of long boreholes along the seam and the combined arrangement of penetrating boreholes and the long boreholes along the seam from the three aspects of gas drainage volume, gas flow line, and drilling construction

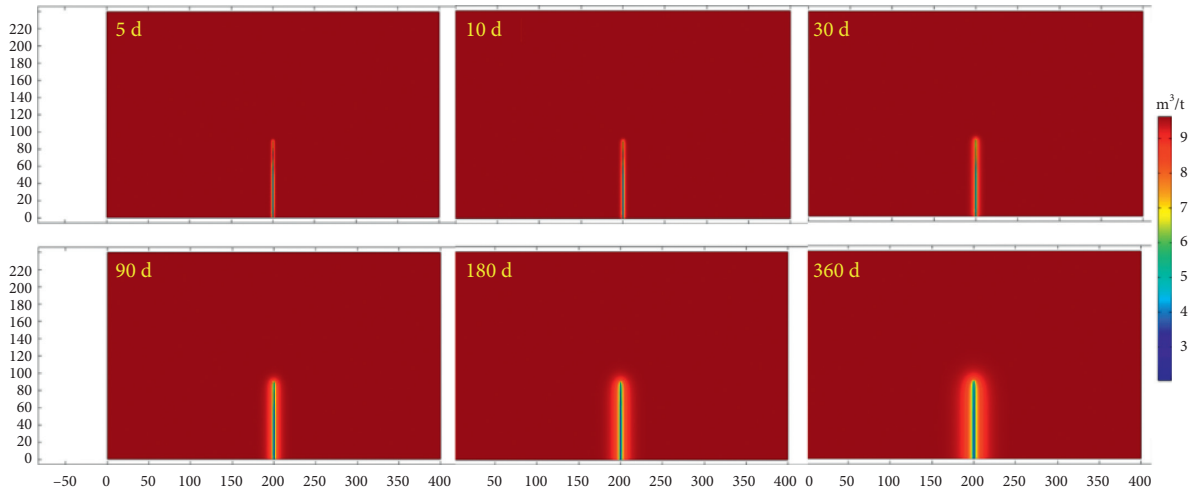
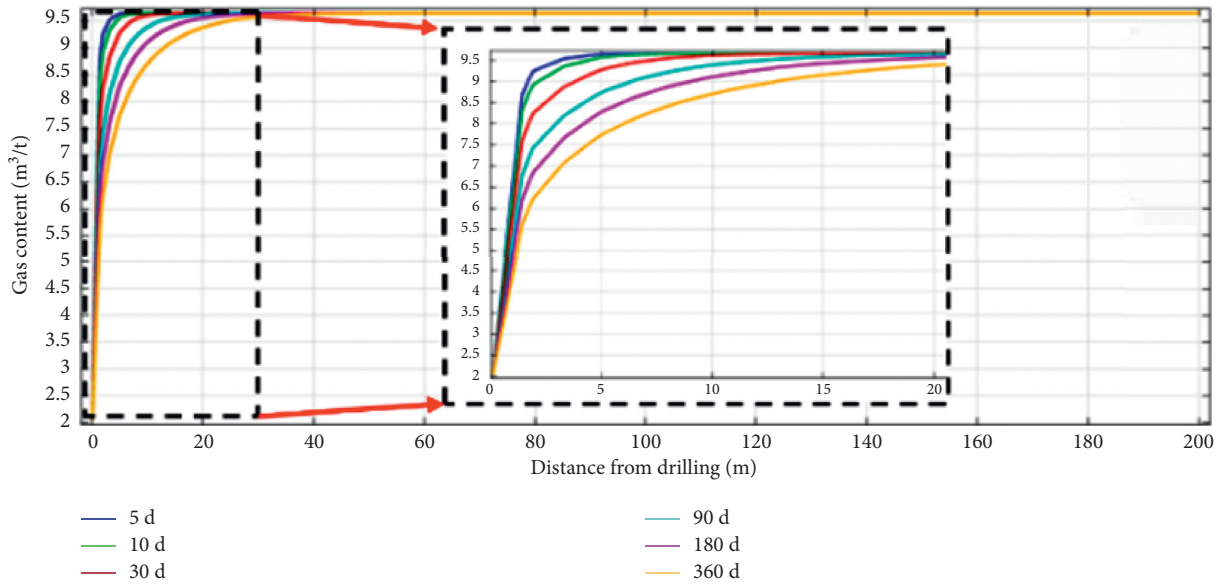


FIGURE 11: Cloud map of coal seam gas content distribution under different drainage time of 90-meter borehole.



(a)

FIGURE 12: Continued.

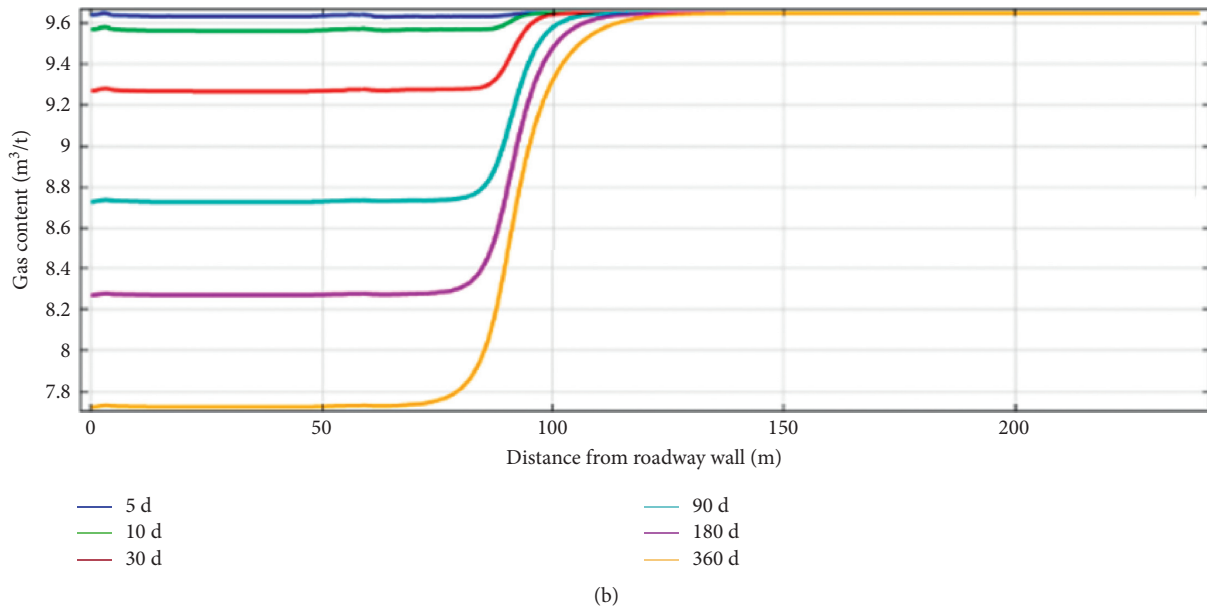


FIGURE 12: Distribution of gas content in 90 m borehole with different drainage time: (a) gas content distribution on the monitoring line in the strike direction; (b) distribution of gas content in the trend direction monitoring line.

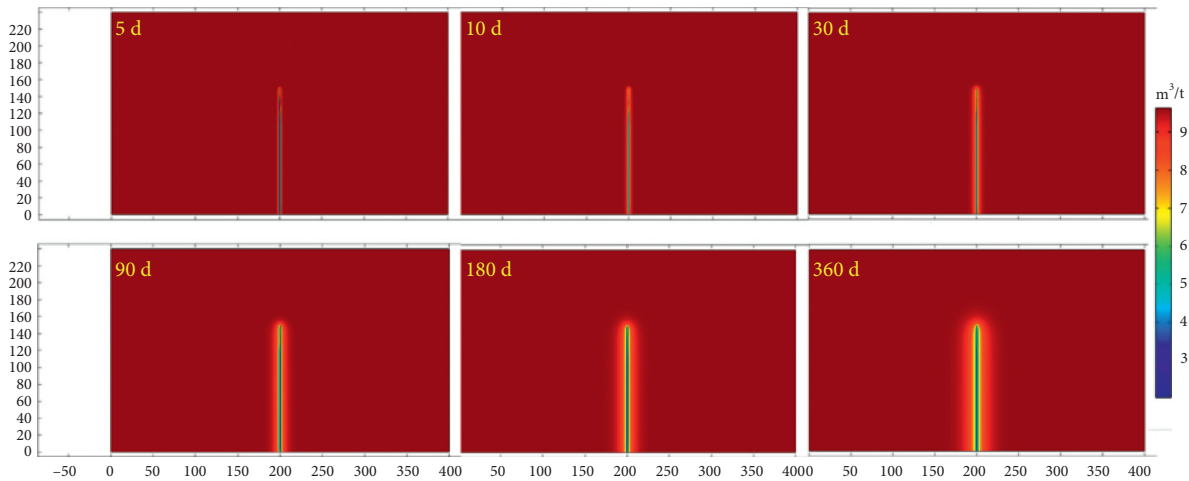


FIGURE 13: Cloud map of coal seam gas content under different drainage time of 150-meter borehole.

cost. It can be seen that long boreholes along the seam have advantages in all aspects. Therefore, it is recommended that the arrangement of long boreholes along the seam is used in gas drainage in the working face.

5.2. Influence of Drilling Length on the Effect of Gas Drainage.

To study the impact of the length of the long borehole along the bedding on gas drainage, numerical simulations of gas drainage with borehole lengths of 90 m, 120 m, 150 m, 180 m, 210 m, and 240 m were carried out. The geometric model is shown in Figure 10.

When the borehole length is 90 m, the gas content distribution around the borehole at different extraction times is shown in Figure 11. It can be seen from Figure 11 that, under the action of the borehole negative pressure, as

the drainage time increases, the gas content around the borehole gradually decreases, and the range of influence of borehole drainage gradually increases.

To quantitatively analyze the distribution of gas content around the borehole under different extraction times, a monitoring line is selected along the direction and inclination of the working face, and the gas content change law on it is analyzed. The monitoring line in the strike direction is 45 m away from the roadway wall, and the monitoring line in the inclined direction is first 5 m away from the borehole. Figure 12 shows the distribution of gas content on the monitoring line under different extraction times. From Figure 12(a), when the borehole length is 90 m, in the strike direction, as the drainage time increases, the gas content of the coal seam gradually decreases. At a distance of 5 m from the borehole, the gas content at a drainage time of 180 days is

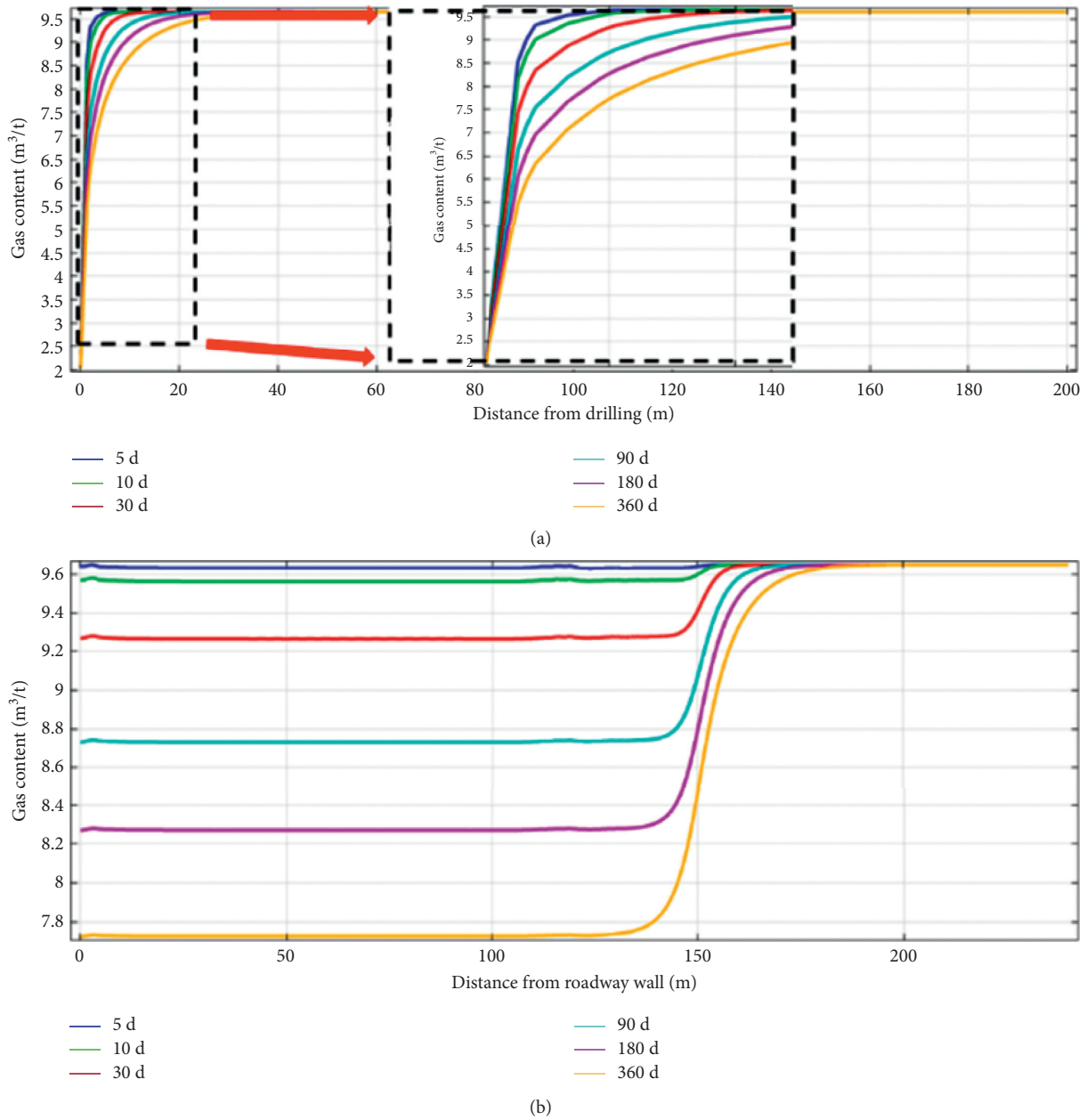


FIGURE 14: Distribution of gas content in 150 m borehole with different drainage time: (a) gas content distribution on the monitoring line in the strike direction; (b) distribution of gas content in the trend direction monitoring line.

reduced by $1.0\text{ m}^3/\text{t}$ and $1.3\text{ m}^3/\text{t}$ compared with the gas content at a drainage time of 30 days and five days. In the direction of the trend, the gas content of the coal seam gradually decreases with the increase of the extraction time. However, because the length of the borehole is only 90 m, part of the gas in the middle and back of the coal seam has not been effectively drained.

When the borehole length is 150 m, the gas content distribution around the borehole under different extraction time is shown in Figure 13. It can be seen from Figure 13 that, under the action of borehole negative pressure, as the drainage time increases, the gas content around the borehole gradually decreases, and the range of influence of borehole

drainage gradually increases. Compared with the 90 m borehole, the 150 m borehole has a broader range of drainage, and the drainage effect is more significant.

In the strike direction, as the drainage time increases, the coal seam gas content gradually decreases. At a distance of 5 m from the borehole, the gas content at 180-day drainage is reduced by $0.94\text{ m}^3/\text{t}$ and $1.26\text{ m}^3/\text{t}$ compared with the gas content at the drainage time of 30 days and five days, and the change is small compared to the 90 m borehole, as shown in Figure 14.

When the borehole length is 240 m, the gas content distribution around the borehole under different extraction time is shown in Figure 15. It can be seen from Figure 15

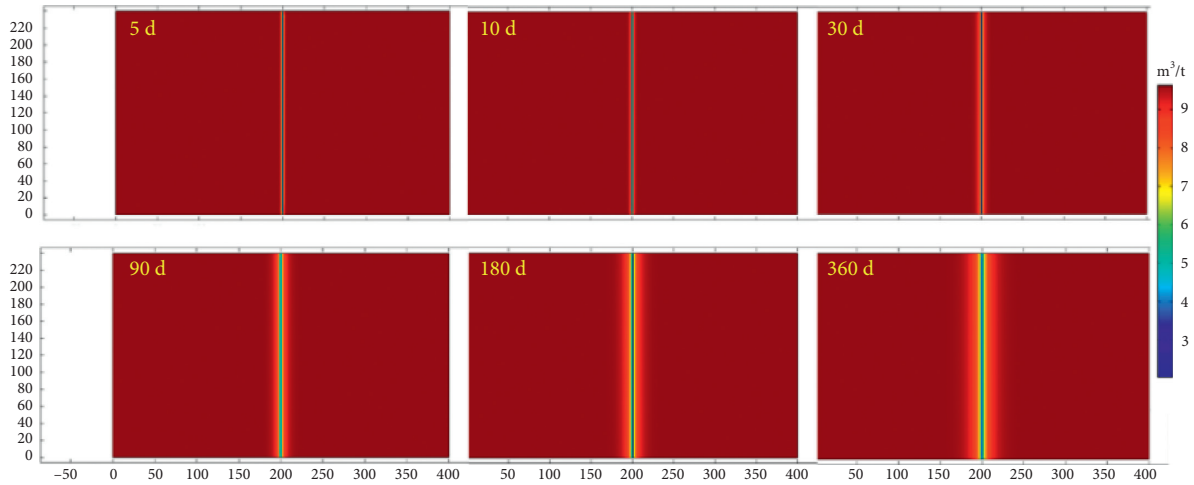


FIGURE 15: Cloud map of coal seam gas content under different drainage time of 240-meter borehole.

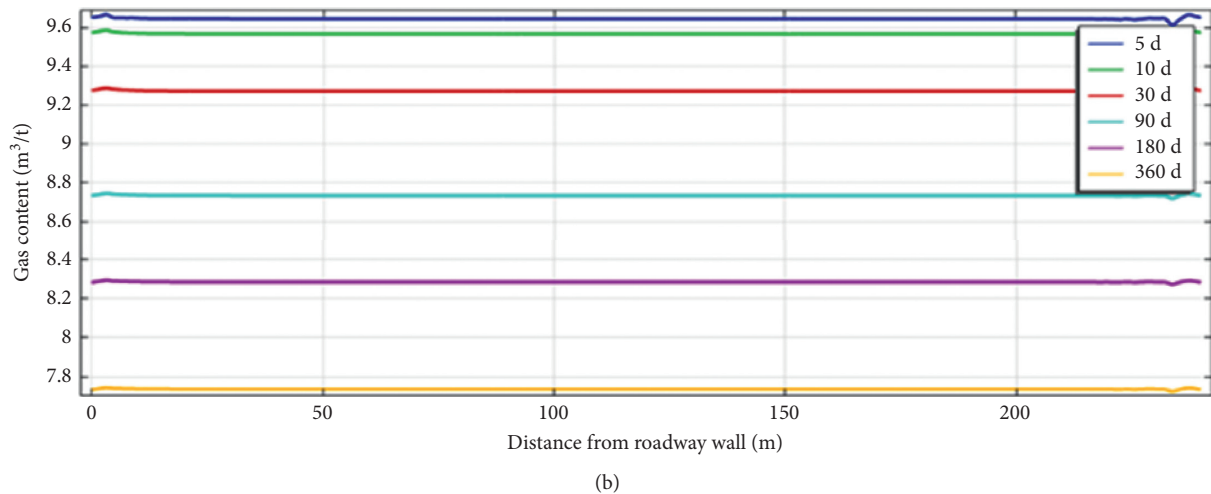
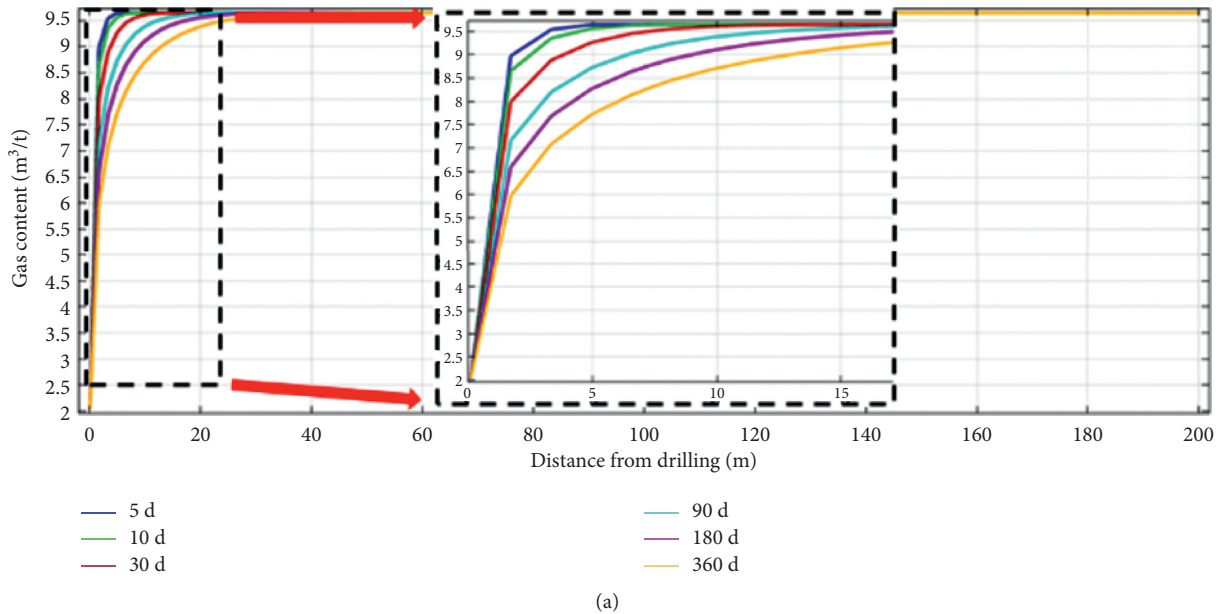


FIGURE 16: Distribution of gas content in 240 m borehole with different drainage time: (a) gas content distribution on the monitoring line in the strike direction; (b) distribution of gas content in the trend direction monitoring line.

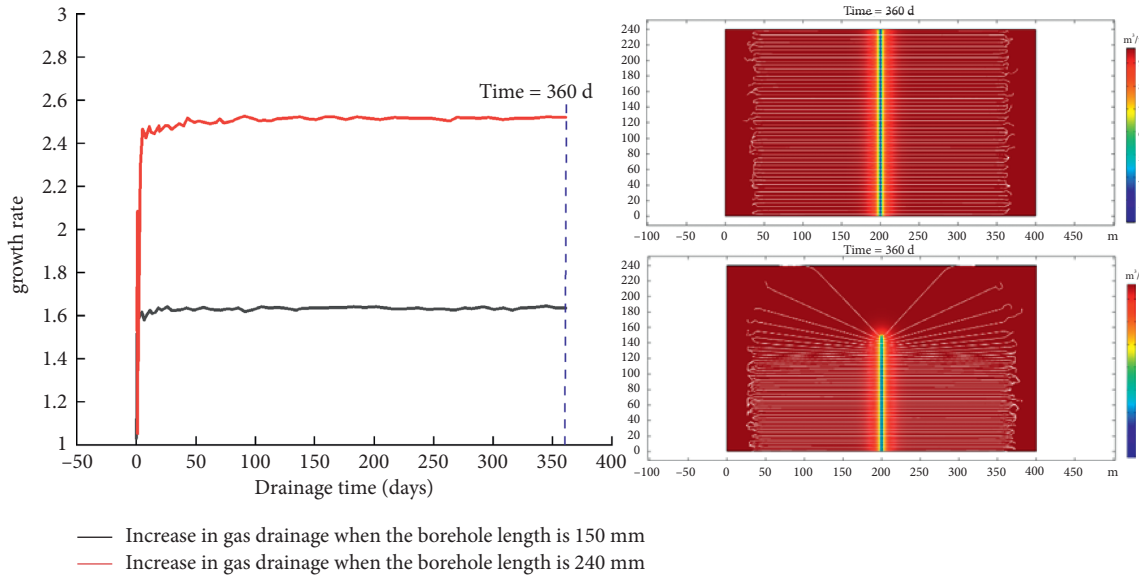


FIGURE 17: Gas drainage ratio under different borehole lengths.

that, under the action of borehole negative pressure, as the drainage time increases, the gas content around the borehole also shows a gradual decrease, and the influence range of borehole drainage further increases.

In the strike direction, as the drainage time increases, the coal seam gas content gradually decreases. In the trend direction, the gas content in the coal seam gradually decreases with the increase of the extraction time, and the gas content at the bottom of the borehole decreases significantly. With the increase of drilling depth, the upward trend value changes less. As the drilling depth increases, the gas at the bottom of the drilling hole can be drained, and the gas content decreases significantly, as shown in Figure 16.

To quantitatively analyze the impact of borehole length on the gas drainage effect, the drainage volume when the borehole length is 90 m is used as the benchmark. The increase in the drainage of the 150 m and 240 m borehole lengths relative to the 90 m borehole can be obtained, as shown in Figure 17. It can be seen from Figure 17 that the longer the borehole length, the better the drainage effect and the greater the impact range of the borehole. When the borehole length is 150 m, the drainage volume is about 1.31 times that of the 90 m borehole; when the borehole length is increased to 240 m, the drainage volume is about 2.50 times that of the 90 m borehole. It can be seen from Figure 17 that the flow line after drilling is perpendicular to the drilling, the gas migration at the tip of the slot conforms to the law of spherical flow, and the gas migration in the middle and rear parts conforms to the radial flow. With the increase of drilling length, the streamline area and the influence range of drilling increase significantly.

6. Conclusions

This paper first elaborates and establishes a multifield coupling model of gas migration in coal. Then, the change value of the residual gas content per unit time is used to

quantify the gas drainage effect of the long borehole. Finally, the COMSOL software was adopted to analyze the drainage effects of different layouts and drilling lengths of long boreholes along the bedding. The main conclusions are as follows:

- (1) A multifield coupling model for gas-containing coal seams was established. The model considers the gas diffusion in the coal matrix, the gas seepage through fractures, the evolution of permeability, and the deformation of coal. At the same time, the dynamic equation of coal diffusion is introduced to make the simulation results more in line with the actual situation.
- (2) By integrating the space of the coupled model and then making the difference in time, the change value of the residual gas content per unit time can be obtained to calculate the gas drainage volume. Furthermore, the gas drainage effect of long boreholes can be quantified.
- (3) Under the combined layout of long boreholes along the seam and penetrating boreholes, the gas content of the long boreholes along the seam area is significantly lower than that of the interbedded borehole drainage area.
- (4) The drainage volume is similar to that under the combined arrangement under the same drainage time. In the early stage of drainage, the drainage volume under the long borehole layout is 1.025 times that of combined drainage, and it gradually decreases in the later stage, down to 0.94 times at the lowest level.
- (5) As the length of the borehole increases, the scope of influence of borehole drainage increases. When the borehole length is 150 m and 240 m, the drainage volume is about 1.31 and 2.50 times that of the 90 m borehole.

The above results provide a particular reference for the layout of long boreholes along the bedding and the determination of reasonable parameters for gas drainage on site.

Data Availability

All the data, models, and code generated or used during the study appear in the manuscript.

Conflicts of Interest

The author declares no commercial or associative interest that represents conflicts of interest in connection with the work submitted.

Acknowledgments

The research presented in this paper was jointly supported by the Natural Science Foundation of Chongqing (Grant No. cstc2020jcyj-msxmX1013).

References

- [1] G. W. Cheng, T. H. Yang, H. Y. Liu et al., "Characteristics of stratum movement induced by downward longwall mining activities in middle-distance multi-seam," *International Journal of Rock Mechanics and Mining Sciences*, vol. 136, pp. 1365–1609, 2020.
- [2] J. Liu, J. Wang, Z. Chen, S. Wang, D. Elsworth, and Y. Jiang, "Impact of transition from local swelling to macro swelling on the evolution of coal permeability," *International Journal of Coal Geology*, vol. 88, no. 1, pp. 31–40, 2011.
- [3] J. Y. Fan, P. Liu, J. J. Li, and D. Jiang, "A coupled methane/airflow model for coal gas drainage: model development and finite-difference solution," *Process Safety and Environmental Protection*, vol. 141, pp. 288–304, 2020.
- [4] D. L. Fu, G. S. Xu, M. Li et al., "Gas generation from coal: taking Jurassic coal in the Minhe Basin as an example," *International Journal of Coal Science & Technology*, vol. 7, no. 3, pp. 611–622, 2020.
- [5] G. Z. Hu, J. L. Xu, T. Ren, Y. Dong, W. Qin, and Z. Shan, "Field investigation of using water injection through in-seam gas drainage boreholes to control coal dust from the longwall face during the influence of abutment pressure," *International Journal of Mining, Reclamation and Environment*, vol. 30, no. 1, pp. 48–63, 2016.
- [6] H. B. Zhao, J. Y. Li, Y. H. Liu, Y. Wang, T. Wang, and H. Cheng, "Experimental and measured research on three-dimensional deformation law of gas drainage borehole in coal seam," *International Journal of Mining Science and Technology*, vol. 30, no. 3, pp. 397–403, 2020.
- [7] C. S. Zheng, M. Kizil, Z. W. Chen, and A. Saiied, "Effects of coal damage on permeability and gas drainage performance," *International Journal of Mining Science and Technology*, vol. 27, no. 5, pp. 783–786, 2017.
- [8] Y. Xue, P. G. Ranjith, F. N. Dang, and J. Liu, "Analysis of deformation, permeability, and energy evolution characteristics of coal mass around borehole after excavation," *Natural Resources Research*, vol. 29, no. 5, pp. 3159–3177, 2020.
- [9] F. B. Zhou, T. Q. Xia, X. X. Wang, Y. Zhang, Y. Sun, and J. Liu, "Recent developments in coal mine methane extraction and utilization in China: a review," *Journal of Natural Gas Science and Engineering*, vol. 31, pp. 437–458, 2016.
- [10] J. J. Hu, C. Gao, H. P. Xie, J. Wang, M. Li, and C. Li, "Anisotropic characteristics of the energy index during the shale failure process under triaxial compression," *Journal of Natural Gas Science and Engineering*, vol. 95, Article ID 104219, 2021.
- [11] C. B. Li, D. C. Yang, H. P. Xie, L. Rin, and J. Wang, "Research on the anisotropic fracture behavior and the corresponding fracture surface roughness of shale," *Engineering Fracture Mechanics*, vol. 255, no. 5, Article ID 107963, 2021.
- [12] Y. K. Ma, E. Y. Wang, D. Xiao, and Z. Li, "Acoustic emission generated during the gas sorption–desorption process in coal," *International Journal of Mining Science and Technology*, vol. 22, no. 3, pp. 391–397, 2012.
- [13] S. Harpalani and R. A. Schraufnagel, "Shrinkage of coal matrix with release of gas and its impact on permeability of coal," *Fuel*, vol. 69, no. 5, pp. 551–556, 1990.
- [14] Z. D. Liu, Y. P. Cheng, L. Wang, H. Wang, J. Jiang, and W. Li, "Analysis of coal permeability rebound and recovery during methane extraction: implications for carbon dioxide storage capability assessment," *Fuel*, vol. 230, pp. 298–307, 2018.
- [15] E. L. Su, Y. P. Liang, X. Y. Chang, Q. Zou, M. Xu, and A. Sasmito, "Effects of cyclic saturation of supercritical CO₂ on the pore structures and mechanical properties of bituminous coal: an experimental study," *Journal of CO₂ Utilization*, vol. 40, Article ID 101208, 2020.
- [16] Q. Q. Liu, Y. P. Cheng, H. X. Zhou, and P. Guo, "A mathematical model of coupled gas flow and coal deformation with gas diffusion and klinkenberg effects," *Rock Mechanics and Rock Engineering*, vol. 48, no. 3, pp. 1163–1180, 2015.
- [17] E. L. Su, Y. P. Liang, Q. L. Zou, and M. Xu, "Numerical analysis of permeability rebound and recovery during coalbed methane extraction: implications for CO₂ injection methods," *Process Safety and Environmental Protection*, vol. 149, pp. 93–104, 2021.
- [18] J. Dong, Y. P. Cheng, K. Jin et al., "Effects of diffusion and suction negative pressure on coalbed methane extraction and a new measure to increase the methane utilization rate," *Fuel*, vol. 191, pp. 70–81, 2017.
- [19] C. A. Mora and R. A. Wattenbarger, "Analysis and verification of dual porosity and CBM shape factors," *Journal of Canadian Petroleum Technology*, vol. 48, no. 2, pp. 17–21, 2009.
- [20] W. Zhao, K. Wang, R. Zhang, and H. Dong, "Influence of combination forms of intact sub-layer and tectonically deformed sub-layer of coal on the gas drainage performance of boreholes: a numerical study," *International Journal of Coal Science & Technology*, vol. 7, no. 3, pp. 571–580, 2020.
- [21] T. Liu, B. Q. Lin, and W. Yang, "Impact of matrix-fracture interactions on coal permeability: model development and analysis," *Fuel*, vol. 207, pp. 522–532, 2017.
- [22] T. Liu and B. Q. Lin, "Time-dependent dynamic diffusion processes in coal: model development and analysis," *International Journal of Heat and Mass Transfer*, vol. 134, pp. 1–9, 2019.
- [23] F. B. Zhou, X. X. Wang, and Y. K. Liu, "Gas drainage efficiency: an input-output model for evaluating gas drainage projects," *Natural Hazards*, vol. 74, no. 2, pp. 989–1005, 2014.
- [24] B. Zhang, J. T. Kang, G. X. Kang, and T. Kang, "Molecular dynamics simulations of CH₄ diffusion in kaolinite: influence of water content," *International Journal of Coal Science & Technology*, vol. 6, no. 4, pp. 556–563, 2019.
- [25] T. Liu, B. Q. Lin, X. H. Fu et al., "Experimental study on gas diffusion dynamics in fractured coal: a better understanding of gas migration in in-situ coal seam," *Energy*, vol. 195, Article ID 117005, 2020.

- [26] S. C. Wang, F. B. Zhou, C. Liu, and Y. Liu, "Computation model for effective radius of gas-extraction drilling in coal mine," *Disaster Advances*, vol. 5, no. 4, pp. 693–697, 2012.
- [27] C. L. Zhang, J. Xu, S. J. Peng, Q. Li, and F. Yan, "Experimental study of drainage radius considering borehole interaction based on 3D monitoring of gas pressure in coal," *Fuel*, vol. 239, pp. 955–963, 2019.
- [28] J. Wang, L. Tang, G. Ding, and C. Su, "Mathnatical description of gas drainage radius for underground gas storage," *Chemistry and Technology of Fuels and Oils*, vol. 54, no. 4, pp. 500–508, 2018.
- [29] H. F. Lin, M. Huang, S. G. Li, and C. Zhang, "Numerical simulation of influence of Langmuir adsorption constant on gas drainage radius of drilling in coal seam," *International Journal of Mining Science and Technology*, vol. 26, no. 3, pp. 377–382, 2016.
- [30] I. Palmer and J. Mansoori, "How permeability depends on stress and pore pressure in coalbeds: a new model," *SPE Reservoir Evaluation and Engineering*, vol. 1, no. 6, pp. 539–544, 1998.
- [31] T. Liu, J. B. Q. Lin, W. Yang et al., "Dynamic diffusion-based multifield coupling model for gas drainage," *Journal of Natural Gas Science and Engineering*, vol. 44, pp. 233–249, 2017.
- [32] Z. J. Pan and L. D. Connell, "Modelling permeability for coal reservoirs: a review of analytical models and testing data," *International Journal of Coal Geology*, vol. 92, pp. 1–44, 2012.
- [33] E. L. Su, Y. P. Liang, Q. L. Zou, F. Niu, and L. Li, "Analysis of effects of CO₂ injection on coalbed permeability: implications for coal seam CO₂ sequestration," *Energy & Fuels*, vol. 33, no. 7, pp. 6606–6615, 2019.

Research Article

LNMR Study on Microstructure Characteristics and Pore Size Distribution of High-Rank Coals with Different Bedding

Jiajia Liu ^{1,2,3}, Jianmin Hu ¹, Mengqi Shen ¹, Ming Yang ^{1,2,3} and Yingxiang Fang ¹

¹Henan Polytechnic University, School of Safety Science and Engineering, Jiaozuo, Henan 454003, China

²Henan Polytechnic University, Collaborative Innovation Center of Coal Work Safety and Clean High Efficiency Utilization, Jiaozuo, Henan 454003, China

³Henan Polytechnic University, Henan Provincial Key Laboratory of Gas Geology and Gas Control Provincial and Ministry of State Key Laboratory Breeding Base, Jiaozuo, Henan 454003, China

Correspondence should be addressed to Jiajia Liu; liujiajia@hpu.edu.cn

Received 7 June 2021; Accepted 21 September 2021; Published 7 October 2021

Academic Editor: Peng Liu

Copyright © 2021 Jiajia Liu et al. This is an open access article distributed under the Creative Commons Attribution License, which permits unrestricted use, distribution, and reproduction in any medium, provided the original work is properly cited.

In order to study the pore structure characteristics of high-rank coals with different bedding, NMR experiments were carried out for high-rank coals with different bedding angles (0°, 30°, 45°, 60°, and 90°). The results show that the distribution of T_2 map of high-rank coal with different bedding is similar to some extent, showing a double peak or triple peak distribution, and the first peak accounts for more than 97% of the total, indicating that small holes are developed in high-rank coal with different bedding, while macropores are not developed. The influence of bedding angle on the fracture proportion is less than 0.3%. Compared with the fracture proportion, the effect of bedding angle on the proportion of microhole, medium hole, and large hole is greater and presents a certain rule. There are certain differences in T_2 cutoff value (T_{2C}) of high-rank coal with different bedding. The relationship between bedding angle and T_{2C} conforms to exponential function, and the correlation degree R^2 is 0.839. The research results provide a theoretical basis for gas extraction and utilization and prevention of gas disaster in coal mines in China.

1. Introduction

Coal is the main source of energy in China and plays an important role in China's economic development. China is rich in coal and coalbed methane reserves, but the conditions of coal reservoirs are complex. The high gas mines account for more than 65%, and the total gas volume is 36 trillion m^3 . China is rich in high-rank coalbed methane resources, accounting for 1/3 of the total high-rank coalbed methane resources. Coalbed methane mainly exists in the coal seam in the state of adsorption. The exploitation of coalbed methane is a continuous process of desorption-diffusion-seepage, which is carried out in the pores and cracks of coal body. Coal has typical anisotropic characteristics in different bedding and joint directions and is a medium with complex pore structure and multiscale structure [1]. Therefore, studying the structural characteristics of pores and fissures of different

bedding high-rank coal samples has important guiding significance for studying the process of gas "desorption-diffusion-seepage" and provides a certain theoretical basis for the extraction and utilization of coal mine gas and the prevention of gas disasters in our country. There are observation methods (such as transmission electron microscopy observation method and scanning electron microscopy observation method) and experimental testing methods (such as cryogenic liquid nitrogen test method, mercury intrusion method, and nuclear magnetic resonance test method) to study the pore structure of coal seams. Among them, the mercury intrusion method can test the pore and macropore structure of the sample, but it will cause irreversible damage to samples [2], while the nuclear magnetic resonance method has advantages of convenient detection and no damage to the test samples.

At present, many scholars at home and abroad have carried out research on the pore structure of coals. Some of

them have conducted research using the mercury intrusion method, nitrogen adsorption method, or low-temperature CO₂ adsorption method: Chen et al. [3] studied the pore structure and fractal characteristics of outburst coal by using the low-temperature liquid nitrogen adsorption test; Qin et al. [4] studied the pore structure characteristics of lignite, bituminous coal, and anthracite by using nitrogen adsorption and mercury intrusion methods; Li et al. [5] studied the pore structure characteristics of low coal ranks in the southern margin of Junggar Basin by using mercury intrusion method; Zhao et al. [6] used the mercury intrusion method to analyze in detail the complex characteristics of the pore structure of structural coal in Qinglong Coal Mine; Lin et al. [7] used nitrogen adsorption and mercury intrusion methods to analyze the pore structure characteristics of middle- and low-rank coals; Zhao et al. [8] comprehensively used high-pressure mercury injection, low-temperature liquid nitrogen adsorption, and low-temperature CO₂ adsorption experimental methods to conduct full-scale pore structure characterization studies on high-rank coals in Qinnan area and concluded that the pores of high-rank coals at all levels are relatively developed; Labani and Wang et al. [9, 10] used mercury intrusion and nitrogen adsorption methods to analyze the internal characteristics of the pore structure of the sample; and Fu et al. [11] used the nitrogen adsorption method to determine the basic characteristic parameters (such as pore volume and pore size distribution). Other researchers have used NMR methods to study: Yao et al. [12] reported a new method that applied low-field nuclear magnetic resonance technology and microfocus CT scanning technology to carry out fine quantitative characterization of coal pore and fissure types, effective porosity, pore structure distribution, and spatial configuration of pore and fissure; Wang et al. [13] used the nuclear magnetic resonance experiment method to analyze the characteristics of coal pore diameter before and after cold leaching in liquid nitrogen; Zheng et al. [14] analyzed the characteristics of movable fluid, bound fluid, and pore size distribution in Huainan low-rank coal reservoir by NMR experiment and concluded that adsorption pore is the most developed in low-rank coal in Huainan, followed by seepage pore and fracture; Xie et al. [15] used low-temperature liquid nitrogen adsorption experiment and low-field NMR experiment to analyze the pore size distribution characteristics of middle-rank coals and high-rank coals and obtained the conversion coefficient C between the relaxation time of NMR T_2 and the pore size distribution of coal micropores; Yang and Liu [16] used low-field NMR experiments to study the pore development characteristics of high-rank coal and concluded that fractures in high-rank coal did not develop, while micropores and small pores are developed; Liu et al. [17] used low-field NMR experiments to explore the reservoir structure characteristics of high-rank coals and concluded that high-rank coals in the direction of parallel bedding and vertical bedding have similar pore size distribution characteristics; Ren et al. [18] studied the characteristics of coal pore size and effective porosity of low-rank coal by low-field NMR experiment; Xu et al. [19] studied the pore

distribution characteristics of coal samples in Pingmei No. 10 Mine by low-field NMR technology; Yao and Liu [20], based on the low-field NMR system experimental analysis of the Longmaxi Formation marine shale in Sichuan Basin, proposed a relatively complete set of fine quantitative characterization technology for shale porosity, permeability, pore type, pore structure, and methane adsorption capacity; Yao et al. [21] used an NMR pore structure model to effectively estimate the pore size distribution of coals; Zhou et al. [22] used the low-field NMR method to study the relationship between fractal analysis and physical properties of pore fractures with low-rank coal; Cai et al. [23] used the nuclear magnetic resonance technology to study parallel bedding coal samples and found that the distribution of nuclear magnetic resonance transverse relaxation saturated water cores has a strong relationship with the pore structure and rank of coals; and Li et al. [24] used the nuclear magnetic resonance technology to study the pore distribution of coals with different structures.

At present, domestic and foreign scholars have conducted relevant research studies on the pore structure and characteristics of low-, medium-, and high-rank coals. However, there are few studies on the pore structure of high-rank coals of different bedding through low-field nuclear magnetic resonance technology. Furthermore, high-rank coals and coalbed methane resources are rich in our country, about a third of the total coalbed methane resources; therefore, it is of great significance to study the pore structure of high-rank coal with different bedding. Because of the advantages of low-field NMR technology, such as fast detection speed and no damage to test samples, the author collected high-rank coal from Zhongmacun Mine of the coking coal group and used NMR technology to test the pore structure characteristics of high-rank coal with different bedding angles (0°, 30°, 45°, 60°, and 90°). The research results provide a theoretical basis for gas extraction and utilization and prevention of gas disaster in coal mines in China.

2. Basic Theory of NMR

NMR is the response of an atomic nucleus to radio frequency magnetization by a magnetic field. Many nuclei have a net magnetic moment and angular momentum (or spin). When there is an external magnetic field, the nucleus moves around the direction of the external magnetic field. When the magnetic nuclei of these spins interact with an external magnetic field, a measurable signal can be generated. If one or both of the number of neutrons and the number of protons in the nucleus are odd numbers, the conditions for generating nuclear magnetic resonance signals are available, such as hydrogen nucleus ¹H, carbon ¹³C, and nitrogen ¹⁴N. Because hydrogen nuclei ¹H are abundant in nature and easy to detect, almost all nuclear magnetic resonance techniques are based on the response of hydrogen nuclei. For the fluid in rock pores, there are three different relaxation mechanisms: free relaxation, surface relaxation, and diffusion relaxation [25]. The transverse relaxation time can be expressed as follows:

$$\frac{1}{T_2} = \frac{1}{T_{2B}} + \frac{1}{T_{2S}} + \frac{1}{T_{2D}}, \quad (1)$$

where T_{2B} is the free relaxation time, T_{2S} is the surface relaxation time, and T_{2D} is the diffusion relaxation time [26]. Free relaxation is the inherent relaxation property of liquids, which is determined by the physical properties of liquids (such as viscosity and chemical composition). The surface relaxation strength varies with the change of rock properties. As with free relaxation, physical properties (such as viscosity and molecules) constitute the control of diffusion coefficients; in addition, environmental conditions, temperature, and pressure also influence diffusion.

Since the experimental environment uses a uniform magnetic field, based on the principle of nuclear magnetic resonance [27], equation (1) can be written as follows:

$$\frac{1}{T_2} = \rho_2 \left(\frac{S}{V} \right), \quad (2)$$

where S is the surface area of the pores, μm^2 ; V is the pore volume [28], μm^3 ; and ρ^2 is the transverse surface relaxation strength of the rock, $\mu\text{m}/\text{ms}$, with an element of m/ms . According to equation (2), the relaxation time T_2 is proportional to the pore radius r :

$$r = CT_2, \quad (3)$$

where r is the pore radius, nm ; C is the conversion coefficient [29, 30]; and T_2 is the transverse relaxation time.

3. Experimental Method and Process

3.1. Laboratory Equipment. In this experiment, the MesomR23-060H-I low-field NMR system of Suzhou Niumai Technology was used (the resonance frequency of the device was 21.67 568 MHz, the magnetic field intensity was 0.5 T, the magnet temperature was constant at $32 \pm 0.01^\circ\text{C}$, and the RF pulse frequency was 21.67 568 MHz). The 2XZ-4B vacuum saturation device and TGL-21M table top high speed refrigerated centrifuge were used. CPMG parameter settings of low-field NMR are shown in Table 1.

The physical map of the experimental test equipment is shown in Figure 1.

3.2. Coal Sample Preparation and Experimental Procedures. Collect fresh coal from Zhongmacun Mine of the coking coal group, and drill $\Phi 25 \text{ mm} \times 50 \text{ mm}$ cylindrical raw coal samples according to the angles of 0° , 30° , 45° , 60° , and 90° with the seam structure. These are ZM1, ZM2, ZM3, ZM4, and ZM5. The production process of the coal sample is shown in Figure 2.

The prepared coal pillars are reserved for the experiment, and the fresh small coal blocks that cannot be prepared into cylindrical coal blocks are tested for the maximum reflectance and microscopic components of the vitrinite coal. The test results are shown in Table 2.

Experiment with the coal samples ZM1, ZM2, ZM3, ZM4, and ZM5 prepared above: first, use the nuclear magnetic resonance system to test the T_2 pattern distribution

TABLE 1: CPMG sequence parameter.

Parameter name	SW (kHz)	TE (ms)	SF (MHz)	RFD (ms)	TW (ms)	NECH
Value setting	250	0.251	21	0.08	5000	10000



FIGURE 1: System diagram of experimental equipment.

of the natural state coal samples, put the coal samples ZM1, ZM2, ZM3, ZM4, and ZM5 into the vacuum saturation device which is saturated with water for 12 hours to fully saturate the coal sample (the quality difference between the two measured coal samples is less than 0.05%), and then test the T_2 spectrum distribution of the saturated coal sample. The saturated coal samples were centrifuged for 0.5 hours at 1.38 MPa centrifugal force, and the centrifuged coal samples were subjected to nuclear magnetic resonance tests [14]. The basic physical parameters of coal samples are shown in Table 3.

4. Experimental Results and Discussion

According to the experimental procedures, the low-field nuclear magnetic resonance system was used to perform nuclear magnetic resonance tests on ZM1, ZM2, ZM3, ZM4, and ZM5. The measured T_2 spectrum in the natural state is shown in Figure 3, the T_2 spectrum in the saturated state is shown in Figure 4, the T_2 spectrum of the coal sample after centrifugation is shown in Figure 5, and the histogram of the coal sample pore size distribution is shown in Figure 6.

Analyzing Figures 3–6, we can see that the T_2 spectrum of the coal sample has a double-peak or three-peak distribution. The T_2 spectrum of ZM4 has a three-peak distribution, and the T_2 spectrum of ZM1, ZM2, ZM3, and ZM5 has a double-peak distribution. The areas of the first peaks of the T_2 spectra of ZM3 and ZM5 are 40 999.437, 29 781.694, 25 264.928, 22 693.186, and 27 466.478, respectively, accounting for 98.61%, 99.664%, 99.524%, 97.363%, and 99.657%, respectively; the areas of the second peak are 577.914, 100.352, 120.783, 568.658, and 99.657, respectively,

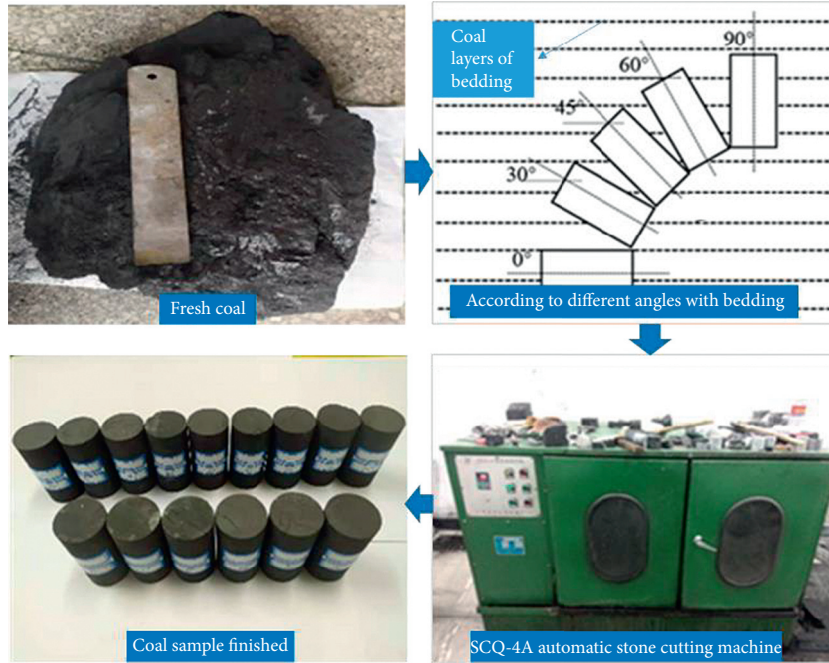


FIGURE 2: Production process drawing of coal samples.

TABLE 2: Microscopic coal and rock component detection results.

Results (%)	Vitrinite	Inertinite	The total organic	Clay soil	Sulfide	Carbonate	Amount of inorganic	Vitrinite average maximum reflectivity (R_{max})
Value	61.7	25.3	87.0	10.9	0.1	2.0	13.0	3.31

TABLE 3: Basic physical property parameters of coal samples.

Coal sample number	Height (mm)	Diameter (mm)	Volume (ml)	Natural state quality (g)	Saturated state quality (g)	Mass after centrifugation (g)
ZM1 (0°)	49.46	25.46	25.17	39.78	40.85	40.38
ZM2 (30°)	49.51	25.50	25.27	37.08	37.55	37.51
ZM3 (45°)	49.55	25.48	25.25	35.80	36.25	36.19
ZM4 (60°)	49.57	25.51	25.32	37.85	38.16	38.10
ZM5 (90°)	49.61	25.48	25.28	36.45	36.72	36.68

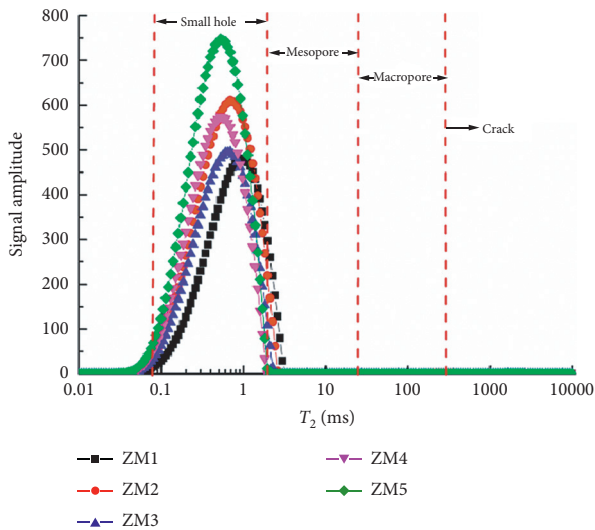


FIGURE 3: T_2 spectrum of coal samples in the natural state.

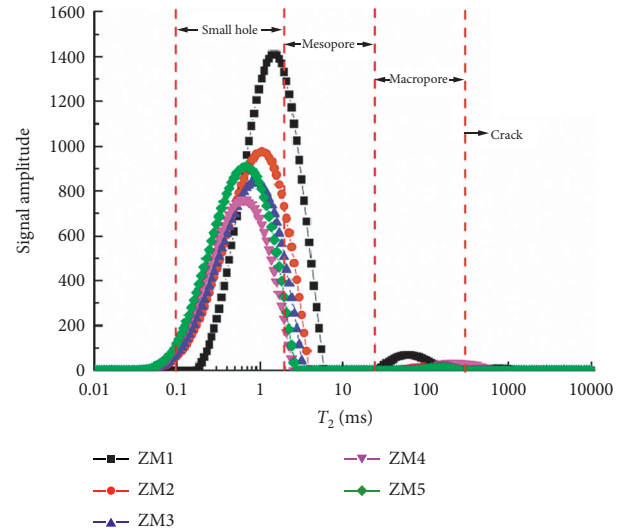


FIGURE 4: T_2 spectrum of coal samples in the saturated state.

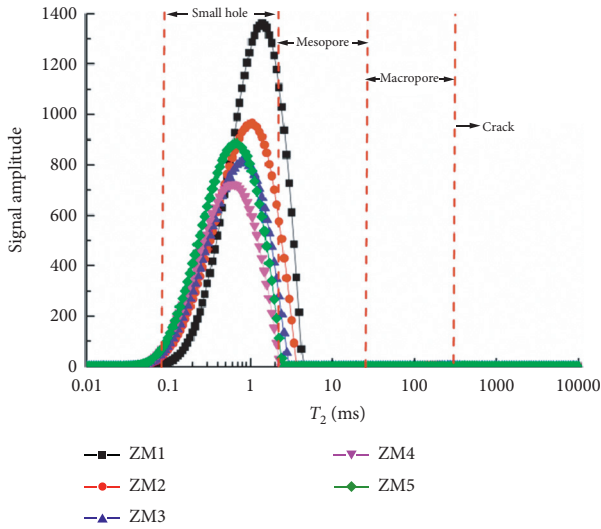


FIGURE 5: T_2 spectrum of coal samples after centrifugation.

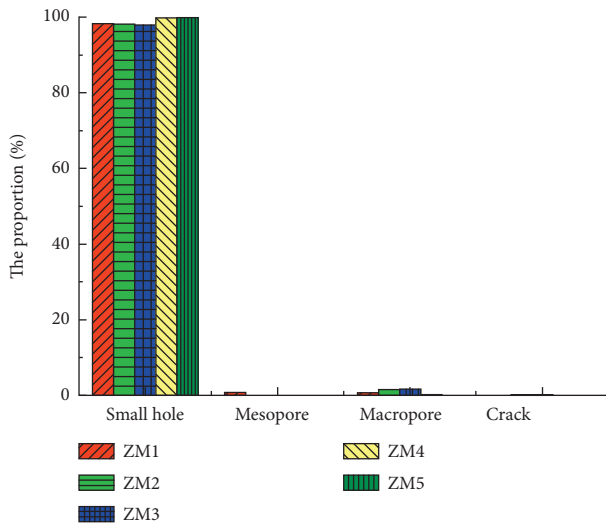


FIGURE 6: The histogram of coal pore size distribution.

and the proportions are 1.39%, 0.336%, 0.476%, 2.44%, and 0.343%, respectively; the area of the third peak of the T_2 spectrum of ZM4 is 45.95, which accounts for 0.197%; the proportion of the first peak of different bedding high-rank coals exceeds 97%, of which the first peak of ZM2 has the highest proportion of 99.664%, and the proportion of the first peak of ZM4 is the lowest, 97.363%; among them, the second peak of ZM4 has the highest proportion of 2.44% and the second peak of ZM2 has the lowest proportion of 0.336%. Further in-depth analysis shows that the T_2 pattern distribution of different bedding high-rank coals has certain similarities. The overall pattern shows that the proportion of small holes is relatively large, followed by the proportion of mesopores and macropores. This shows that high-rank coals with different bedding have developed small holes, while mesopores and macropores are not developed; the T_2 spectrum of ZM4 in the coal sample used in the experiment shows a three-peak distribution. The reason is that the difference in the bedding structure of the coal sample and the

coal sample preparation process have caused some large pores to evolve into large cracks.

Figure 7 shows that the proportions of the pore diameters of different bedding high-rank coals are different. Among the proportions of micropores, ZM5 is the highest at 99.963% and ZM3 is the lowest at 97.977%. This shows that, as the bedding angle increases, the proportion of micropores in coal samples first decreases and then increases; in the proportion of large holes, ZM3 is the highest at 1.726%, and ZM5 is the lowest at 0.0006%. As a whole, as the bedding angle increases, the proportion of large holes in coal samples first increases and then decreases; in the proportion of cracks, high-rank coals of different beddings show an “N” shape (first increase, then decrease, and then increase) distribution law, and the difference between the maximum and minimum proportions of cracks is less than 0.3%. It shows that different bedding angles of high-rank coals have little effect on the ratio of cracks. The difference of the rational angle has little effect on the proportion of cracks. Compared with the proportion of cracks, the bedding angle has an influence of 1.886%, 0.885%, and 1.725% on the proportions of micropores, mesopores, and macropores, respectively.

The T_2 cutoff value can be expressed as T_{2C} . The left side of T_{2C} represents the bound fluid in the adsorption hole, and the right side represents the movable fluid in the percolation hole. We can calculate the bound fluid and movable fluid in the experimental sample through T_{2C} , the schematic diagram of T_{2C} is shown in Figure 8. Draw a cumulative curve for the porosity components of the coal samples before and after centrifugation, and draw a straight line parallel to the time axis based on the maximum value of the cumulative porosity curve after centrifugation (indicated by the dotted line in the figure). This straight line is related to the saturated cumulative pores. The degree curve intersects at a point, denoted as point 1, and then a straight line parallel to the time axis is made based on point 1. This straight line intersects the time axis at point 2, and the value of the time axis corresponding to point 2 is the desired value T_{2C} .

Analyzing Figures 8 and 9, we can see that T_{2C} of different bedding high-rank coals has certain differences. According to the above method, T_{2C} of different bedding high-rank coals ZM1, ZM2, ZM3, ZM4, and ZM5 can be obtained. They conform to the exponential function relationship; as shown in Figure 10, the function expression between them is $y = \exp(1.41647 - 0.02139 * x + 1.35294E - 4 * x^2)$, and the correlation R^2 is 0.839. It can be seen from Figure 10 that, as the bedding angle increases, T_{2C} shows a trend of first decline and then rise. At the beginning, T_{2C} decreases faster with the increase of the angle. When T_{2C} drops to the lowest value, with the increase in bedding angle, T_{2C} began to rise slowly.

Analyzing Figure 10, it can be seen that the water in the pores of high-rank coal with different bedding angles has different degrees of difficulty to be thrown out under the action of external centrifugal force. Based on the T_{2C} calculation method described above, when the direction of the combined force of the centrifugal force and gravity on the water in the pores of the coal sample is closer to the bedding

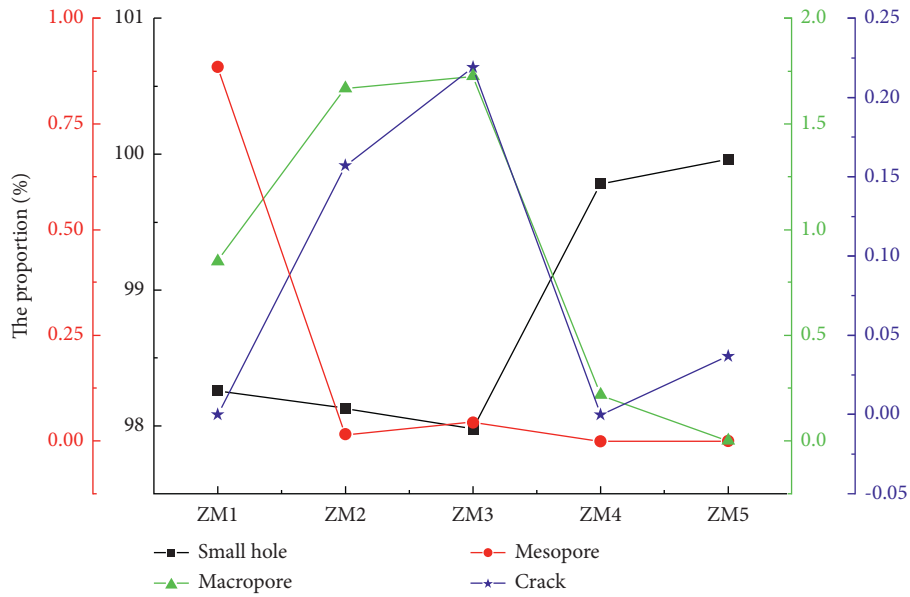


FIGURE 7: Pore proportion of high-rank coal with different bedding.

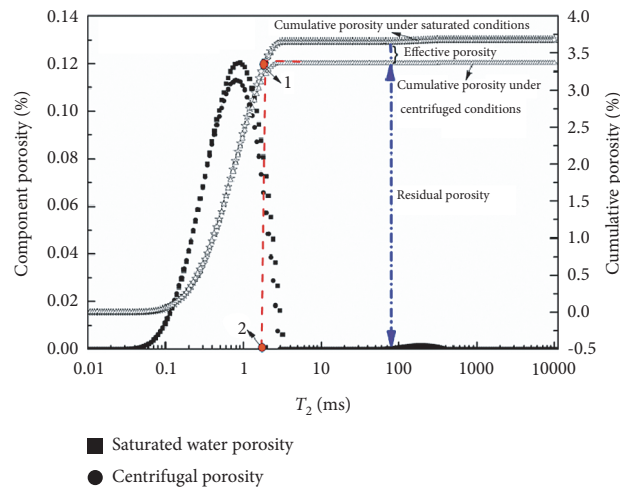


FIGURE 8: Schematic diagram of T_{2C} of ZM3 coal sample.

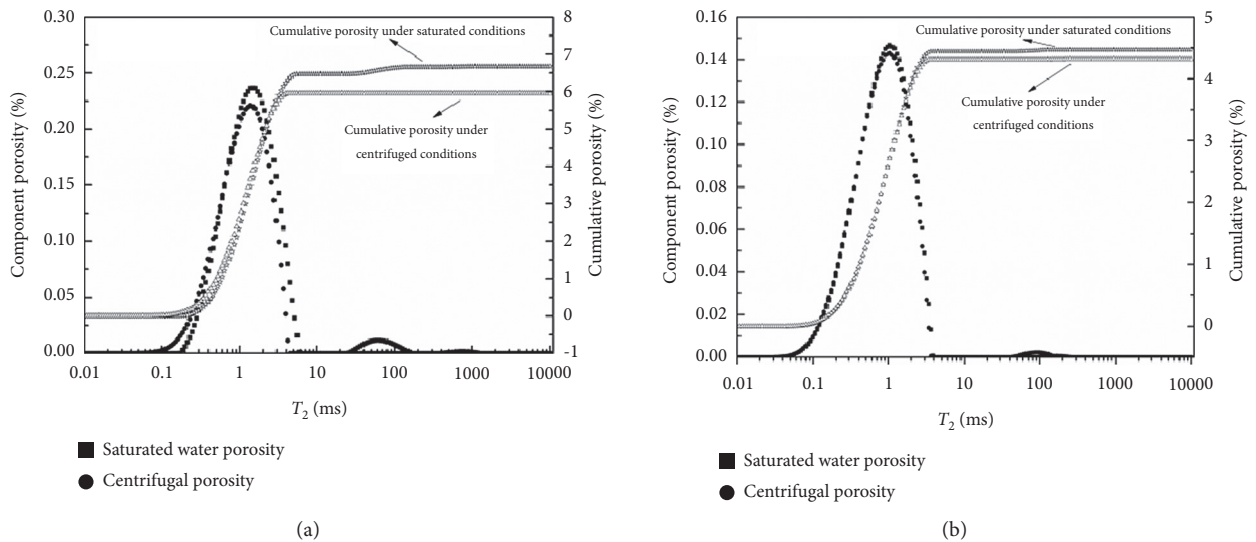


FIGURE 9: Continued.

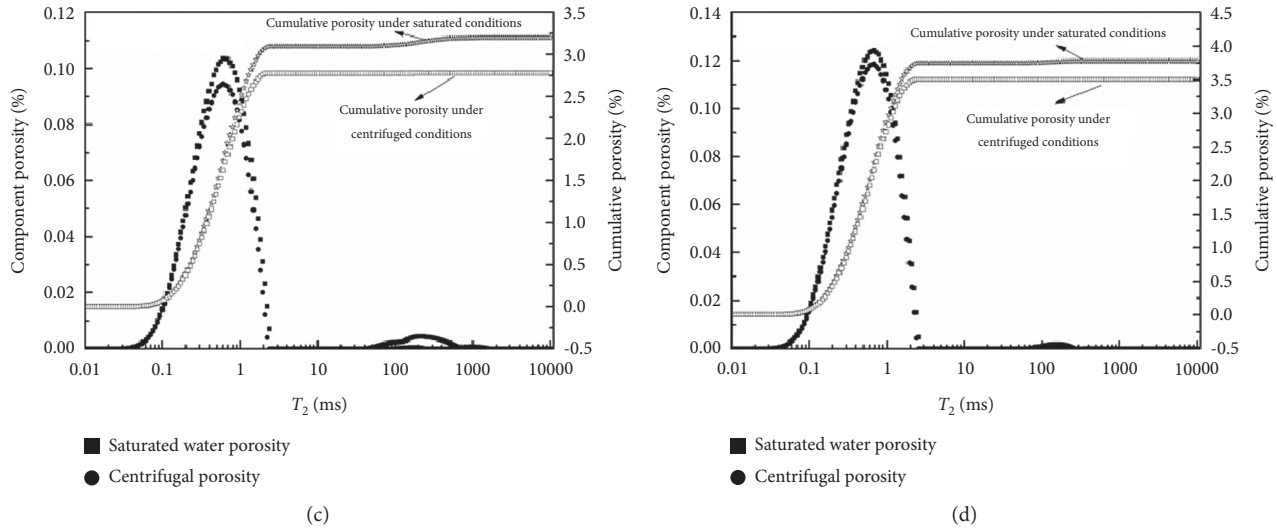


FIGURE 9: Porosity of high-rank coal with different bedding. (a) ZM1, (b) ZM2, (c) ZM4, and (d) ZM5.

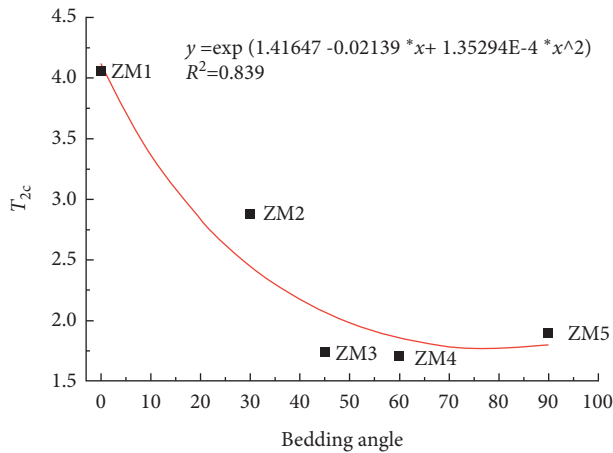


FIGURE 10: T_{2C} of high-rank coal with different bedding.

direction of the coal samples, the water in the pores of the coal samples is easily thrown out; when the resultant direction of centrifugal force and gravity received by the water in the pore of the coal samples is inconsistent with the direction of bedding of the coal samples, the pore wall of the coal samples will give an opposite force to the water in the pore, and the more the resultant direction of centrifugal force and gravity deviates from the direction of bedding of the coal samples, the more difficult the water is to throw out.

5. Conclusions

- (1) The T_2 patterns of different bedding high-rank coals have a certain regularity, showing a double-peak or triple-peak distribution. Their first peak accounts for a relatively high proportion, both exceeding 97%. It is indicated that the micropores of different bedding high-rank coals are developed, while the medium and large pores are not developed.

- (2) The different changing law of the angle is that the proportion of microholes first decreases and then increases with the increase of the bedding angle. The proportion of mesopores first rapidly decreases with the increase of the bedding angle and then basically remains unchanged. The proportion of large holes first increases and then decreases with the increase of the bedding angle.
- (3) The bedding angle and T_{2C} conform to an exponential function relationship. T_{2C} shows a trend of first decline and then rise. At the beginning, T_{2C} decreases faster with the increase of the angle. When T_{2C} drops to the lowest value, as the bedding angle increases, T_{2C} shows a slow upward trend.

Data Availability

The data used to support the findings of this study are included within the article.

Conflicts of Interest

The authors declare that they have no conflicts of interest.

Acknowledgments

This work was supported by the National Natural Science Foundation of China (52074106 and 51734007). This project was also supported by Zhongyuan Postdoctoral Innovative Talent (ZYQR201810171), the China Postdoctoral Science Foundation (2019M652536), the Henan Postdoctoral Foundation (001801016), and the Doctoral Fund of Henan Polytechnic University (B2018-59).

References

[1] A. D. Alexeev, T. A. Vasilenko, and E. V. Ulyanova, "Closed porosity in fossil coals," *Fuel*, vol. 78, no. 6, pp. 635–638, 1999.

- [2] A. C. Patrick, J. R. Cathy, L. Esa et al., "Comparison of NMR cryoporometry, mercury intrusion porosimetry, and DSC thermoporosity in characterizing pore size distributions of compressed finely ground calcium carbonate structures," *Industrial & Engineering Chemistry Research*, vol. 43, no. 43, p. 7920, 2004.
- [3] L. Y. Chen, X. J. Li, Z. H. Shen, B. Juan, Y. Liu, and S. Xu, "Pore structure and fractal characteristics of outburst coal in northern Guizhou," *China Safety Science Journal*, vol. 30, no. 02, pp. 66–72, 2020.
- [4] L. Qin, P. Wang, H. F. Lin, P. Zhao, C. Ma, and Y. Shi, "Advanced characterization of pore structure of liquid nitrogen frozen coal using nitrogen adsorption and mercury intrusion methods," *Journal of Xi'an University of Science and Technology*, vol. 40, no. 6, pp. 945–952, 2020.
- [5] C. F. Li, Y. C. Wei, A. M. Wang, and D. Cao, "Low-ranked coal reservoir pore structure characterized by mercury intrusion—a case study of Southern Junggar basin," *Coal Geology of China*, vol. 30, no. 02, pp. 29–33, 2018.
- [6] J. G. Zhao, M. Wang, and R. Y. Ma, *Study on Pore Structure Characteristics of Qianxi Qinglong Coal Mine Based on Mercury Injection Method*, pp. 1–11, Coal Science and Technology, Beijing, China, 2020.
- [7] H. F. Lin, J. T. Bu, M. Yan, and Y. Bai, "Joint analysis of pore structure characteristics of middle and low rank coal with nitrogen adsorption and mercury intrusion method," *Journal of Xi'an university of Science and Technology*, vol. 39, no. 1, pp. 1–8, 2019.
- [8] J. C. Zhao, *Full Scale Pore Structure of High Rank Coals in the South of Qinshui basin and its Flow Difference*, China University of Mining and Technology, Beijing, China, 2017.
- [9] M. M. Labani, R. Rezaee, A. Saeedi, and A. A. Hinai, "Evaluation of pore size spectrum of gas shale reservoirs using low pressure nitrogen adsorption, gas expansion and mercury porosimetry: a case study from the Perth and Canning basins, western Australia," *Journal of Petroleum Science and Engineering*, vol. 112, no. 3, pp. 7–16, 2013.
- [10] M. Wang and Q. Yu, "Pore structure characterization of Carboniferous shales from the eastern Qaidam basin, China: c," *Journal of Petroleum Science and Engineering*, vol. 152, pp. 91–103, 2017.
- [11] H. Fu, X. Wang, L. Zhang et al., "Investigation of the factors that control the development of pore structure in lacustrine shale: a case study of block X in the Ordos basin, China," *Journal of Natural Gas Science and Engineering*, vol. 26, pp. 1422–1432, 2015.
- [12] Y. Yao, D. Liu, Y. Cai, and J. Li, "Advanced characterization of pores and fractures in coals by nuclear magnetic resonance and X-ray computed tomography," *Science China Earth Sciences*, vol. 53, no. 6, pp. 854–862, 2010.
- [13] C. X. Wang, X. B. Zhang, and F. C. Lu, "Study on coal cracking under liquid nitrogen soaking based on nuclear magnetic resonance and stress analysis," *China Safety Science Journal*, vol. 29, no. 11, pp. 156–163, 2019.
- [14] S. J. Zheng, Y. B. Yao, and Y. D. Cai, "Characteristics of dynamic fluid and pore diameter distribution of low-rank coal reservoirs in the southern margin of Junggar Basin," *Coal Field Geology and Exploration*, vol. 46, no. 1, pp. 56–60, 2008.
- [15] S. B. Xie, Y. B. Yao, and J. Y. Chen, "Study on low-field nuclear magnetic resonance of micro-pore pore structure in coal reservoir," *Acta Coal Sinica*, vol. 40, no. S1, pp. 170–176, 2015.
- [16] M. Yang and Y. P. Liu, "Experimental study on pore characteristics of high-order coal with low-field nuclear magnetic resonance," *China science and technology of work safety*, vol. 12, no. 11, pp. 63–69, 2016.
- [17] S. Q. Liu, S. X. Sang, Y. H. Yang et al., "Structure features of high rank coal in parallel bedding and vertical bedding based on low field nuclear magnetic resonance," *Coal Science and Technology*, vol. 46, no. 10, pp. 110–116, 2018.
- [18] H. K. Ren, A. M. Wang, C. F. Li, D. Cao, and Y. Wei, "Study on porosity characteristics of low-rank coal reservoirs based on nuclear magnetic resonance technology," *Coal Science and Technology*, vol. 45, no. 4, pp. 143–148, 2017.
- [19] X. M. Xu, H. X. Ma, J. W. Tian, J. Wang, and G. Li, "Study on microscopic pore structures of coal based on nuclear magnetic resonance technology," *Safety In Coal Mines*, vol. 48, no. 2, pp. 1–4, 2017.
- [20] Y. B. Yao and D. M. Liu, "Petrophysical properties and fluids transportation in gas shale: a NMR relaxation spectrum analysis method," *Journal of China Coal Society*, vol. 43, no. 1, pp. 181–189, 2018.
- [21] Y. Yao, D. Liu, Y. Che, D. Tang, S. Tang, and W. Huang, "Petrophysical characterization of coals by low-field nuclear magnetic resonance (NMR)," *Fuel*, vol. 89, no. 7, pp. 1371–1380, 2010.
- [22] S. Zhou, D. Liu, Y. Cai, and Y. Yao, "Fractal characterization of pore-fracture in low-rank coals using a low-field NMR relaxation method," *Fuel*, vol. 181, pp. 218–226, 2016.
- [23] Y. Cai, D. Liu, Z. Pan, Y. Yao, J. Li, and Y. Qiu, "Petrophysical characterization of Chinese coal cores with heat treatment by nuclear magnetic resonance," *Fuel*, vol. 108, pp. 292–302, 2013.
- [24] X. Li, Y. Kang, and M. Haghghi, "Investigation of pore size distributions of coals with different structures by nuclear magnetic resonance (NMR) and mercury intrusion porosimetry (MIP)," *Measurement*, vol. 116, pp. 122–128, 2017.
- [25] Y. B. Yao and D. M. Liu, "Petrophysics and fluid properties characterizations of coalbed methane reservoir by using NMR relaxation time analysis," *Coal Science and Technology*, vol. 44, no. 6, pp. 14–22, 2016.
- [26] A. Timur, "Nuclear magnetic resonance study of carbonates rocks," *Log Analyst*, vol. 13, no. 5, pp. 3–11, 1972.
- [27] A. Rahila, F. Y. Ma, X. Zhang, J. Liu, M. Zhong, and X. Zhao, "Application of low-field nuclear magnetic resonance technology in coal petrographic pore structure," *Nuclear Techniques*, vol. 40, no. 12, pp. 43–48, 2017.
- [28] Coates, R. George, L. Z. Xiao, and G. Prammer Manfred, *NMR Logging Principles and Applications*, Gulf Publishing Company, Houston, TX, USA, 1999.
- [29] W. E. Kenyon, "Nuclear magnetic resonance as a petro-physical measurement," *Nuclear Geophysics*, vol. 6, no. 2, pp. 153–171, 1992.
- [30] Y. Yao and D. Liu, "Comparison of low-field NMR and mercury intrusion porosimetry in characterizing pore size distributions of coals," *Fuel*, vol. 95, pp. 152–158, 2012.

Research Article

Goaf Gas Control Improvement by Optimizing the Adjacent Roadway Large-Diameter Boreholes

Wei Wang ^{1,2}, Zongxiang Li,¹ and Hongming Yu²

¹College of Safety Science and Engineering, Liaoning Technical University, Liaoning 123000, China

²Division of Energy, Shuifan Group Co., Ltd., Jinan 25000, China

Correspondence should be addressed to Wei Wang; wangweiwyc@163.com

Received 16 May 2021; Accepted 5 July 2021; Published 22 July 2021

Academic Editor: Zou Quanle

Copyright © 2021 Wei Wang et al. This is an open access article distributed under the Creative Commons Attribution License, which permits unrestricted use, distribution, and reproduction in any medium, provided the original work is properly cited.

This study introduced gas control technology in goaf using adjacent roadway large-diameter (550 mm) boreholes to control gas accumulation in the upper corner of a fully mechanized working face in high-gas coal seams. The gas control process in the upper corner and gas interception in goaf by large-diameter boreholes was analyzed using the CFD model of the gas flow in goaf. The latter considered the control equation of gas flow, the established permeability model of goaf, and the gas emission law in goaf. Using the 2-105 working face of the Tenghui Coal Mine, Shanxi Province, China, as a case study, the distribution patterns of gas concentration and flow field in the goaf for various extraction flow parameters and different positions of boreholes were numerically simulated. The dependences between various locations, drainage flows, and the gas concentration in the upper corner were determined and fitted by engineering equations. The evolution pattern of the spontaneous combustion zone in the goaf under the drainage conditions was also analyzed. The optimal borehole configuration parameters ensuring the extraction flow rate exceeding $3 \text{ m}\cdot\text{s}^{-1}$ and the effective gas control in the upper corner of the working face at a distance of 5 m–15 m behind the working face were identified. The engineering practice proved the feasibility of gas control in the goaf using the adjacent roadway large-diameter borehole. The gas concentrations in the return airflow and the upper corner of the working face were kept below 0.65 and 0.8%, respectively, to ensure production safety and improve the gas utilization efficiency.

1. Introduction

Despite the global trend of green energy promotion, coal resources remain vital to industrial development, accounting for over half of China's power production. With increased mining intensity and burial depth, the coal seam's gas content also keeps increasing. Various low-gas mines have been converted into high-gas ones, with large gas emissions from the working face, and the gas accumulation in the upper corner often exceeds the limit. The gas emission is hazardous and restricts safe coal production. Meanwhile, mining gas utilization via an extraction system is lucrative from the green energy standpoint [1].

To mitigate the mine gas emission and utilization problems, great efforts have been invested in researching the goaf's gas flow. Majdi et al. studied the calculation method of the caving zone's height in the goaf [2]. Guo et al. proposed

the annular fault zone formed above the goaf, constituting the gas accumulation and migration channels [3]. Zhang and Huang derived gas diffusion law in the goaf by studying the gas flow field in the goaf [4]. Zhou et al. applied the two-dimensional model to simulate the fracture's gas flow under mining [5]. Karacan and Esterhuizen developed a comprehensive "dynamic" gas reservoir model by coupling the permeability field with the mechanical model to simulate the effects of gas emission and extraction on gas production in the goaf [6]. Wang et al. proposed a method to reduce the gas content and prevent gas outbursts using the large-diameter borehole gas extraction [7]. Yuan et al. introduced a theory and technology of using large-diameter surface boreholes to control the gas in the goaf, which was successfully implemented in the Huainan Mining Area of China [8]. However, theoretical studies [2–6] on the gas distribution and flow evolution in the goaf provided no practical solutions to the

gas problems arising in the coal mining process. On the other hand, available recommendations for gas control in the goaf proposed in [7, 8] envisaged long construction periods, lacked flexibility and mobility, and failed to solve the problem of gas overrun in the upper corner of the mining face caused by abnormal changes in geological conditions or airflow and abnormal gas emission. Based on the available theoretical achievements, this paper proposes the gas control in the goaf using a large-diameter borehole constructed in the adjacent roadway of the working face. This technology, characterized by high flexibility and productivity, adopts an improved geological drilling machine, producing a large-diameter (550 mm) extraction borehole. The drilling parameters can be easily adjusted, according to particular geological conditions, changes in airflow, and abnormal gas emission. In combination with existing gas control measures, the proposed approach mitigates the problem of local gas accumulation in the working face of high-intensity mining quickly, efficiently, and accurately.

2. Background and Specific Features of the Adjacent Roadway Large-Diameter Drilling Extraction

2.1. Background and Aims of the Proposed Approach. Under the “U-shaped” ventilation mode, the upper corner of the fully mechanized working face in the high-gas coal seam is close to the coal wall and the goaf side; the airflow velocity is very low, and some areas are in the eddy current state. The gas emitted from the goaf circulates near the upper corner and accumulates in the eddy current area. At the same time, the continuous emission of high-concentration gas in the goaf due to air leakage in the working face provides a high amount of gas in the upper corner, easily reaching an overrun state [9]. At present, the common measures taken to mitigate this problem are as follows. The first one is to change the ventilation mode [10] to prevent the gas from forming the eddy current in the upper corner of the working face. The second one envisages the promoted preextraction of the coal seam [11] and reduces gas emissions from the mining seam. The third one is to control the gas in the goaf via pipe burying or spline extraction in the goaf, high-level drilling or roadway extraction, surface drilling extraction [12], etc. These measures are characterized by a long construction period and high costs. Especially in the case of sudden local gas accumulation, a long time is needed for adjustment. Therefore, it is necessary to use rapid, efficient, flexible, and low-cost techniques to reduce local gas accumulation.

2.2. Advantages of the Adjacent Roadway Large-Diameter Extraction. The large-diameter gas extraction boreholes of adjacent roadway construction at the air-return side of the working face shown in Figure 1 can change the eddy current formed at the upper corner of the working face into the original flow field of the goaf, introduce new disturbance, extract the goaf gas in the form of large flow and low negative

pressure, and intercept the gas from the goaf due to the air leakage of the working face to solve the problem of local gas overrun. This technology features mechanized operation, simple process, and low engineering complexity, which can effectively solve the problem of connection and balance of mine “mining and extraction” in terms of time. The borehole spacing and the number of boreholes can be adjusted at any time with the working face advance. With strong flexibility, it can exert an effective interception effect on the emitted goaf gas. The key issue of this technology application is to determine the optimal drilling configuration parameters. The computational fluid dynamics (CFD) numerical simulation can be used to determine the gas concentration field and flow field distribution pattern of the goaf at various large-diameter boreholes’ parameters. Then, the drilling configuration design can be optimized to get the best extraction parameters. The technology of large-diameter drilling in the adjacent roadway to control the goaf is illustrated in Figure 1. A gas drainage process is schematically presented in Figure 1(a), where the extracted gas (i.e., coalbed methane or CBM) is transported via pipelines, with an improved utilization rate of energy resources and environmental protection. Figures 1(b)–1(d) show the specific construction equipment and technology of gas drainage.

3. Numerical Simulation of Large-Diameter Drilling Extraction

3.1. Theories of Goaf Gas Migration. Under the mining and the overlying rock pressure, the size of voids in the goaf exhibits certain trends in the vertical and strike directions. In the vertical direction, the caving zone, fracture zone, and bending subsidence zone are formed [13]. In the strike direction, with different accumulation states and pressure on the coal and rock mass, three areas are formed: the natural accumulation area, the caving load area, and the recompaction area [14]. During the coal seam mining process, the goaf loses its supporting force, and a considerable number of secondary fissures are formed in the caving zone and the fracture zone, which become the main gas migration channels. The coal and rock mass in the caving zone is filled with a considerable amount of broken coal and rock mass, resulting in larger porosity. The fracture zone has a smaller porosity due to the support of the caving zone. The goaf’s porosity shows nonuniform continuous distribution characteristics [15] and presents an O-shaped distribution, as shown in Figure 2.

The height of the fracture and caving zones in the goaf can be obtained through physical analog modeling, numerical simulation, field observations, and theoretical calculations [16]. Determination of these values is conducive to analyzing the physical properties and gas flow characteristics of the goaf. It can provide basic support for the establishment of CFD numerical analysis. According to the law of movement and failure of the overlying coal and rock mass in the goaf, the caving zone and the fracture zone in the goaf can be calculated as follows:

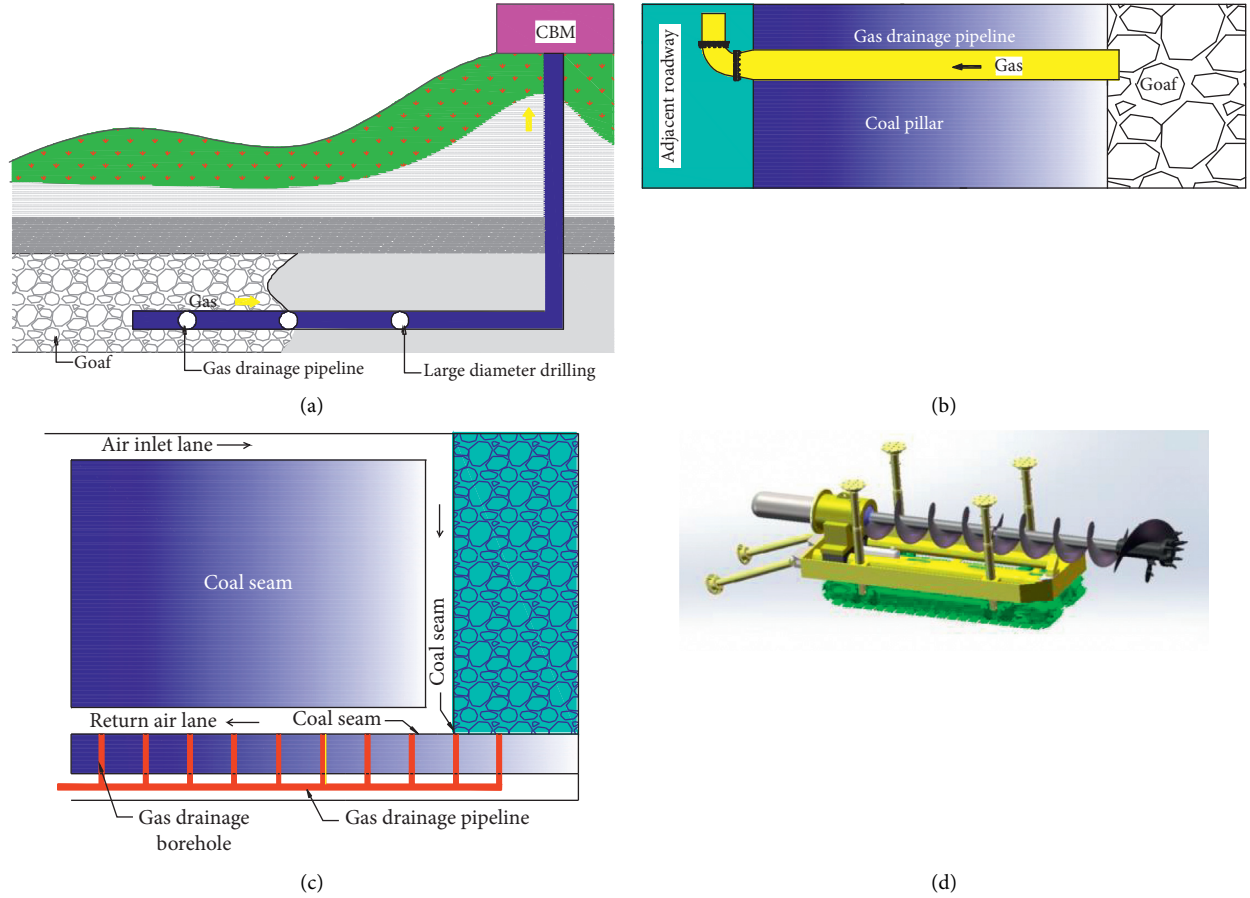


FIGURE 1: Schematic diagram of the large-diameter drilling extraction. (a) Gas drainage diagram. (b) Section diagram of extraction borehole. (c) Plane diagram of extraction drilling. (d) Schematic diagram of drilling rig.

$$H_k = \frac{H - W}{(K_{pb} - 1)} \pm c, \tag{1}$$

$$H_l = \frac{100H}{aH + b} \pm c,$$

where H_k is the caving zone height, H is the mining height, W is the main roof subsidence, K_{pb} is the crushing expansion coefficient of the caving rock, and α is the dip angle of the coal seam, while a, b, c are the coefficients related to the roof

properties, which can be determined according to the empirical formula in [5].

According to the “O”-ring theory, the goaf’s porosity distribution gradually increases from the goaf’s edge to the central compaction area. Based on the mathematical model of a continuous surface of the subsidence of the stope overburden, the porosity distribution model of the caving zone in the goaf has been theoretically deduced [17] in the following form:

$$n(x, y) = 1 + \left(\left(1 + e^{-0.15(l_y - |y|)} \right) \left(1 - \frac{h_d}{h_d + (H - h_d)(K_{pb} - 1)(1 - e^{-(x/2l)})} \right) - 1 \right) \left(1 + \beta\gamma \left(\frac{l_y}{2} - y \right) \sin \alpha \right)^{-1}, \tag{2}$$

where n is the porosity of any point, γ is the volume weight of the caving rock, α is the dip angle of the coal seam, l_y is the dip width of goaf, β is the regression coefficient, h_d is the thickness of the immediate roof, and l is the length of the broken rock block of the main roof.

For the convenience of calculation, the following assumptions are made for the goaf in this study [18]:

- (1) The shearer and all kinds of equipment of the hydraulic prop in the fully mechanized top coal caving face are ignored; only the air leakage from the working face into the goaf is calculated for the goaf gas, and the return air roadway and extraction drilling on gas emission and concentration distribution are studied.

(2) The working face, the inlet, and return air roadways are assumed to be cuboids filled with an incompressible ideal gas.

(3) The goaf is assumed to be porous and isotropic [19].

Therefore, the goaf's gas mixture flow satisfies the mass equation and the momentum equations [20].

The mass equation has the following form:

$$\frac{\partial \rho}{\partial t} + \frac{\partial(\rho\mu)}{\partial x} + \frac{\partial(\rho\nu)}{\partial y} + \frac{\partial(\rho w)}{\partial z} = 0. \quad (3)$$

The momentum equations can be expressed as follows:

$$\begin{aligned} \frac{\partial(\rho\mu\mu)}{\partial x} + \frac{\partial(\rho\mu\nu)}{\partial y} + \frac{\partial(\rho\mu w)}{\partial z} &= \frac{\partial}{\partial x} \left(\mu \frac{\partial \mu}{\partial x} \right) + \frac{\partial}{\partial y} \left(\mu \frac{\partial \mu}{\partial y} \right) + \frac{\partial}{\partial z} \left(\mu \frac{\partial \mu}{\partial z} \right) - \frac{\partial p}{\partial x} + S_u, \\ \frac{\partial(\rho\nu\mu)}{\partial x} + \frac{\partial(\rho\nu\nu)}{\partial y} + \frac{\partial(\rho\nu w)}{\partial z} &= \frac{\partial}{\partial x} \left(\mu \frac{\partial \nu}{\partial x} \right) + \frac{\partial}{\partial y} \left(\mu \frac{\partial \nu}{\partial y} \right) + \frac{\partial}{\partial z} \left(\mu \frac{\partial \nu}{\partial z} \right) - \frac{\partial p}{\partial y} + S_v, \\ \frac{\partial(\rho w\mu)}{\partial x} + \frac{\partial(\rho w\nu)}{\partial y} + \frac{\partial(\rho w w)}{\partial z} &= \frac{\partial}{\partial x} \left(\mu \frac{\partial w}{\partial x} \right) + \frac{\partial}{\partial y} \left(\mu \frac{\partial w}{\partial y} \right) + \frac{\partial}{\partial z} \left(\mu \frac{\partial w}{\partial z} \right) - \frac{\partial p}{\partial z} + S_w. \end{aligned} \quad (4)$$

The turbulent kinetic energy equation is

$$\begin{aligned} \frac{\partial(\rho k)}{\partial t} + \frac{\partial(\rho\mu_i k)}{\partial x_i} &= \frac{\partial[(\mu + (\mu_t/\sigma_k))\partial k/\partial x_j]}{\partial x_j} \\ &+ G_k + G_b - \rho\varepsilon - Y_M + S_k. \end{aligned} \quad (5)$$

The transport equation of the turbulent dissipation rate is given below:

$$\begin{aligned} \frac{\partial(\rho\varepsilon)}{\partial t} + \frac{\partial(\rho\mu_i\varepsilon)}{\partial x_i} &= \frac{\partial[(\mu + (\mu_t/\sigma_\varepsilon))\partial\varepsilon/\partial x_j]}{\partial x_j} \\ &+ C_{1\varepsilon} \times \frac{\varepsilon}{k} (G_k + C_{3\varepsilon} G_b) - G_b - C_{2\varepsilon} \rho \frac{\varepsilon^2}{k} + S_\varepsilon, \end{aligned} \quad (6)$$

where μ_t is the turbulent viscosity, μ_i is the time-averaged velocity, ρ is the density, G_k is the generic term of turbulent kinetic energy k caused by the velocity gradient, S_ε and S_k are user-defined source terms, and $C_{1\varepsilon}$, $C_{2\varepsilon}$, and $C_{3\varepsilon}$ are empirical constants.

If the goaf is regarded as the porous medium, it possesses the additional (viscous and inertial) resistance to the gas mixture in the goaf. By adding the loss term in the momentum equation, including viscous resistance and inertial resistance, the following equation is obtained:

$$S_i = \frac{\mu\nu_i}{k} + 0.5C_2\rho\nu_i|v_i|, \quad (7)$$

where k is the goaf permeability (the reciprocal of viscous resistance), μ is the dynamic viscosity, ν_i is the velocity component in direction i , and C_2 is the inertia resistance coefficient. Due to the small air leakage in the goaf, the inertia resistance is usually neglected.

As shown in equation (7), permeability is the key parameter for simulating the goaf gas migration law. According to Darcy's law [21], the permeability model can

be represented by the Kozeny–Carman equation [22, 23] in the following form:

$$k = \frac{D_p^2}{180} \cdot \frac{n^3}{(1-n)^2}, \quad (8)$$

where D_p is the average particle size ranging from 0.014 to 0.016 m [24] and n is the porosity of the porous medium.

Equation (8) constitutes the governing equation of the gas flow in the goaf. For the particular boundary and initial conditions, the gas flow pattern can be determined.

3.2. Gas Source Analysis. The gas emission in a fully mechanized working face can be calculated using the different-source prediction method, with the coal seam gas content used as the basic parameter [25]. It follows the principle of establishing an empirical formula based on years of detection data according to the gas content of coal seam, the gas gushing pattern of gas gushing source, the occurrence conditions, and mining technical conditions of coal seam [26]. The gas emission of each part is calculated to achieve the gas emission calculation.

Gas emission from a fully mechanized working face includes gas emissions from the mining seam, from the coal remaining in the goaf, and from the adjacent seam, as shown in Figure 3.

The calculation formula of gas emission in the mining seam Q_1 is as follows:

$$Q_1 = \lambda \cdot \frac{m}{H} (W_0 - W_c), \quad (9)$$

and that in the adjacent seam Q_2 is

$$Q_2 = \sum_{i=1}^n (W_{0i} - W_{ci}) \cdot \frac{m_i}{H}. \quad (10)$$

The calculation formula of gas emission from the coal remaining in the goaf Q_3 is

$$Q_3 = l \cdot q_0 \cdot v_0 \left[\exp\left(-\sqrt{\frac{l_1}{v_0 t}}\right) + \exp\left(-\sqrt{\frac{l_2}{v_0 t}}\right) \right], \quad (11)$$

where λ is the gas emission coefficient, W_0 is the original gas content, W_c is the residual gas content, m is the mining seam thickness, i is the parameter of the i -th adjacent seam, l is the perimeter of the roadway fault face, v_0 is the advancing speed of the working face, t is the exposure time of the coal seam (which is taken as six months), l_1 is the strike length of the working face, l_2 is the strike length of the goaf, and q_0 is the gas emission intensity of the coal wall. The latter parameter can refer to the calculation of coal wall gas emission in "Prediction method of mine gas emission" (AQ1018-2006):

$$q_0 = 0.026 \cdot \left[0.0004(V^f)^2 + 0.16 \right] \cdot W_0, \quad (12)$$

where V^f is the volatile content in the coal, taken as 18.79%.

3.3. Details of Numerical Simulation

3.3.1. Basic Parameters of the Working Face. The Tenghui Coal Mine is located in Xiaohua Township, Hejin City, Shanxi Province, China, with the mine field located on the southern edge of the Hedong Coalfield. The strike longwall mining method is adopted for the working face. The average thickness of the coal seam is 5.2 m, the widths of the inlet and return air roadway of the working face are 4 m, the height is 3 m, the length of the working face is 185 m, the mining height is 3 m, the mining width is 5 m, the roof periodic weighting step is 15 m, and the buried depth of the coal seam is 368–480 m. The U-shaped ventilation mode is adopted. The lithology of the roof is sandy mudstone and mudstone, and the lithology of the floor is mudstone and sandy mudstone, which belongs to a medium-hard roof.

According to the previous basic theoretical analysis, the geological conditions of the Hedong Coalfield, the actual on-site test data of the Tenghui Coal Mine working face, the experimentally measured data, and the empirical parameters' values, the calculation formula parameters were obtained and are listed in Table 1. The physical parameters of the numerical model are summarized in Table 2.

3.3.2. Establishment of a Geometric Model of a Fully Mechanized Working Face. According to the actual situation in the coal mining face, the size and boundary conditions were set as follows:

- (1) The size of inlet and return roadways was $10 \times 4 \times 3 \text{ m}^3$, the size of the working face was $185 \times 5 \times 3 \text{ m}^3$, and space was filled with fluid.
- (2) The goaf size was $185 \times 200 \times 57 \text{ m}^3$, in which the fracture zone was 40 m, the caving zone was 17 m, and space was a porous medium.
- (3) Except for the inlet and return air roadways of the working face, all the outer boundaries of the

extraction drilling were set as the "wall," and the interface between the working face and the goaf was set as the "interior." It was assumed that the stope had no material exchange or conditional reaction with the outside environment. The established geometric model is shown in Figure 4(a), and red arrows represent the model's corresponding coordinate system in Figure 2.

3.3.3. Mesh Generation and Model Realization. (1) *Mesh Generation.* The established physical model's calculation domain was meshed using a tetrahedral mesh, as shown in Figure 4(b).

The inlet and return air roadways' mesh sizes were both 0.5 m, and those of the caving and fracture zones in the goaf were 2 m each. When the large-diameter borehole was connected to the goaf, spherical densification was carried out around the goaf, and the densified mesh size was 0.1 m, as shown in Figure 4(c).

(2) *Solver Setting.* The gas concentration and flow field distribution in the goaf were numerically simulated at the borehole distances of 0, 5, 10, 15, and 20 m from the working face under the extraction-free and extraction conditions. It was assumed that the flow rate of the extraction borehole remained unchanged. The simulation conditions were as follows: the inlet velocity of $2.5 \text{ m} \cdot \text{s}^{-1}$ was set at the inlet of the inlet roadway, the "outlet flow" was set at the outlet of the return roadway, the inlet velocity of the large-diameter extraction borehole was $-5 \text{ m} \cdot \text{s}^{-1}$, the borehole diameter was 550 mm, and the vertical distance from the floor was 2 m.

When the goaf was treated as the porous medium, permeability was a parameter to be determined. In the fracture zone, the permeability variation range is usually between 10^{-6} and 10^{-11} m^2 [27]. In this study, the porosity of the fracture zone was taken as a fixed value of 0.03 [28]. Substitution of this value into equation (8) yields the permeability range between 10^{-6} and 10^{-11} . The porosity of the caving zone of the actual working face was substituted into equation (3) to get the porosity distribution, which had a "shovel" shape. This implies large porosity values of the shallow part and two roadway sides and small ones of the middle and inner parts, as shown in Figure 4(d). The porosity value was substituted into equation (8) to obtain the permeability parameters.

A user-defined function (UDF) was employed during the CFD numerical simulation to compile the caving zone's permeability. The "simple" algorithm was selected in the pressure-velocity coupling algorithm, and the renormalization group (RNG) K-epsilon (k - ϵ) turbulence model [29] was adopted to simulate the gas flow mixture in the stope to improve the simulation accuracy.

3.4. Analysis of Simulation Results for Various Conditions

3.4.1. Analysis of Gas Migration Law in Goaf under Drainage Conditions. A coordinate system was established according to Figure 4, with the depth direction, the inclination direction, and the vertical direction of the goaf taken as the X-,

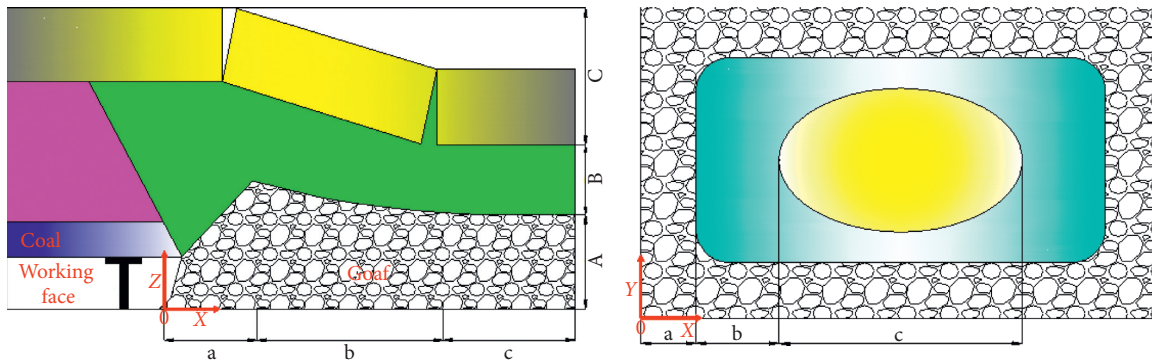


FIGURE 2: Diagram of three horizontal and three vertical zones in the goaf and the coordinate system of the proposed model. (A) Collapse zone. (B) Fracture zone. (C) Bending subsidence zone. (a) Natural accumulation area. (b) Load affected zone. (c) Compaction area.

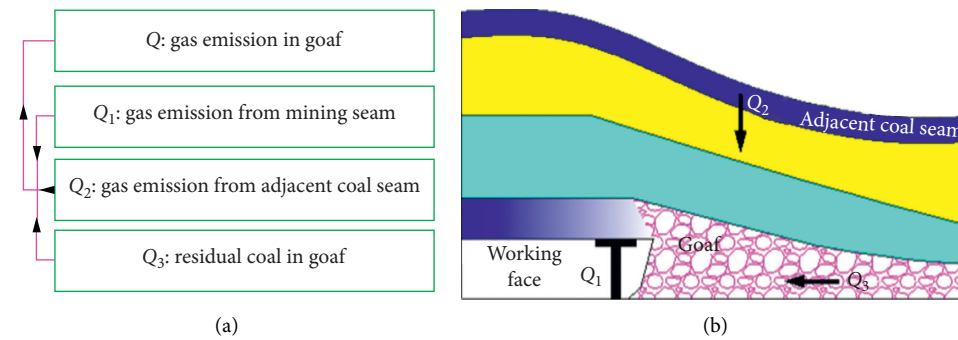


FIGURE 3: Gas source diagram of the working face. (a) Structure diagram of gas source in goaf. (b) Schematic diagram of gas source in goaf.

Y-, and Z-axes, respectively. The range of the X-axis $[-2\text{ m}, 0]$ was regarded as the upper corner of the working surface. According to the coal mine safety regulations, 0.8% of the gas concentration in the upper corner is the critical value, while that below 0.8% is considered to be safe, implying the draining effectiveness.

The numerical simulation results of gas migration under the conditions of $Z = 2\text{ m}$ and no extraction and large-diameter borehole extraction in the goaf area are illustrated in Figure 5. It can be observed from Figure 5(a) that due to air leakage from the working face, the airflow enters the goaf to bring the high-concentration gas in the goaf to the return air side and finally dilutes into the return airflow. Due to the coal wall effect, the air current forms a vortex near the upper corner of the working surface, causing local overrun, with the gas concentration exceeding 6%. The deeper the goaf, the higher the gas concentration, up to 70%, making the goaf a gas reservoir. Therefore, extraction measures must be taken to restrain the upper corner gas from exceeding the limit.

In this paper, simulation schemes with different flow rates and locations listed in Table 3 were designed to explore the impact of large-diameter boreholes on gas migration in goaf. The gas distribution law was obtained by comparison. According to the actual working conditions of the on-site extraction pump, the maximum extraction flow rate of the borehole was $100\text{ m}^3\cdot\text{min}^{-1}$, indicating that the maximum flow rate of the mixed gas in the borehole was $7\text{ m}\cdot\text{s}^{-1}$.

Other boundary conditions and the calculation process of the solver were the same as before. Besides, the gas concentration values in the large-diameter borehole and the upper corner were taken as dependent variables. The numerical simulation results are presented in Figure 6.

Best fitting of the numerical simulation results was performed, yielding the following formula:

$$c = 0.489 + \frac{0.667}{\nu} + 6.62e^{-6y^4} + \frac{3.28}{y \cdot \nu} - 0.00283\nu \cdot y^2, \quad (13)$$

$$R^2 = 0.958, \quad (14)$$

where c denotes the gas concentration in the upper corner, ν is the extraction rate, and y is the distance from the working face, while R^2 is the correlation coefficient, which the value is 0.958 that to indicate a close correlation.

As seen from the fitting formula, when the drilling position is fixed, the higher the extraction rate, the lower the gas concentration in the upper corner. When the extraction rate is constant, the farther the drilling position from the working surface, the higher the gas concentration in the upper corner.

As illustrated in Figure 6(a), with an increase in the extraction rate, the concentration in the gas pipeline gradually grows. The farther the borehole from the working

TABLE 1: Calculation formula parameters' values.

Symbol	Parameter	Value	Unit
$a/b/c$	Calculation parameters of the fracture zone	1.5/3.6/5.6	
H	Mining height	5.2	m
h_d	Thickness of immediate roof	6	m
K_{pb}	Coefficient of rock crushing expansion of the caving zone	1.049	
l	Length of main roof broken rock block	8	m
l_1	Strike length of working face	185	m
l_2	Strike length of goaf	185	m
m	Thickness of mining seam	5.2	m
q_0	Gas emission intensity of coal wall	0.0503	$m^3 \cdot (m^2 \cdot min)^{-1}$
v_0	Advancing speed of the working face	4.2×10^{-3}	$m \cdot min^{-1}$
W_0	Original gas content of coal seam	12.1	$m^3 \cdot t^{-1}$
W_c	Residual gas content	2.81	$m^3 \cdot t^{-1}$
α	Coal seam dip angle	0	$^\circ$
λ	Gas emission coefficient	1.34	

TABLE 2: Physical parameters of the numerical model.

Symbol	Parameter	Value	Unit
H_l	Height of the fracture zone	40	m
H_k	Height of the caving zone	17	m
Q_1	Gas emission of the mining seam	6.49×10^{-6}	$kg \cdot (m^3 \cdot s)^{-1}$
Q_2	Gas emission of the adjacent seam	1.99×10^{-9}	$kg \cdot (m^3 \cdot s)^{-1}$
Q_3	Goaf gas emission amount	1.71×10^{-7}	$kg \cdot (m^3 \cdot s)^{-1}$

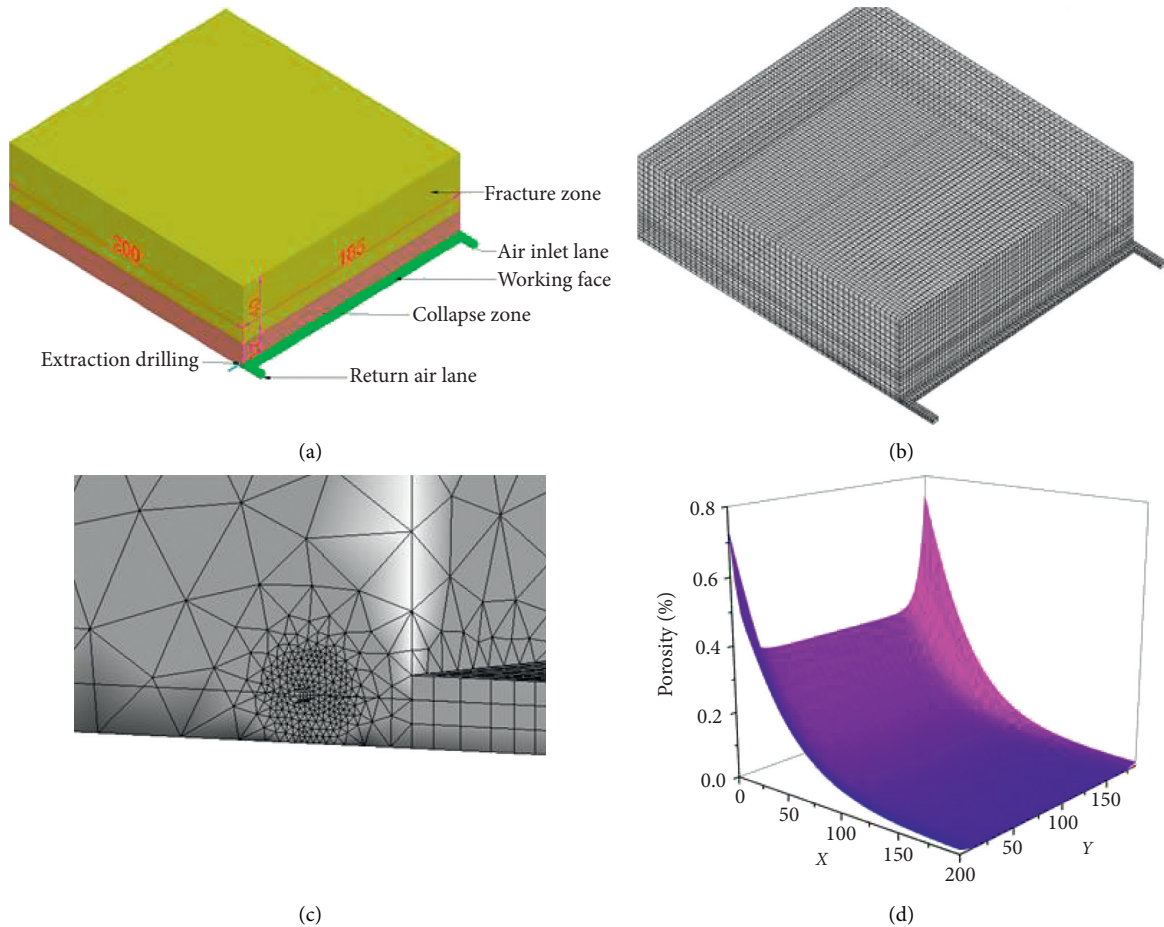


FIGURE 4: Numerical simulation model and porosity distribution of the caving zone. (a) Geometric model of working face. (b) Mesh generation of working face. (c) Distribution law of porosity in goaf. (d) Mesh generation of large-diameter borehole.

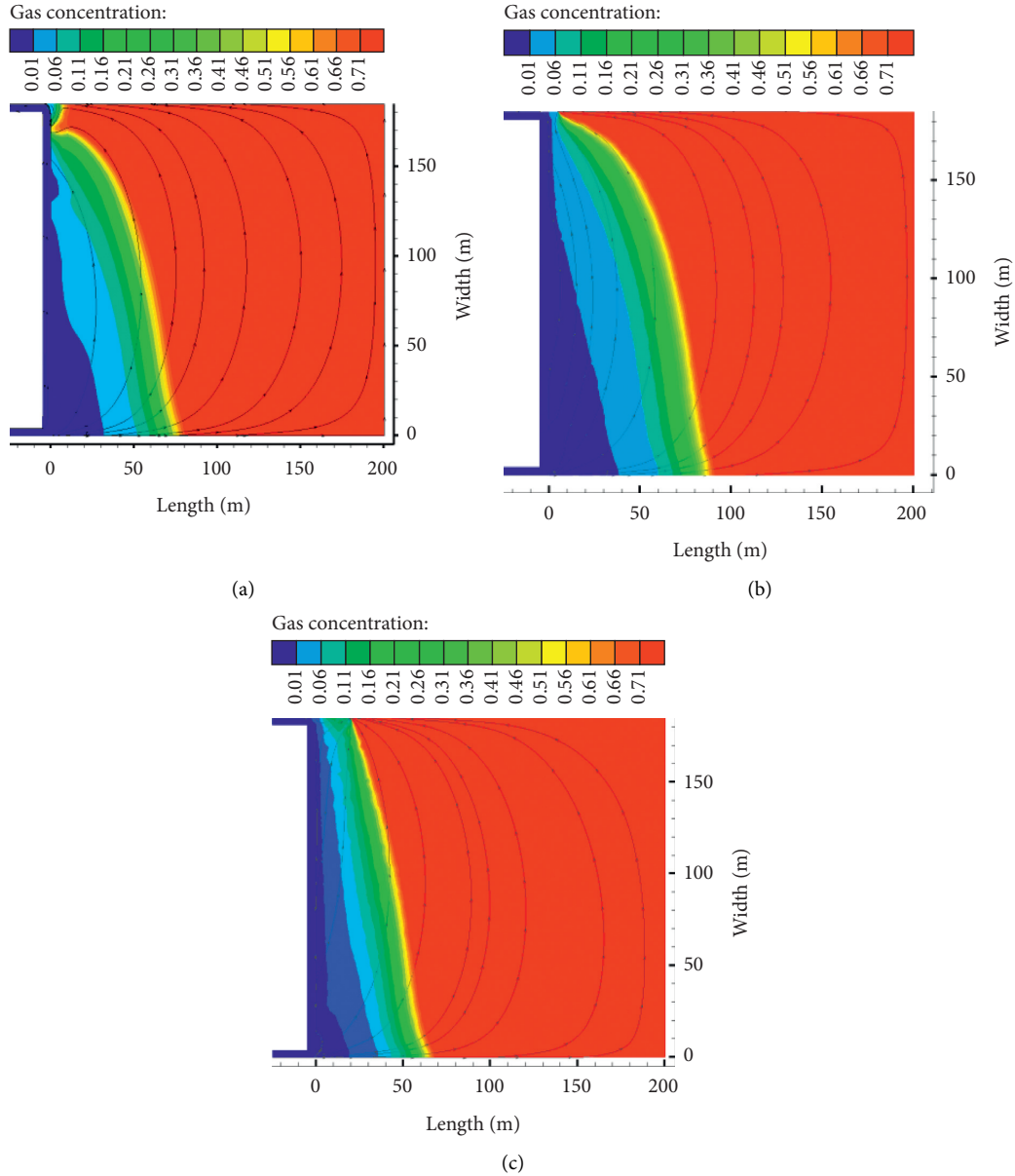


FIGURE 5: Gas distribution in goaf under different parameters. (a) Gas distribution in goaf without drainage. (b) Gas distribution under the condition of drainage ($x = 10 \text{ m}$, $v = 3 \text{ m}\cdot\text{s}^{-1}$). (c) Gas distribution in goaf without drainage ($x = 20 \text{ m}$, $v = 5 \text{ m}\cdot\text{s}^{-1}$).

surface, the higher the gas concentration in the borehole. The gas concentration was in the range from 20 to 60%. Simultaneously, the gas concentration gradient gradually dropped.

In Figure 6(b), the blue area represents the zone where the gas concentration in the upper corner was below 0.8%. It can be observed that the gas concentration in the upper corner gradually decreased as the extraction rate increased. When the borehole extraction rate was lower than $3 \text{ m}\cdot\text{s}^{-1}$, the upper corner's gas concentration decreased faster than that when the extraction rate exceeded $3 \text{ m}\cdot\text{s}^{-1}$. When the borehole was located 10 m behind the working face, the gas concentration in the upper corner was the lowest, and the extraction effect was the best. The farther the borehole from the working surface, the weaker the ability to control the

upper corner. When the borehole was 20 m away from the working surface, the extraction rate exceeded $6 \text{ m}\cdot\text{s}^{-1}$, ensuring that the upper corner gas concentration was less than 0.8%.

The analysis of Figures 5 and 6 and fitting formula (14) revealed that the negative pressure of the borehole changed the distribution of the gas flow field in the goaf. Part of the gas that was directly pumped out contributed to intercepting the gas gushing out of the goaf. Simultaneously, it disturbed the eddy currents formed in the upper corners of the working surface and prevented the local gas accumulation under certain conditions of extraction flow and drilling positions. However, the negative pressure also attracted high-concentration gas in the goaf to move closer to the working face, leading to increased air leakage from the

TABLE 3: Design scheme of numerical simulation parameters.

Drilling location (Y) (m)	Borehole gas velocity (v)
5	$1 \text{ m}\cdot\text{s}^{-1}$, $2 \text{ m}\cdot\text{s}^{-1}$, $3 \text{ m}\cdot\text{s}^{-1}$, $4 \text{ m}\cdot\text{s}^{-1}$, $5 \text{ m}\cdot\text{s}^{-1}$, $6 \text{ m}\cdot\text{s}^{-1}$, $7 \text{ m}\cdot\text{s}^{-1}$
10	$1 \text{ m}\cdot\text{s}^{-1}$, $2 \text{ m}\cdot\text{s}^{-1}$, $3 \text{ m}\cdot\text{s}^{-1}$, $4 \text{ m}\cdot\text{s}^{-1}$, $5 \text{ m}\cdot\text{s}^{-1}$, $6 \text{ m}\cdot\text{s}^{-1}$, $7 \text{ m}\cdot\text{s}^{-1}$
15	$1 \text{ m}\cdot\text{s}^{-1}$, $2 \text{ m}\cdot\text{s}^{-1}$, $3 \text{ m}\cdot\text{s}^{-1}$, $4 \text{ m}\cdot\text{s}^{-1}$, $5 \text{ m}\cdot\text{s}^{-1}$, $6 \text{ m}\cdot\text{s}^{-1}$, $7 \text{ m}\cdot\text{s}^{-1}$
20	$1 \text{ m}\cdot\text{s}^{-1}$, $2 \text{ m}\cdot\text{s}^{-1}$, $3 \text{ m}\cdot\text{s}^{-1}$, $4 \text{ m}\cdot\text{s}^{-1}$, $5 \text{ m}\cdot\text{s}^{-1}$, $6 \text{ m}\cdot\text{s}^{-1}$, $7 \text{ m}\cdot\text{s}^{-1}$
25	$1 \text{ m}\cdot\text{s}^{-1}$, $2 \text{ m}\cdot\text{s}^{-1}$, $3 \text{ m}\cdot\text{s}^{-1}$, $4 \text{ m}\cdot\text{s}^{-1}$, $5 \text{ m}\cdot\text{s}^{-1}$, $6 \text{ m}\cdot\text{s}^{-1}$, $7 \text{ m}\cdot\text{s}^{-1}$
30	$1 \text{ m}\cdot\text{s}^{-1}$, $2 \text{ m}\cdot\text{s}^{-1}$, $3 \text{ m}\cdot\text{s}^{-1}$, $4 \text{ m}\cdot\text{s}^{-1}$, $5 \text{ m}\cdot\text{s}^{-1}$, $6 \text{ m}\cdot\text{s}^{-1}$, $7 \text{ m}\cdot\text{s}^{-1}$

working face. This increased the gas concentration gradient on the return air side, leading to a higher risk of spontaneous combustion in the goaf.

3.4.2. Influence of Large-Diameter Borehole Extraction on Spontaneous Combustion Zone in Goaf. When the gas in the goaf is subjected to high-flow extraction, the air leakage state in the goaf will change, varying the width of the oxidation zone and the air leakage in the goaf. In this paper, the oxygen concentration in the goaf was used as a zoning criterion. The area with the oxygen concentration exceeding 18% in the goaf was identified as a heat dissipation zone, while that with the oxygen concentration in the goaf between 8 and 18% was regarded as an oxidation heating zone. The oxygen concentration in the goaf area in the breath zone was less than 8%. To study the distribution law of the spontaneous combustion zone in the goaf, the distribution variation of the spontaneous combustion zone was compared when the borehole was located at different positions under the condition that the extraction rate of the large-diameter borehole was $6 \text{ m}\cdot\text{s}^{-1}$. In addition, the distribution variation of the spontaneous combustion zones in the goaf under the condition of different extraction rates of the large-diameter borehole was compared when the borehole was located at 10 m.

At $Z = 2$, there was no extraction; when the borehole was located at 10 m, the extraction rate was $6 \text{ m}\cdot\text{s}^{-1}$. When the borehole was located at 20 m, the oxygen concentration distribution cloud diagram was obtained, as shown in Figure 7.

According to the numerical simulation results on oxygen distribution in Tables 4 and 5 and the cloud diagram in Figure 7, larger drilling depths in the goaf corresponded to larger extraction rate, wider spontaneous combustion zone of the goaf, and higher risk of spontaneous combustion.

The disturbance effect of the extraction of large-diameter boreholes caused the spontaneous combustion zone of the goaf to widen and get deeper in the goaf. Therefore, the risk of spontaneous combustion in the goaf increased. The simulation demonstrated that when the borehole was located at a position of 20 m, the mixed gas extraction rate of the borehole was $6 \text{ m}\cdot\text{s}^{-1}$, the maximum width of the spontaneous combustion zone in the goaf was 30 m, and the shortest spontaneous combustion period of the coal seam of the Tenghui Coal Mine was 35 d. This implied that the safe advance rate of the working face was no less than 0.86 m per day.

4. Field Test Results

According to the numerical simulation results, when the flow rate of the extraction borehole was no less than $3 \text{ m}\cdot\text{s}^{-1}$, the borehole located in the range of 5 m–15 m behind the working face inhibited the gas accumulation in the upper corner of the working face. At the flow rate of the extraction borehole no less than $7 \text{ m}\cdot\text{s}^{-1}$, the borehole located [5 m, 20 m] from the working face could inhibit the gas accumulation in the upper corner of the working face. However, the flow rate of $7 \text{ m}\cdot\text{s}^{-1}$ was the maximum limit value that could be assigned to a large-diameter drilling pipeline of the extraction system.

The 2-105 working face was located southwest of the mine field. As the second working face of the first mining area of the mine, it was arranged in the west wing of the first mining area, east-west direction. On the east wing of the working face was the return air roadway, belt transportation lane, and auxiliary transportation lane of the first mining area. The south and west wings were the boundaries of the coal mine field, and the north wing was the 2-104 working face. Combined with the simulation results and the actual conditions of the Tenghui Mine's 2-105 working face, the extraction borehole was designed. The construction site was located in the 2-105 adjacent roadway, which was the preparation roadway for the next working face. The dimensions of the adjacent roadway of the working face were $3 \text{ m} \times 3 \text{ m} \times 4 \text{ m}$, and the roadway length was 800 m.

The engineering design implied a borehole interval (spacing) of 10 m and a borehole distance of 2 m from the floor, considering the production operability and safety. When the extraction borehole entered the goaf and was located 5 m from the working face, the control valve was opened for gas extraction, while the borehole located 15 m from the working face was closed. The control valves of subsequent boreholes were operated in turn, and the flow rate of the extraction borehole was no less than $3 \text{ m}\cdot\text{s}^{-1}$. The boreholes were numbered in increasing order with the distance from the working face, as shown in Figure 8.

With the advance of the working face, when the 1# borehole connected to the goaf entered the goaf and was 5 m from the working face, the 1# borehole control valve was opened for gas extraction. When the 2# borehole entered the goaf and was 5 m from the working face, the 2# borehole control valve was opened for gas extraction, and the 1# borehole control valve was closed simultaneously. The alternate switching of boreholes was similar to the subsequent drilling.

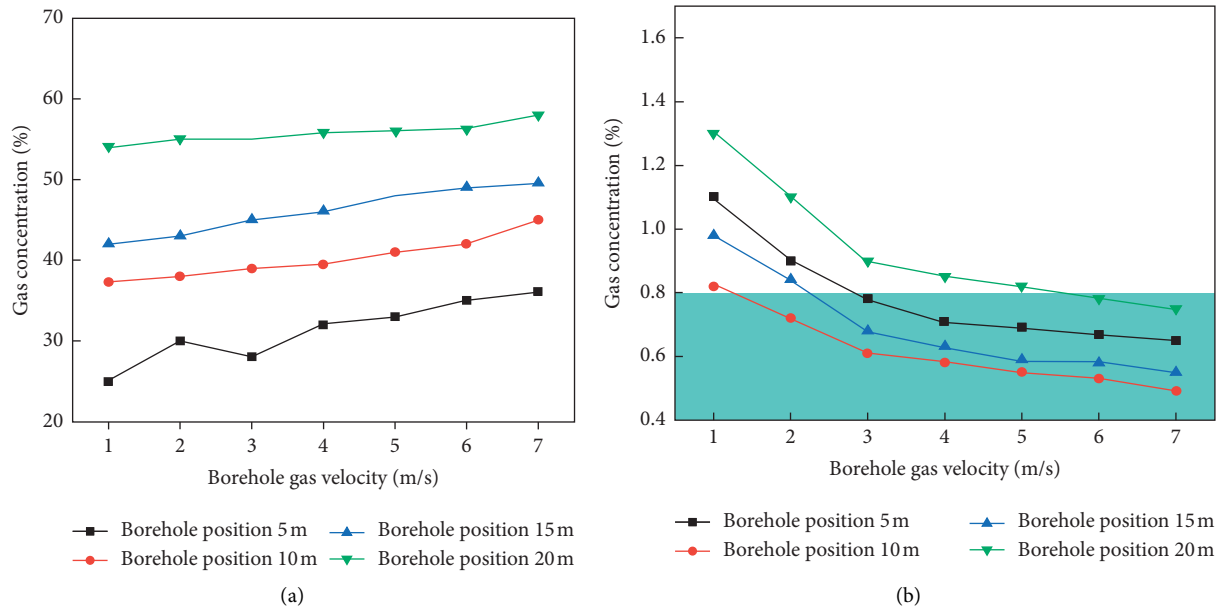


FIGURE 6: Gas concentration of extraction borehole and upper corner under different parameters. (a) Gas concentration in drainage pipeline. (b) Gas concentration in upper corner.

After the 1#, 2#, and 3# large-diameter boreholes started the gas extraction, the gas concentrations in the extraction pipeline, the upper corner, and the return air roadway were recorded per each 1 m, as the working face advanced.

According to the performed investigation of three boreholes, the gas concentration in the upper corner of the working face and the return air roadway was within the controllable range, the gas concentrations in the upper corner and the return air roadway ranged between 0.5 and 0.8% and between 0.45 and 0.61%, respectively. As the working face advanced, with an increase of the distance between the working face and the large-diameter borehole, the evolution curves of gas concentration in the upper corner of the working face and the return air roadway were “V”-shaped. When the borehole was 5 m away from the working face, the gas concentrations in the upper corner and the return air roadway reached their maximal values of 7 and 0.6%, respectively. When the borehole was about 12 m away from the working face, the borehole had the strongest control over the upper corner, the lowest gas concentration in the upper corner was about 0.55%, and the gas concentration in the return air roadway was about 0.45%. As the working face continued to advance, the gas concentration in the upper corner and the return air roadway gradually increased and changed periodically with the opening of the borehole. The variation trend of the gas concentration in the upper corner was consistent with the trend of the simulated data-fitting equation.

The gas concentration in the large-diameter borehole gradually increased. The deeper the borehole into the goaf, the higher the gas concentration in the borehole. When the borehole was located in the shallow part of the goaf, i.e., about 5 m behind the working face, the negative pressure around the borehole was relatively low, and the gas injection

in the goaf was relatively small. The gas concentrations in the pipeline and the upper corner were about 15 and 0.6%, respectively. When the borehole was located 12 m behind the coal mining face, the gas concentration reached the highest value of about 37%. At this time, the gas concentration in the upper corner was maintained at about 0.55%, and then the gas flow in the pipeline tended to be stable. Meanwhile, the gas concentration in the borehole changed periodically with the conversion of the borehole.

The comparative analysis of Figures 8(a) and 8(b) revealed that there was a certain relationship between gas concentrations in the extraction pipeline, the upper corner, and the return air roadway, i.e., when the gas concentration in the extraction pipeline increased, the gas concentration in the upper corner and the return air roadway tended to decrease.

The extraction flow and borehole spacing determined by the numerical simulation were verified in practice. And, when the drilling hole was 10m-12m behind the working face, the extraction effect had been the best effect. During the actual advancement of the working face, the corresponding relationships between the advancing distance and the gas concentration in the upper corner, gas extraction volume, and gas concentration in the return air roadway were observed, and the operation model’s specific parameters in this particular mine were derived.

The main innovation of this paper is that it substantiated and successfully implemented a large-diameter (550 mm) borehole in the roadway adjacent to the working face to control the gas accumulation. To the best of the authors’ knowledge, boreholes with a diameter not exceeding 300 mm have been applied yet for this purpose. According to the relevant definition [30], the underground large-diameter hole generally refers to the near horizontal hole with the final

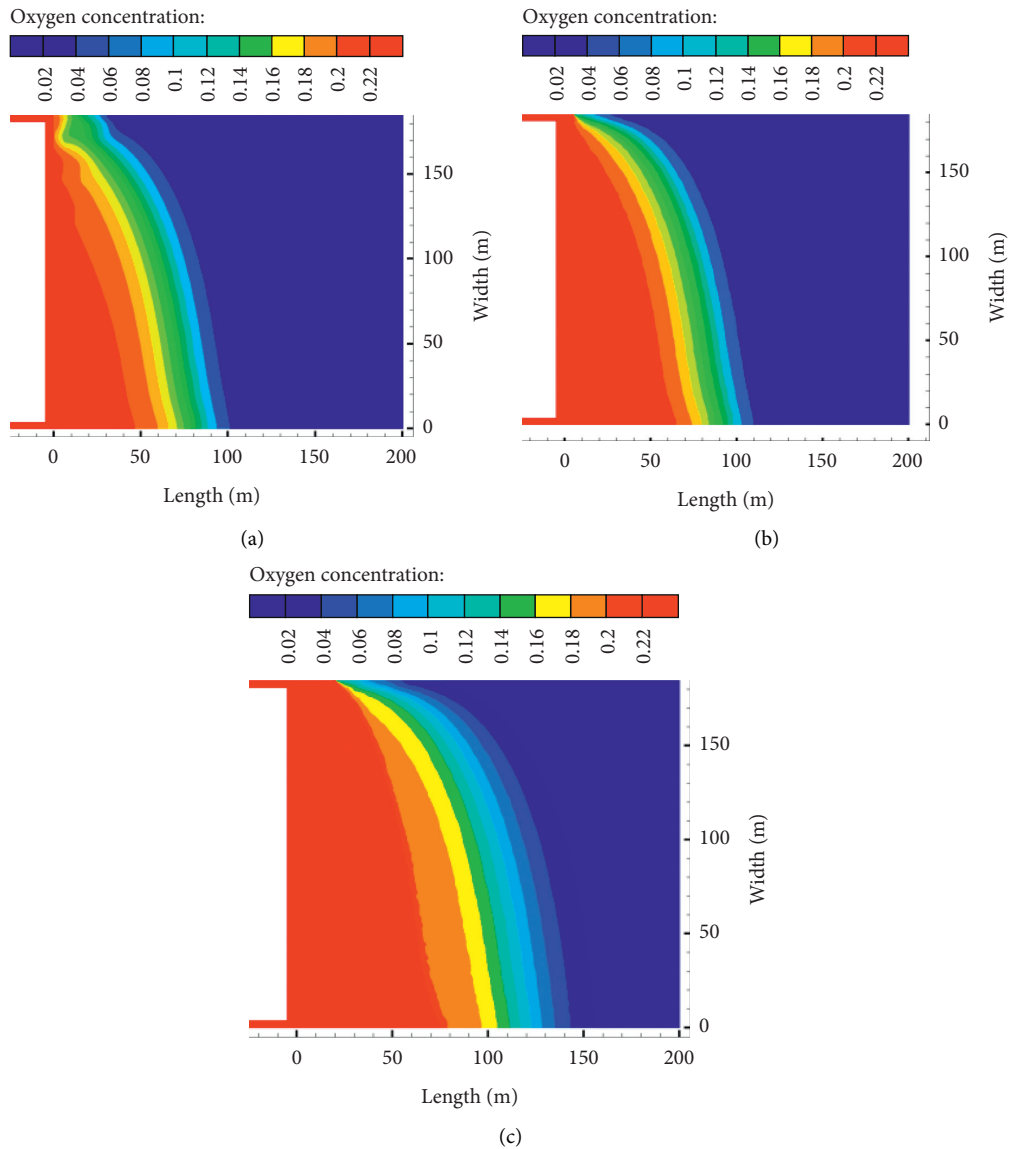


FIGURE 7: Distribution of spontaneous combustion zone in goaf. (a) Oxygen distribution without pumping. (b) Oxygen distribution ($x = 10\text{ m}$, $\nu = 6\text{ m}\cdot\text{s}^{-1}$). (c) Oxygen distribution ($x = 20\text{ m}$, $\nu = 6\text{ m}\cdot\text{s}^{-1}$).

TABLE 4: Distribution of spontaneous combustion zone in goaf at different positions ($\nu = 6\text{ m}\cdot\text{s}^{-1}$).

Extraction location (m)	Inlet side (m)	Middle part (m)	Air-return side (m)
No extraction	65–85	53–75	18–35
5	67–88	70–96	11–25
10	69–91	73–100	16–30
15	73–93	76–105	22–33
20	75–95	80–110	25–36

TABLE 5: Distribution of spontaneous combustion zone in goaf with different extraction rates ($y = 10\text{ m}$).

Extraction rate ($\text{m}\cdot\text{s}^{-1}$)	Inlet side (m)	Middle part (m)	Air-return side (m)
2	64–87	69–93	12–23
4	66–89	72–96	15–27

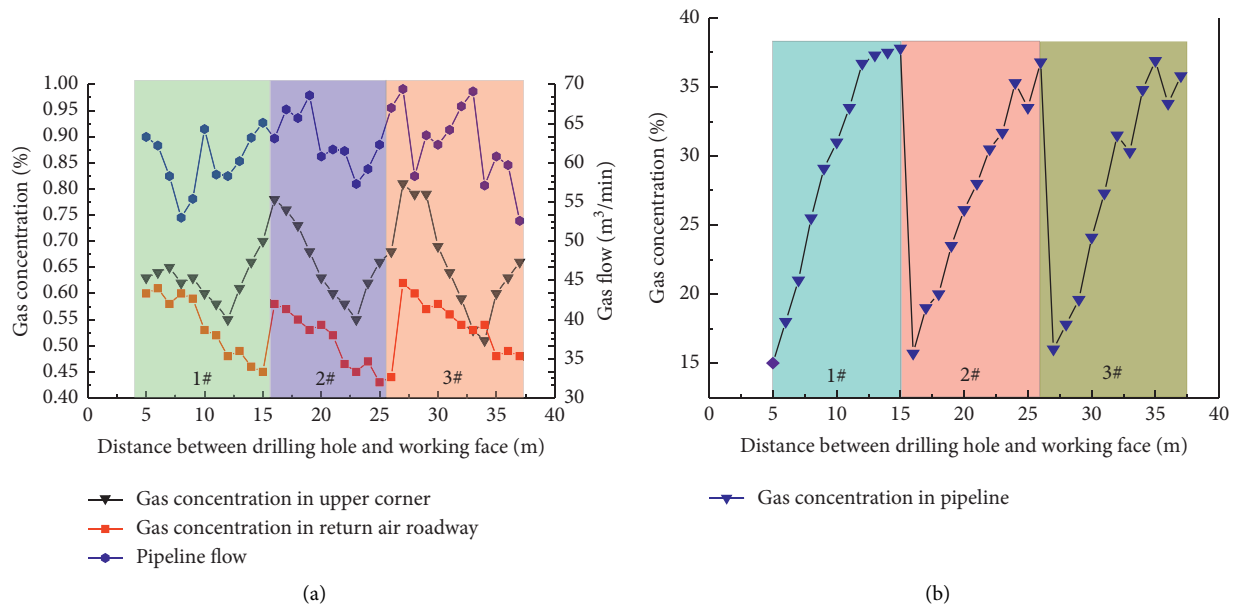


FIGURE 8: Variation of gas concentration in the upper corner, borehole, and return air roadway with the advance of the working face under drainage conditions.

hole diameter of more than 200 mm, which is used for pipeline laying (including ventilation pipe, gas drainage pipe, and drainage pipe), through tunnel rescue (for provision, drainage, escape, etc.) and gas drainage. Thus, the adopted borehole diameter of 550 mm corresponds to large-diameter definition, while larger diameter values are envisaged to be tested in the follow-up study.

5. Conclusions

This study analyzed the gas accumulation patterns caused by the development of fissures in the goaf of the fully mechanized working face, gas storage, and the formation of eddy current in the upper corner. It introduced a technical scheme of gas control in the goaf, which used the adjacent roadway large-diameter boreholes, analyzed gas migration law in the goaf, and determined the optimal configuration parameters.

- (1) Within the CFD framework, firstly, a borehole gas flow simulation scheme was designed under the conditions of different borehole locations and extraction rates. Then, the optimal position of large-diameter drilling was determined through simulation.
- (2) Next, the influence of large-diameter borehole drainage on the spontaneous combustion zone of the goaf was analyzed. Therefore, the optimal drilling configuration parameters based on the upper corner gas concentration in the fully mechanized mining face of the Tenghui Mine were determined: the velocity of the borehole was no less than $3 \text{ m}\cdot\text{s}^{-1}$, the effective range of the borehole placement was 5 m–15 m behind the working face, and the advance rate of the working face was no less than 0.86 m per day.

- (3) The engineering parameters were designed according to the numerical simulation results. By investigating the three boreholes' extraction parameters, it was determined that this process could effectively mitigate the local gas overrun in the target mine. The gas concentration in the upper corner was controlled below 0.8%. The gas concentration in the return air roadway was controlled below 0.65%, which was in line with the coal mine safety regulations' relevant provisions.
- (4) A part of the emitted gas entered the extraction system, which ensured the comprehensive utilization of gas as a clean energy source and provided a solution for similar mines to mitigate gas emission problems.

Data Availability

All data and models used to support the findings of this study are available from the corresponding author upon request.

Conflicts of Interest

The authors declare that there are no conflicts of interest.

References

- [1] Y.-P. Cheng, L. Wang, and X.-L. Zhang, "Environmental impact of coal mine methane emissions and responding strategies in China," *International Journal of Greenhouse Gas Control*, vol. 5, no. 1, pp. 157–166, 2011.
- [2] A. Majdi, F. P. Hassani, and M. Y. Nasiri, "Prediction of the height of distressed zone above the mined panel roof in longwall coal mining," *International Journal of Coal Geology*, vol. 98, pp. 62–72, 2012.

- [3] H. Guo, L. Yuan, B. Shen, Q. Qu, and J. Xue, "Mining-induced strata stress changes, fractures and gas flow dynamics in multi-seam longwall mining," *International Journal of Rock Mechanics and Mining Sciences*, vol. 54, pp. 129–139, 2012.
- [4] H. B. Zhang and Y. F. Huang, "Flow field and gas concentration distribution in the coal mining face and mined-out area with J-shape and U-shape ventilation system using Comsol," *Journal of Physics: Conference Series*, vol. 1168, no. 5, Article ID 052041, 2019.
- [5] H. W. Zhou, J. F. Liu, D. J. Xue, H. Y. Yi, and J. H. Xue, "Numerical simulation of gas flow process in mining-induced crack network," *International Journal of Mining Science and Technology*, vol. 22, no. 6, pp. 793–799, 2012.
- [6] C. O. Karacan and G. S. Esterhuizene, "Reservoir simulation-based modeling for characterizing longwall methane emissions and gob gas vent hole production," *International Journal of Coal Geology*, vol. 71, no. 2-3, pp. 225–245, 2007.
- [7] Y. W. Wang, W. J. Yan, Z. J. Ren, Z. Q. Yan, Z. Liu, and H. Zhang, "Investigation of large-diameter borehole for enhancing permeability and gas extraction in soft coal seam," *Geofluids*, vol. 6, pp. 1–3, 2020.
- [8] L. Yuan, H. Guo, P. Li, and Y. P. Lian, "Theory and technology of goaf gas drainage with large-diameter surface boreholes," *Journal of China Coal Society*, vol. 38, no. 1, pp. 1–8, 2013.
- [9] Y. P. Cheng, D. Y. Zhou, and Q. X. Yu, "Research on extraction and emission laws of gas for pressure-relief in protecting coal seams," *Journal of Mining & Safety Engineering*, vol. 23, no. 1, pp. 13–19, 2006.
- [10] M. Yang and J. L. Gao, "Numerical simulation of the gas distribution in the gobs of u-type and Y-type ventilation mining workfaces," *International Journal on Computer Science and Engineering*, vol. 9, no. 1-2, pp. 147–152, 2012.
- [11] T. K. Lu, H. Yu, T. Zhou, J. Mao, and B. Guo, "Improvement of methane drainage in high gassy coal seam using waterjet technique," *International Journal of Coal Geology*, vol. 79, no. 1-2, pp. 40–48, 2009.
- [12] S. L. Kong, Y. Cheng, T. Ren, and H. Y. Liu, "A sequential approach to control gas for the extraction of multi-gassy coal seams from traditional gas well drainage to mining-induced stress relief," *Applied Energy*, vol. 131, pp. 67–78, 2014.
- [13] C. Zhang, S. H. Tu, and Y. X. Zhao, "Compaction characteristics of the caving zone in a longwall goaf: a review," *Environmental Earth Sciences*, vol. 78, no. 1, 2019.
- [14] V. T. Presler, "Modeling of air-gas and dynamic processes in driving development workings in the gas-bearing coal seams," *Journal of Mining Science*, vol. 38, no. 2, pp. 168–176, 2002.
- [15] M. G. Qian and J. L. Xu, "Study on the 'O shape' circle distribution characteristics of mining-induced fractures in the overlying strata," *Journal of China Coal Society*, vol. 23, no. 5, pp. 466–469, 1998, in Chinese.
- [16] H. P. Kang, J. Lou, F. Gao, J. Yang, and J. Z. Li, "A physical and numerical investigation of sudden massive roof collapse during longwall coal retreat mining," *International Journal of Coal Geology*, vol. 188, pp. 25–36, 2018.
- [17] S. Wang, D. Wang, K. Cao, S. Wang, and Z. Pi, "Distribution law of 3D fracture field of goaf and overlying strata," *Journal of Central South University (Science and Technology)*, vol. 45, pp. 833–839, 2014.
- [18] Y. M. Wang, X. Q. Li, and Z. X. Guo, "Prediction of self-ignition fire propagation and coal loss in an inclined seam," *Heat Transfer Research*, vol. 49, no. 9, pp. 827–845, 2018.
- [19] J. Ma, Y. S. Sun, and B. W. Li, "Simulation of combined conductive, convective and radiative heat transfer in moving irregular porous fins by spectral element method," *International Journal of Thermal Sciences*, vol. 118, pp. 475–487, 2017.
- [20] Y. Nakayama, *Introduction to Fluid Mechanics*, Butterworth-Heinemann, Oxford, UK, 2nd edition, 2018.
- [21] H. Darcy, *Les Fontaines Publiques de la Ville de DIJON: Exposition et Application*, Victor Dalmont, Kraljevica, Croatia, 1856.
- [22] J. Kozeny, "Ueber kapillare leitung des wassers im boden," *Sitzungsberichte der Kaiserlichen Akademie der Wissenschaften*, vol. 136, pp. 271–306, 1927.
- [23] P. C. Carman, "Fluid flow through granular beds," *Transactions of the Institution of Chemical Engineers*, vol. 15, pp. 150–166, 1937.
- [24] G. Wang, H. Xu, M. M. Wu, Y. Wang, R. Wang, and X. Q. Zhang, "Porosity model and air leakage flow field simulation of goaf based on DEM-CFD," *Arabian Journal of Geosciences*, vol. 11, no. 7, p. 148, 2018.
- [25] L. Lunarzewski and W. Les, "Gas emission prediction and recovery in underground coal mines," *International Journal of Coal Geology*, vol. 35, no. 1–4, pp. 117–145, 1998.
- [26] G. Dai, Y. Wang, C. Zhang, Q. Li, and G. Shao, "Forecast of the gas effused from the face in protective seam," *Journal of China Coal Society*, vol. 32, no. 4, p. 382, 2007.
- [27] Z. Qin, L. A. Yan, H. Guo et al., "Investigation of longwall goaf gas flows and borehole drainage performance by CFD simulation," *International Journal of Coal Geology*, vol. 150–151, pp. 51–63, 2015.
- [28] L. M. Yuan and A. C. Smith, "Numerical study on effects of coal properties on spontaneous heating in longwall gob areas," *Fuel*, vol. 87, no. 15-16, pp. 3409–3419, 2008.
- [29] C. G. Speziale, T. B. Gatski, and M. M. Nessim Fitzmaurice, "An analysis of RNG-based turbulence models for homogeneous shear flow," *Physics of Fluids A: Fluid Dynamics*, vol. 3, no. 9, pp. 2278–2281, 1991.
- [30] Z. J. Shi, J. L. Liu, and Q. X. Li, "Development and application of drilling technique and equipment in coal mining area of China," *Coal Science and Technology*, vol. 46, no. 1, pp. 1–6, 2018.

Research Article

Reasonable Scope of Kilometer Drilling in Lower Layer of Extrathick Coal Seam: A Case Study of Tingnan Coal Mine, China

Delong Zou¹ and Xiang Zhang ²

¹Shenyang Research Institute of CCTEG, Shenyang 113122, China

²State Key Laboratory of Coal Resources and Safe Mining, Beijing 100083, China

Correspondence should be addressed to Xiang Zhang; sqt1910101048@student.cumtb.edu.cn

Received 18 May 2021; Revised 14 June 2021; Accepted 26 June 2021; Published 13 July 2021

Academic Editor: Zou Quanle

Copyright © 2021 Delong Zou and Xiang Zhang. This is an open access article distributed under the Creative Commons Attribution License, which permits unrestricted use, distribution, and reproduction in any medium, provided the original work is properly cited.

When stratified mining is adopted in high-gas and extrathick coal seam, a large amount of pressure-relief gas of the lower layer flows into the upper layer goaf along the cracks in the layer, resulting in upper layer working face to frequently exceed the gas limit. And ordinary drilling can no longer meet the requirements of the pressure-relief gas drainage of the lower layer. The 205 working face of Tingnan Coal Mine is taken as the test background in this paper, and based on the “pressure-relief and flow-increase” effect of the lower layer under the action of mining stress during the upper layer mining, the gas drainage of kilometer directional drilling in lower layer is studied. According to the distribution characteristics of support pressure before and after the working face, the pressure-relief principle, fracture development characteristics, and gas migration law of the lower layered coal body are analyzed in the process of advancing the upper layered working face in the extrathick coal seam with high gas. The maximum depth of goaf damage is calculated theoretically, and the Flac^{3D} numerical simulation of the failure deformation of the 205 working face floor is carried out. It is found that the maximum depth of plastic failure of the lower layer is about 13 m. According to the plastic deformation of the lower layer under different vertical depths and the movement of coal and rock mass, it is determined that the reasonable range of kilometer directional drilling in the lower layer is 6–9 m below the floor vertical depth. From 15 m to 45 m in the two parallel grooves, there is no fracture failure with a sharp increase or decrease in the displacement in the local range. Meanwhile, in this part, the roof falling behind is not easy to compaction, and the displacement of the floor is large, which does not cause plastic damage. The degree of pressure relief is more sufficient, and the permeability of the lower layer is good. Therefore, drilling should be arranged as much as possible along the working face in this tendency range. The determination of reasonable arrangement range of kilometer directional drilling in extrathick coal seam provides reference index and theoretical guidance for industrial test of working face and also provides new ideas for gas control of stratified mining face in high-gas and extrathick coal seam.

1. Introduction

Coal resources will continue to dominate China’s energy consumption for a long time in the future [1–5], and gas disasters in the process of coal resource development pose a great threat to safety in production [6–10]. Among them, when stratified mining is adopted in high-gas and extrathick coal seam, the pressure-relief gas of the lower layer flows into the upper layer goaf in large quantities along the cracks passing through strata, resulting in frequent gas overrun in the upper layer working face. It leads to severe challenges in

gas control during the mining of high-gas and extrathick coal seam. At present, the methods of gas control in working face of high-gas and extrathick coal seam in China mainly include high-level gas drainage roadway, gas emission tail roadway, high-level drilling, ground drilling, and upward mesh drilling in floor rock roadway [11–13]. However, none of these methods can achieve directional and long-term extraction of pressure-relief gas in the lower layer, and the economic cost is relatively high. The effect is not ideal, and it is difficult to eliminate the threat of pressure-relief gas from the lower layer to the working face. The common parallel gas

drainage borehole has the disadvantages of long construction period, high cost, and low efficiency. When it is applied to the gas drainage of the ultralong working face of the ultrathick coal seam with high gas, the gas drainage area is limited and cannot meet the requirements of the gas control of the working face. The kilometer directional drilling has the advantages of long coal seam section, open branch holes, large gas extraction area, high extraction efficiency, and slow gas flow attenuation in boreholes. Therefore, determining the reasonable range of the kilometer directional drilling in the lower layer to achieve a wide range of pressure-relief gas drainage in the lower layer for a long time has guiding significance and practical value for gas control work in large mining height working face of superthick coal seam with high gas.

The study of stress distribution and fracture evolution law of stope floor has important guiding significance for determining the reasonable range of kilometer directional drilling in lower layer. Meng et al. [14] established an elastic mechanical model for calculating the stress at any point of the floor according to the distribution law of abutment pressure in front of the working face, and the failure criterion of the floor rock mass is given by combining the Mohr–Coulomb criterion. Wang et al. [15] applied the elastoplastic mechanics theory to analyze the influence of different pressure steps on the failure depth and width of the floor from the perspective of dynamic and static loads, used numerical simulation to study the evolution of stress field and plastic zone of the floor under different pressure steps, and then put forward the prevention and control technology of water inrush from the floor of hydraulic fracturing pressure-relief of the roof. Zhang [16] studied the mechanism of water inrush in deep mines through experiments, and the total stress-strain permeability of different lithology of deep coal seam floor is determined. Xie and Chang [17] revealed the stress distribution characteristics of surrounding rock and the law of strata movement under the condition of no support in the floor of deep roadway through field measurement and numerical simulation. Guo et al. [18] believe that the damage range of surrounding rock and its influence on water-resisting layer of floor drainage roadway under the influence of mining are the key to determine the thickness of water-resisting layer of floor. In summary, a large number of scholars have studied the floor failure theory mainly from the perspectives of water inrush prevention, support failure caused by working face pressure, and roadway maintenance. However, when the stope floor is a coal body, there are few studies on its failure degree crack development and gas emission law. Aiming at the extraction technology of pressure-relief gas, scholars have done a lot of research around the mining protective layer [19–21]. The basic principle is to use the pressure-relief effect of the protected layer in the process of protective layer mining to strengthen the extraction of pressure-relief gas. Therefore, the protected layer is changed from high-gas outburst dangerous coal seam to low gas without outburst dangerous coal seam, so as to realize the safe and efficient mining of coal and gas resources [22–24]. At present, the theory and extraction technology of pressure-relief gas are mostly focused

on the mining of upper and lower protective layers. When stratified mining is used in thick coal seams, there is no more scientific and field industrial test study on pressure-relief extraction of lower stratified coal seams. Kilometer directional drilling gas drainage has been widely used in China. Lu and Xiong [25] introduced in detail the advantages and disadvantages of conventional drilling rigs and underground kilometer directional drilling rigs through field tests. Regional gas drainage test was carried out by using kilometer drilling rig in Sihe Mine, Shanxi Province, which solved the problem of gas overrun during coal roadway excavation [26]. Combined with the newly introduced German DDR-1200 kilometer directional drilling rig, Fang et al. [27] proposed a new method of drilling kilometer directional drilling in the roof fissure zone of the working face to extract gas and constructed a kilometer directional drilling coal and gas comining system. Xia et al. [28] carried out the comprehensive measures of gas extraction, including the wear layer and in-seam kilometer directional feathery drilling combined with multibranch technique. However, there is still a lack of research on whether the kilometer directional drilling can continue to extract gas after the pressure is relieved in the lower layered coal body of the extrathick coal seam. Moreover, pressure-relief gas drainage of the lower layer also involves the flow-solid coupling problem, in which the rock strata are constantly deformed by stress and the gas flow environment is constantly changing. Therefore, the deformation of rock mining and the mechanism of gas flow need comprehensive study to help solve the flow-solid coupling problem in underground gas drainage, which is an important topic for the prevention of the gas disasters [29–31].

In view of this, in this paper, we analyze the pressure-relief mechanism and pressure-relief gas migration law of lower layered coal body. Meanwhile, a combination of theoretical analysis and calculations, numerical simulations, and field tests is used to determine the reasonable range of the kilometer directional drilling group in the lower layer. It can not only help us predrainage the lower layer coal before mining but also achieve the purpose of long-term and high-concentration drainage of pressure-relief gas after mining.

2. Engineering Background

Tingnan Coal Mine is located in central and western Shanxi Province, as shown in Figure 1. The 4# coal seam is the only recoverable coal seam in Tingnan Coal Mine. The general buried depth is +500~700 m, the coal seam thickness is 1.00~23.24 m, and the average thickness is 11.05 m. It is basically a good environmentally friendly power fuel and gasification coal.

The 205 working face is the second large mining height working face in the second panel of Tingnan Coal Mine, with an average thickness of 19 m. It belongs to extrathick coal seam with an average dip angle of 4°. The working face is mined by inclined longwall comprehensive mechanized backward mining method. The upper layer is mined by 6 m, and the lower layer is retained by 13 m. The roof is comprehensively managed by caving method. The average

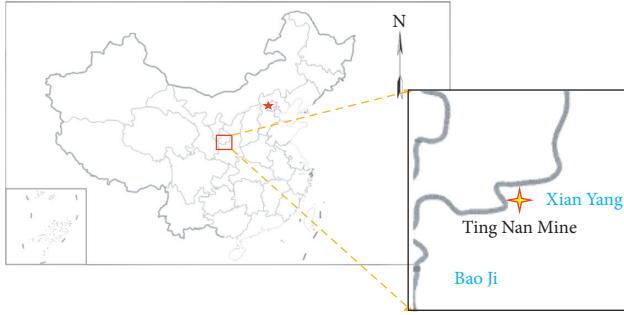


FIGURE 1: Location of Tingnan Coal Mine, Shanxi Province, China.

relative gas emission of 205 working face is $5.44 \text{ m}^3 \cdot \text{t}^{-1}$, and the average absolute gas emission is $34.79 \text{ m}^3 \cdot \text{min}^{-1}$. The recovery rate can reach more than 93% by using one-time full-height mining method, and the residual coal in goaf is less. The lower layer pressure-relief gas becomes the main source of goaf gas. Therefore, the lower layer has become the focus of gas control work. To sum up, predrainage of the coal seam and the lower layer must be carried out before the mining of the working face. At the same time, during the mining process and after the mining, the pressure-relief gas should be extracted by arranging reasonable drilling for a long time and high concentration.

According to the national standard, the gas basic parameters of 4# coal seam in 205 working face were measured in Tingnan Coal Mine. The measurement results are shown in Table 1.

3. Analysis of Pressure-Relief Mechanism and Gas Migration Law of Lower Layer Coal

3.1. Theoretical Analysis of Stratified Pressure-Relief under Mining Field. In the mining process of working face, the relationship between space and time of displacement of lower layer coal and rock mass is three stages: compression of stress concentration zone, expansion of pressure-relief zone, and compaction of recovery zone. About 15 m away from the working face, the in situ stress increases exponentially, and the in situ stress reaches the peak at about 8 m. This area is the compression of stress concentration zone, and the support pressure coefficient n varies from $n \geq 1.5$ to $5\gamma H$. The coal in this part of the region is gradually compacted under the action of higher than the original stress, and the coal seam and floor have a slow downward trend, resulting in compression displacement. In the rear of the working face, the ground stress is less than the original stress, and the concentrated support pressure in the front is transmitted to the bottom of the goaf through the floor coal and rock mass, resulting in floor heave deformation. As the

working face continues to move forward the expansion displacement increases gradually, this area is the expansion of pressure-relief zone. When a certain distance is reached, the coal gangue falling from the goaf far away from the working face is gradually compacted, and the displacement of the floor is gradually restored, but it cannot recover to the initial value. This area is the compaction of recovery zone. The permeability of lower layer coal also experiences a process of decreasing, increasing, and decreasing again. This process repeats as the working face advances, and the floor is continuously damaged periodically.

In this process, the formation and development of the plastic zone are mainly caused by the floor heave of the upper layer floor in actual production. After the upper slicing mining, the surrounding area of goaf is the support pressure concentration area. When the stress of the coal and rock mass in the support pressure action area (area I in Figure 2: active area) exceeds its ultimate strength, the coal mass will produce plastic deformation. At the same time, this part of the coal and rock mass is squeezed in the vertical direction, and the coal mass will inevitably produce expansion deformation in the horizontal direction. The expanded coal and rock mass squeezes the coal and rock mass in the transition area (area II: transition area) and transfers the stress to this area. The coal and rock mass in area II continues to squeeze forward the coal and rock mass in the passive area (area III: passive zone). Because only area III is at the floor of the goaf, it has a relatively large free space and free surface, which causes the coal and rock mass in the transition area and the passive area to expand and uplift to the goaf under the action of the force transmitted by the active area.

In the critical area of expansion zone and compression zone of the lower layer, coal and rock mass are prone to shear failure. In the process of pressure relief, the coal and rock mass in the expansion area is prone to separate layer cracks, vertical cracks, and cross cracks, resulting in a hundred times increase in the permeability coefficient of coal seam. And the coal body in the goaf floor is fully released, which provides a prerequisite basis for efficient extraction of pressure-relief gas in lower layers [32–35].

3.2. Destruction of Lower Stratified Space under Theoretical Calculation

3.2.1. Plastic Solution of Maximum Failure Depth of Floor along Strike. According to the comprehensive calculation formula of ultimate bearing capacity of rock and soil, the ultimate load formula of floor rock mass is proposed.

$$P_0 = (C \cot \varphi_0 + m\gamma H + \gamma x_a \tan \varphi_0) e^{(\pi \tan \varphi_0)} \tan^2 \left(\frac{\pi}{4} + \frac{\varphi_0}{2} \right) + \gamma x_a \tan \varphi_0 - C \cot \varphi_0, \quad (1)$$

TABLE 1: Basic parameter test result of coal seam gas in 205 working face.

Coal seam	4#	
Gas content ($\text{m}^3 \cdot \text{t}^{-1}$)		6.74~6.86
Gas adsorption constant	a ($\text{m}^3 \cdot \text{t}^{-1} \cdot \text{r}^{-1}$)	21.578~22.321
	b (MPa^{-1})	0.879~0.926
Industrial analysis	Moisture (%)	4.78~5.46
	Ash (%)	7.43~7.88
	Volatile (%)	29.45~32.65
Gas pressure (MPa)		0.54~0.624
Coal porosity ($\text{m}^3 \cdot \text{m}^{-3}$) (%)		8.48~8.86
Initial velocity of gas emission (Δp)		0.775
Coal seam permeability coefficient ($\text{m}^2 \cdot \text{MPa}^{-2} \cdot \text{d}^{-1}$)		0.0424
Natural gas flow attenuation coefficient of borehole (d^{-1})		0.0243
Coal dust explosive		Risk of explosion
Coal seam spontaneous combustion tendency		Type II spontaneous combustion

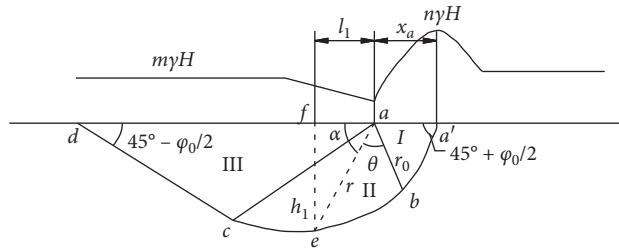


FIGURE 2: Calculation diagram of the most destroy depth in seam floor.

where C is the cohesion of rock mass and x_a is the length of yield zone of coal pillar. The plastic zone of the floor can be divided into three parts, namely, I: active zone, II: swelling rock mass squeezing transition zone, and III: rock mass in the transition zone, which continues to squeeze the passive zone. To determine the maximum depth and length of the failure zone under the condition of ultimate bearing pressure, it can be calculated according to the geometric dimensions of the limit plastic zone in Figure 2.

$$\text{In } \Delta aba', ab = r_0 = \frac{x_a}{2} \cos\left(\frac{\pi}{4} + \frac{\varphi_0}{2}\right),$$

$$\text{In } \Delta aef, h = r \sin \alpha,$$

$$\text{And } \alpha = \frac{\pi}{2} - \left(\frac{\pi}{4} + \frac{\varphi_0}{2}\right) - \theta, \quad (2)$$

$$\text{And so, } h = r_0 e^{(\theta \tan \varphi_0)} \cos\left(\theta + \frac{\varphi_0}{2} - \frac{\pi}{4}\right).$$

From $dh/d\theta = 0$, the maximum depth of the damage zone h can be obtained.

$$\begin{aligned} \frac{dh}{d\theta} &= r_0 e^{(\theta \tan \varphi_0)} \cos\left(\theta + \frac{\varphi_0}{2} - \frac{\pi}{4}\right) \tan \varphi_0 \\ &- r_0 e^{(\theta \tan \varphi_0)} \sin\left(\theta + \frac{\varphi_0}{2} - \frac{\pi}{4}\right) = 0. \end{aligned} \quad (3)$$

$$\text{Hence, } \tan \varphi_0 = \tan\left(\theta + \left(\frac{\varphi_0}{2} - \frac{\pi}{4}\right)\right)$$

$$\theta = \frac{\pi}{4} + \frac{\varphi_0}{2}. \quad (4)$$

Substituting (4) and r_0 into (2), the maximum damage depth of the rock mass h can be obtained.

$$h = \frac{x_a \cos \varphi_0}{2 \cos\left(\frac{\pi}{4} + \frac{\varphi_0}{2}\right)} e\left(\frac{\pi}{4} + \frac{\varphi_0}{2}\right) \tan \varphi_0. \quad (5)$$

Therefore, the horizontal distance l_1 between the maximum failure depth of floor coal and rock mass and the working face end is

$$l_1 = h_1 \tan \varphi_0. \quad (6)$$

According to the field measurement of the mining face in the first and second panel of Tingnan Coal Mine, especially the length of the coal seam yield zone in the 204 working face, it shows that when the working face advances, the influence area of plastic zone width of coal seam is not the peak point, but a dynamic influence range. The distance between the peak abutment pressure of 204 comprehensive working face and the edge of coal body (equal to the width of plastic zone x_a) is 8~11 m.

Using the empirical formula (7) of coal seam yield length (H is the average depth of coal seam in working face), the average buried depth of 205 working face is 580 m, and the length of coal seam yield zone x_a calculated is 8.7 m, which is basically consistent with the field measurement. Therefore,

this formula can be used as the calculation of yield zone length of 205 working face, and finally, x_a is determined to be 3 m.

$$x_a = 0.015H. \quad (7)$$

Substituting (7) into (5), we can obtain that

$$h = \frac{8.7 \cos \varphi_0}{2 \cos((\pi/4) + (\varphi_0/2))} e^{\left(\frac{\pi}{4} + \frac{\varphi_0}{2}\right) \tan \varphi_0}, \quad (8)$$

where coal seam internal friction angle of 205 working face is 28°. The calculated h is 12.89 m and l_1 is 6.85 m. The calculation shows that the 13 m coal body in the lower layer is almost all in the pressure-relief fracture zone.

According to the calculation results, the distribution pattern of plastic failure zone in the lower layer of 205 working face of 4# coal seam in Tingnan Coal Mine is shown in Figure 3.

3.2.2. Distribution Law of Failure Depth along Inclined Floor.

The problem analyzed in this paper is the plane strain state. The stress generated by the self-weight of the rock mass in the floor is equal to γz . The stress analysis is shown in Figure 4; then, the principal stress of M at any point in the floor strata is

$$\sigma_1 = \frac{q}{\pi} (\alpha + \sin \alpha) + \gamma z, \quad (9)$$

$$\begin{aligned} \sigma_2 &= v(\sigma_1 + \sigma_3) \\ &= \frac{2qva}{\pi} + 2\gamma z, \end{aligned} \quad (10)$$

$$\sigma_3 = \frac{q}{\pi} (\alpha - \sin \alpha) + \gamma z. \quad (11)$$

Under the action of multidirectional stress, the failure of rock mass obeys the Mohr–Coulomb failure criterion, that is, $\sigma_1 - K\sigma_3 = R_c$, and after substituting equations (9)–(11),

$$z = \frac{q}{\pi\gamma} \left(\frac{K+1}{K-1} \sin \alpha - \alpha \right) - \frac{R_c}{\gamma(K-1)}, \quad (12)$$

where R_c is the uniaxial compressive strength of rock mass and γ is the volume weight of rock mass.

$$\begin{aligned} K &= \frac{1 + \sin \varphi}{1 - \sin \varphi}, \\ \alpha &= \cos^{-1} \frac{K-1}{K+1}. \end{aligned} \quad (13)$$

According to formula (12), the division map of the failure zone of the floor rock mass can be drawn. As shown in Figure 5, the failure zone develops from inside to outside in the order of 1-2-3-4. It can be concluded that the failure depth of rock mass near the edge of working face is the largest. According to the distribution characteristics of failure depth under the ultimate state of floor shown in Figures 2 and 5, the distribution pattern of floor failure zone can be deduced. Figure 6(a) shows the distribution of the

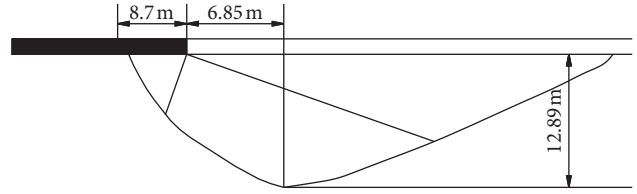


FIGURE 3: Figure of failing zone of 205 working face floor (it is theoretical result).

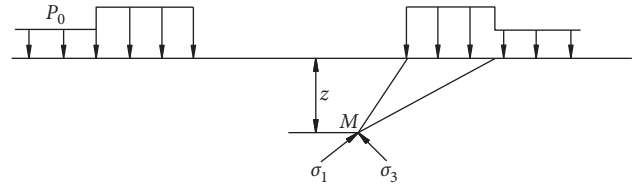


FIGURE 4: The sketch map of stress simplification of coal floor (P_0 : primary stress).

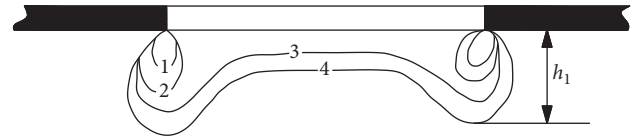


FIGURE 5: Developing process of rock failing zone.

failure zone along the inclined direction of the working face in the near-horizontal coal seam, and Figure 6(b) shows the distribution of the failure zone along the advancing direction (strike) of the working face.

For the near-horizontal coal seam mining, the depth distribution of the floor failure zone along the inclined direction is in the shape of an “inverted saddle,” and the failure depth on both sides is often greater than that in the middle part of the goaf. Therefore, the influence of the failure depth on both sides should be paid attention to when arranging the boreholes.

3.3. Migration Law of Lower Layer Pressure-Relief Gas and Pressure-Relief Gas Extraction Technology.

When the 205 working face is mined, the lower layer is affected by mining. The coal body of the goaf floor heaves to the free space of the goaf and moves, deforms, and even destroys. A large number of primary micropores develop into cracks with large diameters. In this process, the permeability coefficient of coal seam is increased by hundreds of times, and the process of gas “desorption-diffusion-seepage” is accelerated. A large number of bedding tension fractures through-layer fractures and cross fractures formed by the full development of coal fractures provide a network channel for the flow and collection of pressure-relief gas in the lower layer, so the mining of the upper layer will have the effect of “pressure relief and flow increase” on the lower layer [36], as show in Figure 7.

The pressure-relief gas gathers along the bedding in the coal seam, and the gas flows from the high-pressure area to the low-pressure area, which cannot diffuse out of the coal seam. Then, the pressure-relief gas in the area must be

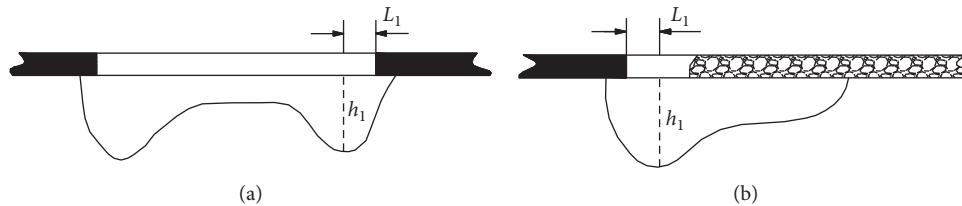


FIGURE 6: Distribution for m of coal floor failing zone in flat seam.

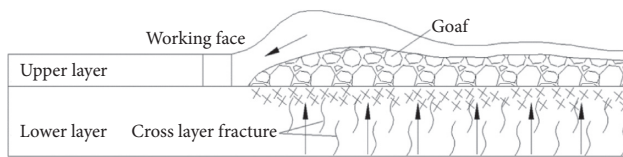


FIGURE 7: Pressure-relief gas flow in lower slice.

extracted under the negative pressure of the extraction borehole. With the increase of the vertical depth, the coal is still in the plastic deformation stage. Therefore, the shear stress and tensile stress gradually decay. The failure ability of the coal is also weakening, and the coal itself is not destroyed in the state of crisp. When the kilometer directional drilling is located in the area where the plastic deformation of the coal body is less than the limit deformation, the drilling will not be damaged or the degree of damage is relatively small, which can achieve better self-stability and maintain the integrity of the drilling, and the fracture can be significantly expanded. In the actual production operation, the kilometer directional drilling is fast in construction and low in cost, which can effectively extract gas. And the biggest advantage of kilometer directional drilling is that it not only can be preextracted before mining, mining while pumping, but also can be continuous pumping after mining. The above provides a strong basis for the selection of downward kilometer directional drilling drainage technology.

4. Numerical Simulation of Floor Failure Deformation of 205 Working Face

4.1. Modelling and Parameter Selection. Figure 8 shows the model established using FLAC^{3D}. Model coordinate system parameters are x (working face dip direction) = 300 m, y (working face mining direction) = 300 m, and z (vertical to coal strata upward) = 160 m. The average dip angle of 4# coal seam in the second panel is 4° , which belongs to the near-horizontal coal seam. When establishing the model, the dip angle of coal seam is simplified to 0° . The thickness of the upper layer was 6 m, and that of the lower layer was 13 m. The length of the working face was 200 m. Per step is 20 m, and a total of 10 steps is excavated. Considering the need to focus on the deformation and stress distribution of the direct bottom and the lower layer, the deformation of the overlying strata is not taken into account. The mining layer, the direct bottom, and the lower layer in the model are refined, and the movement monitoring of the upper layer floor is carried out for every 1 m. The whole model uses brick initial grid. There are 187200 areas and 197213 nodes after grid division.

The uniform vertical downward stress load is applied in the top boundary of the model ($z = 160$ m) so that it is equal to the weight of the overlying strata P . P is equal to the product of the burial depth of the upper surface strata in the model and the average bulk density of the overlying strata. From the surface to the upper surface of the model, the burial depth is about 450 m, and the loess layer is about 170 m. Therefore, the vertical downward uniform stress load P is 8.3 MPa. At the same time, the fixed hinge support is set at the floor. Horizontal displacement constraints are applied at $x = 0$ m, $x = 300$ m, $y = 0$ m, and $y = 300$ m. According to the geological characteristics and mining technical conditions of Tingnan Coal Mine, the Mohr–Coulomb plastic constitutive model and Mohr–Coulomb failure criterion are selected in this simulation, and the large strain deformation mode is adopted in the strain mode. The use of mechanical parameters of coal and rock not only refers to the test data of the laboratory but also combines with the actual investigation. The bulk modulus is obtained according to the empirical value, and the mechanical parameters of rock mass are shown in Table 2.

4.2. Analysis of Numerical Simulation Results

4.2.1. Vertical Stress Distribution Law of Floor during Mining. In the model, the original rock stress is in the original equilibrium state before the 4# coal layer is pushed and mined. After 13978 steps of initial equilibrium, the vertical stress distribution of coal seam is relatively balanced and has a good horizon. The original vertical stress of each coal seam in the model is 8.5~12.28 MPa. The stress of each stratum is similar to the calculated self-weight stress of the overlying rock mass, as shown in Figure 9. After the 10-step push is completed, the total iteration of the model balance is 83367 steps.

With the advance of the upper layer of 4# coal in the model, the original rock stress is redistributed, and the stress concentration area and pressure-relief area appear. In order to better reflect the change of stress distribution in the process of working face advancing, representative vertical stress change distribution maps are selected. In the middle line of the working face along, the strike was selected to advance to 20 m, 60 m, 100 m, 140 m, 180 m, and 200 m sections; see Figure 10.

It can be seen from Figure 10 that the dark blue area at the working face and the cutting hole is the stress concentration area. The maximum stress is 21~23 MPa at 200 m, and the stress concentration coefficient is about 2.3, which is

Center: Rotation:
 X: 1.500e + 002 X: 0.000
 Y: 1.500e + 001 Y: 0.000
 Z: 8.000e + 001 Z: 30.000
 Dist: 9.795e + 002 Mag.: 1.25
 Increments: Ang.: 22.500
 Move: 3.897e + 001
 Rot.: 10.000
 Block group

- Siltstone
- Sandy mudstone
- Aluminous mudstone
- 4 coal lower stratification
- 4 coal upper stratification
- Mudstone
- Coarse sandstone
- Fine sandstone
- Coarse sandstone
- Overlying strata

Axes
 Linestyle

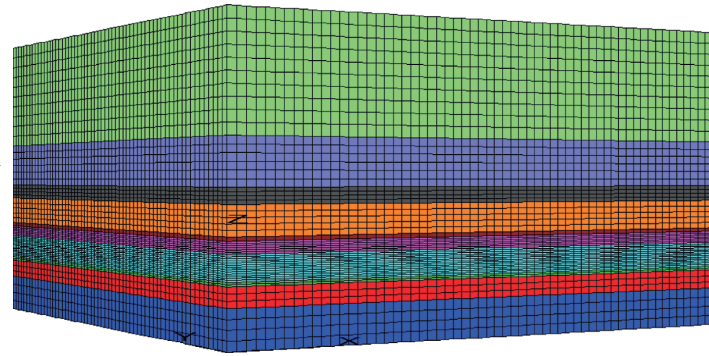


FIGURE 8: Three-dimensional numerical model.

TABLE 2: Physicomechanical parameters of coal and rock layers.

Lithology	Thickness (m)	Bulk modulus (GPa)	Shear modulus (GPa)	Density ($\text{kg}\cdot\text{m}^{-3}$)	Cohesion (MPa)	Internal friction angle (°)	Tensile strength (MPa)
Overlying strata 10	60	4.60	4.45	2500	3.50	38	1.35
Grit stone 9	24	4.53	4.37	2510	2.53	34	1.26
Fine-grained sandstone 8	8	4.64	4.32	2540	4.57	35	1.35
Grit stone 7	15	4.58	4.42	2530	2.57	34	1.28
Mudstone 6	2	4.54	4.31	2560	2.08	32	1.32
Upper layer of 4# coal seam 5	6	1.42	0.57	1400	1.2	28	0.64
Lower layer of 4# coal seam 4	13	1.42	0.57	1400	1.2	28	0.64
Aluminum mudstone 3	2	4.87	4.79	2420	1.76	39	1.31
Sandy mudstone 2	10	4.52	4.34	2560	2.08	36	1.35
Siltstone 1	20	4.67	4.53	2550	4.58	39	1.42

about 7.5 m in front of the working face. At the top and bottom of the working face, orange or red area is called lower than the original rock stress area, which belongs to the pressure-relief area. The pressure relief of the red area of coal and rock is the most sufficient.

With the continuous advancement of the working face, the range of the pressure-relief area is increasing, and the pressure-relief range of the floor is far smaller than that of the roof. When advancing to 160 m, the pressure-relief depth is basically at a stable value and does not become deeper or increase slightly with the advance of the working face. On the whole, the vertical stress of the floor near the cutting hole

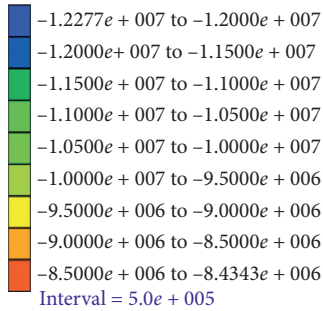
is restored with the advancement of the working face, and the pressure-relief degree of the floor is attenuated from the inside to the outside. The greater the vertical depth from the floor, the smaller the pressure relief and deformation of the coal body. The pressure-relief range is always semielliptic, and the pressure-relief area is basically symmetrically distributed. The pressure-relief range of the roof is much larger than that of the floor. The pressure relief in the middle of the roof is the largest, and the caving is more sufficient than the two sides. It can be seen that compared to the roof, pressure-relief range of floor is limited, and the degree of coal damage is small. It provides the possibility for the complete existence

Center: Rotation:
 X: $1.500e + 002$ X: 0.000
 Y: $1.500e + 002$ Y: 0.000
 Z: $8.000e + 001$ Z: 40.000
 Dist: $9.795e + 002$ Mag.: 1.25
 Increments: Ang.: 22.500
 Move: $3.897e + 001$
 Rot.: 10.000

Contour of SZZ

Magfac = $0.000e + 000$

Gradient calculation



Axes

Linestyle

FIGURE 9: Distribution of vertical stress after premining initial balance.

of kilometer borehole in the lower layer and the completion of gas drainage.

4.2.2. Variation Law of Plastic State of Floor during Mining.

The maximum plastic failure depth of the floor of the working face rises rapidly at the beginning stage. When the working face is advanced to 160 m, the failure tends to be stable and does not expand to the deep with the advance of the working face. When the working face is advanced to 200 m, the maximum failure depth is 14.5 m, as shown in Figure 11.

Therefore, the plastic change of the floor under different vertical depths when the working face advances to 200 m is analyzed, and the plastic change maps of 1 m, 3 m, 6 m, 9 m, 12 m, and 14 m under the vertical depth of the floor are derived, respectively. As shown in Figure 12, the arrow in the figure indicates the direction of the working face.

It can be seen from Figure 12 that, under the floor of 1 m and 3 m, the goaf is plane shear and tensile failure, and the surrounding is mainly shear failure. The coal body was severely damaged, causing dislocation and movement, and the penetration cracks were fully developed. At 6 m below the floor, the “O” shear failure is the main type around the mined-out area, and the tensile failure is the main type in the middle part with a little shear failure. The coal body starts from severe damage to crack damage. At 9 m below the floor, shear failure occurs around the goaf, with a little shear failure in the middle part, and the plastic deformation is very small. The coal body is in a slight disturbance state, and the borehole will not produce substantive collapse in this layer. When it is 12 m below the floor, only continuous shear failure occurs around the goaf. Other areas are basically not

affected by damage, and the coal disturbance is relatively small. When it is 14 m below the floor, only intermittent shear failure occurs around the goaf. Other areas are basically not affected by damage, and coal is basically not affected. The rock strata below 14 m are basically not destroyed.

In general, the maximum plastic failure depth of the floor in accordance with the third chapter is near the two parallel grooves. In the whole mining-induced fracture field of the lower layer, the plastic zone is relatively shallow in the middle of the goaf and deep around it, with the shape of “return” circle.

4.2.3. Variation Law of Displacement of Coal and Rock Mass in Floor during Mining.

When the working face advances to 200 m, the local displacement of the floor has reached the maximum. Therefore, starting from the coal wall of the working face, at 3 m, 5 m, 7 m, and 9 m in the goaf along the strike direction, the section maps are made along the inclination of the working face, and the contour map of the vertical displacement of coal and rock mass is plotted, as shown in Figure 13.

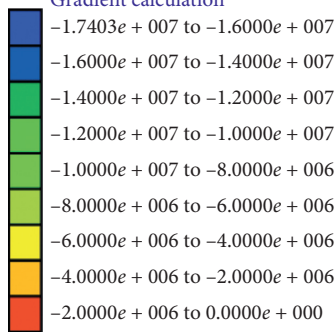
It can be seen from the figure that when the working face is mined for 200 m, the displacement at different depths of the floor is different. The more it goes to the goaf direction, the larger the displacement at the same vertical depth at the same position is. It can be seen from Figure 13 that when the coal wall of the working face is about 20 m away from the goaf, the floor displacement reaches the maximum value. The isoline with a vertical displacement of 0 m of the floor is approximately 24 m below the vertical depth. At the junction of the compression zone and the expansion zone of the

Center: Rotation:
 X: $1.500e + 002$ X: 0.000
 Y: $1.500e + 002$ Y: 0.000
 Z: $8.000e + 001$ Z: 90.000
 Dist: $9.795e + 002$ Mag.: 1.95
 Increments: Ang.: 22.500
 Move: $3.897e + 001$
 Rot.: 10.000

Plane origin: Plane normal:
 X: $1.500e + 002$ X: $1.000e + 000$
 Y: $0.000e + 000$ Y: $0.000e + 000$
 Z: $0.000e + 000$ Z: $0.000e + 000$

Contour of SZZ

Plane: on
 Magfac = $1.000e + 000$
 Gradient calculation



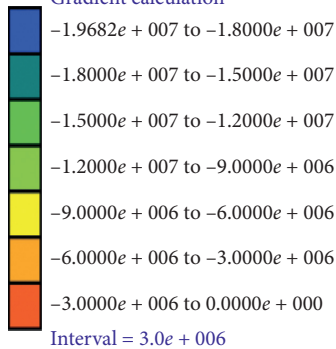
(a)

Center: Rotation:
 X: $1.500e + 002$ X: 0.000
 Y: $1.500e + 002$ Y: 0.000
 Z: $8.000e + 001$ Z: 90.000
 Dist: $9.795e + 002$ Mag.: 1.95
 Increments: Ang.: 22.500
 Move: $3.897e + 001$
 Rot.: 10.000

Plane origin: Plane normal:
 X: $1.500e + 002$ X: $1.000e + 000$
 Y: $0.000e + 000$ Y: $0.000e + 000$
 Z: $0.000e + 000$ Z: $0.000e + 000$

Contour of SZZ

Plane: on
 Magfac = $1.000e + 000$
 Gradient calculation



(b)

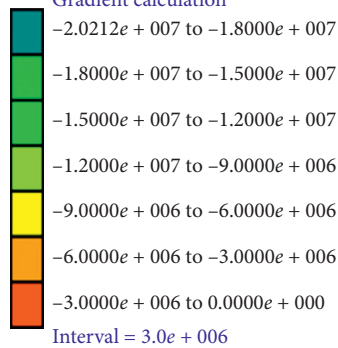
FIGURE 10: Continued.

Center: Rotation:
 X: $1.500e + 002$ X: 0.000
 Y: $1.500e + 002$ Y: 0.000
 Z: $8.000e + 001$ Z: 90.000
 Dist: $9.795e + 002$ Mag.: 1.95
 Increments: Ang.: 22.500
 Move: $3.897e + 001$
 Rot.: 10.000

Plane origin: Plane normal:
 X: $1.500e + 002$ X: $1.000e + 000$
 Y: $0.000e + 000$ Y: $0.000e + 000$
 Z: $0.000e + 000$ Z: $0.000e + 000$

Contour of SZZ

Plane: on
 Magfac = $1.000e + 000$
 Gradient calculation



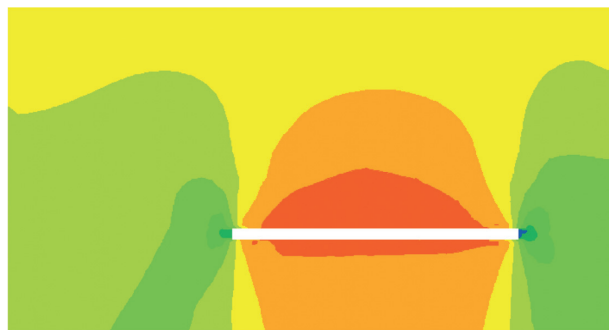
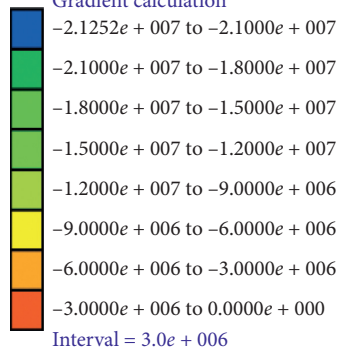
(c)

Center: Rotation:
 X: $1.500e + 002$ X: 0.000
 Y: $1.500e + 002$ Y: 0.000
 Z: $7.999e + 001$ Z: 90.000
 Dist: $9.795e + 002$ Mag.: 1.95
 Increments: Ang.: 22.500
 Move: $3.897e + 001$
 Rot.: 10.000

Plane origin: Plane normal:
 X: $1.500e + 002$ X: $1.000e + 000$
 Y: $0.000e + 000$ Y: $0.000e + 000$
 Z: $0.000e + 000$ Z: $0.000e + 000$

Contour of SZZ

Plane: on
 Magfac = $1.000e + 000$
 Gradient calculation



(d)

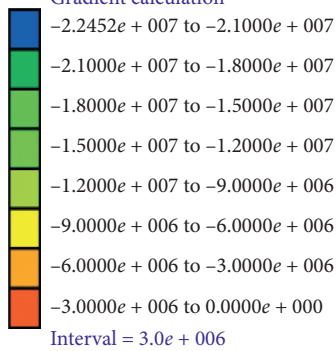
FIGURE 10: Continued.

Center: Rotation:
 X: $1.500e + 002$ X: 0.000
 Y: $1.500e + 002$ Y: 0.000
 Z: $7.999e + 001$ Z: 90.000
 Dist: $9.795e + 002$ Mag.: 1.95
 Increments: Ang.: 22.500
 Move: $3.897e + 001$
 Rot.: 10.000

Plane origin: Plane normal:
 X: $1.500e + 002$ X: $1.000e + 000$
 Y: $0.000e + 000$ Y: $0.000e + 000$
 Z: $0.000e + 000$ Z: $0.000e + 000$

Contour of SZZ

Plane: on
 Magfac = $1.000e + 000$
 Gradient calculation



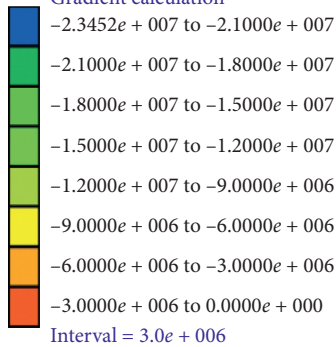
(e)

Center: Rotation:
 X: $1.500e + 002$ X: 0.000
 Y: $1.500e + 002$ Y: 0.000
 Z: $7.999e + 001$ Z: 90.000
 Dist: $9.795e + 002$ Mag.: 1.95
 Increments: Ang.: 22.500
 Move: $3.897e + 001$
 Rot.: 10.000

Plane origin: Plane normal:
 X: $1.500e + 002$ X: $1.000e + 000$
 Y: $0.000e + 000$ Y: $0.000e + 000$
 Z: $0.000e + 000$ Z: $0.000e + 000$

Contour of SZZ

Plane: on
 Magfac = $1.000e + 000$
 Gradient calculation



(f)

FIGURE 10: Vertical stress of the section along the trending direction (different advance length). (a) Working face advancing 20 m. (b) Working face advancing 60 m. (c) Working face advancing 100 m. (d) Working face advancing 140 m. (e) Working face advancing 180 m. (f) Working face advancing 200 m.

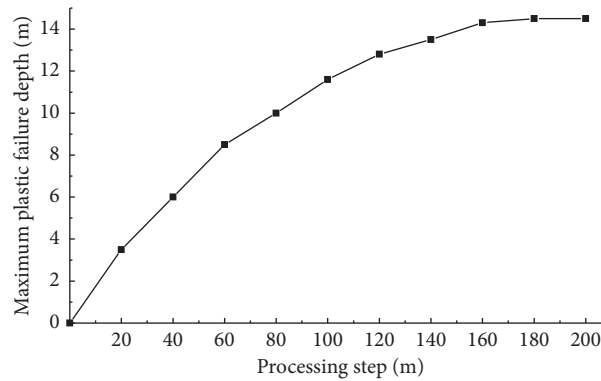


FIGURE 11: Maximum depth of floor plastic failure in different steps.

working face, namely, near the two parallel grooves, the lower layer of coal is prone to shear failure. In this area, the floor failure depth is the largest, and the displacement of coal and rock mass is the largest. Therefore, the lower layer of coal movement for 0 m contour is approximately “inverted saddle” shape.

To sum up, in the case of relatively small displacement under the floor, no large plastic damage will be caused, and the borehole will not be damaged.

5. Reasonable Range Analysis of Kilometer Borehole

5.1. Depth Range of Borehole along Floor. According to the theoretical calculation and numerical simulation results, the maximum floor failure depth of 205 working face is determined to be about 13 m. Comprehensive analysis of the simulation results shows that the coal and rock mass is in the fully pressure-relief area when the vertical depth of the floor is 0~3 m and is completely in the plastic plane failure. The displacement of coal and rock mass can reach more than 70 mm, and the damage degree is serious, so the stability and integrity of kilometer drilling are greatly threatened. In the range of 3~6 m, the coal body is still in the fully pressure-relief area, and the plastic failure is mainly plane. The moving distance to the goaf can reach more than 40 mm. The vertical and cross cracks are fully developed, which provides a channel for the gas flow below. At 6 m below the floor, only local plastic failure occurs in the coal body. The degree of pressure relief is reduced, and the displacement is about 20 mm. The failure of the coal body is relatively reduced, and the cracks are fully developed. The arrangement of long boreholes with kilometer strike in this area can not only maintain integrity for a long time but also effectively prevent the pressure-relief gas from entering the goaf through vertical cracks. At 6~9 m, the coal body is mainly fractured. The borehole can maintain the original shape and can extract the pressure-relief gas from the lower layer for a long time, which provides a reliable guarantee for the lower layer mining. At 6~9 m, the failure of coal body is dominated by tensile fracture, and the borehole can maintain the original shape, which can be used to extract the pressure-relief gas in the lower layer for

a long time, and provide reliable guarantee for the lower layer mining. Under 12 m, there is only plastic failure near the groove in the coal body, and the displacement is less than 10 mm, so the borehole can be arranged at this position. However, because the lower layer is only 13 m, the borehole will not be fully utilized and the benefit will not be maximized. At the same time, the pressure-relief gas of the coal body in the region flows upward, and the pressure-relief gas is cut off by the upper part of the drilling group under the action of pressure difference so that it cannot cross to the goaf.

In summary, when the borehole is arranged in the coal seam with relatively small plastic failure and floor displacement, it is about 6~9 m below the vertical depth of the floor, which can ensure that the possibility of borehole collapse is low. Therefore, the borehole can achieve the purpose of continuous drainage in the process of advancing the working face.

5.2. Tendency Range of Borehole along Working Face. Due to the sufficient roof caving in the middle of the goaf, the dense filling, and the support of the left coal pillars on both sides, the coal on both sides can be in a noncompaction state for a long time compared with the middle compaction area. Therefore, along the inclination of the working face, within a certain width on both sides, the gas concentration is high, the degree of pressure relief is sufficient, and the floor kilometer drilling can maximize its role.

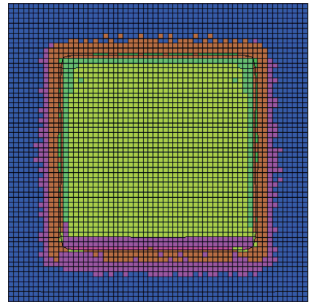
At 150 m of the central line of the working face, within 60 m from the coal wall of the working face to the goaf, the vertical displacement of the coal and rock with the floor droop depth of 1 m, 3 m, 6 m, 9 m, and 13 m was taken, shown in Figure 14. At the coal wall of the working face, the coal and rock mass of the floor moves downward. From the coal wall to the goaf 20 m, the displacement has been increased, and the inflection point appears at 20 m. Due to the stress recovery and roof caving, the displacement begins to decrease. At 1 m and 3 m, the floor displacement variation reaches 0.18 m and 0.14 m, and the displacement variation is relatively intense, which is very easy to cause coal damage. With the increase of the vertical depth, the displacement difference decreases and the displacement values decrease accordingly. The displacement difference at 6 m, 9 m, and

Center: Rotation:
 X: $1.500e + 002$ X: 90.000
 Y: $1.500e + 002$ Y: 0.000
 Z: $7.993e + 001$ Z: 0.000
 Dist: $1.051e + 003$ Mag.: 1.25
 Increments: Ang.: 22.500
 Move: $3.897e + 001$
 Rot.: 10.000

Plane origin: Plane normal:
 X: $0.000e + 000$ X: $0.000e + 000$
 Y: $0.000e + 000$ Y: $0.000e + 000$
 Z: $4.400e + 001$ Z: $1.000e + 000$

Block state

- Plane: on
- None
- Shear-n shear-p
- Shear-n shear-p tension-p
- Shear-p
- Shear-p tension-p
- Tension-n shear-p tension-p
- Tension-n tension-p
- Tension-p



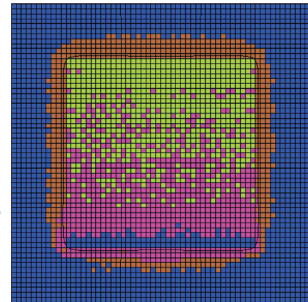
(a)

Center: Rotation:
 X: $1.500e + 002$ X: 90.000
 Y: $1.500e + 002$ Y: 0.000
 Z: $7.993e + 001$ Z: 0.000
 Dist: $1.051e + 003$ Mag.: 1.25
 Increments: Ang.: 22.500
 Move: $3.897e + 001$
 Rot.: 10.000

Plane origin: Plane normal:
 X: $0.000e + 000$ X: $0.000e + 000$
 Y: $0.000e + 000$ Y: $0.000e + 000$
 Z: $4.200e + 001$ Z: $1.000e + 000$

Block state

- Plane: on
- None
- Shear-n shear-p
- Shear-p
- Shear-p tension-p
- Tension-p



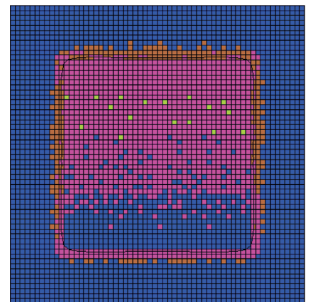
(b)

Center: Rotation:
 X: $1.500e + 002$ X: 90.000
 Y: $1.500e + 002$ Y: 0.000
 Z: $7.993e + 001$ Z: 0.000
 Dist: $1.051e + 003$ Mag.: 1.25
 Increments: Ang.: 22.500
 Move: $3.897e + 001$
 Rot.: 10.000

Plane origin: Plane normal:
 X: $0.000e + 000$ X: $0.000e + 000$
 Y: $0.000e + 000$ Y: $0.000e + 000$
 Z: $3.900e + 001$ Z: $1.000e + 000$

Block state

- Plane: on
- None
- Shear-n shear-p
- Shear-p
- Shear-p tension-p



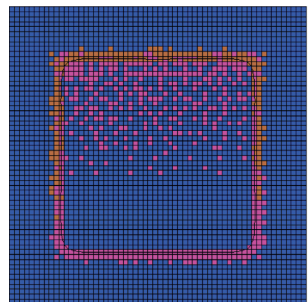
(c)

Center: Rotation:
 X: $1.500e + 002$ X: 90.000
 Y: $1.500e + 002$ Y: 0.000
 Z: $7.993e + 001$ Z: 0.000
 Dist: $1.051e + 003$ Mag.: 1.25
 Increments: Ang.: 22.500
 Move: $3.897e + 001$
 Rot.: 10.000

Plane origin: Plane normal:
 X: $0.000e + 000$ X: $0.000e + 000$
 Y: $0.000e + 000$ Y: $0.000e + 000$
 Z: $3.600e + 001$ Z: $1.000e + 000$

Block state

- Plane: on
- None
- Shear-n shear-p
- Shear-p



(d)

FIGURE 12: Continued.

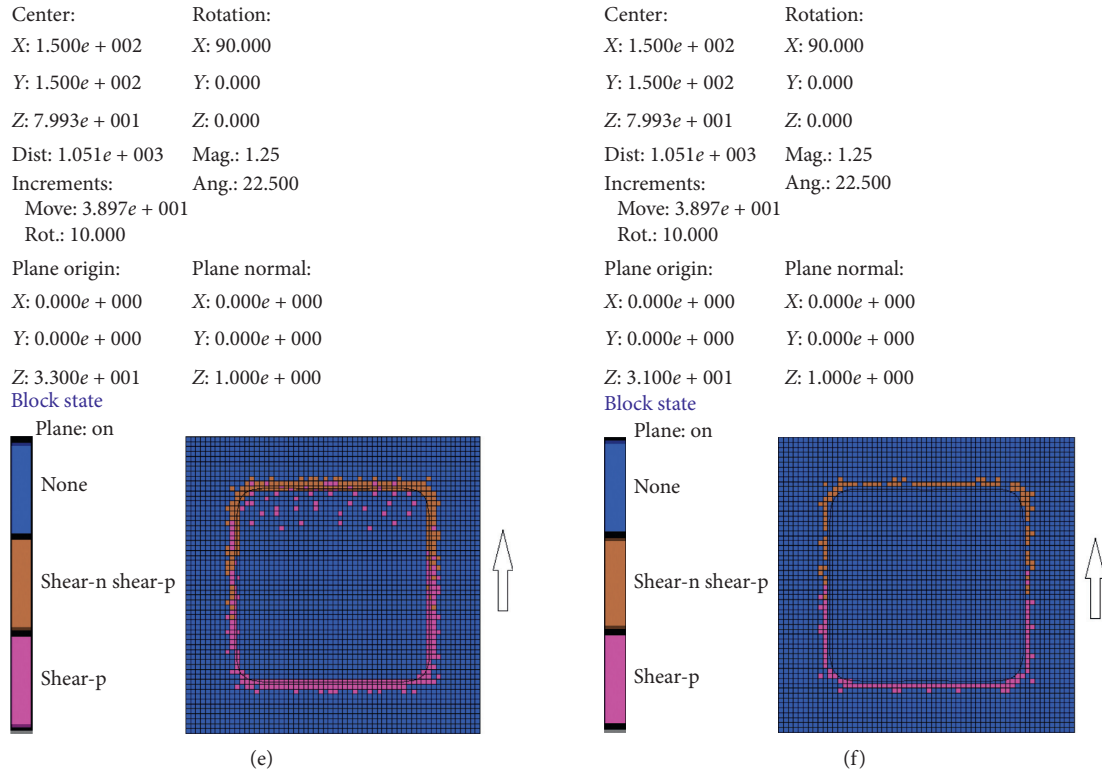


FIGURE 12: Figure of plastic zone under different depths of working face. (a) 1 m under the floor. (b) 3 m under the floor. (c) 6 m under the floor. (d) 9 m under the floor. (e) 12 m under the floor. (f) 14 m under the floor. Legend: none: no shear failure occurred in the unit; shear-p: shear failure occurred in the element; shear-n: the unit is generating shear failure; tension-p: units were damaged by tension; tension-n: the unit is undergoing tensile damage.

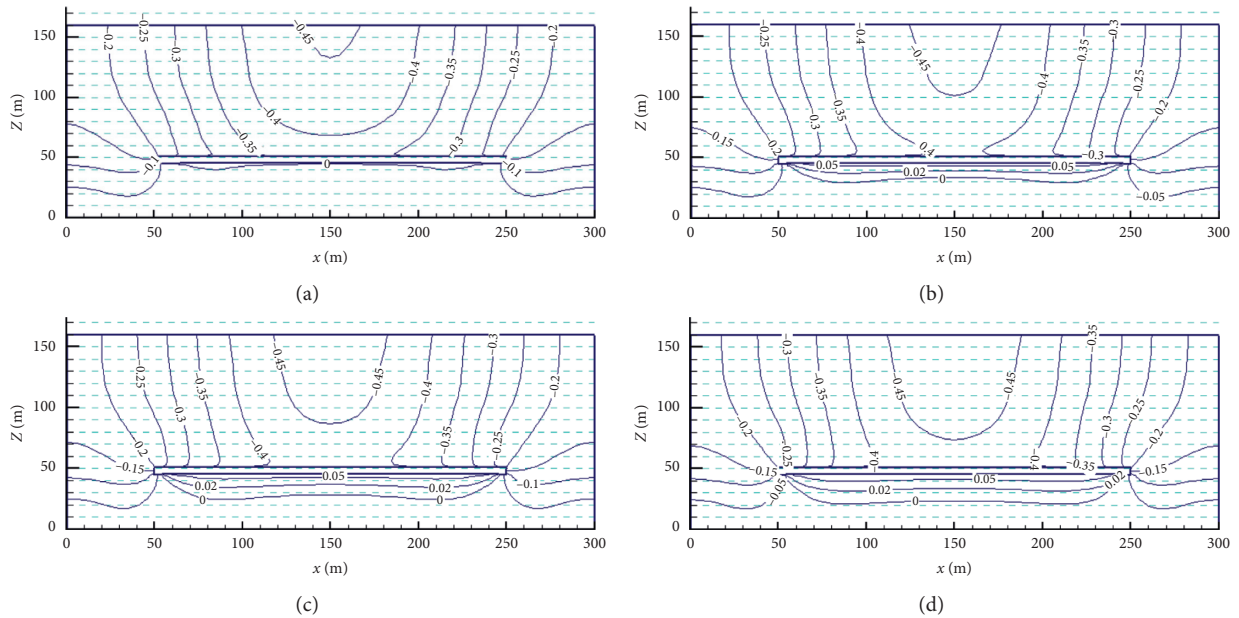


FIGURE 13: Contour map of displacement of the section along the tendency direction. (a) 3 m from coal seam of working face. (b) 5 m from coal seam of working face. (c) 7 m from coal seam of working face. (d) 9 m from coal seam of working face.

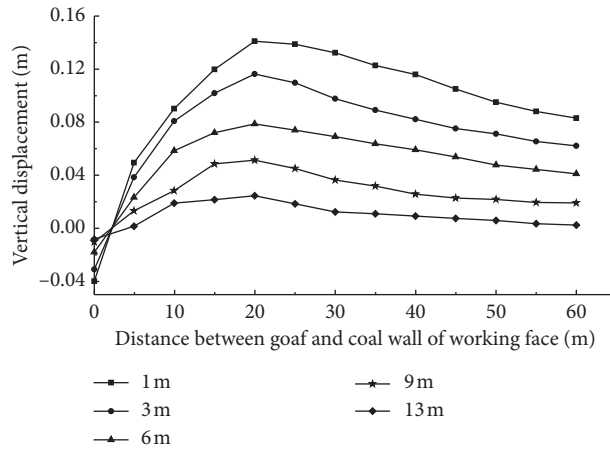


FIGURE 14: Variation of vertical movement with different distance in the floor (centerline of working face).

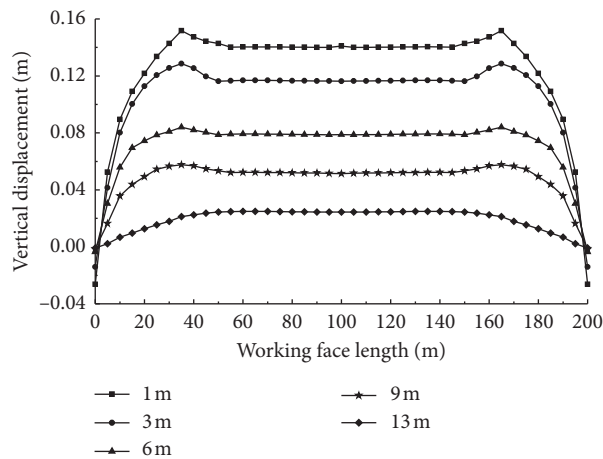


FIGURE 15: Variation of vertical movement with different distance in the floor (coal wall to 20 m in goaf).

13 m is 0.09 m, 0.06 m, and 0.03 m, respectively, which are less than the diameter of the kilometer borehole.

The displacement of the floor at 20 m away from the goaf of the working face reaches its peak, so the displacement at different vertical depths is taken every 5 m along the inclination of the working face, as shown in Figure 15.

As the vertical depth increases, the amount of displacement decreases, and the amount of displacement reaches the peak at the staggered 35 m in the two troughs. At the centerline of the working face, due to the caving of the roof, the displacement is minimal, and the degree of pressure relief and permeability is small relative to the periphery. The displacements at 1 m and 3 m below the vertical depth of the floor vary greatly, and the saddle-like protrusions are very obvious. The displacement difference within 20 m is large, which is likely to cause fractured destruction of the coal body. Therefore, borehole layout in this area is easy to collapse. Below 6 m, the saddle-like protrusions tend to relax obviously, and from 15 m to 45 m in the two troughs, the

displacement does not increase or decrease sharply in a local range. At the same time, this part of the area is located in the “O” circle, the roof falling behind is not easy to compaction, the floor displacement is large, there is no plastic damage, the degree of pressure relief is sufficient, and the permeability of the lower layer is good. Based on the above, the optimal effect of gas drainage can be achieved by arranging more kilometers of boreholes in the range.

6. Conclusions

In this paper, the 205 working face of Tingnan Coal Mine is taken as the background. For the purpose of controlling the stratified pressure-relief gas, the theoretical analysis of the failure depth and type of the floor is carried out by combining the theoretical calculation and numerical simulation. Through the verification of field test, the reasonable range of kilometer drilling is obtained. The specific conclusions are as follows:

- (1) Through theoretical calculation, the maximum plastic failure depth of the floor of 205 working face is 12.89 m, and the maximum failure depth is 6.85 m away from the coal wall of the working face. The lower layer coal is all in the pressure-relief range, resulting in that goaf gas mainly comes from the lower layer pressure-relief coal body. In the stratified mining of extrathick coal seam with high gas, under the effect of “pressure relief and flow increase,” a large number of pressure-relief gases gushed into the working face, which became the main source of gas emission in the working face.
- (2) The numerical simulation of the upper slicing mining of 4# coal seam in 205 working face of Tingnan Coal Mine is carried out. Through the vertical stress analysis of different advancing distances of the working face, the plastic failure degree of each section under different vertical depths of the floor is analyzed. The results show that when advancing to 200 m, the 13 m coal body in the lower slicing is all in the pressure-relief range.
- (3) Numerical simulation is carried out to determine the reasonable range of 205 working face lower layer kilometer drilling. Based on the analysis of the stress distribution, plastic deformation, and displacement of floor, the range and law of the pressure-relief area under the bottom plate are obtained [37].

Data Availability

The data used to support the findings of this study are available from the corresponding author upon request.

Conflicts of Interest

All the authors declare that they have no conflicts of interest.

Acknowledgments

Special thanks are due to Yanwen Zhang for her contribution to this paper in some data analysis work. This research was funded by the Innovative Training Program for College Students (C202012145, C202012135, and C202112003).

References

- [1] F. Du, K. Wang, G. Wang, Y. Huang, and L. Yi, “The mechanism of damage in gas-bearing coal-rock combination bodies and gas seepage in coals,” *Energy Sources, Part A: Recovery, Utilization, and Environmental Effects*, vol. 43, no. 10, pp. 1181–1201, 2021.
- [2] A. Liu, S. Liu, P. Liu, and K. Wang, “Water sorption on coal: effects of oxygen containing function groups and pore structure,” *International Journal of Coal Science and Technology*, vol. 2, pp. 1–20, 2021.
- [3] A. Liu, S. Liu, P. Liu, and S. Harpalani, “The role of sorption-induced coal matrix shrinkage on permeability and stress evolutions under replicated in situ condition for CBM reservoirs,” *Fuel*, vol. 294, Article ID 120530, 2021.
- [4] H. Wang, B. Tan, Z. Shao, Y. Guo, Z. Zhang, and C. Xu, “Influence of different content of FeS₂ on spontaneous combustion characteristics of coal,” *Fuel*, vol. 288, Article ID 119582, 2021.
- [5] H. Wang, X. Fang, F. Du et al., “Three-dimensional distribution and oxidation degree analysis of coal gangue dump fire area: a case study,” *The Science of the Total Environment*, vol. 772, Article ID 145606, 2021.
- [6] F. Du, K. Wang, X. Zhang, C. Xin, L. Shu, and G. Wang, “Experimental study of coal-gas outburst: insights from coal-rock structure, gas pressure and adsorptivity,” *Natural Resources Research*, vol. 29, no. 4, pp. 2481–2493, 2020.
- [7] D. Guo, P. Lv, J. Zhao, and C. Zhang, “Research progress on permeability improvement mechanisms and technologies of coalbed deep-hole cumulative blasting,” *International Journal of Coal Science and Technology*, vol. 7, no. 2, pp. 329–336, 2020.
- [8] X. Li, S. Chen, E. Wang, and Z. Li, “Rockburst mechanism in coal rock with structural surface and the microseismic (MS) and electromagnetic radiation (EMR) response,” *Engineering Failure Analysis*, vol. 124, no. 6, Article ID 105396, 2021.
- [9] K. Wang and F. Du, “Coal-gas compound dynamic disasters in China: a review,” *Process Safety and Environmental Protection*, vol. 133, pp. 1–17, 2020.
- [10] Q. Zou, B. Lin, C. Zheng et al., “Novel integrated techniques of drilling-slotting-separation-sealing for enhanced coal bed methane recovery in underground coal mines,” *Journal of Natural Gas Science and Engineering*, vol. 26, pp. 960–973, 2015.
- [11] D. Fu, G. Xu, L. Ma et al., “Gas generation from coal: taking jurassic coal in the Minhe basin as an example,” *International Journal of Coal Science & Technology*, vol. 7, no. 3, pp. 611–622, 2020.
- [12] S. V. Valiulin, A. A. Onischuk, A. M. Baklanov et al., “Effect of coal mine organic aerosol on the methane/air lower explosive limit,” *International Journal of Coal Science & Technology*, vol. 7, no. 4, pp. 778–786, 2020.
- [13] Q. X. Yu, Y. P. Cheng, C. L. Jiang, and S. N. Zhou, “Principles and applications of exploitation of coal and pressure relief gas in thick and high-gas seams,” *Journal of China University of Mining and Technology*, vol. 33, no. 2, pp. 3–7, 2004.
- [14] X. R. Meng, C. H. Xu, Z. N. Gao, and X. Q. Wang, “Stress distribution and damage mechanism of mining floor,” *Journal of China Coal Society*, vol. 35, no. 11, pp. 1832–1836, 2010.
- [15] P. P. Wang, Y. X. Zhao, Y. D. Jiang et al., “Characteristics and control technology of water inrush from deep coal seam floor above confined aquifer in Xingdong coal mine,” *Journal of China Coal Society*, vol. 45, no. 7, pp. 2444–2454, 2020.
- [16] Y. Zhang, “Mechanism of water inrush of a deep mining floor based on coupled mining pressure and confined pressure,” *Mine Water and the Environment*, vol. 40, pp. 366–377, 2021.
- [17] G. X. Xie and J. C. Chang, “Study on overcutting-bolting & grouting-backfilling concrete to control the floor heave of deep mine roadway,” *Journal of China Coal Society*, vol. 35, no. 8, pp. 1242–1246, 2010.
- [18] X. F. Guo, Y. G. Li, G. D. Zhou, Z. J. He et al., “Stability analysis and reasonable layout of floor drainage roadway above confined water and under mining influence,” *Geofluids*, vol. 2021, Article ID 5578717, 11 pages, 2021.
- [19] A. Liu, S. Tu, F. Wang, Y. Yuan, C. Zhang, and Y. Zhang, “Numerical simulation of pressure relief rule of upper and lower protected coal-seam in thin-protective-seam mining,” *Disaster Advances*, vol. 6, pp. 16–25, 2013.

- [20] H. Z. Zhu, P. Liu, and Z. Y. Tong, "Numerical simulation research and application on protected layer pressure relief affection under different coal pillar width," *Procedia Engineering*, vol. 84, pp. 818–825, 2014.
- [21] W. Zhao, K. Wang, R. Zhang, H. Dong, Z. Lou, and F. An, "Influence of combination forms of intact sub-layer and tectonically deformed sub-layer of coal on the gas drainage performance of boreholes: a numerical study," *International Journal of Coal Science & Technology*, vol. 7, no. 3, pp. 571–580, 2020.
- [22] Y. P. Cheng, D. Y. Zhou, Q. X. Yu, H. X. Zhou et al., "Research on extraction and emission laws of gas for pressure-relief in protecting coal seams," *Journal of Mining & Safety Engineering*, vol. 23, no. 1, pp. 12–18, 2006.
- [23] Q. Zou, H. Liu, Z. Cheng, T. Zhang, and B. Lin, "Effect of slot inclination angle and borehole-slot ratio on mechanical property of pre-cracked coal: implications for ECBM recovery using hydraulic slotting," *Natural Resources Research*, vol. 29, no. 3, pp. 1705–1729, 2020.
- [24] Q. Zou, H. Liu, Y. Zhang, Q. Li, J. Fu, and Q. Hu, "Rationality evaluation of production deployment of outburst-prone coal mines: a case study of Nantong coal mine in Chongqing, China," *Safety Science*, vol. 122, Article ID 104515, 2020.
- [25] J. Lu and K. J. Xiong, "Application of horizontal 1000 m directional drilling rig to mine gas drainage," *Coal Science and Technology*, vol. 39, no. 12, pp. 92–95, 2011.
- [26] X. M. Zhu, T. M. Jiang, and H. D. Miao, "Local gas drainage trial in Sihe mine," *Coal Science and Technology*, vol. 2, pp. 33–35, 2003.
- [27] X. Q. Fang, Y. Q. Geng, and M. Wang, "Kilometer directional drilling: simultaneous extraction of coal and gas from a high gas coal seam," *Journal of China University of Mining and Technology*, vol. 41, no. 6, pp. 885–892, 2012.
- [28] T. Q. Xia, H. Y. Ren, H. Li, and C. K. Du, "A method to remove gas hazard around underground thrust faults kilometer directional featherly drilling," *Thermal Science*, vol. 23, no. 6, pp. 3767–3774, 2019.
- [29] K. Wang, F. Du, and G. Wang, "Investigation of gas pressure and temperature effects on the permeability and steady-state time of Chinese anthracite coal: an experimental study," *Journal of Natural Gas Science and Engineering*, vol. 40, pp. 179–188, 2017.
- [30] H. Wang, X. Yang, F. Du et al., "Calculation of the diffusion coefficient of gas diffusion in coal: the comparison of numerical model and traditional analytical model," *Journal of Petroleum Science and Engineering*, vol. 205, Article ID 108931, 2021.
- [31] X. Wu, Y. Peng, J. Xu, Q. Yan, W. Nie, and T. Zhang, "Experimental study on evolution law for particle breakage during coal and gas outburst," *International Journal of Coal Science & Technology*, vol. 7, no. 1, pp. 97–106, 2020.
- [32] F. Du and K. Wang, "Unstable failure of gas-bearing coal-rock combination bodies: insights from physical experiments and numerical simulations," *Process Safety and Environmental Protection*, vol. 129, pp. 264–279, 2019.
- [33] Y. B. Guan, H. M. Li, and J. C. Lu, "Research on No. 9 coal seam floor's fracture regularity in Xiandewang coal mine," *Journal of China Coal Society*, vol. 28, no. 2, pp. 121–125, 2003.
- [34] F. K. Xiao, L. Q. Duan, and Z. H. Ge, "Laws of floor breaking in coal mining face and gas extraction application," *Journal of China Coal Society*, vol. 35, no. 3, pp. 417–419, 2010.
- [35] C. Xin, F. Du, K. Wang, C. Xu, S. Huang, and J. Shen, "Damage evolution analysis and gas-solid coupling model for coal containing gas," *Geomechanics and Geophysics for Geo-Energy and Geo-Resources*, vol. 7, no. 1, p. 7, 2021.
- [36] Q. X. Qi, W. B. Ji, J. H. Yuan, Z. H. Cheng et al., "Theory, in-situ observation on the floor connected crack field and its effects on methane extraction," *Journal of China Coal Society*, vol. 39, no. 8, pp. 1552–1558, 2014.
- [37] X. Y. Yu, Q. Wang, B. C. Zhao, and L. F. Wang, "Analysis on mine strata pressure law of high cutting coal mining face and suitability of powered support," *Coal Technology*, vol. 33, no. 5, pp. 154–156, 2014.